Wavefront shaping approaches for spectral domain optical coherence tomography

Von der Fakultät für Mathematik und Physik
der Gottfried Wilhelm Leibniz Universität Hannover

zur Erlangung des akademischen Grades
Doktor der Naturwissenschaften
Dr. rer. nat.

genehmigte Dissertation von

M.Sc. Jonas Peter Kanngießer

2020

Referent:	Prof. Dr. habil. Bernhard Roth Hannoversches Zentrum für Optische Technologien Leibniz Universität Hannover
Korreferent:	Prof. Dr. habil. Alexander Heisterkamp Institut für Quantenoptik Leibniz Universität Hannover
Korreferent:	Prof. Dr.-Ing. habil. Wolfgang Kowalsky Institut für Hochfrequenztechnik Technische Universität Braunschweig
Tag der Promotion:	16.10.2020

Für Kathleen

Abstract

Optical coherence tomography (OCT) enables sub-surface three dimensional imaging with micrometer resolution. The technique is based on the time-of-flight gated detection of light which is backscattered from a sample and has applications in non-destructive testing, metrology and contact-less and non-invasive medical diagnostics. With scattering media such as the human skin, the penetration depth is limited to just a few millimetres, on the other hand, and OCT imaging hence allows to investigate superficial sample layers only.

Scattering of light is a deterministic process. As a consequence, manipulation of the beam incident to a turbid sample yields control over the scattered field. Following this approach, a number of groups demonstrated iterative wavefront optimization algorithms to be able to focus light transmitted through or backscattered from opaque media. First applications to optical coherence tomography were shown to extend the penetration depth as well as to improve the signal-to-noise ratio when imaging biological tissue.

This work explores practical approaches to combine wavefront shaping techniques with OCT imaging. To this end, a compact spectral domain (SD-) OCT design is developed which enables single-pass and independent wavefront control at the reference and at sample beam. Iterative optimization of the phase pattern applied to the sample beam is shown to selectively enhance the amplitude of the OCT signal received from scattering media. In a more sophisticated approach, the acquisition of the time-resolved reflection matrix, which yields the linear dependence of the OCT signal on the field at the sample beam, is demonstrated. Subsequent wavefront optimization based on a phase conjugation algorithm is shown to enhance the OCT signal but not image artefacts, even though no attempt is made to actively suppress these artefacts. The approach is comparable to iterative wavefront optimization but yields a substantially improved acquisition speed. First imaging applications demonstrate the algorithm to enhance the signal-to-noise ratio and the penetration depth with scattering media, such as biological tissue, and to reduce the observed speckle contrast, similar to compounding algorithms. Furthermore, the acquisition of the reflection matrix and subsequent signal enhancement based on binary amplitude-only (on/off) beam shaping is presented for the first time. The technique can be implemented with digital micromirror devices which enable high-speed implementations.

The presented techniques constitute substantial improvements compared to previous works and yield promising results in the context of depth-enhanced OCT imaging with scattering biological tissue. Approaches to further enhance the performance and the acquisition speed for real-time *in-vivo* imaging applications are discussed.

Keywords optical coherence tomography (OCT), interferometry, turbid media, wavefront shaping, phase conjugation

Contents

1 Introduction **1**

2 Principles of optical coherence tomography **5**
2.1 Time-domain OCT . . . 5
2.1.1 Axial ranging . . . 7
2.1.2 Axial resolution and impact of spectral bandwidth . . . 8
2.1.3 Imaging . . . 9
2.2 Fourier-domain OCT . . . 11
2.2.1 Axial ranging and image artefacts . . . 12
2.2.2 Imaging . . . 15
2.2.3 Phase shifting approaches . . . 17
2.2.4 Practical aspects of SD-OCT . . . 19
2.3 Imaging scattering biological tissue . . . 20
2.3.1 Optical properties of biological tissue . . . 21
2.3.2 Impact of scattering on OCT imaging . . . 22

3 Principles of wavefront shaping **25**
3.1 Adaptive optics . . . 25
3.2 Time reversal and phase conjugation . . . 27
3.2.1 Imaging applications and the optical memory effect . . . 28
3.3 Iterative wavefront shaping . . . 30
3.3.1 Principles . . . 30
3.3.2 Feedback types and imaging applications . . . 33
3.3.3 Algorithms . . . 34
3.3.4 Acquisition time . . . 35
3.4 Transmission matrix approaches . . . 36
3.4.1 Principles and acquisition . . . 37
3.4.2 Application to focusing . . . 40
3.4.3 Imaging applications . . . 41
3.4.4 Singular value decomposition . . . 42
3.4.5 Acquisition time and enhancements . . . 43

4 State of the art: Applications of wavefront shaping to optical coherence tomography **45**
4.1 OCT designs . . . 45
4.2 Exploiting the reflection matrix to suppress multiple scattered light . . . 46
4.3 Spectral and temporal shaping of scattered light . . . 48

4.4 Wavefront shaping techniques for direct OCT signal enhancement 51
4.4.1 Technical implementation 51
4.4.2 Non-invasive focusing 52
4.4.3 Depth-enhanced imaging 53
4.5 Remaining problems 54

5 Double interferometer OCT design for independent beam shaping 57
5.1 Experimental design 57
5.1.1 Optical design 57
5.1.2 Experimental implementation 59
5.1.3 Data acquisition 60
5.2 SLM calibration and characterization 61
5.2.1 Principles 61
5.2.2 Polarizer alignment 61
5.2.3 Beam position calibration 62
5.2.4 Switching time 62
5.2.5 Phase shifting characteristics and correction 63
5.2.6 Dispersion 65
5.3 OCT calibration and characterization 68
5.3.1 Spectral calibration 68
5.3.2 Spatial resolution 68
5.3.3 Spectral resolution and axial sensitivity 69
5.4 Analysis of the design 71
5.4.1 Analytic model 71
5.4.2 Numerical calculation 75
5.4.3 Independent phase manipulation 75
5.4.4 Experimental phase manipulation 76
5.4.5 Independent beam shaping 76

6 Iterative wavefront shaping 79
6.1 Algorithm and implementation 79
6.2 Local signal enhancement 80
6.2.1 Axial localization 80
6.2.2 Lateral localization 82
6.3 Comparison to adaptive optics 84
6.4 Imaging applications 86

7 Reflection matrix approach 89
7.1 Matrix formalism applied to spectral domain OCT 89
7.1.1 Definition of the time-resolved reflection matrix 89
7.1.2 Phase conjugation applied to optical coherence tomography 92
7.2 Experimental implementation 93
7.2.1 Reflection matrix acquisition 93
7.2.2 Phase conjugation 94

7.2.3 Speckle compounding . . . 94
7.3 Selective signal enhancement with artefact suppression . . . 95
7.4 Impact of image artefacts . . . 96
7.4.1 Target signal dominated by mutual interference components . . . 98
7.4.2 Target signal dominated by mirror artefacts . . . 98
7.4.3 Target signal dominated by autocorrelation artefacts . . . 100
7.4.4 Impact of the double interferometer OCT design . . . 100
7.4.5 Overlapping signal components . . . 101
7.4.6 Experimental validation . . . 102
7.5 Quantitative signal enhancement . . . 103
7.6 Axially extended signal enhancement . . . 106

8 Reflection matrix approach applied to binary amplitude-only wavefront shaping 109
8.1 Principles . . . 109
8.1.1 Matrix acquisition . . . 109
8.1.2 OCT signal enhancement . . . 109
8.2 Experimental implementation . . . 111
8.2.1 Reflection matrix acquisition . . . 111
8.2.2 Mode superposition approach . . . 111
8.2.3 Segment superposition approach . . . 112
8.3 Selective signal enhancement . . . 113
8.4 Impact of image artefacts . . . 114
8.5 Quantitative signal enhancement . . . 116

9 Imaging Applications 121
9.1 Principles . . . 121
9.2 Impact of phase conjugation on imaging . . . 122

10 Discussion 127
10.1 Double interferometer OCT design . . . 127
10.2 Acquisition speed and improvements . . . 127
10.2.1 Reflection matrix acquisition . . . 128
10.2.2 Image acquisition . . . 130
10.3 Comparison of phase-only and binary amplitude-only wavefront control . 131
10.4 Depth enhanced imaging . . . 132
10.5 Applications and outlook . . . 133

11 Conclusion 135

References 151

Resume 153

List of publications 155

Acknowledgements 159

List of Figures

2.1 Principle of optical coherence tomography 6
2.2 Axial ranging with time-domain OCT 10
2.3 Principle of OCT imaging 11
2.4 Axial ranging with Fourier domain OCT 13
2.5 SD-OCT imaging and image artefacts 17
2.6 Phase shifting approaches for SD-OCT imaging 18
2.7 OCT image of the human fingernail and nailfold region 21
2.8 Impact of scattering on OCT imaging 23

3.1 Principle of closed-loop sensor based adaptive optics 26
3.2 Principle of time reversal and phase conjugation 28
3.3 Principle of digital optical phase conjugation 29
3.4 Principle of the optical transmission matrix 31
3.5 Principle of iterative wavefront shaping 32
3.6 Experimental designs for transmission matrix acquisition 37
3.7 Self-referenced transmission matrix measurement 39

4.1 OCT designs enabling wavefront manipulation 46
4.2 Coupling of temporal and spatial degrees of freedom in a scattering medium 49

5.1 Experimental design 58
5.2 Photograph of the experimental design 59
5.3 Estimation of SLM switching time 63
5.4 Principle of self-referenced two-beam interferometry for SLM calibration . 64
5.5 SLM phase modulation characteristics and gamma correction 65
5.6 Principle of SLM dispersion measurement 66
5.7 SLM dispersion 67
5.8 Depth of field of the OCT system 69
5.9 Impact of spectral resolution on the SD-OCT signal 70
5.10 Model of the OCT design 72
5.11 Calculated double interferometer OCT signal 74
5.12 SLM-based phase shifting with the OCT system 77

6.1 Iterative wavefront shaping with a layered sample and misaligned reference beam 81
6.2 Impact of sample displacement on signal enhancement through wavefront shaping 83
6.3 Effect of sensorless adaptive optics correction on the OCT signal 84

6.4 Impact of sample displacement on the OCT signal with adaptive optics correction . . . 85
6.5 Full A-scan optimization with iterative wavefront shaping . . . 87

7.1 Selective signal enhancement through phase conjugation . . . 96
7.2 Full A-scan optimization with phase conjugation . . . 97
7.3 Effect of phase conjugation on mutual interference and mirror signals . . . 99
7.4 Impact of image artefacts on phase conjugation . . . 102
7.5 Quantitative signal enhancement . . . 105
7.6 Phase conjugation with extended targets . . . 107

8.1 Principle of binary amplitude-only wavefront manipulation . . . 110
8.2 Signal enhancement through binary amplitude-only wavefront manipulation 113
8.3 Impact of image artefacts on the mode superposition algorithm . . . 115
8.4 Impact of image artefacts on the segment superposition algorithm . . . 116
8.5 Quantitative signal enhancement with binary amplitude-only wavefront modulation . . . 119

9.1 Pseudocode for SD-OCT imaging based on phase conjugation with the time-resolved reflection matrix . . . 122
9.2 Application of phase conjugation to imaging . . . 123
9.3 SNR estimation of the enhanced OCT signal . . . 124
9.4 Phase conjugation with biological tissue . . . 125

10.1 Double interferometer design implemented with a commercial SD-OCT system . . . 128

List of Abbreviations

OCT	optical coherence tomography
TD-OCT	time domain optical coherence tomography
FD-OCT	Fourier domain optical coherence tomography
SD-OCT	spectral domain optical coherence tomography
SS-OCT	swept source optical coherence tomography
FF-OCT	full field optical coherence tomography
FFT	fast Fourier transform
IFFT	inverse fast Fourier transform
DFT	discrete Fourier transform
IDFT	inverse discrete Fourier transform
IFT	inverse Fourier transform
FWHM	full width at half maximum
HWHM	half width at half maximum
NA	numerical aperture
DOF	depth of field
FOV	field of view
SNR	signal-to-noise ratio
PSF	point spread function
LSP	least scattered photons
MSP	multiple scattered photons
LC	liquid crystal
LCOS	liquid crystal on silicon
PAN	parallel aligned nematic
LUT	look up table
SLM	spatial light modulator
MEMS	micro-electro-mechanical system
DM	deformable mirror
DMD	digital micromirror device
CASS	collective accumulation of single scattering

1 Introduction

Optical coherence tomography (OCT) is a non-invasive technique which enables sub-surface three dimensional imaging with micrometer resolution. In principle, the approach utilizes broadband light sources which feature a low coherence length as well as an interferometric detection scheme to determine the time-of-flight distribution of light which is backscattered from a partially transparent sample. Neglecting the effects of multiple scattering, the time-of-flight directly reflects the penetration depth of light in the sample and, hence, allows to locate the position of backscattering sample features. The technique was introduced in 1991, almost 30 years ago, by the group of James Fujimoto [1]. The potential for medical diagnostics was quickly realized and led to the first commercial system to be released already in 1996 (*Stratus*, Humphrey Systems, now Carl Zeiss Meditec, Germany) [2]. Nowadays, OCT imaging has become a major tool in the clinical field of ophthalmology due to the capability of high-resolution *in-vivo* three dimensional retinal imaging [3, 4]. Further applications include gastrointestinal [5, 6], intravascular [7, 8], dermatological [9–12] or dental diagnostics [13, 14] as well as functional extensions such as polarization sensitive [15, 16], spectroscopic [17–19] or angiographic OCT [20–22], which allow to investigate the tissue birefringence, the chemical structure, or the perfusion non-invasively, respectively.

The image contrast of OCT systems is based on the capability to suppress multiple scattered light, which features a random time-of-flight distribution, compared to weakly scattered signal components whose time-of-flight corresponds to the position of reflective sample features. Due to strong scattering of light, the penetration or imaging depth with biological samples such as the human skin typically is restricted to values in the range of one to two millimetres [9, 11, 12]. As a consequence, the diagnostic value is limited with such samples in case relevant features, for example tissue lesions or pathological changes, extend beyond that range.

On the other hand, scattering of light is a deterministic process in case the turbid sample is assumed to be static. In terms of linear system theory, for example, the turbid medium can be considered to be described by a highly complicated but constant transfer function. As a consequence, light which is transmitted trough or reflected from the sample can be manipulated by shaping the wavefront of the incident beam. In a seminal work, the first experimental implementation was presented in 2007 by Ivo Vellekoop and Allard Mosk, who demonstrated an iterative wavefront optimization algorithm to be able to create a focus from scattered light [23]. The approach resulted in a high number of similar works to follow with applications for focusing and imaging through turbid media and biological tissue. In another approach, Sébastien Popoff et al. demonstrated the acquisition of the optical transmission matrix of a scattering sample in 2010 [24]. The transmission matrix describes the linear dependence of scattered light on the beam

which is incident to the sample, similar to the transfer function. The approach allows to investigate the sample's scattering properties and has applications for focusing and imaging with turbid media as well.

The combination of iterative wavefront shaping with optical coherence tomography was initially demonstrated by Reto Fiolka et al. in 2012 [25]. The group demonstrated the approach to be able to non-invasively focus light to small particles which are hidden behind a scattering layer or behind biological tissue. First imaging applications were demonstrated by Jaeduck Jang et al. in 2013 [26]. The group utilized an iterative algorithm to optimize the wavefront at the sample beam of a spectral domain optical coherence tomography (SD-OCT) system. The approach was shown to enhance the amplitude of the detected OCT signal, and, in later works, the signal-to-noise ratio (SNR) and the penetration depth when imaging scattering media and biological tissue [27–29]. The technique requires a rather high number of signal acquisitions, on the other hand, and is too slow for typical *in-vivo* imaging applications. In another approach, Youngwoon Choi et al. presented the acquisition of the time-resolved reflection matrix in 2013 [30]. Similar to the transmission matrix, the reflection matrix describes the dependence of the time-of-flight gated backscattered field, which is the acquired OCT signal, on the field which is applied to the sample beam. The reflection matrix can be captured with a SD-OCT system and applications to selectively enhance the amplitude of the detected OCT signal were demonstrated [30]. The technique is comparable to iterative wavefront optimization but allows to significantly increase the acquisition speed. Applications to depth-enhanced OCT imaging are not reported to date, though.

Previous works demonstrated wavefront shaping techniques to yield promising results in the context of depth-enhanced OCT imaging with scattering media, for example for non-invasive deep tissue diagnostics. On the other hand, publications are scarce and a number of open questions on how the OCT signal is affected by the approach remain. A system which is sufficiently fast for typical *in-vivo* imaging applications is not yet demonstrated, as well. This work extends on the previous results and provides a detailed literature survey to review the current state of the art. A compact experimental design for wavefront modulation at the sample beam of a SD-OCT system is presented which can be implemented with high-speed commercial systems. With this system, a number of different wavefront shaping approaches, including iterative optimization, phase conjugation based on the time-resolved reflection matrix and binary amplitude-only (on/off) wavefront shaping, are investigated. Principal effects on the resulting OCT signal are discussed. First imaging applications are shown to increase the contrast and the penetration depth of the OCT signal when imaging biological tissue.

This work is structured as follows: **Chapter 2** discusses principles and fundamentals of time-domain and spectral domain optical coherence tomography as well as the impact of scattering. The analytic discussion will be required for later chapters. **Chapter 3** presents fundamentals of wavefront shaping techniques and closely related approaches. Applications for focusing and imaging with strongly scattering media are reviewed. **Chapter 4** elaborates on the application of these approaches to focusing with broad-band light sources and to OCT imaging. Techniques for depth enhanced OCT imaging through wavefront shaping are discussed.

Chapters 5 to 9 present the main results achieved in this work. In **Chapter 5** a compact SD-OCT design is described which enables independent wavefront control at the reference and at the sample beam, respectively. The setup is used for the experimental part of this work and details about implementation, data processing and calibration are given. Furthermore, an analytic model is presented to demonstrate how the design performs compared to a conventional OCT system. The model is supported by numerical and experimental data. The focus of **Chapter 6** is on optical coherence tomography combined with iterative wavefront optimization at the sample beam. The approach is compared to sensorless adaptive optics, which is implemented with the same experimental design, and is shown to locally enhance the amplitude of the OCT signal. **Chapter 7** discusses on a comparable approach which is based on the acquisition of the time-resolved reflection matrix from the SD-OCT signal and on a phase conjugation algorithm for subsequent wavefront optimization. The technique yields a substantial improvement in acquisition speed compared to the iterative approach. In **Chapter 8** the acquisition of the time-resolved reflection matrix and subsequent wavefront optimization is demonstrated with binary amplitude-only beam shaping. **Chapter 9** presents first imaging applications of phase conjugation with the time-resolved reflection matrix. A final critical review of the techniques demonstrated in this work is presented in **Chapter 10**. Potential applications and approaches to further enhance the performance aiming towards *in-vivo* imaging are discussed.

2 Principles of optical coherence tomography

Optical coherence tomography (OCT) enables non-invasive label-free three-dimensional imaging with microscopic resolution. The technique is closely related to white light and low coherence interferometry as well as to optical coherence domain reflectometry which was originally developed to locate defects in optical fibres [31, 32] and soon proved to be feasible for biomedical imaging [33, 34]. The group of James Fujimoto presented the first OCT system for imaging of *ex-vivo* biological tissue in 1991 [1]. First *in-vivo* imaging applications were presented in 1993 independently by Fercher et al. [35] and by Swanson et al. [36]. OCT systems were found to be well-suited for ophthalmic diagnostics. Features of interest, such as the human retina, are rather thin and obstructed by transparent structures of the eye only. The first commercial ophthalmic OCT system was released in 1996 (*Stratus*, Humphrey Systems, now Carl Zeiss Meditec, Germany) [2]. The utilization of near-infrared light sources centred at 1300 nm enabled OCT imaging with thick biological tissue due to weaker scattering compared to 800 nm sources, which are used for ophthalmic OCT devices, and brought the technique to other clinical fields [37–39]. Since those early applications, OCT systems underwent major technological advancements resulting from novel light sources, improved detectors and detection schemes as well as enhanced data processing algorithms and extensions for functional imaging. OCT has become a major diagnostic tool for ophthalmology [2–4]. Further applications include dermatological [9–12] or dental diagnostics [13, 14] to just name a few. The implementation of endoscopic OCT probes enabled gastrointestinal [5, 6] and intravascular [7, 8] imaging. Functional extensions include spectroscopic OCT which enables three dimensional imaging while yielding additional spectroscopic information of the sample [17–19] as well as angiographic OCT which allows to quantify the perfusion of living tissue non-invasively [20–22].

2.1 Time-domain optical coherence tomography

OCT is based on the interference of broadband light which allows to determine the time-of-flight or the optical path length distribution of the electromagnetic wave reflected at a sample. Typically, OCT systems use point-wise sample illumination, i.e. the beam is focused at the sample similar to confocal microscopy. The reflected beam is collected by the imaging optics and superimposed with a static reference beam which has a well-known optical path length. A sensor detects the intensity of the superimposed reference and sample beam. Interference is detected only in case the optical path length difference of both beams is smaller than the coherence length of the light source. Scanning the

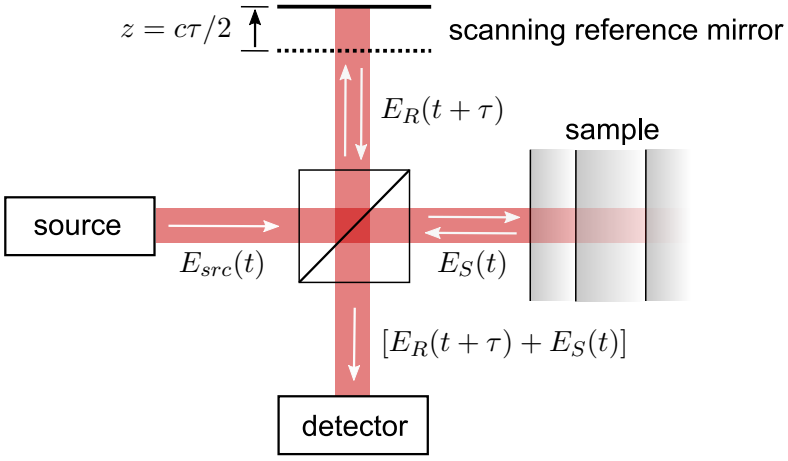

Figure 2.1: **Principle of optical coherence tomography** The technique is comparable to a Michelson interferometer with the sample placed at one interferometer arm. Scanning the length of the reference arm allows to determine the time-of-flight of the beam which is backscattered from the sample. Variables are discussed in the text body.

length of the reference arm while observing the amplitude of the interference signal, hence, allows to determine the time-of-flight or the optical path length at the sample beam, which corresponds to the distance between the reflection site and the OCT system. Most samples are partially transparent and light reflected from sub-surface layers of the sample can be detected as well. Point-wise sample illumination, thus, yields the sample's depth-resolved reflectivity profile parallel to the beam axis. This signal is termed *A-scan* analogue to ultrasonic imaging. Laterally scanning the sample beam in one direction yields a cross-sectional image perpendicular to the sample surface, termed *B-scan*. The position of the sample surface as well as the sample's internal structure can be determined from this signal, for example. Lateral scanning in two direction yields a three-dimensional volume scan.

The principle of optical coherence tomography is well-understood by considering a Michelson interferometer with the sample placed at one interferometer arm (Fig. 2.1). The beam incident to the interferometer is described by it's electric field $\widetilde{E}_{src}$, which is coupled to the magnetic field through Maxwell's equations. Considering one-dimensional propagation parallel to the optical axis and neglecting polarisation effects, the field can be described by a superposition of plane waves with angular frequency ω, wavenumber k and spectrum $s(\omega)$ [40]:

$$\widetilde{E}_{src}(z',t) = \Re\{E_{src}(z',t)\} \tag{2.1}$$

$$E_{src}(z',t) = \int_0^\infty s(\omega) e^{i(kz'-\omega t)}\, d\omega \tag{2.2}$$

z' and t yield the axial and temporal coordinates, respectively. In case linear operations are considered only, it is valid to describe the source beam by it's analytic field $E_{src}(z',t)$

[40]. The intensity of the electromagnetic field is proportional to $\left\langle |E_{src}|^2 \right\rangle$ with angle brackets denoting temporal averaging [40].

The incident field E_{src} is divided at the beamsplitter, reflected at the two interferometer arms, recombined and detected. The field in the plane of the detector, thus, reads $E_R(t) + E_S(t)$, where E_R describes the field returned from the reference arm and E_S the field returned from the sample. Displacing the reference mirror by the distance z increases the length of the reference arm and introduces an additional temporal delay $\tau = 2\,z/c$ to the reflected reference beam. The intensity of the superimposed beams reads at the detector [40–43]:

$$\begin{aligned} I^{TD}(\tau) &\propto \left\langle |E_R(t+\tau) + E_S(t)|^2 \right\rangle \\ &= \left\langle |E_R(t)|^2 \right\rangle + \left\langle |E_S(t)|^2 \right\rangle + 2\Re\{\Gamma_{RS}(\tau)\} \end{aligned} \tag{2.3}$$

The first two terms correspond to the intensity returned from the reference and sample beam, respectively. The third term yields the interference of the two beams which is described by the real part of the field cross-correlation $\Gamma_{RS}(\tau)$, which is also termed cross coherence or mutual coherence function [40, 41, 44, 45]:

$$\Gamma_{RS}(\tau) = \langle E_R(t+\tau) E_S^*(t) \rangle \tag{2.4}$$

$$\Gamma_{RS}(\tau) = \Gamma_{SR}^*(-\tau) \tag{2.5}$$

2.1.1 Axial ranging

In this Section, the cross-correlation $\Gamma_{RS}(\tau)$ is shown to reflect the time-of-flight distribution of the backscattered sample beam. The effect allows to determine the axial position of backscattering sample features and, thus, enables three dimensional imaging.

We consider the field of the source beam to read $E_{src}(t)$ at a single plane (fixed coordinate z') in front of the interferometer. Within the presented one dimensional model, the field $E_R(t)$, which is reflected from the reference arm and which is observed at the detector, is temporally delayed by $t_R = 2\,l_R/c$ compared to the source field. l_R is the length of the reference arm and t_R yields the corresponding (double-pass) time-of-flight. Assuming a 50:50 intensity splitting ratio for the beam splitter, the reference field reads at the detector:

$$E_R(t) = \frac{1}{2} r_R E_{src}(t + t_R) \tag{2.6}$$

The factor r_R describes the amplitude reflectivity of the reference mirror.

In a similar way we may consider a one dimensional sample featuring N reflective layers which are displaced by the distance l_{sn} from the beamsplitter, respectively [46]. The number n corresponds to the layer index. The field reflected from the sample, thus, reads:

$$E_S(t) = \frac{1}{2} \sum_{n=1}^{N} r_{sn} E_{src}(t + t_{sn}) \tag{2.7}$$

The factor r_{sn} describes the amplitude reflectivity of the individual sample layers. $t_{sn} = 2\,l_{sn}/c$ yields the temporal delay corresponding to the individual reflections. For the sake of simplicity a uniform sample refractive index is assumed.

The field cross-correlation resulting from interference of the reference and sample beam reads:

$$\Gamma_{RS}(\tau) = \frac{1}{4} r_R \sum_{n=1}^{N} r_{sn}^{*} \left\langle E_{src}(t+\tau+t_R) E_{src}^{*}(t+t_{sn}) \right\rangle \tag{2.8}$$

$$= \Gamma_{src}(\tau) \circledast \frac{1}{4} r_R \sum_{n=1}^{N} r_{sn}^{*} \delta(\tau - (t_{sn} - t_R)) \tag{2.9}$$

$\Gamma_{src}(\tau)$ yields the autocorrelation of the source field $E_{src}(t)$ which is also termed (temporal) coherence or self coherence function [40, 44]. The field autocorrelation is calculated similar to the cross-correlation (Eq. 2.4). $\delta(\tau)$ describes the delta distribution, the operator $\circledast$ indicates convolution with respect to the temporal coordinate τ.

Equation 2.9 reveals the capability of optical coherence tomography for axial ranging. The cross-correlation $\Gamma_{RS}(\tau)$ features signal peaks which are centred at $\tau = t_{sn} - t_R$ and which are scaled by $|r_{sn}|$. The peak position, thus, reflects the time-of-flight t_{sn} which corresponds to backscattering at the individual sample layers subtracted by the time-of-flight t_R of the reference beam. The peak amplitude corresponds to the reflectivity of the respective sample layers. The shape and the width of the peaks, and hence the temporal resolution, is described by the coherence function $\Gamma_{src}(\tau)$ of the light source.

The time-of-flight directly relates to the single-pass optical path length $z = c\tau/2$. Neglecting the effects of multiple scattering, the penetration depth of light into the sample, and hence the physical position of backscattering layers, can be determined from the optical path length and from the sample‘s refractive index profile. The OCT signal, hence, typically is illustrated in terms of the path length scale z rather than in terms of the time-of-flight τ.

2.1.2 Axial resolution and impact of spectral bandwidth

The coherence function of the light source is determined by it's spectrum. According to the Wiener Khinich theorem, the power spectral density and the field autocorrelation, which is the self coherence function $\Gamma_{src}(\tau)$, form a Fourier transform pair [44–47]. The coherence function, thus, is found from the inverse Fourier transform (IFT) of the source power spectral density $S(\omega) = |s(\omega)|^2$ (compare Eq. 2.2):

$$\Gamma_{src}(\tau) = \frac{1}{2\pi} \int_{-\infty}^{\infty} S(\omega) e^{i\omega t}\, d\omega \tag{2.10}$$

Assuming a Gaussian source spectrum centred at ω_0, with spectral bandwidth Δ_ω and with total (spectrally integrated) power S_0, the corresponding coherence function is found to be Gaussian, as well [46, 48]:

$$S(\omega) = S_0 \frac{1}{\sqrt{2\pi\Delta_\omega^2}} e^{-\frac{(\omega-\omega_0)^2}{2\Delta_\omega^2}} \tag{2.11}$$

$$\Gamma_{src}(\tau) = S_0 \frac{1}{2\pi} e^{-\frac{1}{2}\Delta_\omega^2\tau^2} e^{i\omega_0\tau} \tag{2.12}$$

The temporal width of the coherence function, thus, reads $\Delta_\tau = 1/\Delta_\omega$. The corresponding full width at half maximum (FWHM) reads $\Delta_\tau^{FWHM} = 8\,ln(2)/\Delta_\omega^{FWHM}$. Typically, it is more convenient to determine the spectrum of the light source in terms of the wavelength λ, though. Assuming the source central wavelength to be λ_0, the FWHM of the coherence function reads [43, 49]:

$$\Delta_\tau^{FWHM} = \frac{4\,ln(2)}{\pi c} \frac{\lambda_0^2}{\Delta_\lambda^{FWHM}} \tag{2.13}$$

In general, a large source spectral bandwidth yields a sharply peaked coherence function and, hence, in a high temporal resolution of the OCT system.

2.1.3 Imaging

Figure 2.2(a) illustrates a schematic time domain optical coherence tomography (TD-OCT) system which is similar to the previous model (Fig. 2.1). TD-OCT systems capture the intensity of the superimposed reference and sample beam at a point detector while scanning the length z or the temporal delay $\tau = 2\,z/c$ at the reference beam. A full scan yields a single depth scan, also termed A-scan, at the point at which the sample is illuminated.

Figure 2.2(b) illustrates the A-scan signal which is expected with a layered sample according to the previous discussion. The signal features a constant offset which corresponds to the summed intensities of the reference and sample beam and which results from the incoherent superposition of both beams (Eq. 2.3). Rapidly oscillating signal peaks are observed in case the time-of-flight at the reference beam matches the time-of-flight which is corresponding to a reflection at the sample (compare Eq. 2.9). Speaking in terms of reference mirror displacement, signal peaks are observed in case the length of the reference arm matches the distance between the OCT system and the reflecting sample layer. The mirror displacement z, hence, directly corresponds to the optical path-length scale of the OCT scan.

The envelope of the interference peaks is described by the normalized source coherence function $|\Gamma_{src}(\tau)|$. The axial resolution of the TD-OCT system hence corresponds to the FWHM of these peaks. In terms of the mirror displacement z, this value reads (compare Eq. 2.13) [43, 49]:

$$\Delta_z^{FWHM} = \frac{c}{2}\Delta_\tau^{FWHM} \tag{2.14}$$

The A-scan, i.e. the sample‘s axial reflectivity profile, is acquired from the envelope of the TD-OCT signal. This quantity is experimentally accessibly by rectifying and low-pass filtering the AC signal (Fig. 2.2(b)), for example.

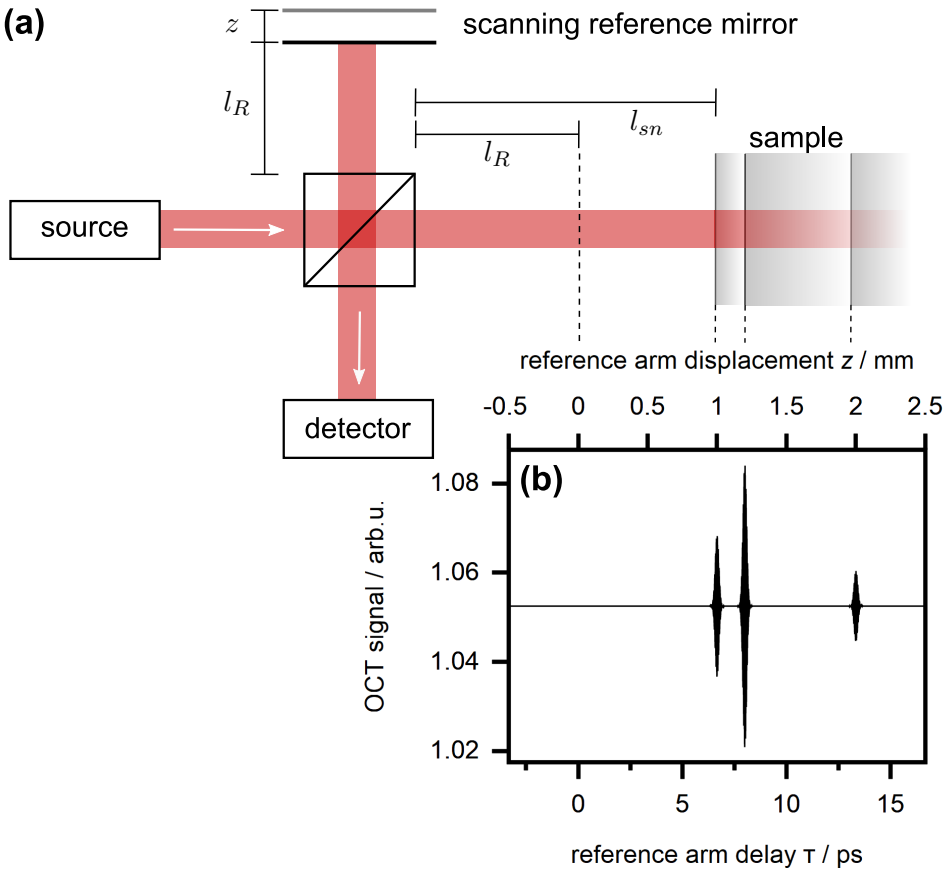

Figure 2.2: **Axial ranging with time-domain OCT** (a) Schematic interferometer setup. (b) Expected TD-OCT signal in terms of temporal delay τ at the reference arm or in terms of mirror displacement z. A rapidly oscillating interference signal is observed whenever the total reference arm length $l_R + z$ matches the path length l_{sn} corresponding to a reflection at the sample.

A schematic of a typical OCT setup for imaging applications is illustrated in Fig. 2.3. Most OCT designs employ fibre optic components due to their compactness and high optical stability compared to free space designs [46]. An interferometric detection scheme equivalent to a Michelson interferometer can be created with a single two by two fibre optic coupler (Fig. 2.3). A low numerical aperture (NA) objective lens is used to focus the sample beam at the specimen. Scanning the length of the reference arm yields the sample‘s depth-resolved reflectivity profile at the point of illumination. Additional mirror scanners allow to displace the sample beam laterally to acquire multiple depth profiles at different positions. Lateral beam scanning in one direction, hence, yields cross-sectional sample images, scanning in two directions yields volume images.

The lateral resolution of the OCT system depends on the beam size at the sample. The sample beam optics can be treated similar to a confocal setup, with the confocal pinhole

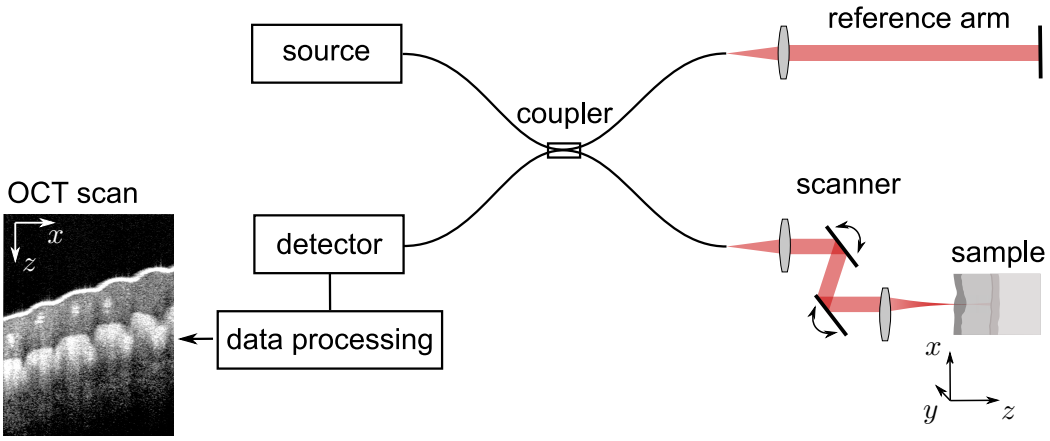

Figure 2.3: **Principle of OCT imaging** Most practical OCT systems are based on fibre optic interferometers. A set of scanning mirrors allows to scan the sample beam laterally to enable cross-sectional and volume imaging.

created by the optical fibre (Fig. 2.3) [46]. For such a system the lateral resolution Δ_x^{FWHM} reads [46]:

$$\Delta_x^{FWHM} = 0.37 \frac{\lambda_0}{\mathrm{NA}} \tag{2.15}$$

The number Δ_x^{FWHM} corresponds to the intensity FWHM which is detected from a point reflector placed in the focal plane of the objective lens in case the sample is laterally scanned.

The depth of field (DOF) describes the axial range at which the sample beam remains tightly focused. The DOF depends on the Rayleigh length of the sample beam and, hence, becomes smaller in case the sample beam is more tightly focused. With most OCT systems, low NA objective lenses are used to achieve a large DOF. Axial imaging is performed by scanning the reference mirror over distances of several millimetres. A large DOF, hence, is required to maintain a comparable lateral resolution and sensitivity at the full axial field of view (FOV) of the OCT system. In case a low NA objective lens is used, the impact of the imaging optics on the axial sensitivity of the OCT system can be neglected. The axial resolution, hence, is dominated by the width of the source coherence function Γ_{src} only (Sec. 2.1.2). In contrast to conventional optical imaging approaches, the lateral and axial resolution of OCT systems, thus, can be tuned independently.

2.2 Fourier-domain optical coherence tomography

The cross-correlation with a well-defined reference field yields the time-of-flight of the sample beam and, in turn, enables non-invasive sub-surface imaging (Sec. 2.1.1). TD-OCT systems acquire the cross-correlation by scanning the length (or the temporal delay) of the reference beam and by capturing the intensity of the superimposed fields with a

scalar detector (Eq. 2.3). The field cross-correlation closely relates to the power spectral density of the superimposed beams, on the other hand. A signal which is equivalent to the TD-OCT A-scan hence can be calculated from the spectrum without mechanically scanning the reference arm, as well.

Two different approaches established to acquire the power spectral density for OCT imaging practically. Spectral domain optical coherence tomography (SD-OCT) systems utilize broadband light sources, which are used for TD-OCT systems as well, and replace the scalar detector of the TD-OCT system with an imaging spectrograph consisting of a spectrometer and a high-speed camera. A single camera frame yields a full spectrum from which the A-scan signal is calculated. High-speed and high-sensitivity cameras are required to enable high A-scan rates, though. In an alternative approach termed swept source optical coherence tomography (SS-OCT), the spectral raw data can be acquired sequentially by using a wavelength scanning laser and a scalar detector such as a photodiode. A single wavelength sweep yields the raw spectral data which is used to calculate the A-scan. SS-OCT systems allow to use high-sensitivity scalar (point) detectors as well laser sources which feature a high instantaneous power. High-speed wavelength scanning sources are required to achieve frame rates which are sufficiently fast for real-time OCT imaging. Data processing is similar for SD-OCT and SS-OCT systems. Both techniques calculate the time-domain A-scan signal from the inverse Fourier transform of the spectral raw data and, hence, are described by the more general term Fourier domain optical coherence tomography (FD-OCT). This term is used in this Chapter unless the discussion explicitly applies to SD or SS-OCT systems only.

Adolf Fercher et al. presented the first SD-OCT system in 1995 and demonstrated the approach to be able to determine the intraocular distances of model eyes [50]. The first SS-OCT system was presented in 1997 by Stephen Chinn et al. [51]. First *in-vivo* SD-OCT ocular imaging was demonstrated 2002 by Wojtkowski et al. and proved the imaging capability of the technique to be similar to TD-OCT systems [52]. FD-OCT approaches were largely unnoticed, however, until three independent groups demonstrated the technique to yield a superior SNR compared to TD-OCT systems in 2003 [53–55]. This discovery triggered a push in OCT development and resulted in most contemporary OCT systems to be based on Fourier domain techniques. The experimental device which is developed in this work is based on a SD-OCT system, as well. This Section discusses principles and fundamentals.

2.2.1 Axial ranging and image artefacts

Most of the considerations which are presented in Sec. 2.1 for TD-OCT devices hold for FD-OCT systems, as well. The major difference is the way the A-scan signal is acquired. In contrast to TD-OCT systems, the reference arm is kept static with fixed arm length l_R or fixed temporal delay t_R (compare Sec. 2.1.1 and Fig. 2.2). The scalar intensity detector is replaced with a sensor which captures the power spectral density of the superimposed reference and sample beam. This data reads:

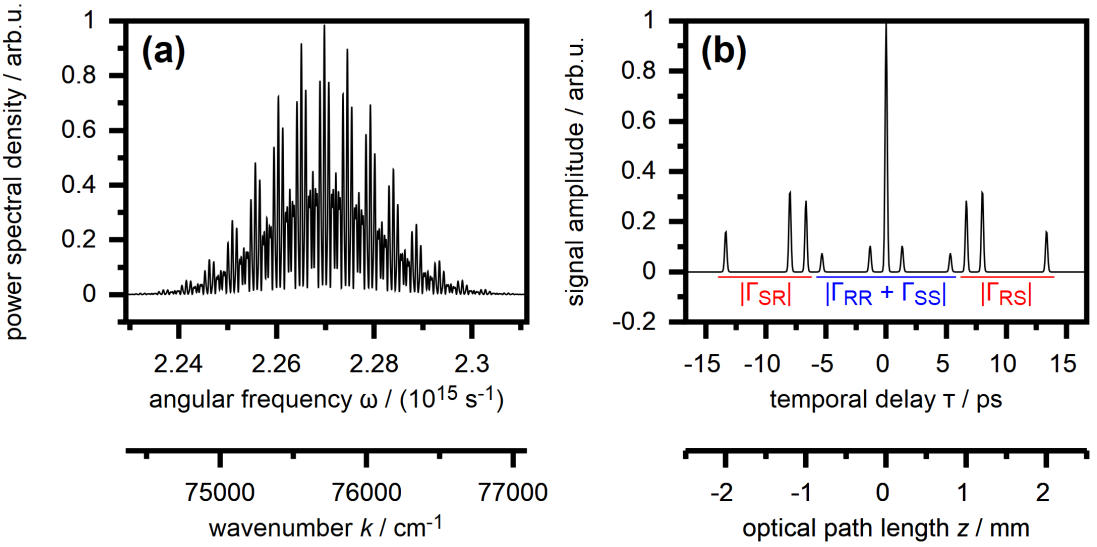

Figure 2.4: **Axial ranging with Fourier domain OCT.** (a) Raw power spectral density acquired with a FD-OCT system. Fringes are observed due to interference of the reference and sample beam. (b) Amplitude of the FD-OCT signal which is calculated from the inverse Fourier transform of Panel (a). Signal contributions according to Eq. 2.17 are labelled. Compare to Fig. 2.2.

$$\begin{aligned} I^{SD}(\omega) &= \left\langle |E_R(\omega) + E_S(\omega)|^2 \right\rangle \\ &= \left\langle |E_R(\omega)|^2 \right\rangle + \left\langle |E_S(\omega)|^2 \right\rangle + \langle E_R(\omega) E_S^*(\omega) \rangle + \langle E_R^*(\omega) E_S(\omega) \rangle \end{aligned} \tag{2.16}$$

The terms E_R and E_S correspond to the fields backscattered from the reference and sample beam, respectively. The first two terms, hence, describe the respective power spectral densities. The third and fourth term yield the cross power spectral densities of both beams. The time domain signal $I^{SD}(\tau)$, which corresponds to a single A-scan, is calculated from the inverse Fourier transform of the spectral data $I^{SD}(\omega)$. According to the Wiener Khinchin theorem (compare Eq. 2.10) this signal yields the autocorrelation of the superimposed fields $[E_R(t) + E_S(t)]$, which reads:

$$\begin{aligned} I^{SD}(\tau) &= F^{-1}\left\{ I^{SD}(\omega) \right\} \\ &= \Gamma_{RR}(\tau) + \Gamma_{SS}(\tau) + \Gamma_{RS}(\tau) + \Gamma_{SR}(\tau) \end{aligned} \tag{2.17}$$

The terms Γ_{RR} and Γ_{SS} describe the autocorrelation of the reference and sample beam, respectively. Γ_{SR} and Γ_{RS} yield the cross-correlation of both beams according to Eq. 2.4.

Often times it is more convenient to acquire the spectral signal in terms of the wavenumber $k = \omega/c$. The IFT of this signal directly yields the SD-OCT signal in

terms of the (double-pass) optical path length $z' = c\tau$. The single-pass path length $z = z'/2$, which relates to the physical dimensions of the sample, corresponds to half that number (compare Sec. 2.1.1).

Figure 2.4 illustrates the amplitude of the SD-OCT signal which is expected for the same layered sample which was previously considered to illustrate the TD-OCT signal (Fig. 2.2(b)). Contributions from individual signal components (Eq. 2.17) are labelled. The term $\Gamma_{RS}(\tau)$ corresponds the cross-correlation of the reference and sample beam and is termed *mutual interference signal* in this work. According to the previous discussion which was given for the TD-OCT signal, $\Gamma_{RS}(\tau)$ features signal peaks which are centred at $t_{sn} - t_R$ (Sec. 2.1.1), where t_{sn} is the time-of-flight corresponding to reflections at different sample layers and t_R is the time-of-flight of the (static) reference beam. The mutual interference signal yields signal peaks which correspond to the axial position of backscattering sample layers shifted by the length of the reference arm (compare Sec. 2.1.1). The axial zero position of the SD-OCT signal, hence, corresponds to the length of the static reference beam projected on the sample beam. The peak width, i.e. the axial resolution of the OCT system, is determined by the coherence function of the light source (Eq. 2.9) which depends on the source bandwidth (Sec. 2.1.2).

According to the definition of the cross-correlation, the fourth term in Eq. 2.17 reads $\Gamma_{SR}(\tau) = \Gamma^*_{RS}(-\tau)$ (Eq. 2.5). The term $\Gamma_{SR}(\tau)$, hence, yields a copy of the mutual interference signal which is mirrored with respect to the temporal axis, i.e. with respect to the axial scale of the OCT image, and which is complex conjugated. This signal arises from the SD-OCT signal being Hermitian symmetric as a consequence of the raw spectral data being real valued. $\Gamma_{SR}(\tau)$ is termed *mirror artefact* in this work.

The terms $\Gamma_{RR}(\tau)$ and $\Gamma_{SS}(\tau)$ yield the autocorrelation of the reference and sample beam, respectively. Analogue to the discussion given for the mutual interference signal (Sec. 2.1.1), in terms of the one dimensional model these signal components are found to read [46]:

$$\Gamma_{RR}(\tau) + \Gamma_{SS}(\tau) = \Gamma_{src}(\tau) \circledast \frac{1}{4}\left[\left(|r_R|^2 + \sum_{n=1}^{N} |r_{sn}|^2\right)\delta(\tau) + \sum_{n=1}^{N}\sum_{\substack{n'=1 \\ n'\neq n}}^{N} r_{sn} r^*_{sn'}\,\delta(\tau - (t_{sn'} - t_{sn}))\right] \tag{2.18}$$

The autocorrelation signal yields a peak, termed *DC signal*, at $\tau = 0$ which is proportional to the source coherence function $\Gamma_{src}(\tau)$ and to the total reflectivity of the reference and the sample arm [46]. If multiple reflections occur at different depth-layers of the sample, additional signals arise from mutual interference of these signals. These signal contributions are termed *autocorrelation artefacts*. The axial position at which these signal components are detected within the OCT scan correspond to the respective time-of-flight difference $t_{sn'} - t_{sn}$, where t_{sn} is the time-of-flight associated with the reflection at the n-th sample layer.

In contrast to TD-OCT systems, which capture a real-valued intensity signal (Eq. 2.3), the signal captured with FD-OCT systems is complex-valued. The magnitude $|I^{SD}(\tau)|$ of the complex-valued FD-OCT signal can be understood to reflect the visibility of fringes which are observed in the raw spectral data (Fig. 2.4). The signal phase $arg(I^{SD}(\tau))$ reflects the spectral offset of these fringes. As is evident from the definition of the cross-correlation (Eq. 2.4), the phase of the mutual interference signal directly relates to the phase of the complex-conjugated sample beam field. The effect allows to recover the phase of the backscattered sample beam from the SD-OCT signal and is discussed in Chap. 7 in detail.

The experimentally detected power spectral density is necessarily real-valued. The FD-OCT signal which is acquired from the inverse Fourier transform of this data, hence, is Hermitian symmetric. Furthermore, the IFT of the spectral raw data yields the autocorrelation of the superimposed reference and sample beam rather than the cross correlation of both fields. As a consequence, compared to TD-OCT systems additional image artefacts result (Eq. 2.17), but only the mutual interference signal $\Gamma_{RS}(\tau)$ reflects the time-of-flight distribution of the sample beam which yields a depth-resolved image of the sample.

DC and autocorrelation signals typically are detected close to $\tau = 0$ and do not depend on the length of the reference beam (Eq. 2.18). The axial position at which mutual interference and mirror signals are detected is affected by the reference arm length, on the other hand (Eq. 2.9). The axial zero position of the OCT signal corresponds to the length of the reference beam projected on the sample beam. In case the length of the reference arm is changed, mutual interference and mirror signals shift to opposite directions. As a consequence, the reference arm length typically can be aligned such that the mutual interference signal does not overlap with image artefacts, which allows to obtain an unambiguous image from the sample. The effect is further illustrated in the following Section.

2.2.2 Imaging

Imaging is performed with FD-OCT systems in the same way as with TD-OCT systems. The sample beam is focused to the specimen and laterally scanned (Fig. 2.3). An A-scan is taken at each lateral position and yields the sample‘s depth-profile at the respective point of illumination. Cross sectional or volume images can be constructed from multiple depth-profiles.

In contrast to TD-OCT systems, the respective A-scans are acquired by capturing the power spectral density of the sample beam superimposed with the static reference beam, rather than by mechanically scanning the length of the reference beam and capturing the intensity of the superimposed fields. The axial FOV, thus, is not determined by the length over which the reference mirror can be displaced, but by the spectral resolution of the OCT system. The effect is discussed in Sec. 2.2.4 in detail. Similar to TD-OCT systems, the axial and lateral resolution of FD-OCT devices depends on the bandwidth of the light source (Sec. 2.1.2) and on the NA of the imaging optics (Sec. 2.1.3), respectively.

Practical imaging is demonstrated with a commercial SD-OCT system (*Telesto II*,

Thorlabs, United States). Figure 2.5(a) illustrates a B-scan which is acquired from an OCT resolution test target (*APL-OP01*, Arden Photonics, United Kingdom) which features multiple reflecting lines engraved to a glass substrate at different depths. The B-scan consists of 1000 individual A-scans which are taken while incrementing the lateral position of the sample beam by 5 µm, respectively. Each column of the B-Scan corresponds to the amplitude profile of a single A-scan. Figure 2.5(b) illustrates a B-scan which is received from a roll of transparent adhesive tape.

The individual components of the OCT signal are labelled in Fig. 2.5 according to the previous discussion. The DC signal is observed at $z = 0$. Typically, the amplitude of the DC artefact exceeds the amplitude of the other signal components by far. The DC artefact is hardly visible in the scans presented in Fig. 2.5, however, since this artefact can effectively be suppressed by determining the OCT signal once without a sample present and subtracting this signal from the subsequent OCT scans. The approach is enabled with the commercial OCT system by default.

Autocorrelation artefacts (AC) correspond to mutual interference of multiple reflections at different layers of the sample. The path length at which the signal is detected, hence, depends on the path length difference of the interfering beams, which is determined by the internal sample structure and which is close to zero for thin samples. The sample presented in Fig. 2.5(b) features a curved surface, but the layer thickness is homogeneous. As a consequence, autocorrelation artefacts appear as multiple parallel lines which are detected at constant path lengths z, respectively. Autocorrelation artefacts do not depend on the length of the reference beam and are not affected if the reference mirror is moved.

The sample's mutual interference signal is detected at depths beyond 1 mm for the scans presented in Fig. 2.5. This signal component accurately reflects the sample‘s three dimensional structure. The absolute axial position at which the mutual interference signal is observed depends on the path length difference between the sample and the static reference beam. Hence, the three dimensional shape of the sample surface as well as the internal structure can be determined from the OCT signal. For the presented data, the reference beam is chosen to be approximately 1 mm shorter compared to the sample beam. As a consequence, the OCT signal corresponding to the reflection at the sample surface is detected at this depth. The tilt of the sample presented in Fig. 2.5(a) as well as the surface curvature of the sample presented in Panel (b) are evident from the mutual interference signal. In case the length of the reference beam is reduced or in case the sample is moved farther away from the OCT system, mutual interference signals are shifted to larger path lengths z.

Due to the Hermitian symmetry of the OCT scan, the signal which is detected at positive and at negative path lengths is equivalent. Typically, the signal detected at negative depths hence can be neglected for imaging. An unambiguous image of the sample is received in case the mutual interference signal does not overlap with image artefacts or with it‘s mirror image. This can be achieved by changing the length of the reference arm to shift the axial position of the mutual interference signal.

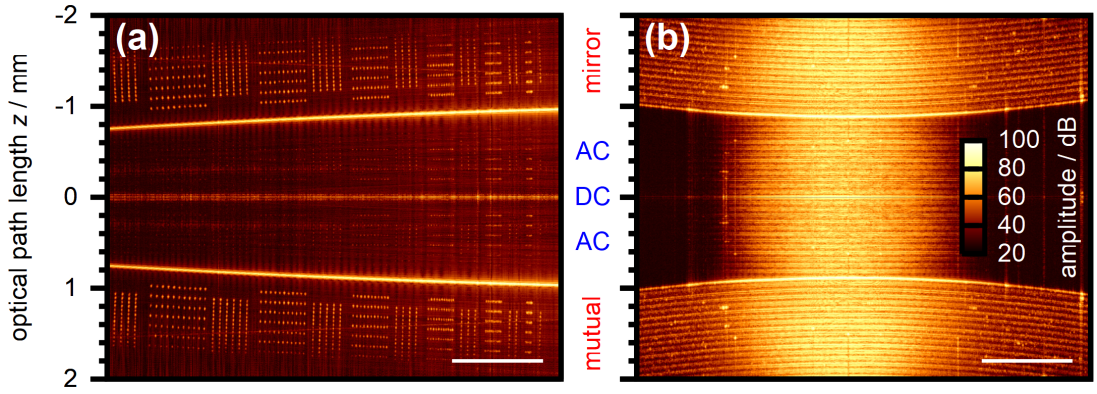

Figure 2.5: **SD-OCT imaging and image artefacts.** B-scan taken with a commercial SD-OCT system at (a) an OCT resolution test target and (b) at an adhesive tape roll. Individual signal components are labelled according to the previous discussion (compare Fig. 2.4). Scalebar 1 mm.

2.2.3 Phase shifting approaches

Due to the finite spectral resolution, FD-OCT systems are most sensitive to signals which are detected close to $z = 0$. The effect is discussed in Sec. 2.2.4 in detail. At this axial position, DC and autocorrelation artefacts are observed, on the other hand, and the mutual interference signal hence needs to be shifted to larger path lengths to not overlap with image artefacts. Furthermore, due to the Hermitian symmetry of the OCT scan, signals detected at positive and at negative depths are equivalent. The unambiguous OCT scan, thus, is limited to the positive depth range only and the axial field of view is limited to half the FOV which is actually accessibly with the OCT system. Suppressing DC, autocorrelation and mirror artefacts greatly increase the image quality and allows to use the full axial FOV.

Fercher et al. first demonstrated the suppression of SD-OCT image artefacts in 1999 by sequentially acquiring multiple OCT signals while manipulating the phase difference between the reference and sample beam [56]. A number of groups picked up that approach and presented improved algorithms [52, 57–60] as well as techniques which allow to acquire multiple phase-shifted OCT signals in parallel [60–62]. In addition to suppressing image artefacts, phase shifting techniques were further found to enhance the SNR of the OCT signal [52, 57, 58, 60–62].

Phase shifting approaches are based on the acquisition of multiple OCT signals $I_\phi^{SD}(\tau)$ taken with a varying phase difference ϕ between the interferometer arms. Considering phase manipulation at the reference beam, for example by mounting the reference mirror to a piezoelectric actuator, the effect on the SD-OCT signal is found from Eq. 2.17 and from the definition of the cross-correlation (Eq. 2.4):

$$I_\phi^{SD}(\tau) = \Gamma_{RR}(\tau) + \Gamma_{SS}(\tau) + \Gamma_{RS}(\tau)e^{i\phi} + \Gamma_{SR}(\tau)e^{-i\phi} \tag{2.19}$$

Mutual interference signals and mirror artefacts depend linearly on the relative phase

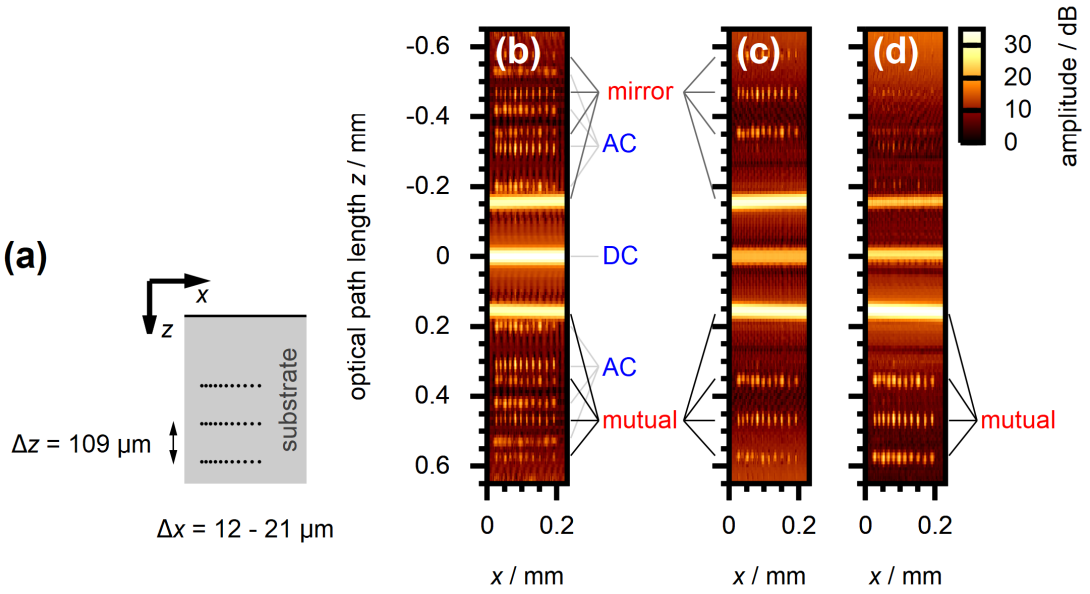

Figure 2.6: **Phase shifting approaches for SD-OCT imaging.** (a) Structure of the sample drawn to the same scale as the OCT images. (b) Conventional SD-OCT signal taken at the sample. The individual signal components are labelled according to the previous discussion. (c) Signal captured with a two-step phase shifting algorithm (Eq. 2.20). (d) Signal captured with a four-step phase shifting algorithm (Eq. 2.21).

difference ϕ between the reference and sample beam, but show an opposite behaviour. DC and autocorrelation artefacts remain static.

A simple differential algorithm allows to eliminate DC and autocorrelation artefacts ($\Gamma_{RR}(\tau)+\Gamma_{SS}(\tau)$) from two successive OCT scans which are taken with a relative phase shift of π applied to the reference beam [52]:

$$\begin{aligned} I^{SD}_{2Step}(\tau) &= \frac{1}{2}\left[I^{SD}_{0}(\tau) - I^{SD}_{\pi}(\tau)\right] \\ &= \Gamma_{RS}(\tau) + \Gamma_{SR}(\tau) \end{aligned} \tag{2.20}$$

This algorithm was demonstrated, in fact, in 2002 with the very first *in-vivo* application of SD-OCT imaging [52].

The acquisition of multiple signals with at least one non-complementary phase shift applied allows to additionally suppress mirror artefacts. A simple four-step phase shifting algorithm, for example, reads [46, 57]:

$$\begin{aligned} I^{SD}_{4Step}(\tau) &= \frac{1}{4}\left[I^{SD}_{0}(\tau) - I^{SD}_{\pi}(\tau) - i\left(I^{SD}_{\pi/2}(\tau) - I^{SD}_{3\pi/2}(\tau)\right)\right] \\ &= \Gamma_{RS}(\tau) \end{aligned} \tag{2.21}$$

The impact of phase shifting approaches is demonstrated in Fig. 2.6. Panel (a) illustrates the structure of group two of the OCT resolution test target whose B-scan with a commercial device is presented in Fig. 2.5(a). Panel (b) presents a B-scan which is taken at the sample with the SD-OCT system developed in this work. In contrast to the previous acquisition, the length of the reference arm is chosen such that autocorrelation and mutual interference signals overlap. The structure of the sample, thus, cannot easily be identified from the OCT signal. Figure 2.6(c) illustrates the impact of the differential two step algorithm (Eq. 2.20) on the OCT scan. DC and autocorrelation artefacts are suppressed. Figure 2.6(d) illustrates the image which is acquired with the four step algorithm (Eq. 2.21). All image artefacts except the mutual interference signal are suppressed.

2.2.4 Practical aspects of spectral-domain OCT

Spectral resolution and axial sensitivity

Practical FD-OCT systems feature a finite spectral resolution. For SD-OCT devices this number is determined by the optical resolution of the spectrograph and by the pixel size of the connected camera. For SS-OCT devices the resolution depends on the instantaneous linewidth of the light source and on the temporal integration time of the detector. The finite resolution causes fine spectral features to be smoothed and, hence, reduces the visibility of high-frequency spectral fringes. These features relate to OCT signals which are detected at large temporal delays τ or at large optical path length differences z, on the other hand. The sensitivity of FD-OCT systems, hence, is observed to drop along the axial direction and is highest for low-frequency spectral fringes which correspond to sample features detected close to $z = 0$. This effect adds up with the axial signal drop due to the imaging optics, whose detection sensitivity is highest close to the focal plane [46].

The spectral resolution of FD-OCT systems can be characterized by a spectral point spread function (PSF). The experimentally determined spectral raw data $I^{SD}_{exp}(\omega)$ corresponds to the convolution of the true spectrum $I^{SD}(\omega)$ with the PSF:

$$I^{SD}_{exp}(\omega) = \mathrm{PSF}(\omega) \circledast I^{SD}(\omega) \tag{2.22}$$

The OCT signal is calculated from the IFT of the spectral raw data. According to the convolution theorem, this signal reads:

$$I^{SD}_{exp}(\tau) = F^{-1}\left\{\mathrm{PSF}(\omega)\right\} I^{SD}(\tau) \tag{2.23}$$

Compared to the previous theoretical discussion, an additional term arises which is multiplied with the (ideal) A-scan signal $I^{SD}(\tau)$. This term corresponds to the IFT of the spectral PSF and describes the axial sensitivity loss of the OCT system due to the finite spectral resolution.

For a quantitative discussion it is more convenient to evaluate the spectral data in terms of the wavenumber $k = \omega/c$ and the resulting OCT signal in terms of the single-pass optical path length $z = c\tau/2$. For SD-OCT systems, the PSF which describes the

optical resolution of the spectrograph can be assumed to be a Gaussian function with FWHM width δ_k^{opt} [46]. The IFT of the PSF is proportional to $exp(-(\delta_k^{opt})^2/(4\,ln(2)))$, which is another Gaussian function with half width at half maximum (HWHM) of $z_{3dB} = 2\,ln(2)/\delta_k^{opt}$ [46]. The amplitude of the OCT signal which is detected at $z = z_{3dB}$, hence, is reduced by 50 % compared to the signal which would be received if the same sample feature was detected close to $z = 0$.

Furthermore, the finite pixel size of the spectrograph camera causes an additional binning of the spectral raw data. This effect can be taken into account by convolving the spectrum with a rectangular function with window size δ_k^{bin} [53]. The window size corresponds to the spectral range which is covered by the individual camera pixels. Analogue to the PSF of the spectrometer optics (Eq. 2.23), the effect on the A-scan signal is described by multiplying the ideal OCT signal with the IFT of that function. This term is found to be proportional to $sinc(\delta_k^{bin} z/2)$. The practical impact is demonstrated in Sec. 5.3.3 with the SD-OCT system developed in this work.

Discretisation and field-of-view

SD-OCT systems utilize fast digital cameras embedded to the spectrograph to acquire the spectral raw data. The experimentally acquired data, thus, is discretized due to the finite pixel size and finite pixel number. The OCT signal is calculated from the inverse discrete Fourier transform (IDFT) of the digitized spectrum instead as from the analytic inverse Fourier transform. The IDFT requires the spectral raw data to be uniformly sampled with respect to the frequency scale ω or the wavenumber scale k and in turn yields a discrete time-domain signal, as well.

Considering the raw spectrum to be acquired at M points with uniform spectral spacing d_ω or $d_k = d_\omega/c$, the A-scan calculated from the IDFT of the raw spectral data has M discrete points, as well. The temporal spacing of the discrete OCT signal reads $d_\tau = 2\pi/(M d_\omega)$ [46, 63, 64]. The spacing of the corresponding single pass optical path length scale reads $d_z = c\,d_\tau/2 = \pi/(M d_k)$. The axial FOV of the OCT system, hence, is limited to the depth range between $\pm z_{max}$ with $z_{max} = M d_z/2 = \pi/(2 d_k)$ [46]. Furthermore, in contrast to the analytic IFT, the OCT signal calculated from the IDFT is periodic with respect to the total pixel count M or with respect to the total path length range $2z_{max}$ [63, 64]. This periodicity causes OCT signals which are detected from reflections beyond the observable FOV ($\pm z_{max}$) to be wrapped back to this range [53].

2.3 Imaging scattering biological tissue

Figure 2.7 illustrates a SD-OCT signal which is taken with a commercial device (*Telesto II*, Thorlabs, United States) at a human fingernail and nailfold region. The scan features a strong signal which corresponds to the reflection caused by the large refractive index difference at the tissue-air interface. This signal allows to accurately determine the sample‘s surface topology based on the OCT signal. The signal amplitude which is received

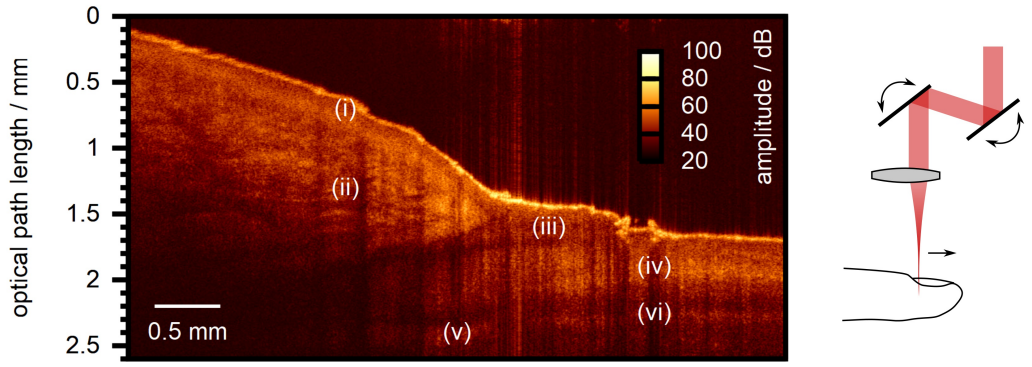

Figure 2.7: **OCT image of the human fingernail and nailfold region** (i) epidermis, (ii) dermis, (iii) cuticle, (iv) nail plate, (v) nail matrix, (vi) nail bed. Labelled according to [65].

from sub-surface sample features is expected to correspond to the respective backscattering probability. This value depends on the microscopic tissue structure and, thus, allows to distinguish different tissue layers based on their OCT signal. Reflections from the epidermis, the dermis, the nail plate and the nail bed cause quite different signals and can be identified from the presented scan. The axial (depth-) scale of the OCT signal reflects the optical path length travelled in the sample and, thus, allows to determine the size of anatomical features, provided the tissue refractive index is known.

Obviously, the penetration depth of the OCT system is limited to approximately 1.5 mm with the presented data. This effect is evident by observing the signal received from the nail plate. When the lateral scan position is moved towards the proximal end of the finger, tissue layers covering the nail plate become thicker. The OCT signal which is corresponding to the reflection at the nail plate drops below the noise floor and cannot be observed any more. This work discusses the application of wavefront shaping approaches to OCT imaging, ultimately to extend the SNR and penetration depth when imaging *in-vivo* biological tissue. This Section briefly covers aspects of tissue optical properties and factors determining the penetration depth of OCT systems.

2.3.1 Optical properties of biological tissue

Biological tissue is highly heterogeneous at length scales covering a few nanometres up to several centimetres in case of macroscopic tissue structures. Light transmission trough such a heterogeneous sample can be modelled at a principle level by considering a medium with random refractive index fluctuations and solving the wave equations. The approach, based on the extended Huygens-Fresnel principle, was originally developed to describe optical propagation in the atmosphere [66, 67] and was later adopted to OCT imaging with biological tissue [37, 68]. Random refractive index fluctuations were shown to decrease the spatial coherence of the beam upon propagation through the medium which, in turn, reduces the signal intensity detected with an OCT system [37, 67, 68].

A more intuitive approach approximates the biological medium with a number of

statistically distributed discrete scattering particles [69]. The macroscopic optical properties are determined by the particle size-distribution, the scattering probability which depends on the scattering cross-section and on the particle density, and by the scattering phase-function which determines the probability density distribution of the scattering angle [69]. The model can easily be transferred to Monte Carlo simulations which enable quantitative numerical studies and allow an intuitive interpretation of the impact of tissue optical properties on the OCT signal.

The scattering phase function is often written in terms of the Henyey-Greenstein function which was found to fit the experimental data well for human skin, for example [70, 71]. The Henyey-Greenstein function describes the angular probability density of scattering events in terms of a single parameter g, termed scattering anisotropy, which ranges from -1 (backscattering only) to 1 (forward scattering only). Most human tissue is experimentally found to be predominantly forward-scattering with values of g greater than 0.7 [71–73]. With increasing wavelength the scattering probability, often described in terms of the scattering coefficient, is observed to drop and forward-scattering, i.e. scattering at small deflection angles, becomes more dominant [73, 74].

The absorption of light, and hence the visual appearance of tissue, is determined by the spectral absorption characteristics of individual chromophores and by the chromophore concentration. Typically, the behaviour is dominated by the absorption of blood and water [73] which are weakly absorbing in the spectral range from 600 nm to 1300 nm [73, 75]. At near-infrared wavelengths the effects of scattering dominate over absorption. Most OCT systems, thus, utilize light sources centred at 1300 nm due to weak absorption and due to the decreased scattering probability at this wavelength.

2.3.2 Impact of scattering on OCT imaging

Early investigations on the impact of scattering assumed ideal discrimination of multiple scattered light by OCT systems [76–78]. In case an opaque medium is placed in front of the structure which is imaged, light which is scattered at the medium does not reach the detection aperture of the OCT system. The model is illustrated in Fig. 2.8(a). The OCT signal, hence, is expected to be proportional to the fraction of light which reaches the sample structure without scattering. According to Beer‘s law this value is expected to drop exponentially with increasing thickness of the scattering layer or with increasing penetration depth in the medium [76].

Practical OCT systems have a finite acceptance angle and, hence, do detect light which is scattered at small deflection angles (Fig. 2.8(b)) or which is randomly scattered to the imaging system after multiple large-angle scattering events (Fig. 2.8(c)), on the other hand. The single-scattering approximation, thus, was found to be valid at low penetration depths and for large-angle scattering samples only [79, 80]. Signal contributions from multiple scattered light become more significant with increasing penetration depth and cause the negative slope of the detected OCT signal to be less steep than expected from Beer‘s law [68, 78–81].

An intuitive understanding of the impact of scattering on the OCT signal can be taken from Monte Carlo studies which simulate the light distribution in the turbid

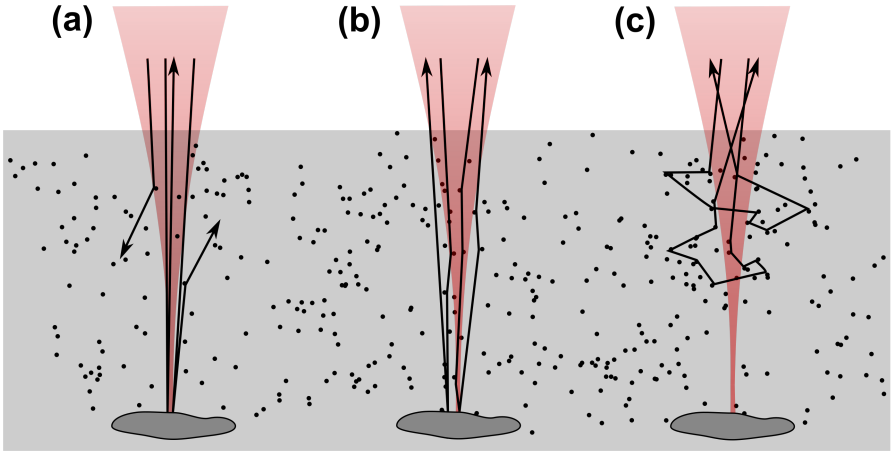

Figure 2.8: **Impact of scattering on OCT imaging.** (a) Single scattered light is detected only. (b) Multiple small-angle forward scattered light is detected. (c) Multiple large-angle scattered light is detected.

medium by randomly propagating a high number of discrete particle-like photon packets. Each photon packet undergoes a random walk which is determined by the sample‘s macroscopic optical properties such as scattering probability and the phase function. The OCT signal is simulated by recording the number of photons which are backscattered to the finite detection aperture and by tracking the respective path lengths [79, 82, 83]. The OCT signal which is detected at optical path lengths z can be divided in contributions from photon packets whose penetration depth into the sample nearly matches their path length (Fig. 2.8 Panels (a) and (b)) and in contributions from photon packets with the same propagation length but which were scattered at shallower sample layers only (Fig. 2.8(c)) [82, 83]. According to Wang et. al the former are termed least scattered photons (LSP) and the latter multiple scattered photons (MSP) [83]. Obviously, MSP signal contributions are not related to the morphology of the sample at the depth at which the OCT signal is detected.

The penetration depth of OCT systems is determined by the rejection of MSP compared to LSP signal contributions when imaging scattering media. The average number of scattering events and the incident angle on the detector relative to the optical axis were shown to be substantially lower for LSP compared to MSP [82, 83]. Thus, the rejection of multiple scattered light and the penetration depth with scattering media can be increased by choosing a low acceptance angle or low NA imaging optics [79]. Considering the optical properties of the sample, the penetration depth of OCT systems is found to be increased with weakly scattering samples (low scattering coefficient) and with predominantly forward scattering samples (high scattering anisotropy g) [79, 83]. The average number of scattering events is higher for MSP signal contributions and rises with increasing penetration depth for the LSP as well as for the MSP signal [82, 83]. The LSP signal which allows to image the sample morphology is found to correspond single-scattered photon packets at low penetration depths only. With increasing penetration

depth contributions from multiple small-angle scattered photons dominate [83].

An absolute number for the penetration depth of OCT systems with scattering media is difficult to give. This value depends on a number of parameters such as the optical properties of the sample, the dynamic range and the spectral resolution (Sec. 2.2.4) of the OCT system, the imaging optics and the power and the shape of the illuminating beam. With human skin the penetration depth typically is found to be in the range of one to two millimetres for 1300 nm OCT systems [9, 11, 12].

3 Principles of wavefront shaping

Scattering of light is a deterministic process at time scales at which the turbid medium can be considered static. Knowledge of the sample‘s scattering properties or of the distortions which are introduced to the optical beam while propagating through the medium, hence, allows to counteract or even to harness the effects of scattering for imaging applications. This Chapter explores principles and fundamentals of wavefront shaping approaches, which enable focusing and imaging in turbid media by manipulating the wavefront of the beam which is incident to the sample. Applications to optical coherence tomography are discussed in Chap. 4.

3.1 Adaptive optics

Probably most contemporary devices which exploit active wavefront control for imaging with optically inhomogeneous media are based on adaptive optics. The technique was originally developed to enable diffraction limited detection and optical focusing in the presence of turbulences and inhomogeneities of the atmosphere, for example for astronomic and for military purposes [85, 86], and can be implemented for microscopic and OCT imaging, as well [84, 87–91].

Adaptive optical systems actively control the beam which is backscattered from or which is incident to the sample such that the effects of optical aberrations and scattering are cancelled. Sensor based approaches require a point-like guide star located near the object which is supposed to be imaged [85]. In case the medium between the object and the imaging system is optically homogeneous, light detected from the guide star can be described by a flat wave in the far field. Inhomogeneities of the medium cause deformations from this ideal wavefront and, in turn, result in a loss of image quality. Hartmann-Shack sensors or holographic techniques are used to detect the shape of the wavefront which is emitted from the guide star after transmission through the turbid medium. A wavefront shaping element such as a deformable mirror (DM) allows to correct wavefront deformations and, hence, to obtain a diffraction limited signal from the guide star with the imaging system. The wavefront correction is valid for light sources located close to the guide star, too, and hence a diffraction limited image of the vicinity of the guide star can be obtained, as well.

In another approach, the wavefront correction can be applied to a beam which is incident to the sample to create a diffraction limited focal spot near the guide star instead. In the context of optical coherence tomography this high-resolution imaging is enabled since the sample can be scanned with a fine focal spot [84, 88, 90, 91]. Methods to create artificial guide stars allow imaging at an arbitrarily chosen position in the

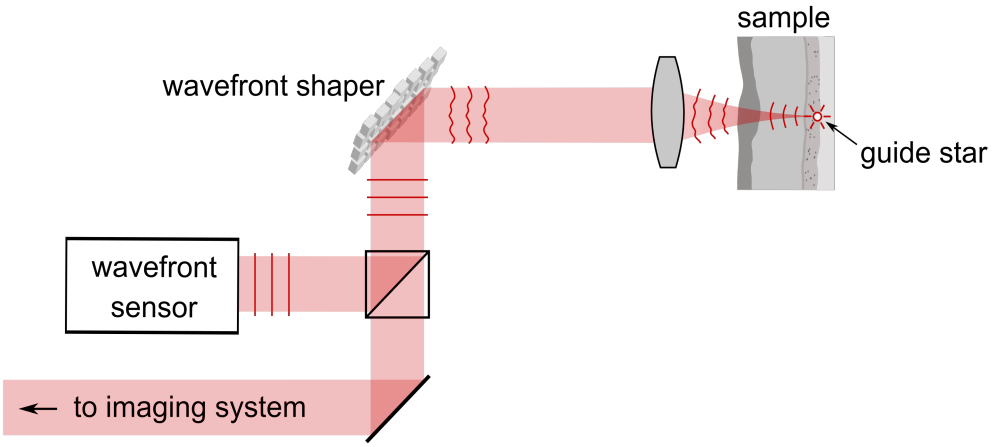

Figure 3.1: **Principle of closed-loop sensor based adaptive optics.** Light emitted from a point-like guide star is detected at a sensor which quantifies aberrations of the wavefront. A closed-loop control is implemented to dynamically correct deviations from the ideal (flat) wavefront with a wavefront shaping element such as a deformable mirror. The approach enables diffraction-limited imaging in the vicinity of the guide star. Image adapted from [84]

sample. For retinal imaging, for example, a low-NA probe beam for which aberrations at the anterior eye are negligible can be focused to the retina [84].

With strongly scattering samples such as opaque biological tissue it is not easily possible to create a guide star inside the medium, on the other hand. Some approaches are discussed in Sec. 3.2.1. In case no guide star is available, methods for sensorless wavefront correction can be implemented [87, 89]. The technique tries to find an optimal wavefront correction which is applied by the DM and which cancels optical aberrations by optimizing some metric of the signal acquired with the imaging system, for example the total image intensity [87, 89]. The approach is similar to iterative wavefront shaping which is discussed in Sec. 3.3.

A full review of adaptive optical systems is beyond the scope of this work. In general, algorithms used for adaptive optics are tuned for fast wavefront optimization with weakly scattering samples. This is achieved, for example, by estimating the corrective wavefront from a low number of Zernike polynomials [85]. The effect of wavefront correction can be understood by considering the optimized wavefront to counteract aberrations present on the optical system. In contrast, the beam shaping algorithms which are discussed in the remainder of this work are optimized for strongly scattering samples for which adaptive wavefront optimization algorithms are not effective since deformations of the scattered wave are highly heterogeneous, random-like, and may even exceed the spatial resolution of the wavefront shaping element.

3.2 Time reversal and phase conjugation

Perhaps the most intuitive way to utilize wavefront shaping approaches to deal with strongly scattering media is based on the time reversal symmetry of the wave equations. Considering the beam which is incident to the turbid sample to be described by it‘s electric field $E_{src}(x, y, t)$, the field which is detected at a receiver behind the sample is described by the term $E_{out}(x, y, t)$. In case of monochromatic illumination a granular (speckle) pattern is observed at the detector. With a pulsed or broadband source the signal at the receiver is spatially and temporally blurred compared to the incident field. The wave equations which determine the propagation of the electromagnetic field are symmetric with respect to forward and backward travelling waves. Thus, illuminating the sample back-surface with the time-reversed field $E_{out}(x, y, -t)$ causes the electromagnetic wave to backtrack the propagation in the scattering sample and, thus, to recover the shape of the initial source field $E_{src}(x, y, t)$ at the sample front face after transmission trough the medium (Fig. 3.2).

Time reversal experiments were initially demonstrated with acoustic waves which obey wave equations equivalent to the electromagnetic field [92]. Ultrasonic transducers enable temporal tracking of the instantaneous pressure wave and can be used both as a source as well as a receiver. Constructing a *time reversal mirror* from an array of multiple transducers hence allows to detect the scattered wave spatially and temporally resolved and to directly play the time-reversed field back to the medium. In case a point source in front of the sample is used, the time-reversed acoustic wave which is applied from the other side of the sample creates a spatial focus at the position of the original source and recovers the temporal profile of the source field after propagating through the scattering layer [92, 93] (Fig. 3.2). The size of the focal spot was shown to correspond to the lateral correlation length of the field which is scattered at the sample. This number can be significantly smaller than the diffraction limited spot size which is corresponding to the numerical aperture of the time reversal mirror‘s transducer array [92, 93]. Further reports demonstrated a time reversal mirror which is consisting of a single transducer element and which, hence, is capable of temporal beam shaping only to be sufficient for temporal [93] and lateral [94] focusing of the scattered wave.

Time-reversal approaches cannot directly be translated to optical radiation since present sensors are not able to temporally track the rapid oscillations of the electromagnetic field. Holographic and interferometric methods allow to detect and to manipulate the amplitude and phase of monochromatic electromagnetic waves, on the other hand. In case of monochromatic radiation, phase conjugation is equivalent to time reversal. The first application was demonstrated in 1966 by Emmett Leith and Juris Upatnieks who recorded a hologram of an object hidden behind a scattering layer [95]. Utilizing the hologram to apply the phase conjugated field to the backside of the scattering layer was demonstrated to recover the object‘s image at it‘s original position at the other side of the turbid medium [95]. In case the field emitted from a point source, i.e. a focused laser beam or a small fluorescent particle, is holographically detected, the approach allows to focus light to the position of this guide star by applying the phase conjugated field to the other side of the turbid layer (Fig. 3.2). The technique, hence, is similar to

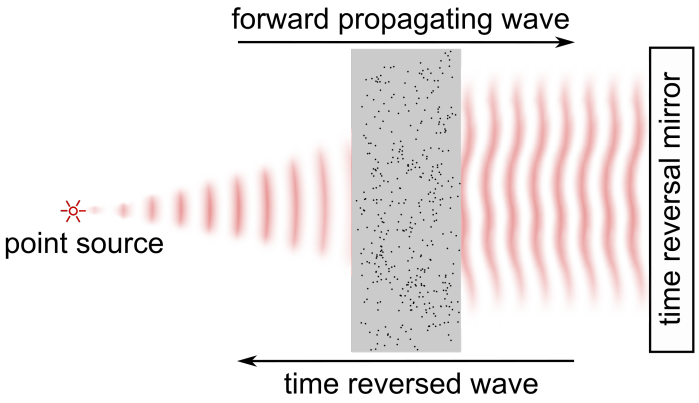

Figure 3.2: **Principle of time reversal and phase conjugation.** The field emitted from a (point) source is recorded after propagation through a scattering sample. Applying the time-reversed or the phase conjugated field to the backside of the sample corresponds to a reversal of propagation direction and recovers the shape of the source field at the front side.

sensor based adaptive optics which requires a point-like guide star, as well (Sec. 3.1). In 2008, Yaqoob et al. demonstrated phase conjugation with a photorefractive crystal to be feasible for focusing light through thick biological tissue [96]. Purely digital phase conjugation approaches were reported after 2010 and utilize interferometric techniques such as phase shifting or off-axis interferometry to digitally record the phase of the scattered field and spatial light modulators (SLMs) to create the phase-conjugated beam [97–100] (Fig. 3.3). Recent reports demonstrated phase conjugation approaches to be sufficiently fast to focus light through living biological tissue [101–103].

3.2.1 Imaging applications and the optical memory effect

Optical phase conjugation requires a point source or guide star placed behind the scattering layer whose emission can be detected in front of the medium. Applying the phase conjugated field to the specimen creates a focal spot at the position of the guide star. In principle, this focus can be scanned for applications such as fluorescence imaging. On the other hand, optical phase conjugation is highly sensitive to minor displacements between the optical system and the scattering sample since the phase conjugated beam adapts to the sample‘s microstructure. In case the sample is moved, the transmitted field decorrelates and the focal spot is lost [96, 101]. Judkewitz et al. demonstrated that predominantly forward scattering media allow to laterally shift the transmitted field without immediately decorrelating by shifting the incident beam (shift/shift correlations) [104]. The effect is valid for small lateral beam displacements only and allows to scan the focal spot which is created through phase conjugation over a narrow field of view. This FOV can be sufficient for imaging of microscopic sample structures such as individual cells hidden behind the scattering layer [104–106] but, in general, is too small to investigate macroscopic objects.

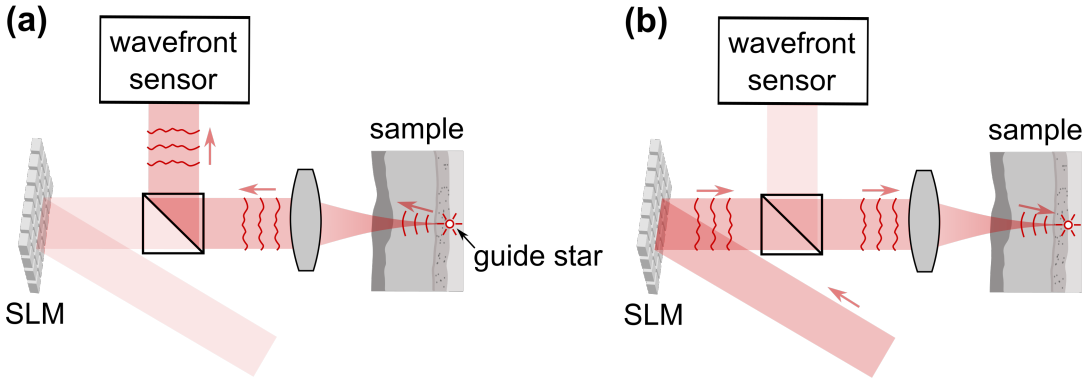

Figure 3.3: **Principle of digital optical phase conjugation.** (a) Light emitted from a point-like guide star is detected after transmission through the scattering layer. In contrast to adaptive optics, high-resolution wavefront sensing techniques such as phase shifting interferometry are used. (b) A SLM allows to play the phase-conjugated wavefront back to the sample. A focal spot at the position of the original guide star is created.

Hsieh et al. demonstrated scanning of the focal spot behind the scattering layer and imaging by exploiting correlations of the scattered field known as the optical memory effect [99]. In case the field incident to a thin turbid medium is tilted by a small angle, the field which is scattered from the sample is tilted accordingly without fully decorrelating (tilt/tilt correlations) [104, 107]. The effect allows to laterally shift the speckle field which is observed behind the scattering medium or the focal spot created through optical phase conjugation by tilting the beam incident to the sample. The effect is limited to narrow tilt angles and to thin turbid layers, on the other hand. The lateral FOV over which the beam can be effectively scanned before the scattered field decorrelates and the focal spot is lost is proportional to the axial distance between the scattering layer and the focal spot and inversely proportional to the thickness of the turbid medium [104, 108]. With biological samples, typically the FOV is limited to a few microns [105].

Imaging, hence, is limited to the close vicinity of guide stars whose emission can be detected to find a phase conjugated wave. Non-invasive imaging is implemented by embedding virtual guide stars, e.g. fluorescent particles, to the sample [109–111]. Those markers may not distribute homogeneously in the sample, are subject to photobleaching and may even be cytotoxic, on the other hand. Xu et al. presented a label free approach in 2011, termed time-reversed ultrasonically encoded optical focusing (TRUE). The technique uses an ultrasonic transducer to create an acoustic focus in the sample. Light scattered at this focus is frequency shifted due to interaction with the acoustic wave and serves as a virtual point source embedded to the sample. The frequency shifted light is backscattered to the optical system and recorded at a photorefractive crystal which, in turn, allows to play back the phase conjugated field to the sample and to create an optical focus at the position of the ultrasonic focus. The technique requires single-sided sample access only and was shown to be sufficiently fast to be applied to living biologi-

cal tissue [112]. The approach was demonstrated with holographic (analogue) [109, 112] and with digital phase conjugation systems [113, 114]. A focal spot can be created at an arbitrarily chosen target position, depending on the position of the ultrasonic focus. The approach, hence, enables scanning of macroscopic sample structures for optical imaging [113, 114].

3.3 Iterative wavefront shaping

Phase conjugation experiments demonstrate the possibility to create a focal spot from scattered light, provided the correct phase pattern which accounts for scattering at the medium is applied to the beam incident to the sample. For most practical applications a point-like guide star embedded to the medium and coherent detection of the field emitted from that source are not possible, though. Iterative wavefront shaping approaches enable focusing through scattering media, as well, and require to probe the intensity of the scattered field at the position of the supposed focal spot only.

3.3.1 Principles

In a seminal work, Ivo Vellekoop and Allard Mosk first demonstrated focusing through turbid media by iteratively optimizing the shape of the wavefront incident to the sample in 2007 [23]. The approach can be understood by considering the spatial light modulator, which is used for wavefront manipulation, to be an array of sources illuminating the sample (Fig. 3.4(a)). The phase and amplitude of the individual sources can be controlled electronically, depending on the type of spatial light modulator used. In most practical implementations liquid crystal on silicon (LCOS) devices are employed which enable phase-only wavefront manipulation. Experiments with micro-electro-mechanical systems (MEMS) such as DMs or digital micromirror devices (DMDs) are reported as well are discussed in Sec. 3.3.4.

After transmission through the scattering medium the electromagnetic field features a spatially fluctuating phase and amplitude pattern. The field observed at a detector array behind the scattering medium corresponds to the linear superposition of contributions emitted from the individual source elements, or SLM pixels (Fig. 3.4) [23]:

$$E_m^{det} = \sum_{n=1}^{N} t_{mn} E_n^{src} \tag{3.1}$$

The terms E_n^{src} and E_m^{det} correspond to the complex field amplitudes at the n-th source and at the m-th detector element, respectively. t_{mn} is the sample's complex-valued and random-like transmission matrix which describes the linear relation between the incident and the scattered field (compare for example [108]).

Considering a single detector pixel with index m_t, the field observed at this position corresponds to a sum of complex numbers with random amplitude and random phase (Eq. 3.1). Assuming the individual contributions to be statistically independent and the phase to be uniformly distributed, the amplitude of the scattered field $|E_{m_t}^{det}|$ is expected

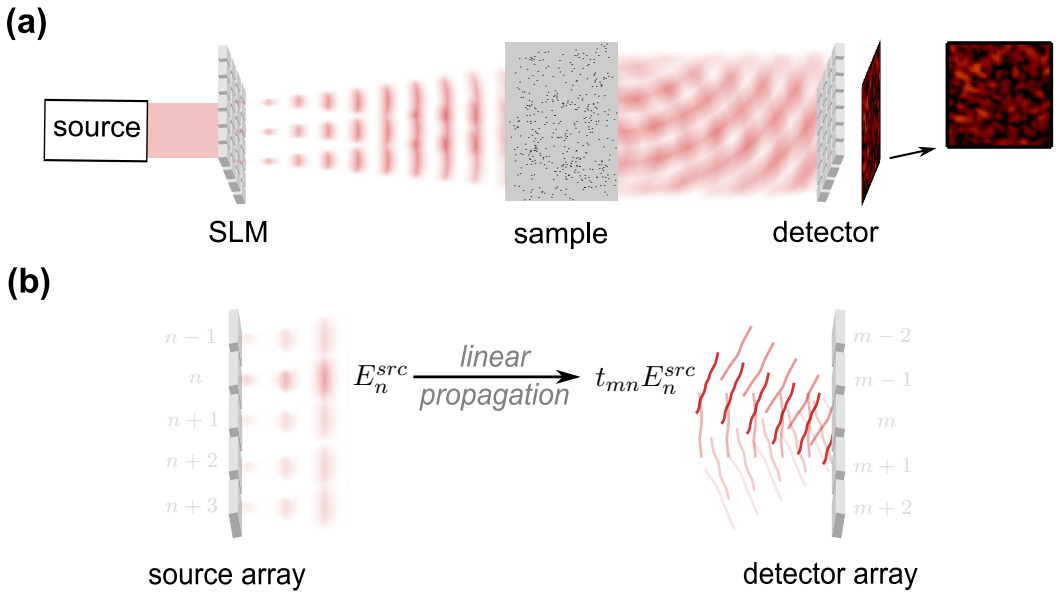

Figure 3.4: **Principle of the optical transmission matrix.** (a) The beam incident to a scattering sample is modulated by a spatial light modulator (SLM). In case of monochromatic radiation a speckle pattern is observed behind the sample. (b) The field reflected from the SLM is considered to be composed of a number of independent sources indexed n. Since propagation in the sample is linear, the field observed at the m-th detector pixel can be described based on the incident field E_n^{src} and the static and complex-valued transmission matrix t_{mn} (Eq. 3.1) [23].

to be Rayleigh distributed, which is the well-known behaviour for monochromatic laser speckle [44]. In contrast, in case all contributions $t_{mn}E_n^{src}$ from the individual source modes exactly match in phase, the field amplitude as well as the intensity $|E_{m_t}^{det}|^2$ become maximal. A high intensity, i.e. a focal spot, results at the target pixel m_t, which can be understood to be an effect of constructive interference of the scattered field.

The sample's transmission matrix t_{mn} is static, but the phase of the incident field E_n^{src} can experimentally be manipulated with the SLM. The optimized phase pattern which is applied by the SLM is found by probing the intensity at the target position m_t at which the focus is supposed to be created and by iteratively optimizing the phase pattern such that the intensity is maximized. The approach is illustrated in Fig. 3.5. Algorithms for wavefront optimization are discussed in Sec. 3.3.3.

The most straight forward way to probe the intensity of the scattered field is to place a detector behind the turbid medium. Detector-based approaches allow to investigate the impact of wavefront shaping on the scattered field and to test dependencies on experimental parameters. The lateral size of the shaped focus is found to correspond to the lateral correlation length, i.e. the speckle size, of the scattered field [115], similar to

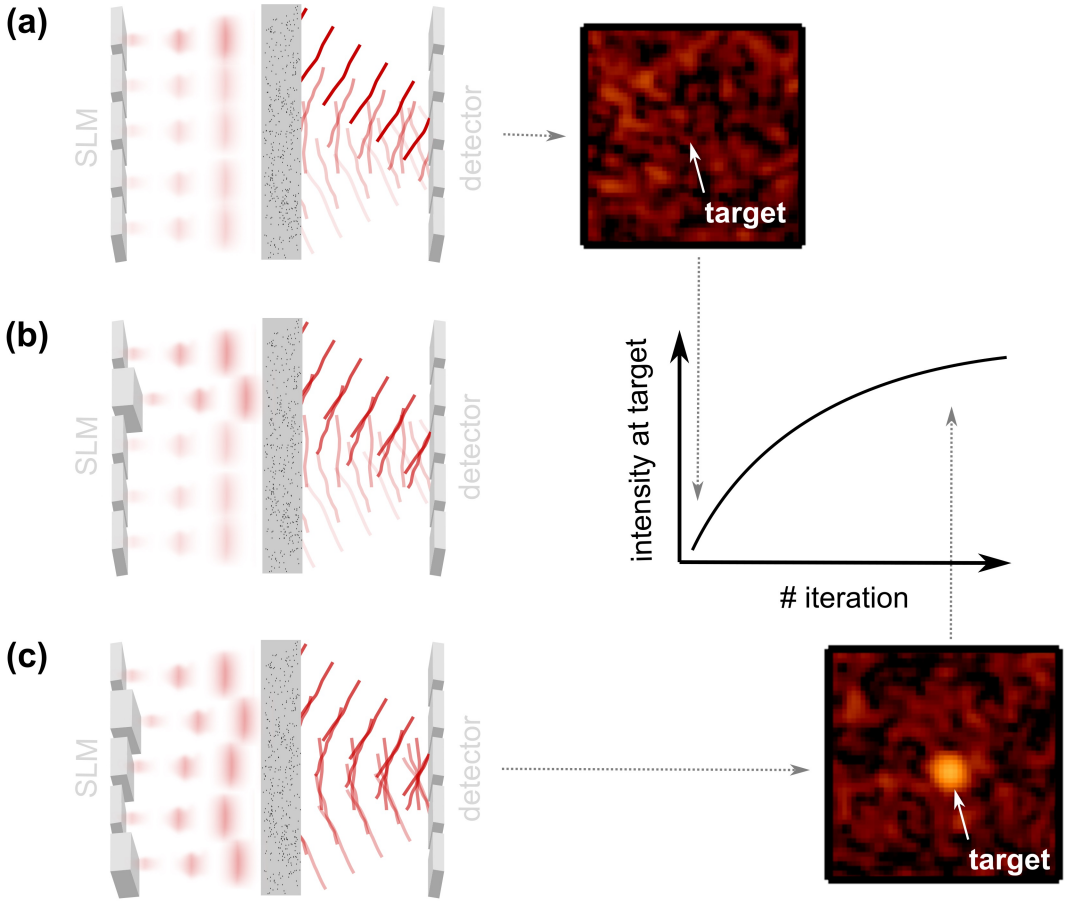

Figure 3.5: **Principle of iterative wavefront shaping.** (a) A flat wavefront incident to a scattering sample results in a speckle pattern to be observed at a detector placed behind the medium. (b) The phase of individual segments of the incident wavefront can be manipulated using a SLM. Due to the linearity of propagation, the phase of the respective contributions to the scattered field shifts accordingly. A high intensity at an arbitrarily chosen target at the detector is observed if a high number of field contributions match in phase at this position. The wavefront shaping algorithm iteratively optimizes the phase pattern applied to the incident beam such that the intensity at the target is maximized. (c) A high-intensity focal spot on top of a speckle pattern results with the final optimized wavefront.

phase conjugation approaches [92, 93]. The focal spot is observed to be created on top of a speckle background (Fig. 3.5). The local intensity enhancement at the target compared to the out-of-target intensity rises with increasing number N of source elements, which corresponds the number of independent wavefront segments controlled by the SLM [23, 116, 117], and drops with increasing target size [116–118]. A number of theoretical investigations found a linear dependence on the number of wavefront segments in case the transmission matrix is assumed to obey Gaussian scattering statistics [23, 115, 118–120]. The efficiency of iterative wavefront shaping further depends on the type of wavefront modulation used. Naturally, the approach is expected to perform best in case the phase and the amplitude of the incident beam can be manipulated [115, 119]. Most practical implementations are based on phase-only wavefront control enabled with LCOS SLMs. The peak intensity of the focal spot is expected to read approximately 78 % of the value achieved with full-complex wavefront control [23, 115, 118, 119]. Binary amplitude-only wavefront control, which is for example realized with digital micromirror devices, results in an expected focal spot intensity of approximately 16 % of the value achieved with complex-valued wavefront control [120].

3.3.2 Feedback types and imaging applications

Imaging based on iterative wavefront shaping is, similar to optical phase conjugation (Sec. 3.2.1), performed either by creating a single focal spot inside the sample and scanning this focus using the optical memory effect or by sequentially scanning the position at which the focus is created. The former method is limited to a narrow FOV at which a single optimized wavefront is able to create a focus behind the turbid layer before the scattered field decorrelates. The latter technique requires to optimize the wavefront which is incident to the sample at each lateral scan position anew. Opposed to optical phase conjugation, which is a single-shot technique, iterative wavefront shaping typically requires a high number of acquisitions to find a single optimized wavefront. The latter approach, thus, faces serious challenges regarding the acquisition speed.

Iterative wavefront shaping techniques require some means to determine the intensity of the scattered field at the target at which a focal spot is supposed to be created only, but no guide star whose complex-valued field is detected after transmission through the scattering layer (Sec. 3.2). Vellekoop et al. demonstrated non-invasive focusing by embedding fluorescent particles to the sample which can be used as point-like intensity probes [118]. Wavefront shaping is enabled by maximizing the total fluorescence emission which is detected in front of the sample. In case fluorescence from multiple particles is detected simultaneously, the observed signal does not reflect the intensity at a single spatially confined target, on the other hand, and the wavefront shaping algorithm can fail to create a single focal spot. To overcome this problem a non-linear probe, for example the two photon fluorescence signal emitted from a small particle, can be taken to create a feedback for the wavefront shaping algorithm instead [121, 122]. Indeed, Katz et al. showed a non-linear optical feedback to be necessary to focus light in case the fluorophores are densely packed [123]. Once the optimized wavefront is found, the focal spot can be scanned for fluorescence imaging behind the scattering layer [105, 106,

122, 123]. The FOV of the technique is limited to the vicinity of the intensity probe which was the original target for focusing (compare Sec. 3.2.1).

Non-invasive and label free wavefront shaping was demonstrated similar to TRUE (Sec. 3.2.1) with feedback probes created from light which is scattered at a focused acoustic wave [124] or by measuring the amount of light which is locally absorbed at the target position. The local absorption can be quantified from the sample‘s photoacoustic response [125–128], which is the acoustic signal detected with an ultrasonic transducer after absorption of a short laser pulse in the sample. Both techniques probe the intensity at the focal position of the transducer and, thus, allow to scan the position at which the wavefront shaping algorithm creates an optical focus by scanning the focus of the transducer [126, 127]. The combination of wavefront shaping and photoacoustic imaging is of particular interest since the width of the optical focus can be significantly smaller than the width of the transducer‘s diffraction limited acoustic focus [127, 128]. Detection of the acoustic signal after sample excitation with a focused beam, thus, enables photoacoustic imaging below the resolution limit of the transducer [127]. Tzang et al. proposed an alternative method to quantify the local absorption at the target which is based on the direct detection of the sample‘s thermal expansion with an OCT system [129]. The approach is complementary to photoacoustic feedback and enables non-invasive optical focusing, as well. In contrast to photoacoustic feedback, the technique cannot directly be applied for imaging, on the other hand, and the penetration depth is limited by the penetration depth of the OCT system, which is low compared to photoacoustic systems for most biological samples. Non-invasive wavefront shaping directly based on the OCT signal was first demonstrated in 2012 and is discussed in detail in Chap. 4.

3.3.3 Algorithms

This Section intends to provide a brief discussion on some of the most popular algorithms for iterative wavefront shaping which were implemented in the scope of this work. In general, the algorithms try to find an optimized pattern to be applied to the spatial light modulator such that the feedback signal, which reflects the intensity at the target, is maximized (Fig. 3.5). In most practical implementations the modulated beam is either imaged or focused from the plane of the SLM to the sample. Due to their iterative nature, wavefront shaping algorithms require no knowledge of the sample's optical properties and correct for aberrations and misalignments present in the optical setup, as well.

The number of degrees of freedom of the wavefront incident to the sample matches the pixel count of the SLM, which typically is in the range of 10^6 or higher for most modern devices. This number is too high to optimize iteratively within a reasonable time span and, thus, most algorithms group multiple pixels to larger segments with uniform amplitude and phase each. The number of degrees of freedom of the incident wavefront matches the number of independent segments in this case.

The algorithm originally proposed by Vellekoop and Mosk optimizes the phase delay at each individual wavefront segment one after another [23, 130]. At each segment, a number of different phase delays is tested (e.g. ten uniformly sampled phases from 0 to 2π) and the phase which results in a maximum intensity at the target is chosen,

respectively. The full wavefront is constructed by sequentially repeating this procedure for all segments within the beam aperture. The run-time of the algorithm, thus, depends on the number N of optimized wavefront segments and on the number m of different phase-values applied to each segment. Full wavefront optimization, thus, requires to apply mN phase patterns to the SLM and to measure the resulting intensity at the target position, respectively.

The sequential algorithm probes the field which is reflected from a single SLM segment one at a time. In case a high number of segments, i.e. small segment sizes, are used, the algorithm becomes sensitive to experimental noise due to the low intensity of light reflected from the individual segments. To overcome this problem, phase patterns which span the full aperture of the beam at once are tested instead. The approach was first demonstrated with the partitioning algorithm presented by Ivo Vellekoop and Allard Mosk in 2008 [130]. Conkey et al. presented a genetic algorithm in 2012 which has been used in a high number of wavefront shaping experiments reported in literature since and which was implemented in the scope of this work, too [131]. The genetic algorithm creates an initial set, or population, of random phase patterns. Each phase pattern is ranked according to the intensity which results at the target once it is applied to the SLM. The patterns are optimized by repeatedly creating new generations of phase masks from the previous population. New phase patterns are blended from two randomly chosen phase masks from the previous generation whereas the selection probability rises with increasing rank. Additionally, random fluctuations are included to newly generated patterns (mutation). The mutation probability is set to drop for later generations to allow the algorithm to converge. The genetic algorithm was demonstrated to outperform the sequential algorithm in the presence of experimental noise and with temporally unstable samples [131].

3.3.4 Acquisition time

Acquisition time is a critical factor when the technique is supposed to be applied to living biological samples. Due to macroscopic sample movements, respiration, blood flow and cellular movement the physical structure of the sample quickly changes and the scattered field decorrelates. As a consequence, the focal spot created through optical phase conjugation or through iterative wavefront shaping quickly decays at time scales down to a few milliseconds [101–103, 112].

The acquisition time required to find an optimized wavefront which focuses scattered light to a single spot depends, in general, on the number N of independent segments or degrees of freedom of the incident wavefront, on the number m of signal acquisitions which are required to find the optimal phase for each wavefront segment, and on the time required for each individual signal acquisition. The efficiency of wavefront shaping is expected to rise with increasing number N which, hence, typically is chosen to be as high as possible within a reasonable optimization time (Sec. 3.3.1). The number of acquisitions m which are required to find the optimal phase for each wavefront segment is determined by the optimization algorithm. If the modulation characteristics of the SLM is unknown, this number needs to be high in order to find the phase iteratively.

With a well defined modulation characteristics, techniques similar to phase shifting interferometry can be employed to find the optimal segment phases. A minimal number of $m = 3$ acquisitions for each wavefront segment results. The technique is similar to transmission matrix approaches which are discussed in the next Section. A number of high-speed wavefront shaping systems are reported which are based on a parallelized optimization algorithm originally reported by Meng Cui in 2011 [132]. The algorithm requires, in principle, a minimum number of $m = 2$ acquisitions per degree of freedom of the incident wavefront. Choi et al. demonstrated another optimization algorithm in 2013 which enables wavefront shaping with SD-OCT systems and which requires a single ($m = 1$) acquisition for each segment of the optimized wavefront [30]. The technique is strongly related to transmission matrix approaches presented in the next Section and is discussed in detail in Chap. 7.

The time required for a single signal acquisition depends on the speeds of wavefront control and feedback detection. Typically, the acquisition speed is limited by the frame rate of the spatial light modulator rather than by the detector. Liquid crystal devices which are often used for phase-only wavefront manipulation feature response times in the range of several milliseconds (150 ms for the device used in this work) and, thus, are not suited for fast systems. Most high-speed wavefront shaping approaches, thus, are based on micro-electro-mechanical systems such as DMs [25, 105, 106, 122, 133] or DMDs [26, 134] which feature frame rates in the kHz up to the MHz range and which, hence, enable wavefront optimization well below 1 ms per independent wavefront segment [133, 134]. DMs enable phase only modulation but come with a low number of independent pixels. DMDs, on the other hand, feature a high pixel count but enable binary amplitude (on/off) modulation only, which results in a reduced efficiency of the optimized wavefront compared to phase-only wavefront control (Sec. 3.3.1). Recently, Feldkhun et al. implemented Cui's parallel wavefront shaping algorithm [132] with wavefront manipulation based on acousto-optic modulators [135]. The approach was shown to be extremely fast and enabled wavefront shaping with $N = 100$ independent wavefront segments in only 10 µs [135].

3.4 Transmission matrix approaches

Optical propagation in a scattering but static sample is considered to be a linear and time-invariant process in case the intensity of the electromagnetic field is low. The linear relation between the scattered field and the field incident to the sample can be described through the complex-valued transmission matrix t_{mn} which quantifies the sample's scattering properties (Eq. 3.1). Knowledge of the transmission matrix allows to reconstruct the incident field by detecting the scattered field, i.e. for imaging, or to optimize the wavefront incident to the medium such that an arbitrary field distribution is created after scattering, for example for focusing similar to iterative wavefront shaping.

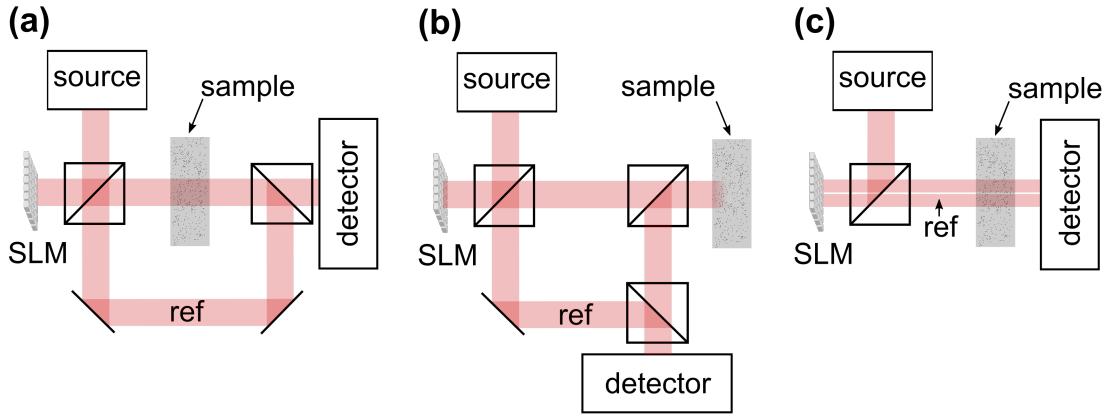

Figure 3.6: **Experimental designs for transmission matrix acquisition.** (a) Transmission geometry with external reference beam. (b) Reflection geometry with reference beam. (c) Self-referenced transmission geometry. Abbreviations: *SLM* spatial light modulator, *ref* reference beam.

3.4.1 Principles and acquisition

In principle, the transmission matrix can easily be determined experimentally according to the definition given in Eq. 3.1. Switching on a single segment of the beam incident to the sample ($E_n^{src} = 1$ if $n = n'$, zero otherwise) and detecting the complex-valued field E_m^{det} which is scattered to a detector placed behind the medium directly yields the column of the reflection matrix $E_m^{det} = \sum_{n=1}^{N} t_{mn} E_n^{src} = t_{mn'}$ which corresponds to the respective wavefront segment. The full matrix is determined by iterating all segments. This approach is kept for almost all practical transmission matrix acquisition methods which are reported in literature and which are discussed in this work. The measurement of the complex-valued scattered field necessitates interferometric acquisition techniques which, in turn, require to superimpose the scattered field with a static reference beam (Fig. 3.6 Panels (a) and (b)). In many practical applications the implementation of a reference beam which is bypassing the sample is not possible, however, since an optical access to the sample back surface is not available or not practical.

In 2008 it was reported by Vellekoop et. al. that during iterative wavefront shaping a sinusoidal intensity fluctuation is observed at the target if a single wavefront segment is modulated while the rest of the beam remains static [118]. A brief analysis of this observation reveals that a fraction of the beam which is reflected at the SLM without being modulated can be used as reference for the interferometric acquisition as well, even though this beam is scattered at the sample (Figs. 3.6(c) and 3.7(a)). The approach allows to determine the transmission matrix without additional external reference beam.

Similar to the previous Section, the electric field incident to the sample is assumed to read E_n^{src} in the plane of the spatial light modulator, where n is the index of the respective wavefront segments (Fig. 3.4). Considering modulation at the n'-th segment only while leaving the rest of the beam static, the field which is scattered to the m-th

pixel of a detector placed behind the medium reads (Fig. 3.7(b)):

$$E_m^{det} = t_{mn'} E_{n'}^{src} + E_m^{ref} \tag{3.2}$$

The term E_m^{ref} corresponds to those parts of the beam which are not manipulated by the SLM and which are scattered to the m-th element of the detector, as well. This term, hence, is considered static and reads $E_m^{ref} = \sum_{n=1\neq n'}^{N} t_{mn} E_n^{src}$ according to Eq. 3.1. The intensity at the detector in case only the phase $\phi_{n'}^{src} = arg(E_{n'}^{src})$ of the modulated wavefront segment is changed is found from the interference law (compare Eqs. 2.3 and 2.4) [118]:

$$I_m^{det}(\phi_{n'}^{src}) \propto |t_{mn'}|^2 \, |E_{n'}^{src}|^2 + |E_m^{ref}|^2 + 2\Re\{\Gamma_m(\phi_{n'}^{src})\} \tag{3.3}$$

The interference term (third term) corresponds to the real part of the field cross-correlation Γ_m [118]:

$$\begin{aligned} \Gamma_m(\phi_{n'}^{src}) &= t_{mn'} \left(E_m^{ref}\right)^* E_{n'}^{src} \\ &= |t_{mn'}||E_m^{ref}| \, e^{i(arg(t_{mn'}) - \phi_m^{ref})} \, |E_{n'}^{src}| e^{i\phi_{n'}^{src}} \end{aligned} \tag{3.4}$$

Obviously, we find $\Re\{\Gamma_m\} \propto cos(\phi_{n'}^{src} + \text{const.})$, i.e. the intensity at the detector features a cosine fluctuation in case the phase $\phi_{n'}^{src}$ of the n'-th wavefront segment is modulated (Fig. 3.7(c)).

In principle, the term Γ_m probes the amplitude and the phase of the transmission matrix t_{mn}. This information can be used to find an optimized wavefront which results in focusing at the detector, similar to iterative wavefront shaping [118]. A major generalization of the concept was proposed by Sébastien Popoff et al. who presented the first experimental acquisition of the optical transmission matrix in 2010 [24].

First, instead as with a single point detector as presented by Vellekoop et. al [118], the scattered field can be investigated at a large detector array with a high number of pixels simultaneously. This consideration is included to the previous equations through the subscript m, which reflects the index of the detector element or detector pixel.

Second, Popoff et al. noted that the transmission matrix can be recovered from the interference signal through algorithms well-known from phase shifting interferometry. The group proposed a four step algorithm (compare Eq. 2.21) which reconstructs the transmission matrix from the intensity $I_m^{det}(\phi_{n'}^{src})$ (Eq. 3.3) which is detected with four discrete phase shifts $\phi_{n'}^{src}$ applied to the modulated part of the incident beam, respectively [24, 119]. Taking Eqs. 3.3 and 3.4 into account, this algorithm yields [24, 119]:

$$\begin{aligned} t_{mn'}^{obs} &= \frac{1}{4}\left[\left(I_m^{det}\left(\phi_{n'}^{src} = 0\right) - I_m^{det}(\pi)\right) + i\left(I_m^{det}\left(\frac{3\pi}{2}\right) - I_m^{det}\left(\frac{\pi}{2}\right)\right)\right] \\ &= t_{mn'}\left(E_m^{ref}\right)^* \end{aligned} \tag{3.5}$$

This is the n'-th row of the observed transmission matrix t_{mn}^{obs}. The exact transmission matrix t_{mn} is not accessible experimentally since the reference field E_m^{ref} which is used for the interferometric acquisition results from parts of the beam which are scattered at the sample and, hence, have an unknown amplitude and phase profile (Fig. 3.7).

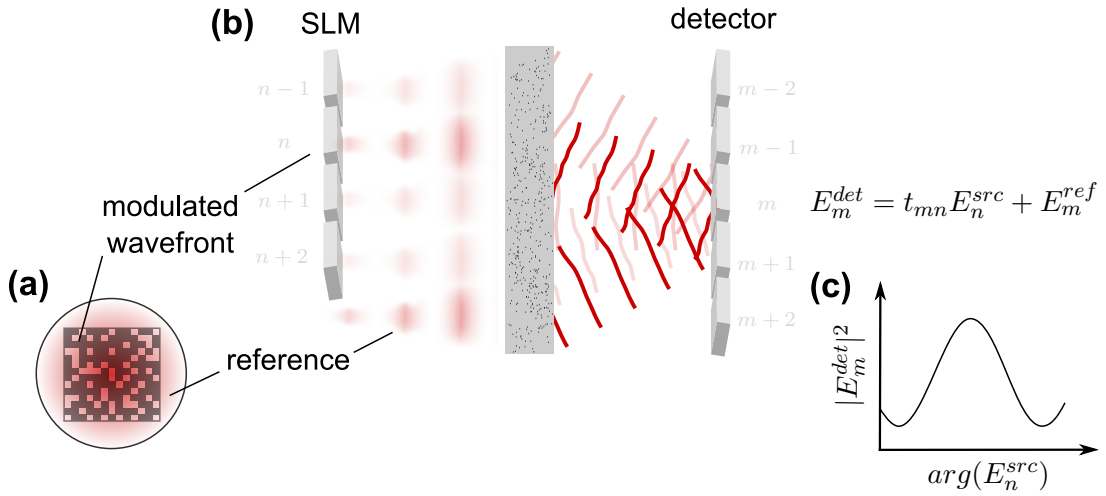

Figure 3.7: **Self-referenced transmission matrix measurement.** (a) Beam in the plane of the SLM. A fraction of the beam incident to the sample is modulated. Another part of the beam remains static and serves as a reference for interferometric acquisition. (b) The modulated and the static reference beam are both scattered at the sample and interfere at the detector (compare Fig. 3.4). (c) A sinusoidal intensity fluctuation is observed in case the phase of the modulated part of the wavefront is changed. The phase and amplitude of the scattered field which results from sample illumination with the modulated wavefront segment, i.e. one column of the transmission matrix, can be determined from this signal using phase shifting algorithms.

Third, in a more general way the transmission matrix t_{mn} describes the linear relation between the complex amplitudes E_n^{src} of the n-th optical basis mode incident to the sample and the amplitude E_m^{det} at the m-th scattered mode [24, 119]. The modes correspond to an (arbitrarily chosen) orthogonal basis of the electromagnetic field at the planes of wavefront manipulation and detection, respectively. So far, this work considered wavefront manipulation on a pixel-by-pixel basis in both planes only. This basis is indeed shown to be orthogonal [136] and is well-suited to describe the scattered field in the plane of the detector since it aligns well with the pixelated signal received with a scientific camera, for example.

In case a pixel-by-pixel or segment-by-segment basis is chosen to describe the field which is incident to the sample, similar to iterative wavefront shaping the system can be sensitive to experimental noise (compare Sec. 3.3.3). The individual basis modes correspond to spatially non-overlapping segments of the wavefront and, thus, their respective intensity is low compared to the total power of the beam. Instead, the transmission matrix can be determined for a set of modes which span a large fraction of the beam. Typically, a plane wave or a Hadamard basis is chosen. The individual modes of the plane wave basis can be created with a phase-only SLM by applying a set of linear phase ramps with different tilt angle for each mode, respectively [30]. In case of a Hadamard

basis the phase patterns which create the individual modes correspond to the respective rows of a Hadamard matrix [24, 119]. The values of the Hadamard matrix read 1 or -1, which correspond to phase delays of 0 and π. The row-vectors of the matrix are mutually orthogonal by definition. The total number of modes matches the dimension of the Hadamard matrix and typically is a power of two since the matrix can easily be constructed for this case.

To summarize, the optical transmission matrix is acquired experimentally by using a spatial light modulator to sequentially apply a set of basis modes to the beam which is incident to the sample. Each mode spans a large fraction of the beam, but a part of the beam remains unmodulated to provide a static reference for the interferometric acquisition (Fig. 3.7(a)). A detector which is placed behind the scattering sample captures the intensity of the scattered field (Fig. 3.7(b)). The SLM is used to shift the phase offset of the respective mode which is incident to the sample, but not the phase of the static part of the wavefront. Multiple acquisitions with different phase delays allow to reconstruct the complex-valued scattered field from the intensity which is captured at the detector (Eq. 3.5). The field which results from sample illumination with a single mode corresponds to a single column of the observed transmission matrix (Eq. 3.5). The full matrix is captured by repeating this procedure for all modes.

3.4.2 Application to focusing

Once the transmission matrix is experimentally determined, a wavefront which creates a focal spot from scattered light at the m_t-th detector pixel, similar to iterative wavefront shaping, can be calculated from the complex-conjugate of the corresponding matrix row [24, 118, 119]:

$$E_n^{src,opt} = \left(t_{m_t n}^{obs}\right)^* \tag{3.6}$$

The phase of the incident wavefront reads $arg(E_n^{src,opt}) = -arg(t_{m_t n}) + \phi_{m_t}^{ref}$ according to the definition of the observed transmission matrix (Eq. 3.5). The intensity at the detector once the optimized wavefront is applied to the sample is evident by inserting Eq. 3.6 in Eq. 3.1:

$$I_m^{det} \propto \left| \sum_{n=1}^{N} |t_{mn}| e^{i\, arg(t_{mn})}\, |E_n^{src}| e^{i(-arg(t_{m_t n}) + \phi_{m_t}^{ref})} \right|^2 \tag{3.7}$$

For an arbitrarily chosen detector element ($m \neq m_t$) Eq. 3.7 corresponds to a sum of random phasors. In contrast, at the target pixel m_t the individual contributions add up in phase and, indeed, a high intensity results:

$$I_{m_t}^{det} \propto \left| \sum_{n=1}^{N} |t_{m_t n}| |E_n^{src}| \right|^2 \left| e^{i\phi_{m_t}^{ref}} \right|^2 \tag{3.8}$$

Utilizing the transmission matrix for single-point focusing is equivalent to iterative wavefront shaping [119] and, hence, the same considerations regarding the focusing efficiency apply (Sec. 3.3.1). In contrast to the previous approach, the transmission matrix

needs to be determined once and the optimized wavefront can directly be calculated afterwards without further acquisitions or iterative optimization algorithms. The transmission matrix describes the scattered field at the complete field of view of the detector and, hence, a wavefront which creates a focal spot from scattered light an any position within the FOV can be found without needing to reacquire the matrix. Furthermore, multiple wavefronts optimized for different target positions can be superimposed for simultaneous focusing [24]. To this end a m-element target vector $E_m^{det,target}$, which describes the supposed field at the detector after wavefront shaping, may be defined. The vector elements, for example, are chosen to be unity if the index m corresponds to a detector pixel at which a focus is supposed to be created and zero otherwise. The optimized incident wavefront reads in this case according to Eq. 3.6 [24]:

$$E_n^{opt} = \sum_{m=1}^{M} \left(t_{mn}^{obs} \right)^* E_m^{det,target} \tag{3.9}$$

3.4.3 Imaging applications

Transmission matrix as well as iterative wavefront shaping approaches both enable focusing of scattered light but require some means to determine the intensity of the scattered field after transmission through the medium. In contrast to iterative wavefront shaping, which tries to maximize the intensity at the target by iteratively optimizing the incident wavefront (Fig. 3.5), transmission matrix approaches track small intensity fluctuations which result from interference of the phase-modulated wavefront with a static reference field (Fig. 3.7). A number of iterative wavefront shaping algorithms utilize this effect, as well, and cannot clearly be distinguished from transmission matrix approaches, for example the parallelized algorithm which was presented by Meng Cui [132] and which was implemented with a number of high-speed wavefront shaping systems (Sec. 3.3.4). As a major difference, the transmission matrix determines the scattered field at a spatially extended field of view simultaneously, in contrast to point detection in case of iterative wavefront shaping. Transmission matrix approaches, thus, enable focusing at any point within the FOV once the matrix is determined whereas iterative wavefront shaping approaches require to repeat the optimization algorithm at each target position.

Non-invasive techniques to determine the local optical intensity inside a scattering sample were demonstrated for iterative wavefront shaping (Sec. 3.3.2) and can be applied to transmission matrix approaches, as well. Chaigne et al., for example, demonstrated the acquisition of the transmission matrix from the photoacoustic response of a scattering sample [137]. Youngwoon Choi et al. demonstrated the acquisition of the matrix and optical focusing based on the sample‘s OCT signal [30]. This approach is discussed in detail in Chaps. 4 and 7. Imaging can be performed by scanning the position of the focal spot, similar to the methods discussed in Sec. 3.3.2. In contrast to the iterative wavefront shaping, utilizing the transmission matrix enables scanning beyond the correlation length of scattered light since the matrix can be used to recalculate new wavefronts for focusing at different scan positions. The FOV of the approach is limited to the FOV of the detector which was used to determine the transmission matrix.

Additionally, knowledge of the transmission matrix in principle allows to directly reconstruct the electromagnetic field which is emitted from a hidden object by detecting the scattered field after transmission through the turbid layer [24, 119, 138, 139]. The technique enables imaging through the scattering layer but requires detailed knowledge of the transmission between the object and the detection plane, i.e. calibration of the imaging system with a high-resolution wavefront measurement in the plane of the hidden object. The approach was demonstrated for imaging with a static scattering layer placed in a microscopic setup [139] but is not feasible for imaging with dynamically changing (living) biological tissue.

Similar to the transmission matrix, the reflection matrix of a scattering sample can be determined by changing the detection geometry [140, 141]. The approach requires single-sided sample access only and, thus, allows to utilize a static reference beam for interferometric detection of the back-scattered light [140, 141] (Fig. 3.6(b)). As a consequence, fast single-shot interferometric acquisition techniques such as off-axis holography can be used [141]. Knowledge of the reflection matrix allows to investigate the sample‘s scattering properties [141] and enables focusing of back-scattered light similar to the transmission matrix (Sec. 3.4.2). The application to imaging is not as straightforward as with the transmission matrix, on the other hand, since light backscattered from different depths of the sample is detected simultaneously. A number of groups utilized time-of-flight gating to detect the reflection matrix with light backscattered from a selected depth only. The technique combines reflection matrix approaches with OCT imaging and is discussed in Sec. 4.2 in detail.

3.4.4 Singular value decomposition

A singular value decomposition of the transmission or reflection matrix allows to quantify the scattering properties of the sample. A detailed discussion of this effect is beyond the scope of this work, however. Recent studies further demonstrated correlations between modes which correspond to large eigenvalues and strongly scattering particles which are embedded to the sample. This correlations enable non-invasive focusing and imaging.

The DORT method (french acronym for decomposition of the time reversal operators) tries to identify dominant scatterers present in the turbid sample from a singular value decomposition of the time reversal operator $TT^{\dagger}$ [142]. This operator is calculated from the reflection or from the transmission matrix T and, in principle, describes the relation between the target field distribution for optical phase conjugation and the resulting scattered field after application of the phase conjugated wave to the sample [142] (compare Eqs. 3.1 and 3.9). The eigenvalues of the time reversal operator yield modes which are scaled by the phase conjugation process only, i.e. modes for which the scattered field after phase conjugation actually matches the target light distribution. The eigenvalues quantify the corresponding scaling factors. In many practical implementations the singular value decomposition of the time reversal operator $TT^{\dagger}$ is found from the decomposition of the transmission matrix T instead, which yields equivalent eigenvectors [140].

Prada et al. demonstrated in the context of ultrasonic time reversal (Sec. 3.2) that large eigenvalues of the time reversal operator are associated with dominant scatterers

present in the sample [142]. Namely, in case single-scattered waves are detected only, a one-to-one association exists and, hence, coupling the wavefront to the sample which corresponds to the largest eigenvalue creates a focus at the strongest reflecting particle [142]. Popoff et al. implemented the approach with the optical reflection matrix acquired from a scattering sample and demonstrated non-invasive focusing to strongly reflecting particles hidden inside the medium [140]. Imaging in the vicinity of dominant scatterers can be performed similar to iterative wavefront shaping by exploiting the optical memory effect to laterally scan the focal spot (Sec. 3.3.2). In another approach, an image of dominant scattering particles embedded to the sample can directly be constructed from the eigenvectors corresponding to the largest eigenvalues of the time reversal operator, as well [143].

The approach is valid in the case the detected reflection matrix is dominated by single-scattered waves only, however [140, 142]. The application to strongly scattering samples was recently demonstrated by Aumry Badon and is based on the suppression of signal contributions from multiple scattered light prior to the singular value decomposition of the matrix [143]. The approach is similar to full field optical coherence tomography and is discussed in Sec. 4.2. Seungwoon Jeong et. al. demonstrated the singular value decomposition with a comparable system to enable non-invasive focusing in the presence of multiple scattered light. The approach is discussed in Sec. 4.4.2.

3.4.5 Acquisition time and enhancements

The same considerations made for iterative wavefront shaping (Sec. 3.3.4) apply for the acquisition speed of transmission and reflection matrix approaches, as well. Namely, the total acquisition time depends on the total number of independent modes or wavefront segments incident to the sample, on the number of signal acquisitions per mode (three for phase shifting algorithms, one for off-axis holography) and on the speed of the detector and the spatial light modulator. High-speed systems, thus, need to enable fast SLMs for wavefront manipulation. In principle, most approaches discussed in Sec. 3.3.4 can be employed, as well.

4 State of the art: Applications of wavefront shaping to optical coherence tomography

Optical coherence tomography utilizes confocal and coherence gating to suppress multiple scattered light and to enable imaging in turbid media. In practical applications the rejection of multiple scattered light is not complete, however, and a significant fraction of the OCT signal arises from multiple small-angle scattering events. These signal contributions reflect the sample morphology, as well, and become relevant when strongly forward scattering media such as biological tissue are imaged (Sec. 2.3.2).

This Chapter discusses current state of the art techniques to combine OCT and wavefront shaping for depth enhanced imaging with scattering samples. In principle, two approaches are reported to date. The acquisition of the sample's reflection matrix combined with full field optical coherence tomography (FF-OCT) enables additional rejection of multiple scattered light for depth enhanced imaging with turbid samples. The technique exploits correlations between the incident beam and the single scattered reflected wave and is discussed in Sec. 4.2. In another approach, iterative wavefront shaping or optical phase conjugation based on the reflection matrix is used for non-invasive focusing of multiple scattered light inside the sample. The OCT signal depends linearly on the amplitude of the electromagnetic field and, thus, the received signal can directly be enhanced by focusing small-angle scattered light to the detection volume. This work focuses on the latter technique, which can be implemented with full field as well as with scanning OCT systems. A detailed discussion of the approach is given in Secs. 4.3 and 4.4. Remaining problems which are supposed to be covered in this work are discussed in Sec. 4.5.

4.1 OCT designs

Reflection matrix as well as iterative wavefront shaping techniques require to include a spatial light modulator to the OCT system which enables wavefront manipulation at the beam illuminating the sample. Designs which are reported to date are illustrated in Fig. 4.1, assuming a reflective SLM is used. The Mach-Zehnder design (Fig. 4.1(a)) allows to separate the reference from the sample beam and enables independent wavefront shaping by including the SLM to the sample beam only. The field which is backscattered from the sample is not manipulated again at the SLM prior to detection. On the other hand, the design is rather bulky, requires a high number of optical components and a high mechanical stability, and cannot directly be implemented to existing

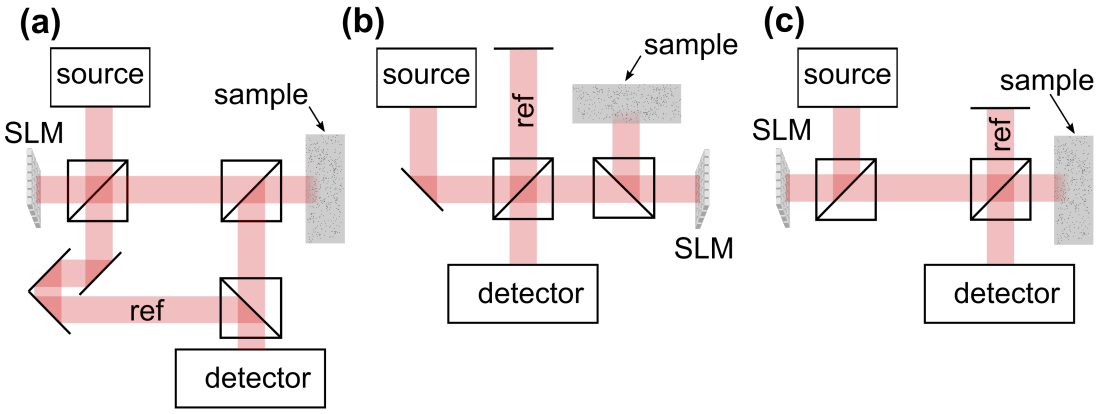

Figure 4.1: **OCT designs enabling wavefront manipulation.** (a) Mach-Zehnder design. The SLM manipulates the sample beam only [30, 143–147]. (b) SLM at sample arm. The sample beam passes the SLM again after reflection at the sample [25]. (c) SLM at source beam. The sample and the reference beam are affected simultaneously by wavefront manipulation with the SLM [26–29]. Abbreviations: *SLM* spatial light modulator, *ref* reference beam.

OCT systems which are based on a Michelson interferometer (Fig. 2.3). Figure 4.1(b) illustrates a Michelson interferometer based OCT design. Placing the SLM at the sample beam enables wavefront shaping while leaving the reference beam static. The field which is backscattered from the sample passes the SLM again prior to detection, on the other hand. Figure 4.1(c) illustrates another design based on a Michelson interferometer. Placing the SLM at the source beam allows to feed the shaped wavefront to a conventional OCT scan head which includes the optics of the reference and the sample beam [26]. The approach causes the shaped wavefront to be coupled to the reference beam as well, on the other hand. As a consequence, the reference beam does not remain static during the acquisition of OCT signals with differently shaped wavefronts applied.

4.2 Exploiting the reflection matrix to suppress multiple scattered light

The reflection matrix describes the linear dependence between the backscattered field and the field which is incident to the sample. Typically, light reflected from different depths is detected simultaneously and, hence, the matrix cannot directly be used for imaging (Sec. 3.4.3). The acquisition of the reflection matrix requires single-sided sample access only and, in contrast to transmission matrix approaches, a static reference beam can be added for interferometric acquisition of the complex-valued backscattered field (Fig. 3.6). Utilizing a broadband instead of a monochromatic light source allows to detect the reflection matrix time-of-flight or depth selectively. The approach is similar to time domain optical coherence tomography since interference at the detector is only

observed from the fraction of backscattered light whose optical path length matches the length of the reference beam (Fig. 2.2). The reference arm length, hence, determines the depth from which backscattered light is detected during the acquisition of the matrix.

Experimental devices to capture the time-gated reflection matrix are similar to FF-OCT systems with wavefront manipulation at the sample beam. In contrast to conventional FF-OCT systems, a spatially coherent source needs to be employed to enable beam shaping with the SLM, however. The reference beam is supposed to remain static and the field which is reflected from the sample should not pass the SLM again between scattering and detection. Hence, all reports demonstrating the experimental acquisition of the time-gated reflection matrix are based on the Mach-Zehnder design to date (Fig. 4.1(a)) [30, 143–147]. The suppression of multiple scattered light is demonstrated with full-field imaging configurations only, which project the conjugate of the objective focal plane to a scientific camera [143, 145–147]. As a consequence, the spatial frequency spectrum or the angle-resolved image of the field which is backscattered from the sample is observed. Complex-valued signal acquisition is enabled through interferometric techniques such as phase shifting interferometry [143, 147] or off-axis holography [145, 146].

Kang et al. demonstrated the acquisition of the time-gated reflection matrix with a set of plane wave basis modes incident to the sample at different angles, respectively [145]. The reflection matrix corresponds to the complex-valued backscattered field which is captured in case of sample illumination with the individual modes and, thus, quantifies the angle-resolved backscattered field depending on the angle of illumination. The reflection matrix contains contributions from single scattered and from multiple scattered light. In case of single scattering at an object which is placed inside the turbid layer, however, the change in lateral momentum of the backscattered wave reflects the spatial frequency of the hidden object, which is the object‘s transfer function [145]. Depth enhanced OCT imaging is achieved by collective accumulation of single scattering (CASS). Reflection matrix elements with equal momentum difference between the incident and the backscattered wave correspond to the same component of the object transfer function and match in phase. In contrast, the phase of signal contributions from multiple scattered light is randomly distributed. Hence, the summation of complex-valued reflection matrix elements with equal momentum difference enhances single-scattered signal contributions compared to the contributions from multiple scattered light and yields the object transfer function, from whose Fourier transform an image of the hidden object is received [145].

The approach was experimentally demonstrated to be feasible for micrometer resolution full-field imaging of samples hidden below tissue samples up to 0.9 mm thick [145]. Recently, an improved implementation of the technique was demonstrated which utilizes random phase patterns for the acquisition of the reflection matrix instead of a plane wave basis [146]. To further enhance the penetration depth, optical aberrations present in the sample are identified and corrected for in post-processing. The approach, in principle, applies an additional digital phase-correction to the experimentally acquired reflection matrix which is iteratively optimized such that the total intensity of the CASS image becomes maximal. The final optimized phase map reflects aberrations which are present in the sample [146].

Badon et al. demonstrated the suppression of multiple scattered light based on spatial correlations of the incident and the backscattered field [143]. The group utilized a spatial light modulator to scan the position of point illumination at the sample and acquired the respective full-field image by Fourier transforming the angle-resolved backscattered field, which is captured with the experimental device. The reflection matrix, thus, yields the spatial distribution of the backscattered field depending on the point of illumination. In principle, a wide field OCT image with confocal illumination and detection can be constructed from the diagonal elements of the matrix. This technique is equivalent to conventional FF-OCT imaging [143]. In another approach, the OCT signal corresponding to single-scattered light is expected to be detected close to the position of illumination, i.e. near the diagonal elements of the reflection matrix. Off-diagonal elements hence are removed to suppress signal contributions from multiple-scattered light [143]. A subsequent singular-value decomposition of the filtered matrix allows to identify strongly reflecting particles embedded to the sample, similar to the techniques discussed in Sec. 3.4.3. The approach was experimentally demonstrated to enable micrometer resolution imaging of objects hidden below biological tissue up to 0.8 mm thick [143].

Very recently, Badon et al. demonstrated an enhanced post-processing method based on the distortion matrix [148]. The distortion matrix describes the difference of the reflection matrix which is acquired with point-by-point sample illumination to the signal which is expected in case the beam is reflected at an ideal point-source in the sample plane and back propagated through a homogeneous non-scattering medium. A singular value decomposition of the distortion matrix additionally allows to identify and correct for optical aberrations present in the sample, similar to the iterative approach presented by Kang et al. [146], and enables imaging [148].

4.3 Spectral and temporal shaping of scattered light

The discussion on wavefront shaping and transmission matrix approaches which is given in Chap. 3 considered monochromatic radiation and manipulation and detection of the optical wavefront in the spatial domain only. For OCT imaging broadband light sources are required, however, and the signal is captured time-of-flight dependent, i.e. in the temporal (Sec. 2.1) or spectral (Sec. 2.2) domain. This Section illustrates general aspects of wavefront shaping with broadband sources and discusses temporal and spectral shaping of scattered light based on spatial manipulation of the beam which is incident to the turbid sample.

A number of reports demonstrated iterative wavefront shaping by probing the sample‘s non-linear optical response, for example the emitted two photon fluorescence, and optimizing the incident wavefront such that this signal is maximized [121–123] (Sec. 3.3.2). To this end, Ti:Sapphire sources were used, which can be employed for OCT imaging as well, and spatial focusing of scattered light was demonstrated experimentally with the pulsed sources [121–123]. To maximize the sample‘s non-linear optical response, the pulsed illumination needs not only to be spatially focused but temporally focused as well to yield a high instantaneous intensity at the fluorophore, however [121]. As a conse-

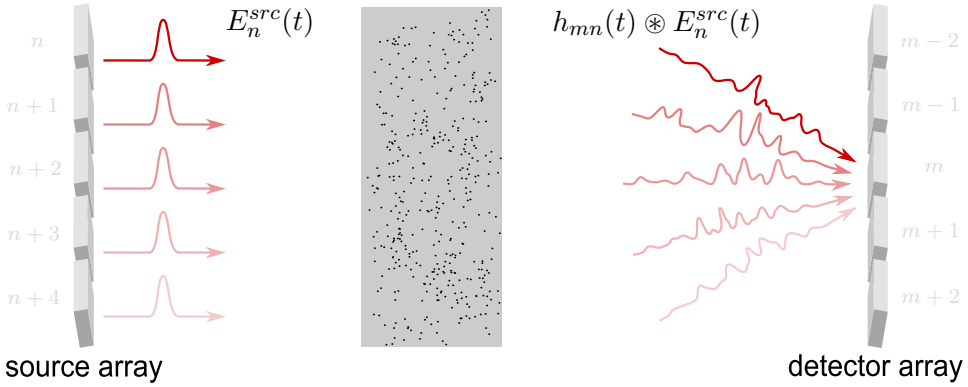

Figure 4.2: **Coupling of temporal and spatial degrees of freedom in a scattering medium.** Illuminating a sample with varying spatial modes causes different spatial (not shown, see Fig. 3.4) and temporal speckle profiles to be observed behind a turbid sample. Spatial shaping of the incident beam enables temporal manipulation of the scattered field.

quence, iterative wavefront shaping with a non-linear optical feedback probe results in spatial and temporal compression of the scattered laser pulse. The effect was directly observed by Katz et al. in 2011 [121].

Typical phase-only SLMs which are used for wavefront shaping experiments allow to (axially) shift the modulated beam by only one to two wavelengths, which is not sufficient to significantly change the temporal profile of the beam. Fortunately, the turbid medium couples the spatial profile of the incident beam to the temporal and spectral shape of the scattered field. The effect can be understood by considering the scattering medium to be a linear and time invariant system. Adopting the model given in Sec. 3.3 and Fig. 3.4, transmission from the n-th element of the incident wavefront to the m-th element of the scattered beam can be described based on the sample's impulse response $h_{mn}(t)$:

$$E_m^{det}(t) = \sum_{n=1}^{m} h_{mn}(t) \circledast E_n^{src}(t) \tag{4.1}$$

In contrast, the optical transmission matrix t_{mn} describes the propagation of monochromatic radiation only (Eq. 3.1). The symbol $\circledast$ denotes the convolution operator. The approach is equivalent to descriptions based on the sample's Green function [119, 149].

Each segment of the incident beam or, more general, each incident mode $E_n^{src}(t)$ gives rise to a different spatial and temporal field distribution $h_{mn}(t) \circledast E_n^{src}(t)$ in the detection plane [121, 150]. The effect is illustrated in Fig. 4.2 and can be understood by taking into account that the individual incident modes couple to different areas of the scattering sample. Thus, different temporal and spatial profiles result depending on the respective trajectory of the scattered field.

Spatial manipulation of the beam incident to the sample yields control over the temporal profile after scattering. For example, light can selectively be coupled to trajectories

which give rise to the same temporal delay. In another approach, scattered light can be spatially and temporally focused by manipulating the spatial phase profile of the incident beam without actually manipulating the temporal profile. Due to the linearity of propagation, phase manipulation of the respective incident modes shifts the corresponding contributions to the scattered field accordingly (Fig. 3.5). The phase profile of the incident beam, thus, can be optimized such that constructive interference is created from scattered light at one point in space and time, similar to the approaches which are discussed in Chap. 3 for monochromatic radiation.

Aulbach et al. initially demonstrated shaping and compression of a short laser pulse based on iterative wavefront optimization in 2011 [151]. The group superimposed the scattered pulse with a static reference beam at a point detector placed behind the turbid sample [151]. The approach selectively detects light which is scattered to the position of the detector at the temporal delay which matches the temporal delay of the reference beam. Spatial and temporal focusing at the detector was demonstrated with an iterative algorithm which optimizes the phase profile of the incident beam such that the detector signal is maximized [151]. In a similar approach, Mounaix et al. demonstrated the full field acquisition of the scattered field after sample illumination with a pulsed source. The technique allows to determine the transmission matrix from light whose path length matches the length of the reference beam only, i.e. which is detected at a given temporal delay [152]. The approach hence is similar to the acquisition of the time-gated reflection matrix, which is discussed in Sec. 4.2, but determines the scattered field in transmission geometry. Phase conjugation based on the time-gated transmission matrix was shown to enable spatial and temporal focusing of scattered light [152, 153] (compare Sec. 3.4.2).

A turbid medium couples the spatial profile of the incident beam to the spectrum of scattered light, as well. Fourier transforming Eq. 4.1 yields [149, 154–157]:

$$E_m^{det}(\omega) = \sum_{n=1}^{N} h_{mn}(\omega) E_n^{src}(\omega) \tag{4.2}$$

As with the temporal profile, each mode $E_n^{src}(\omega)$ which is incident to the sample gives rise to a different spatial and spectral profile $h_{mn}(\omega)E_n^{src}(\omega)$ at the detection plane [121, 149, 150, 154, 156]. Hence, spectral shaping of the scattered field is enabled through spatial manipulation of the beam incident to the sample as well, similar to temporal shaping [150, 154, 158].

Equation 4.2 is equivalent to describing the scattered field in terms of the spectrally resolved transmission matrix $t_{mn}(\omega)$ which can be determined experimentally with a monochromatic source tuned to different wavelengths, for example [156, 157]. Knowledge of the spectrally resolved transmission matrix was shown to yield spatial control over the scattered field, similar to the monochromatic transmission matrix (Sec. 3.4), and temporal or spectral control, as well [153, 156, 157].

4.4 Wavefront shaping techniques for direct OCT signal enhancement

4.4.1 Technical implementation

The combination of wavefront shaping and optical coherence tomography was first demonstrated in 2012 by Reto Fiolka et al. [25]. The group included a deformable mirror to the sample arm of a TD-OCT system (Fig. 4.1(b)) and implemented Meng Cui's parallelized iterative wavefront shaping algorithm to optimize the amplitude of the OCT signal which is received from a scattering sample [25, 132]. The combination with SD-OCT was demonstrated by Jaeduck Jang et al. [26] and by Youngwoon Choi et al. [30] in 2013. Both groups implemented algorithms which are similar to transmission matrix approaches (Sec. 3.4).

Jang et al. included a digital micromirror device to the source beam of a SD-OCT system [26] (Fig. 4.1(c)). The DMD enables high-speed wavefront manipulation and the optical design allows to feed the shaped wavefront to the scan head of a conventional SD-OCT system, which includes the optical elements of the reference and sample beam and which enables high-speed object scanning. On the other hand, the DMD enables binary amplitude wavefront manipulation only. To overcome this problem, Jang et al. noted that the phase of the beam which is diffracted at the DMD can be manipulated by laterally shifting the amplitude pattern which is applied to the device [26]. The group, thus, implemented a wavefront shaping algorithm which uses the DMD to sequentially create different basis modes and which captures the OCT signal for 25 different lateral positions of the respective amplitude pattern at the DMD screen. A wavefront which enhances the OCT signal received at an arbitrarily chosen time-of-flight is then calculated. For each basis mode, the lateral position of the corresponding amplitude pattern is chosen which yields the highest signal amplitude at the target. The phase of the OCT signal is neglected. Subsequently, the laterally shifted patterns from all modes are superimposed and applied to the DMD. Similar to transmission matrix approaches, a wavefront which enhances the signal at any position within the axial field of view of the OCT system can be found without further signal acquisition. In contrast, however, the approach is purely based on the intensity of the acquired OCT signal. The phase of the incident field is not directly manipulated and the phase of the scattered field cannot be detected since the reference beam does not remain static in case different wavefronts are applied due to the optical design (Fig. 4.1(c)).

In contrast, Choi et al. presented a Mach-Zehnder based SD-OCT design with a phase-only SLM placed at the sample beam [30] (Fig. 4.1(a)). The design features a static reference beam and enables the acquisition of the complex-valued SD-OCT signal from just a single acquisition of the spectral raw data (Sec. 2.2). The group utilized the SLM to apply a set of different basis modes to the sample beam. The resulting SD-OCT signal corresponds to the time-of-flight resolved backscattered field, respectively. Similar to the acquisition of the optical transmission matrix (Sec. 3.4.1), the time-of-flight resolved reflection matrix, hence, can be acquired by iterating the respective basis modes and saving the resulting complex-valued OCT signal to the corresponding column of the

matrix [30]. The total number of measurements which are required to capture the full reflection matrix, thus, is at least three times lower compared to phase shifting algorithms (Sec. 3.4.1) and matches the number N of incident modes exactly. The group further demonstrated a phase conjugation algorithm equivalent to the approach discussed in Sec. 3.4.2 to be able to calculate an optimized wavefront from the reflection matrix which selectively enhances the received SD-OCT signal once the wavefront is applied to the sample beam. Phase conjugation with the time-resolved reflection matrix, hence, yields similar results to the iterative optimization algorithm which was demonstrated by Jang et al. [26]. A significantly reduced number of signal acquisitions is required, however. On the other hand, the approach requires a static reference beam to capture the reflection matrix and phase-only modulation to apply the optimized wavefront.

4.4.2 Non-invasive focusing

OCT signal enhancement based on wavefront shaping, in principle, focuses backscattered light at a given time-of-flight to the position of the imaging system‘s detector [30], similar to the experiments in transmission geometry reported by Aulbach et al. [151] (Sec. 4.3). If the technique is supposed to be used for depth enhanced imaging it is important to investigate in which way the approach affects the light distribution inside the scattering sample. Ideally, one wishes the detected OCT signal to be proportional to the electric field which is single scattered at the object to be imaged. Using wavefront shaping to maximize the OCT signal in this case enhances the intensity at the detection volume, i. e. at the object, and enables non-invasive focusing. With practical systems these ideal conditions cannot be met, however, since OCT devices detect multiple scattered light to some extent, as well (Sec. 2.3.2). Even in the presence of multiple scattered light, the amplitude and the SNR of the OCT signal can be enhanced in case light is focused to the position of the hidden object, though.

Fiolka et al. demonstrated non-invasive optical focusing by embedding small reflecting particles behind a forward scattering turbid layer and using an iterative wavefront shaping algorithm to enhance the OCT signal which is detected from these particles [25]. The technique requires the target particles to be sparsely distributed to ensure the detected signal corresponds to the reflection at a single particle only. In case multiple particles are simultaneously present at the detection volume the approach is observed to produce a split focus [159] since the OCT signal is proportional to the field reflected from either particle. The technique further requires to clearly identify the OCT signal which is resulting from the respective target particles, i.e. the particles need to be visible in the OCT scan. For depth enhanced imaging one actually is interested in the case conventional OCT imaging is not possible, though, i. e. signal contributions from multiple scattered light dominate compared to weakly scattered light.

Jeong et al. demonstrated non-invasive focusing inside a scattering sample based on a singular value decomposition of the time-gated reflection matrix [144] (compare Sec. 4.2). In principle, the largest eigenvalue and the corresponding eigenvector of the matrix reflect the wavefront with the highest intensity after reflection at the sample. In case a strongly reflecting target object is hidden inside the turbid medium, this wavefront was shown

to preferentially couple light to trajectories which interact with the target compared to trajectories without any target interaction [144]. In terms of OCT imaging, the former signal contributions reflect the sample morphology whereas the latter are considered signal noise from multiple scattered light. The effect becomes stronger the smaller the object gets and was demonstrated to enable non-invasive focusing at the hidden target [144].

Choi et al. demonstrated the acquisition and singular value decomposition of the reflection matrix with a monochromatic source and compared the approach to iterative wavefront shaping based on the backscattered field [160]. The group demonstrated the iterative wavefront shaping algorithm to preferentially couple light to those eigenmodes of the scattering sample which correspond to the largest eigenvalues [160]. The experiment was recently repeated with time-gated acquisition similar to optical coherence tomography [161]. Due to the preferential coupling to high-reflectivity eigenmodes, iterative wavefront shaping based on the OCT signal was demonstrated to focus light to a strongly reflecting target embedded to the sample as well [161], similar to the previous approach based on the singular value decomposition of the time-gated reflection matrix [144].

The previous reports considered a partitioning algorithm (compare [130]) for iterative wavefront optimization [160, 161]. Other iterative optimization algorithms are expected to find comparable wavefronts and iterative wavefront shaping further is equivalent to point-wise focusing based on phase conjugation with the reflection matrix (Sec. 3.4.2). Hence, no matter what kind of wavefront optimization procedure is utilized, light which is scattered at strongly reflecting sample structures and the corresponding contributions to the OCT signal are expected to be predominantly enhanced with wavefront shaping, even in case these signal features cannot clearly be identified in the original OCT signal due to multiple scattering.

4.4.3 Depth-enhanced imaging

To date, imaging based on the direct enhancement of the OCT signal through wavefront shaping approaches, in contrast to the techniques discussed in Sec. 4.2, is demonstrated by the group of YeongKeun Park with the system which was presented by Jang et al. in 2013 only [26–29] (Sec. 4.4.1). Iterative wavefront shaping is utilized to selectively enhance the amplitude of the SD-OCT signal at a given time-of-flight one at a time. Depth enhanced imaging is enabled by optimizing the incident wavefront for signal enhancement at different positions in the axial field of view individually and by stitching a full depth-scan from the in-target point-optimized OCT signals [26].

The acquisition time required to capture a single A-scan is determined by the time required to find the optimized wavefronts, similar to the acquisition of the reflection matrix, and by the time which is required to subsequently scan the axial position of point-wise signal enhancement for imaging. The former is determined by the optimization algorithm whereas the latter corresponds to the pixel count at the axial FOV of the optimized A-scan. In contrast to comparable wavefront optimization algorithms, the method proposed by Jang et al. requires a rather high number of acquisitions (Sec. 4.4.1).

Due to high-speed wavefront manipulation enabled with a DMD and due to efficient data processing the optimization of a single depth-scan could be demonstrated within 15 s for a set of 300 basis modes and for 200 pixels at the optimized A-scan, nonetheless [28]. Cross-sectional imaging is enabled by scanning the position of sample illumination and repeating the full optimization process at each lateral position, respectively. The approach was shown to enable depth-enhanced SD-OCT imaging with biological samples [27–29] and to be sufficiently fast for in-vivo imaging with anaesthetized and fixated mice [28].

4.5 Remaining problems

A number of approaches demonstrated depth enhanced FF-OCT imaging based on the acquisition of the time-gated optical reflection matrix (Sec. 4.2). The technique, in principle, exploits correlations between the incident and the backscattered sample beam to additionally suppress multiple-scattered light which is detected by the OCT system. The acquisition of the time-gated reflection matrix requires sophisticated optical designs which cannot easily be implemented with existing OCT devices. Furthermore, the approach was demonstrated with phase-only liquid crystal spatial light modulators only, which are subject to low frame rates and, hence, cause long acquisition times which prohibit in-vivo imaging. The concept, thus, is not further pursued in this work.

The group of YeongKeun Park demonstrated depth enhanced OCT imaging based on iterative wavefront shaping (Sec. 4.4.3). The presented system can easily be implemented by modifying existing SD-OCT systems to include a DMD for wavefront manipulation at the source beam (Fig. 4.1(c)). The approach potentially enables high-speed imaging since fast spatial light modulators as well as commercial SD-OCT heads, which include beam scanning optics, can be used. The experimentally demonstrated system still required 15 s to capture a single A-scan, however. This number is too high for in-vivo imaging applications with most biological samples and is mainly caused by the inefficient optimization algorithm, which requires a large number of iterations.

In contrast, Choi et al. demonstrated a potential high-speed algorithm which enables OCT signal enhancement based on the time-resolved reflection matrix. The number of acquisitions required to capture the matrix is reduced 25-fold compared to the algorithm presented by Jang et al. (Sec. 4.4.1). On the other hand, the approach requires a sophisticated optical design, since the reference beam is required to remain static during the acquisition of the reflection matrix, and phase-only modulation of the beam which is incident to the sample. As a consequence, the approach cannot be implemented by modifying existing SD-OCT systems and the utilization of fast micro-electro-mechanical systems for wavefront manipulation is not yet demonstrated. One column of the time-resolved reflection matrix is taken from a single acquisition of the complex-valued SD-OCT signal. The matrix, in principle, is supposed to reflect the complex-valued backscattered field which results from sample illumination with the respective basis modes. The mutual interference component of the complex SD-OCT signal is proportional to the field which is backscattered from the sample, but image artefacts which are additionally detected

with SD-OCT systems are not (Sec. 2.2.1). To date, a detailed theoretical investigation on how the time-resolved reflection matrix relates to the complex-valued SD-OCT signal is not yet reported and the impact of image artefacts on the acquisition of the matrix and on subsequent phase conjugation for OCT signal enhancement is not discussed.

Jang et al. and Choi et al. both demonstrated the amplitude of the OCT signal to be enhanced as an effect of iterative wavefront shaping or optical phase conjugation. Yu et al. demonstrated the iterative algorithm to enhance the penetration depth of OCT systems when imaging scattering media [27]. The group defined the penetration depth to correspond to that optical path length at which the amplitude of the enhanced OCT signal drops below the noise threshold of the imaging system [27]. The group did not investigate whether signal contributions from multiple scattered light are enhanced by wavefront shaping as well, though, and thus it is not clear whether an actual benefit for imaging with turbid media exists. Imaging applications of phase conjugation with the time-resolved reflection matrix are not yet demonstrated at all.

The upcoming Chapters try to resolve some of these open problems.

5 Double interferometer OCT design for independent beam shaping

In this Chapter, a compact spectral domain OCT design is presented which enables independent and single-pass beam shaping at the reference and sample arm using a single spatial light modulator, respectively. The system differs from a conventional SD-OCT layout only in the optical design at the source arm of the interferometer and, thus, can easily be implemented to existing SD-OCT systems to take advantage of pre-designed or commercial components.

This Chapter illustrates the optical design of the OCT system used in this work and discusses calibration and data acquisition methods necessary to capture a signal. A further analytic and numerical discussion of the presented OCT layout compared to conventional SD-OCT designs is provided. Supporting experimental data is given. Parts of the contents presented in this Chapter have already been published [162].

5.1 Experimental design

5.1.1 Optical design

The experimental OCT system used in this work is illustrated in Fig. 5.1. In principle the system is based on a double-interferometer design with a Linnik-type interferometer for SD-OCT signal acquisition (right half of Fig. 5.1) and a Michelson interferometer introduced at the source path (left half of Fig. 5.1). The Linnik-design of the second interferometer allows to align the length and focal position of the reference arm independently. More important, the design matches the dispersion at both interferometer arms since equal optical components are used [163, 164]. Both arms of the Michelson interferometer use non-overlapping parts of a reflective spatial light modulator as end mirror. This allows to utilize a single SLM to independently shape both beams.

A number of previous works demonstrated comparable double-interferometer OCT designs, predominantly for the use with common-path OCT systems [165–171]. The approach allows to manually align the path-length difference between the reference and sample beam, which is not possible with conventional common path devices. The design can be understood by considering the arm lengths at the Michelson interferometer to be $l_{1,2}$ and at the Linnik interferometer to be $l_{R,S}$, respectively (Fig. 5.1). Due to the double-interferometer design four distinct beams are created which potentially produce an interference signal at the detector. The relative temporal delay of the individual beams differs, however, and is determined by the arm lengths of the two interferometers. The beam which is reflected at the bottom-half of the SLM and reflected at the reference

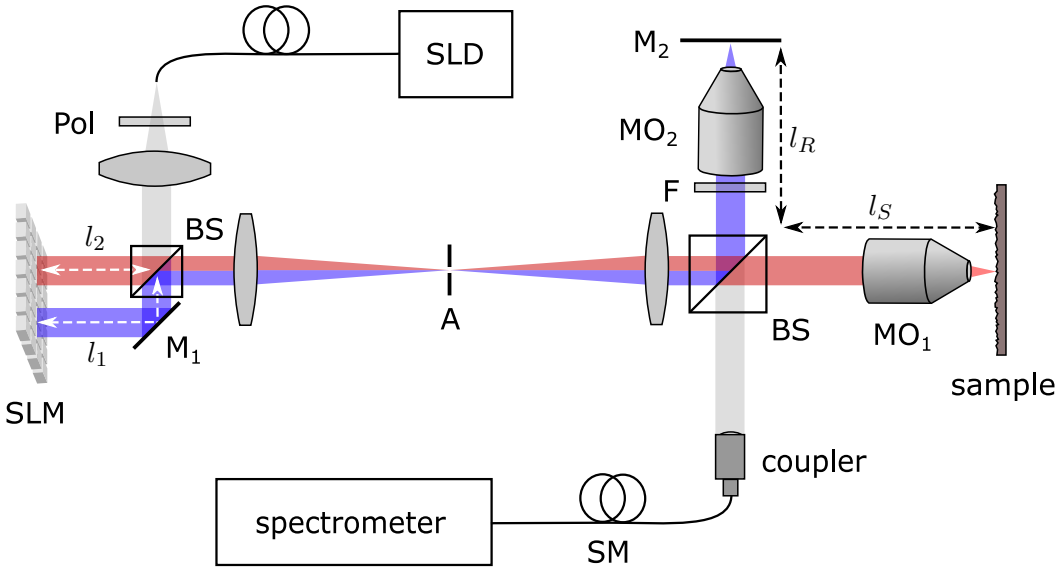

Figure 5.1: **Experimental design.** Abbreviations: *SLD* superluminescent diode, *Pol* linear polarizer, *BS* non-polarizing 50:50 beamsplitter, *SLM* spatial light modulator, *M* mirror, *A* aperture, *F* neutral density filter, *MO* microscope objective, *SM* single-mode optical fibre. Image reproduced from [162][1].

arm of the Linnik interferometer is delayed by $(l_1 + l_R)/c$. The beam reflected at the SLM screen bottom half and reflected at the sample is delayed by $(l_1 + l_S)/c$. Similarly, the beams reflected at the top half of the SLM and reflected at either arm of the Linnik interferometer are delayed by $(l_2 + l_{R,S})/c$, respectively.

By choosing $l_1 > l_2$ and $l_R < l_S$ the lengths of the interferometer arms can be aligned such that $l_1 + l_R = l_2 + l_S$. In this case the beam which is reflected at the bottom half of the SLM and from the Linnik interferometer's reference arm (blue beam in Fig. 5.1) has the same optical path length as the beam which is reflected at the top-half of the SLM screen and from the sample (red beam in Fig. 5.1). The OCT system detects mutual interference from these two beams which are considered to be the effective reference and sample beam, respectively [166–171]. Both beams are modulated at different parts of the spatial light modulator and do not pass the SLM again prior to detection. The approach, hence, enables independent and single-pass beam shaping at both beams.

The other two beams are delayed by $l_1 + l_S$ and by $l_2 + l_R$ (Fig. 5.1). These beams are significantly longer or shorter compared to the effective reference arm length $l_1 + l_R$, respectively, due to the imbalanced arm lengths of the two individual interferometers ($l_1 > l_2$ and $l_R < l_S$). As a consequence, mutual interference with these beams is not detected which, in principle, is an effect of the limited spectral resolution of the OCT system. A more detailed theoretical discussion is given in Sec. 5.4.

[1]This article is licensed under a Creative Commons Attributions 4.0 International License (`http://creativecommons.org/licenses/by/4.0/`).

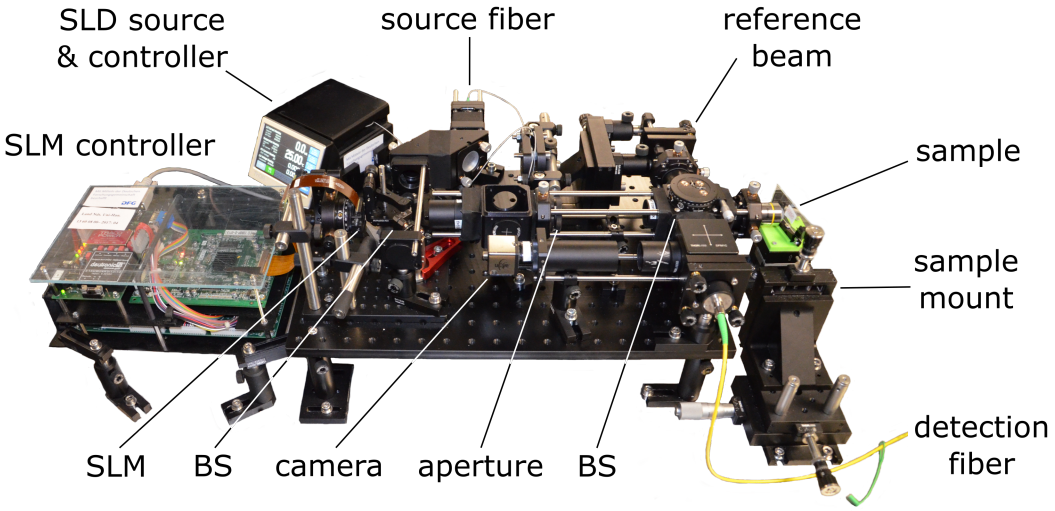

Figure 5.2: **Photograph of the experimental design.** Abbreviations: *SLM* spatial light modulator, *BS* beamsplitter.

5.1.2 Experimental implementation

Figure 5.2 illustrates a photograph of the OCT setup with important elements labelled. The system utilizes a fibre-coupled superluminescence diode with a nominal center wavelength of 830 nm, FWHM bandwidth of 20 nm and maximal output power of 13 mW (*SLD830S-A10*, Thorlabs, USA). The source is operated by a current and temperature stabilized laser diode driver (*CLD1015*, Thorlabs, USA). Light from the source is transmitted through a linear polarizer (*LPVIS050-MP*, Thorlabs, USA) and collimated with a plano-convex lens ($f = 35$ mm). An additional graduated iris aperture placed directly next to the lens allows to define the beam diameter. A 50:50 beam splitting cube (*BS011*, Thorlabs, USA) divides the source beam to illuminate two different halves of the SLM in combination with a mirror. For wavefront manipulation a phase-only liquid crystal on silicon spatial light modulator is used (*NIR11* display and *HEO1080P* controller, Holoeye, Germany). The device has a resolution of 1920×1080 pixel with a nominal pitch of 8 µm, respectively, and provides a phase shift of at least 2π at the spectral range from 420 to 1064 nm. The SLM is imaged to the objective lens MO_1 using a $4f$-design with two plano-convex lenses ($f = 100$ mm). An aperture placed in the Fourier plane allows to block higher diffraction orders of light reflected at the SLM. The Linnik interferometer consists of a 50:50 beam splitting cube (*BS013*, Thorlabs, USA) and two identical infinity-corrected objective lenses with a numerical aperture of 0.25 (*PlanN 10x*, Olympus, Japan). The reference arm optics are mounted to a linear translation stage to align it‘s length. An absorptive neutral density filter (typical ND 1.0) in combination with a zero-aperture iris diaphragm (*SM1D12CZ*, Thorlabs, USA) allow to manipulate the reference beam‘s intensity. Light reflected from the reference and from the sample arm is coupled to a single-mode optical fibre (*P3-780A-FC-5*, Thorlabs, USA). For fibre cou-

pling a five-axis fibre port (*PAF-X-18-A*, Thorlabs, USA) was used for the experiments presented in this and in the next Chapter. To improve the stability in later acquisitions the port was exchanged for an aspheric lens ($f = 15.3$ mm, NA 0.16) placed at a fixed distance from the fibre tip. The alignment necessary for fibre coupling is achieved by mounting both fibre and aspheric lens to a single tip-tilt platform. The SD-OCT signal is detected by coupling the optical fibre to a spectrograph (*SR500i* and *DV420A-OE* camera, Andor, United Kingdom). The spectral resolution of the device determines the axial field of view of the OCT system and is discussed in Sec. 5.3.3.

For simplicity the optical design does not include a scanner at the sample beam. Instead the sample is mounted to a set of three perpendicularly aligned manual translation stages for coarse alignment and to a three-axis piezoelectric stage (*P-611.2s* and *P-622.ZCD*, Physik Intrumente, Germany) for fine alignment and automated sample scanning and imaging.

Furthermore, an additional tube lens and a CMOS camera placed behind a removable mirror allows to use the system as a microscopic setup, e.g. to image the sample and to align it to the OCT system.

5.1.3 Data acquisition

The different algorithms which are discussed in this work are implemented with a set of customized Matlab functions. The individual approaches are explained in the respective Sections. At this point just a brief overview on how the OCT signal is acquired from the detection hardware without details on implementation is presented. This data processing is common to all other algorithms used in the upcoming Chapters.

The spectral raw-data is captured from the spectrograph camera via an USB connection by using the application programming interface provided by the manufacturer. This data comes as a vector of 1024 16-bit integers which reflect the power spectral density detected at the camera. The corresponding wavelength-scale depends on the orientation of the spectrometer grating and is retrieved from a previous calibration, which is loaded from a text file (Sec. 5.3.1). The wavelength scale is converted to the corresponding spectroscopic wavenumber scale $\nu = 1/\lambda$. In a next step the detected power spectral density is linearly interpolated and upsampled to a uniformly spaced wavenumber grid with 2048 pixels. The spectral data is then transformed to a single OCT A-scan by calculating the complex-valued inverse Fourier transform using Matlab's *ifft* algorithm. The resulting data yields the OCT signal for the depth range $z = 0$ to $z = 2z_{max}$, where z_{max} is the maximal depth-range of the OCT signal. Finally the left and right halves of the data are swapped using a *fftshift* algorithm. The complex-valued A-scan for the depth range from $-z_{max}$ to $+z_{max}$ results.

The depth-scale which corresponds to the OCT signal is determined by the spacing of the resampled spectral data. The depth scale is calculated from the equations given in Sec. 2.2.4 and is divided by a factor two to describe the OCT signal in terms of the single-pass optical path length, i.e. the penetration depth in the sample.

The OCT signal received from the inverse fast Fourier transform (IFFT) of the raw spectral data reads $I^{SD}[m]$ and is complex-valued. For most figures presented in this

work a logarithmic scale is used to illustrate the signal amplitude $|I^{SD}[m]|$. The amplitude of the OCT signal actually corresponds to the auto and cross-correlations of the backscattered reference and sample beams, which is the inverse Fourier transform of the detected power spectral density (Sec. 2.2.1). The signal amplitude $|I^{SD}[m]|$, hence, is considered to be a power quantity and, as a consequence, the signal level in decibel (dB) is calculated according to $10\,log_{10}(|I^{SD}[m]|)$ (i.e. 10 dB/decade) for all illustrations which are presented in this work.

5.2 SLM calibration and characterization

5.2.1 Principles

In this work, a liquid crystal on silicon (LCOS) SLM designed for phase only modulation is used. The SLM display consists of a thin parallel aligned nematic (PAN) liquid crystal (LC) layer on top of a CMOS backplane, which reflects light transmitted through the LC and sets the respective voltage which is applied to the individual pixels of the display at the same time [172, 173].

PAN LCOS SLMs enable phase-only wavefront shaping through electrically controlled birefringence [172]. The liquid crystal molecules are aligned parallel to the long axis of the SLM screen [172]. The nematic LC layer, thus, is anisotropic and optically birefringent [174, 175] with the extraordinary optical axis being aligned parallel to the orientation of the crystals [175]. The application of an external voltage tilts the LC molecules parallel to the electric field [174, 175]. In case the field is applied parallel to the axis of incident light, i.e. perpendicular to the plane of the LC display, the extraordinary refractive index of the LC layer changes [174, 175].

The device enables phase-only wavefront modulation in case the polarization of incident light is aligned parallel to the extraordinary optical axis of the LC layer. The quantitative phase delay depends on the wavelength of modulated light and on the applied voltage, which needs to be calibrated to achieve a defined phase shifting behaviour.

5.2.2 Polarizer alignment

To operate the SLM correctly the incident light needs to be linearly polarized with the polarization orientation aligned to the extraordinary optical axis of the device. To this end a linear polarizer mounted to a rotation stage in front of the SLM is included to the optical design (Fig. 5.1).

In general, linearly polarized light becomes elliptically polarized after reflection at the birefringent SLM display [174]. The ellipticity depends on the angle φ_0 between the polarization direction and the orientation of the extraordinary axis, and on the phase delay $\Delta\phi$ at the extraordinary axis. The intensity which is transmitted through a crossed polarizer (analyser) placed behind reads [174, 176]:

$$I(\Delta\phi, \varphi_0) = I_0\, sin^2\,(2\varphi_0)\; sin^2\left(\frac{1}{2}\Delta\phi\right) \tag{5.1}$$

To align the orientation of the polarizer an additional analyser and a CMOS camera to monitor the transmitted intensity are introduced behind the SLM. A set of uniform phase patterns is applied to the SLM to introduce a random phase shift $\Delta\phi$ at the extraordinary optical axis. The integrated camera image is proportional to the intensity transmitted through the crossed polarizer. The intensity is not expected to be a uniformly distributed random variable with this measurement. The variance of the observed intensity is expected to be proportional to $sin^2(2\varphi_0)$, nonetheless (Eq. 5.1). The polarizer can, thus, be aligned parallel to the extraordinary axis of the SLM ($\varphi_0 = 0$) by finding the polarizer orientation at which the variance of the detected intensity becomes minimal. The approach allows to align the polarizer with an accuracy of two degree, which is the minimal angular resolution of the rotation platform to which the polarizer is mounted.

5.2.3 Beam position calibration

For the approaches presented in this work knowledge of the positions at which the two beams are reflected at the SLM with respect to the screen coordinates is required (compare Fig. 5.1). A custom Matlab application is used to create a set of two concentric ring patterns at the SLM. The diffracted beam is imaged with a CMOS camera placed at the position of the objective lens of the OCT system. The position of both beams at the SLM screen is determined by manually cropping the diameter of the source beam and changing the position of the concentric ring patterns at the SLM while observing the diffracted beam. The beam positions are saved to a text file and read upon initialization of the OCT system.

5.2.4 Switching time

LCOS spatial light modulators are known for rather low frame rates which are affected by the thickness of the liquid crystal layer and by the applied voltages [173, 175]. The switching time is experimentally estimated by displaying a random reference phase pattern to the SLM screen and capturing the resulting static speckle pattern at a CMOS camera. Then, other random phase patterns iterating with the reference pattern are applied and the image resulting from illumination with the reference pattern is captured, respectively. The correlation of these images with the image resulting from static illumination is calculated depending on the refresh rate of the SLM. Figure 5.3 illustrates the corresponding data. A correlation close to unity is achieved with update intervals above 150 ms. In this case, the reference image captured with repeated SLM updates matches the static image.

The presented method gives a rather coarse estimation of the refresh rate achievable with the SLM since the timing cannot be controlled exactly, mainly due to the unbuffered signal acquisition via an USB connection. The proof-of-concept experiments presented in this work are not optimized for a high acquisition speed. To ensure well-defined beam shaping a temporal delay of 150 ms is introduced between any refresh of the SLM screen and subsequent data acquisition with the methods presented in this work.

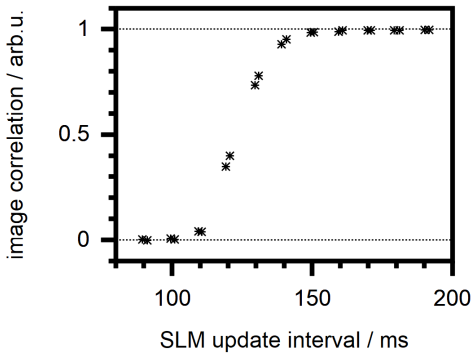

Figure 5.3: **Estimation of SLM switching time.** The graph illustrates the correlation of the diffracted beam detected with dynamic SLM updates with the corresponding image acquired with a static SLM pattern.

5.2.5 Phase shifting characteristics and correction

The SLM used in this work is digitally addressed at a single 8-bit color channel of a high definition media interface (HDMI). The device, thus, can be used similar to a second screen connected to a personal computer, whereas the grayscale values applied to the individual pixels determine the respective phase shift which is applied to the beam. The mapping between the applied grayscale value and the phase delay which is resulting at the near infrared beam used for the OCT system is determined with a customized calibration procedure based on self-referenced two beam interferometry. The approach is modified from the work presented by Fuentes et al. [177].

The SLM is used to create two distinct beams (probe and reference beam) by filling the pattern with a binary grating which blocks the zeroth diffraction order except for the aperture of the two beams (Fig. 5.4(a)). Since the phase modulation characteristics of the SLM is yet to be determined, the gray levels corresponding to the grooves and bars of the binary grating are manually chosen such that a maximum diffraction efficiency is observed. A CMOS camera (*DCC 1545M*, Thorlabs, USA) captures the intensity of the diffracted beam without any further optical elements in between. To this end a removable mirror is inserted to the experimental setup behind the SLM.

Another static Ronchi grating is applied to the reference beam (Fig. 5.4(a)). The grating period is chosen such that the first diffraction order overlaps with the probe beam in the plane of the camera. Due to the tilt between the two beams a linear fringe pattern is observed on top of some residual undiffracted light (Fig. 5.4(b)). In case the uniform grayscale of the SLM pattern corresponding to the probe beam is changed the fringe positions shift according to the applied phase delay.

The phase shifting characteristics of the SLM is determined experimentally by capturing a cross-sectional intensity profile of the linear fringe patterns which are observed with different grayscale values at the probe beam. The corresponding data is drawn to Fig. 5.4(c). A customized Matlab script is implemented to track the fringe positions

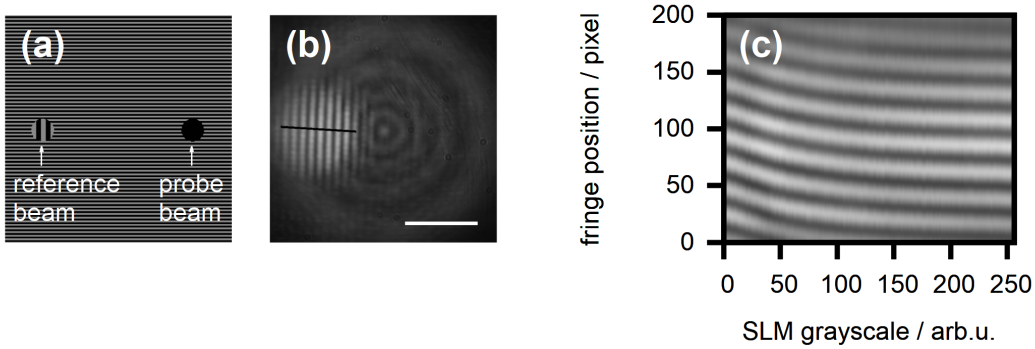

Figure 5.4: **Principle of self-referenced two-beam interferometry for SLM calibration.** (a) Pattern applied to the SLM. The reference beam remains static. The graysale at the aperture corresponding to the sample beam is varied. (b) Intensity pattern captured at the camera after free propagation. Scalebar 1 mm. A cross-sectional intensity profile of the interference fringes is taken. (c) Fringe profiles taken for different grayscale values applied to the probe beam. The fringe displacement reflects the phase shift at the probe beam.

observed with the individual measurements based on intensity thresholding. The relative phase shift at the probe beam is calculated from the relative displacement of the interference fringes, a displacement by one fringe period corresponds to a phase shift of 2π [177]. The implemented algorithm labels and tracks individual fringes and, thus, allows to investigate phase shifts larger than 2π without phase wrapping.

Two beam interferometry requires a spatially coherent light source. This condition is met by the single-mode fibre coupled source used for the OCT system. Furthermore, the coherence length of the source needs to be larger than the path length difference between the two interfering beams. For the data presented, the lateral displacement between the reference and probe beam was chosen to be 2 mm in the plane of the SLM. The camera was placed at a distance of 30 cm which results in a geometrical path length difference of 7 µm, which is well below the coherence length of the source. The method, thus, allows to calibrate the SLM directly with the broadband source used for the OCT system.

The phase shifting characteristics acquired by two beam interferometry is illustrated in Fig. 5.5(a). Obviously the behaviour is non-linear and exceeds the desired range of 2π. In principle, this non-linearity can be compensated digitally by adapting the grayscale image which is applied to the SLM. In practical applications a linear phase shift vs. grayscale characteristics is more convenient, however.

The individual pixels of the SLM screen are digitally addressed by the controller via a pulse code modulation scheme [172]. The alignment of the liquid crystal molecules, i.e. the effective phase shift, is determined by the root mean square voltage at the respective pixels [173]. The mapping between the 8-bit image which is transferred from the personal computer to the SLM and the voltage which is actually applied to the individual pixels

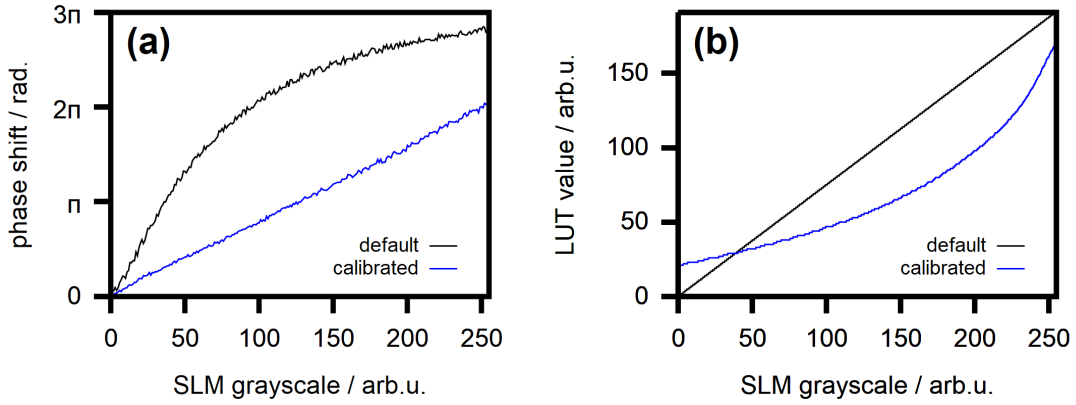

Figure 5.5: **SLM phase modulation characteristics and gamma correction.** (a) Phase modulation characteristics acquired from self-referenced two beam interferometry. (b) Gamma look up tables applied to the SLM controller, respectively.

is set by a gamma look up table (LUT) which is saved to the controller. The phase modulation characteristic presented in Fig. 5.5(a) is taken with a default linear LUT (Fig. 5.5(b)).

A LUT which is resulting in a customized phase shifting behaviour can estimated from the values $\gamma^{lin}[n]$ of the default linear LUT and from the phase shift $\phi^{lin}[n]$ which is measured with that LUT applied [178]. The index n corresponds to the 8-bit brightness of the image applied to the SLM. The values of the custom LUT $\gamma^{custom}[n]$ are found by interpolating $\gamma^{custom}[n]$ (query values) at the positions of the desired phase shifts $\phi^{custom}[n]$ (query points) from the values $\gamma^{lin}[n]$ of the default LUT (sample values) and the measured phases $\phi^{lin}[n]$ (sample points). To mitigate the effect of experimental noise a polynomial fit to the experimentally acquired phase shift $\phi^{lin}[n]$ is taken for the calculation

Figure 5.5 illustrates the LUT calculated for linear 2π phase shifting with the OCT source and the experimentally acquired characteristic once the LUT is saved to the SLM controller. Indeed, the desired linear behaviour is achieved. The custom LUT effectively crops the voltage range which is applied to the SLM. Due to this effect and due to the digital addressing scheme of the SLM display, the LUT contains only 150 independent elements, i.e. independent phase shifts, opposed to 256 independent values of the 8-bit image which is sent from the personal computer to the SLM controller.

5.2.6 Dispersion

The wavelength dependency of the phase delay applied by the spatial light modulator can be estimated by including the device to the OCT setup presented in Fig. 5.1. In case a sample consisting of a single strongly reflecting layer is placed in front of the OCT system a linear fringe pattern is observed in the power spectral density which is

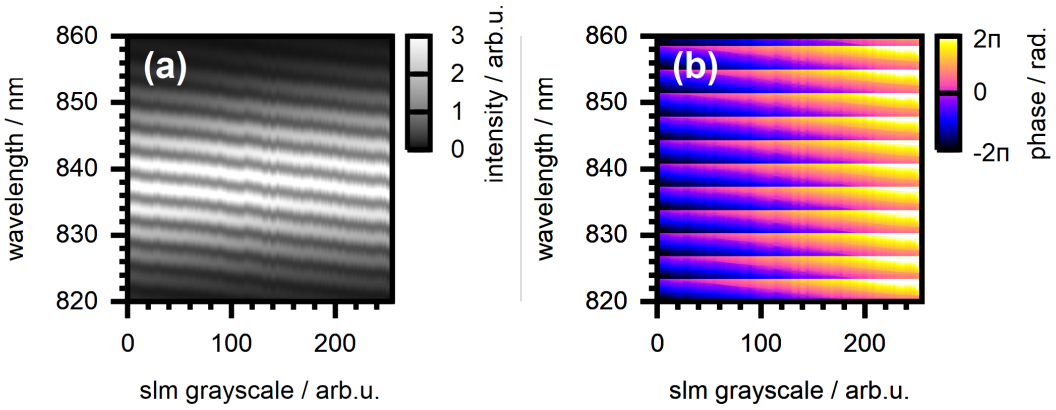

Figure 5.6: **Principle of SLM dispersion measurement.** (a) Spectral raw-data acquired with a single-reflecting sample and with the SLM manipulating the phase at the reference beam. (b) Unwrapped phase shift acquired at each pixel of the raw-spectrum individually. Image adapted from [162].

acquired by the spectrograph. Indeed, the period of this fringe pattern corresponds to the path length differences between the sample and reference beam and the fringe positions correspond to the relative phase differences. This effect is exploited by SD-OCT systems which acquire the sample‘s image from the inverse Fourier transform of the spectral data (Sec. 2.2).

To estimate the dispersion of the SLM the spectral raw data is considered only. When imaging a single-reflecting sample such as a silver mirror the signal, in principle, reads [46, 57]:

$$I(k) = A(k) + B(k)\,cos(k\Delta l + \phi(k) + \phi_0(k)) \tag{5.2}$$

$\Delta l = l_R - l_S$ corresponds to the path-length difference between the reference and sample beam. $A(k)$ and $B(k)$ denote the offset and amplitude of fringes observed in the spectral raw data. $\phi_0(k)$ is a constant phase offset and $\phi(k)$ an additional wavelength-dependent phase shift. The SLM is now used to manipulate the phase at one of the interfering beams with the setup presented in Fig. 5.1 and the spectral raw data $I(k)$ is captured for each gray-value applied to the SLM screen. The spectra are then low-pass filtered to suppress artefacts present in the OCT signal which do not correspond to the reflection at the mirror. The resulting data is illustrated in Fig. 5.6(a).

The intensity fluctuations which are observed at the individual pixels of the spectrograph, i.e. at the individual rows in Fig. 5.6(a), reflect the phase shift $\phi(k)$ which is observed at the corresponding wavelength as a result of modulation by the SLM. The phase shift is recovered by estimating the parameters $A(k)$ and $B(k)$ from the minimal and maximal intensities of the raw data, normalizing the data according to $(I(k) - A(k))/B(k)$ [176] and taking the inverse cosine. The unwrapped wavelength-dependent phase shift is illustrated in Fig. 5.6(b). Since the phase unwrapping algorithm

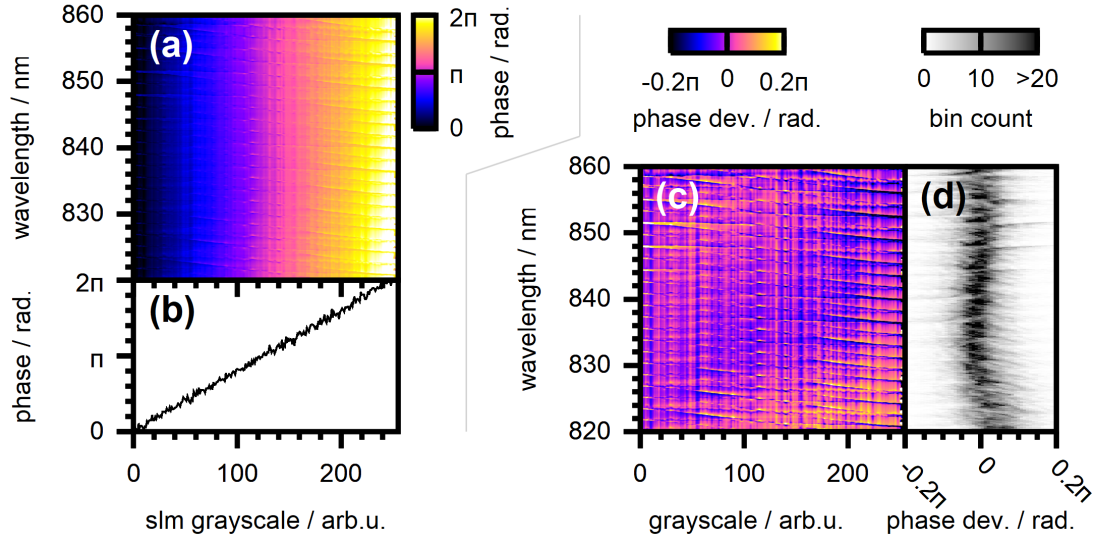

Figure 5.7: **SLM dispersion.** (a) Wavelength-dependent phase shift acquired after subtraction of the reference data. (b) Spectral mean of Panel (a). (c) Wavelength-dependent phase deviation from the spectral mean. (d) Colour-coded histograms of the phase deviation. Each row corresponds to the histogram of the corresponding row in Panel (c). Image adapted from [162].

is unable to distinguish positive from negative phase slopes in practical applications it does not matter whether the SLM is used to manipulate the reference or sample beam. To account for phase instabilities of the experimental design the measurement is alternated with reference phase acquisitions, which is the same measurement with zero voltage applied to the SLM.

The wavelength dependent phase delay resulting from modulation with the SLM after subtraction of the reference data is illustrated in Fig. 5.7(a). This data is taken after previous gamma correction (Sec. 5.2.5) and, hence, the wavelength-averaged phase shift features a linear 2π modulation, as intended (Fig. 5.7(b), compare Fig. 5.5(a)).

Figure 5.7(c) illustrates the deviation between the wavelength-dependent phase shift and a polynomial fit the spectral mean (Fig. 5.7(b)). Strong fluctuations are observed with this signal. The presented approach is sensitive to intensity fluctuations of the raw data close to the observed fringe minima and maxima due to the large slope of the inverse cosine at arguments close to ± 1. As a consequence, discontinuities in the acquired phase shift result at the positions which correspond to these local extrema (and at the extrema of the reference data). These measurement artefacts are evident in Fig. 5.7 Panels (a) and (c). To estimate the wavelength-dependency of the SLM nonetheless, Fig. 5.7(d) illustrates the color-coded histograms for the data acquired at each wavelength, respectively. From this data the wavelength-dependent deviation of the applied phase shift compared to the spectral mean is estimated to be smaller than $\pm 0.1\pi$. This value is considered to be sufficient for the algorithms presented in this work.

5.3 OCT calibration and characterization

5.3.1 Spectral calibration

The software package provided by the spectrograph manufacturer for manual control (*Solis v.4*, Andor, United Kingdom) provides a default spectral calibration and allows to rotate the spectrometer grating such that the desired spectral range is imaged to the camera. With the grating used in this work a spectral range of approximately 40 nm can be imaged at once.

The spectral scale was manually calibrated by imaging the fluorescence emitted from a HeNe Laser (Aerotech, USA) and comparing the position of the observed spectral peaks to their nominal wavelength [179]. The spectrograph software‘s manual calibration tool was then used to recalibrate the device. The final spectral scale was saved to a text-file and is read by the customized OCT software upon initialization.

The central wavelength of the superluminescence diode is observed to shift to larger wavelengths in case the diode is operated at low power. Hence, the spectral calibration was taken for different positions of the spectrometer grating such that the central wavelengths 830, 835 and 840 nm are imaged.

5.3.2 Spatial resolution

Axial resolution

The axial resolution of the SD-OCT system depends on the bandwidth of the light source and on the spectral range which is captured by the spectrograph. The source is specified for a FWHM bandwidth of 20 nm. From the Eqs. 2.13 and 2.14 the nominal axial resolution achieved with the source is found to be 15.2 µm at air.

Due to the digital signal acquisition the OCT signal is discretized with respect to it‘s axial scale. The axial sampling interval d_z is determined by the spectral range covered by the spectrograph (Sec. 2.2.4). With the wavelength calibration used for the central wavelength of 830 nm a value of $d_z = 8.3$ µm is found. With the calibration for a central wavelength of 840 nm, which is used for the low power operation of the light source, a resolution of $d_z = 8.5$ µm results.

The FWHM axial resolution which is expected with the source corresponds to about two pixel of the discretized OCT signal. The experimentally acquired peak width is further increased due to leakage of the discrete Fourier transform. This effect, in principle, occurs whenever the position of the reflecting layer does not exactly align to the discrete axial grid of the OCT signal. In this case the spectral window from which the inverse discrete Fourier transform is calculated is not an exact multiple of the period of the spectral interference fringes and, as a consequence, a broadened peak results in the OCT A-scan [63]. This effect prohibits to test the axial resolution of the OCT system directly by investigating the peak width with a sample such as a plain mirror.

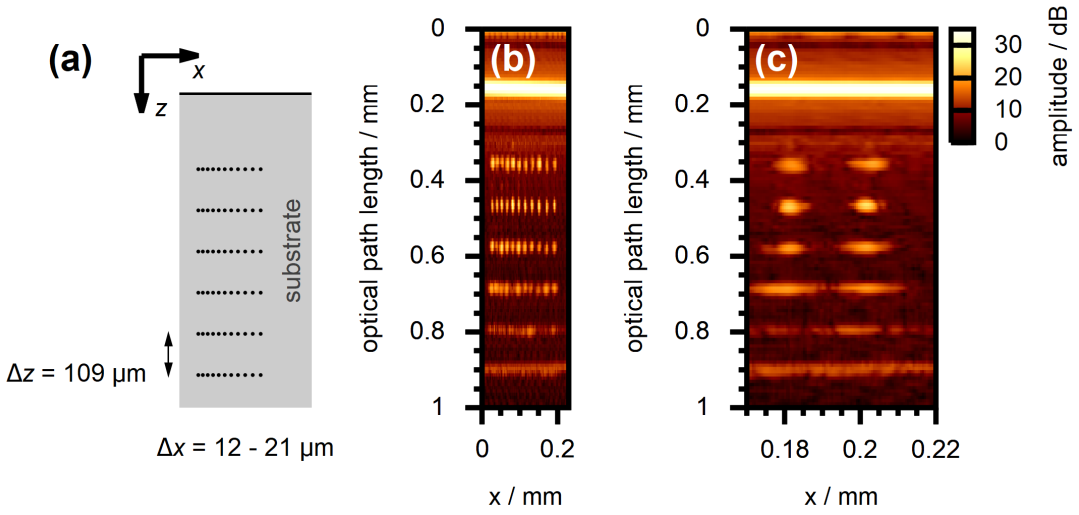

Figure 5.8: **Depth of field of the OCT system.** (a) Structure of the resolution test target. (b) Scan taken at the sample with a four-step phase shifting algorithm. Compare Fig. 2.6(d). (c) The same scan with 10× magnification of the lateral scale.

Lateral resolution and depth of field

The lateral resolution of the OCT system and the depth of field are determined by the NA of the imaging optics, similar to confocal microscopy. For a beam diameter of 4 mm which is used for most experiments presented in this work the objective lens is underfilled and an effective NA of 0.14 results. With this value the FWHM lateral resolution is calculated to be 2.76 µm (Eq. 2.15).

The effect of the imaging optics is evident when taking a closer look to an OCT scan which is acquired with a resolution test target (*APL-OP01*, Arden Photonics, United Kingdom). Such a scan is illustrated in Fig. 5.8. The location of the focal plane of the imaging optics is clearly visible from the scan since the lateral resolution is maximal at the corresponding depth. The lateral FWHM of the signal detected from sample structures at the focal plane is found to be (3.5 ± 0.5) µm with the presented data. The resolution of sample features which are displaced from the focal plane quickly decreases due to the limited DOF of the imaging optics. This effect is accepted in this work since the choice of rather high-NA imaging optics increases the total intensity which is detected by the OCT system, on the other hand.

5.3.3 Spectral resolution and axial sensitivity

The axial field of view of the SD-OCT system is limited by the spectral sampling of the acquired raw data (Sec. 2.2.4). The maximal sampling interval is found to be $d_k = 3,91\ \mathrm{cm}^{-1}$. This value corresponds to a (single-sided) FOV of $z_{max} = 4.0$ mm for

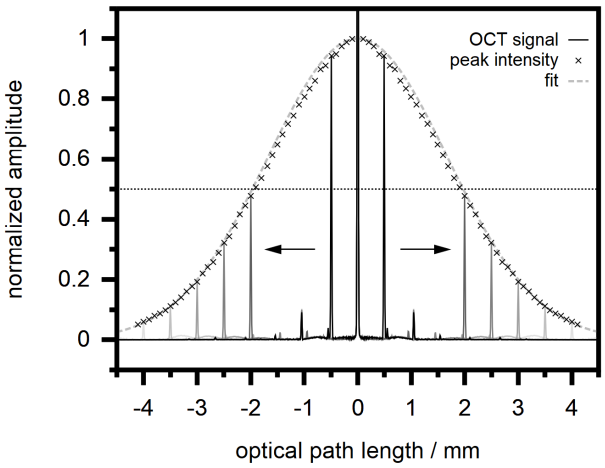

Figure 5.9: **Impact of spectral resolution on the SD-OCT signal.** The solid black line illustrates the signal acquired from a strongly reflecting sample. The arrows indicate the axial shift of the sample's mutual interference and mirror signal when the length of the reference arm is reduced. The points illustrate the respective peak amplitudes as the reference arm length, i.e. the axial position of the detected signal, is scanned. Gray lines showcase individual A-scans for illustratory purposes. The dashed line illustrates the product of a *sinc* function and a Gaussian fit to the experimental data.

the OCT system. The observed image is always wrapped to the range $\pm z_{max}$ (Sec. 2.2.4). The amplitude of wrapped signal components which correspond to reflections outside of the axial FOV is not reduced due to the discretization of the spectral raw data alone, on the other hand (Sec. 2.2.4).

In contrast, the finite optical resolution of the spectrograph reduces the visibility of high-frequency interference fringes. As a consequence, the OCT system is less sensitive to signals detected from large depths or from sample features located outside of the axial FOV (Sec. 2.2.4). The effect is demonstrated in Fig. 5.9 which illustrates the OCT signal taken at a single strongly reflecting surface. Image artefacts are not suppressed. Hence, a strong DC signal is present at $z = 0$ and the signal is symmetric with respect to it's depth scale. The strong signal peak observed at a depth of 0.5 mm corresponds to the reflection at the sample. The axial position at which the signal is detected shifts in case the length of the reference arm is changed. The observed peak amplitude, which is illustrated by the points drawn to Fig. 5.9, drops with increasing displacement. This effect is independent from the effects of the imaging optics finite depth of field, which is discussed in Sec. 5.3.2. From the data presented in Fig. 5.9 the axial range at which the signal amplitude is observed to drop by less then a factor of two is found to be 1.9 mm, which is about half the axial FOV of the system. This corresponds to a sensitivity loss of -3 dB. The sensitivity at the edge of the axial FOV ($z = 4.0$ mm) is observed to drop by -12.2 dB. These values have to be compared to the dynamic range of the OCT

device, on the other hand. With the presented system this value is found to be at least 30 dB and, hence, signal features within the axial FOV can safely be detected.

In Sec. 2.2.4 analytic expressions were given which describe the axial sensitivity loss expected for the OCT system. Fitting these expressions to the experimental data presented in Fig. 5.9 allows to estimate the optical resolution of the spectrograph. To this end a fill factor of 100 % is considered for the camera which is attached to the spectrograph. The spectral range covered (and integrated) by the individual pixels, hence, corresponds to the spectral sampling interval d_k. To estimate the spectrometer‘s optical resolution the data presented in Fig. 5.9 is normalized by the sensitivity loss expected from spectral binning alone, described by a *sinc* function. Subsequently, a Gaussian fit to the resulting data is calculated (Sec. 2.2.4). The FWHM of the fit function reads 4.2 mm, which corresponds to a FWHM optical resolution of $\delta_k^{opt} = 6.58$ cm^{-1} (compare Sec. 2.2.4). This value will be used in the next Section. The product of the *sinc* function and the Gaussian fit, which together yield the expected axial sensitivity loss, is illustrated in Fig. 5.9.

5.4 Analysis of the design

5.4.1 Analytic model

The presented double interferometer OCT design is intended to enable independent beam shaping at the reference and sample beam. So far, only a heuristic explanation of the approach is given, however. This Section provides a more sophisticated analysis. Similar to the discussion given in Sec. 2.1 the OCT system can be described within a one-dimensional model by considering a set of two cascaded interferometers. The model is illustrated in Fig. 5.10.

The double interferometer design is easily understood by first considering the signal which is expected with a conventional SD-OCT device. Such a system is based on a single interferometer which corresponds to the right Panel in Fig. 5.10. The signal I^{SD} which is expected for the conventional SD-OCT design is composed from autocorrelation artefacts Γ_{RR} and Γ_{SS} resulting from the reference and the sample beam, respectively, from mirror artefacts Γ_{SR} and from the mutual interference signal Γ_{RS} which reflects the morphology of the sample (Eq. 2.17). Analytic expressions for the respective terms in case a one-dimensional layered sample is considered are given in Eqs. 2.9 and 2.18. As is evident from these equations the mutual interference and autocorrelation signals are found from the convolution of the coherence function (or autocorrelation) $\Gamma_{src}(\tau)$ of the light source with some term which basically reflects the structure of the sample. The same applies to the mirror signal Γ_{SR}, as is easily verified from the symmetry of the cross-correlation (Eq. 2.5).

The analytic expressions given for the OCT signal (Eqs. 2.9, 2.17 and 2.18) still hold for the double-interferometer design if the term Γ'_{src} is considered to correspond to the autocorrelation of the field E'_{src} which is incident at the second interferometer (Fig. 5.10), instead as to the autocorrelation Γ_{src} of the field E_{src} which is directly emitted from the light source. E'_{src} is found from the convolution of E_{src} with the (one dimensional)

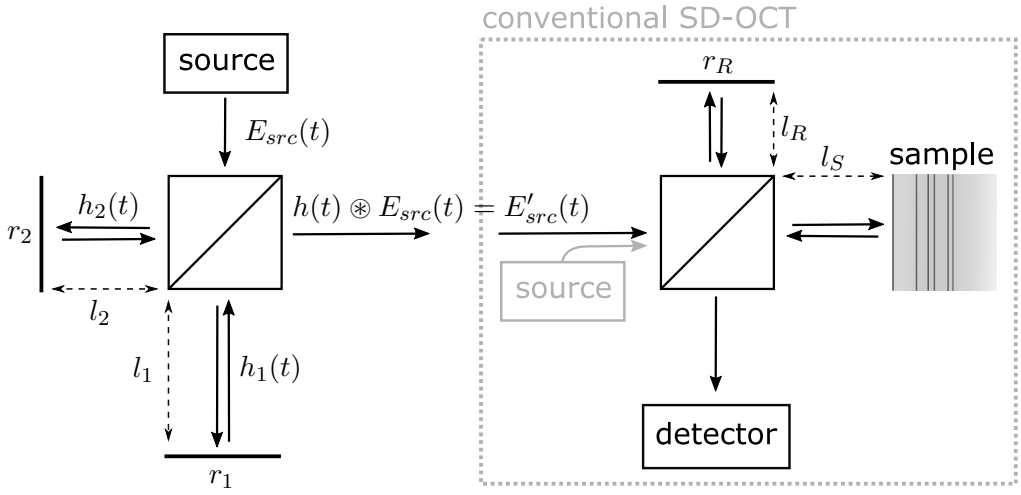

Figure 5.10: **Model of the OCT design.** The OCT system is modelled from two cascaded one dimensional Michelson interferometers. The signal expected with the conventional OCT system is discussed in Chap 2. The effect of the additional interferometer is described by it's impulse response $h(t)$. Variables are explained in the text body. Image adapted from [162].

impulse response of the first interferometer:

$$E'_{src}(t) = h(t) \circledast E_{src}(t) \tag{5.3}$$

Making use of the identity $[f \circledast g] * [f \circledast g] = [f * f] \circledast [g * g]$ [180, 181], where $*$ denotes the cross-correlation according to Eq. 2.4, the autocorrelation of the field incident to the second interferometer reads:

$$\Gamma'_{src}(\tau) = H(\tau) \circledast \Gamma_{src}(\tau) \tag{5.4}$$

$\Gamma_{src}(\tau)$ is the coherence function (or autocorrelation) of the light source. $H(\tau)$ describes the autocorrelation of the impulse response $h(t)$ of the first interferometer. Now, as previously discussed the SD-OCT signal is found from the convolution of Γ'_{src} with some structural terms. For a conventional OCT system ($\Gamma'_{src} = \Gamma_{src}$) this signal reads $I^{SD}(\tau)$. The signal expected with the double interferometer OCT, thus, reads according to Eq. 5.4:

$$I^{SD}_{double}(\tau) = H(\tau) \circledast I^{SD}(\tau) \tag{5.5}$$

The impulse response $h(t)$ of the first interferometer can be written in terms of the impulse responses $h_1(t)$ and $h_2(t)$ of the respective arms, i.e. $h(t) = h_1(t) + h_2(t)$ (Fig. 5.10). The autocorrelation, thus, reads analogue to the previous discussion given for the SD-OCT signal (Eq. 2.4):

$$H(\tau) = H_{11}(\tau) + H_{22}(\tau) + H_{12}(\tau) + H_{21}(\tau) \tag{5.6}$$

The signal which is expected for the double interferometer design yields:

$$\begin{aligned} I^{SD}_{double}(\tau) = &\left[H_{11}(\tau) \circledast I^{SD}(\tau)\right] + \left[H_{22}(\tau) \circledast I^{SD}(\tau)\right] \\ &+ \left[H_{12}(\tau) \circledast I^{SD}(\tau)\right] + \left[H_{21}(\tau) \circledast I^{SD}(\tau)\right] \end{aligned} \tag{5.7}$$

H_{11} and H_{22} correspond to the autocorrelation of the beams which are reflected at either interferometer arm, respectively. H_{12} and H_{21} correspond to the cross-correlation, i.e. mutual interference, of the two beams (Eq. 2.4).

Now, to give a more intuitive understanding, the impulse responses of the two interferometer arms are quickly found in terms of the one dimensional model (Fig. 5.10):

$$h_1(t) = r_1/2\ \delta(t + 2l_1/c) \tag{5.8}$$
$$h_2(t) = r_2/2\ \delta(t + 2l_2/c) \tag{5.9}$$
$$H_{11}(\tau) = |r_1|^2/4\ \delta(\tau) \tag{5.10}$$
$$H_{22}(\tau) = |r_2|^2/4\ \delta(\tau) \tag{5.11}$$
$$H_{12}(\tau) = r_1 r_2^*/4\ \delta(\tau + 2\Delta l/c) \tag{5.12}$$
$$H_{21}(\tau) = r_1^* r_2/4\ \delta(\tau - 2\Delta l/c) \tag{5.13}$$

$l_{1,2}$ and $r_{1,2}$ describe the lengths and amplitude reflectivities of the two interferometer arms, respectively (Fig. 5.10). $\Delta l = l_1 - l_2$ yields the arm length difference. With this result the OCT signal reads in terms of the depth-scale $z = c\tau/2$ (compare [162]):

$$I^{SD}_{double}(z) = (|r_1|^2 + |r_2|^2)/4\ I^{SD}(z) + r_1 r_2^*/4\ I^{SD}(z + \Delta l) + r_1^* r_2/4\ I^{SD}(z - \Delta l) \tag{5.14}$$

To summarize, as an effect of the double interferometer design the SD-OCT signal which is expected for a conventional SD-OCT system is reproduced three-fold. The first term in Eq. 5.14 describes the signal which corresponds to the incoherent superposition of the two beams which are reflected at the first interferometer. As a result the signal is reproduced at it's original depth-axis and scaled by the total reflectivity $(|r_1|^2 + |r_2|^2)/4$. In contrast, the second and third term result from mutual interference of the beams reflected at the first interferometer. The corresponding OCT signal, hence, is axially shifted by Δl, which is the distance matching the arm length difference of the first interferometer. These signal components allow to shape the reference and sample beam independently by manipulation the field only at the first interferometer, on the other hand. The effect is discussed in the next Section.

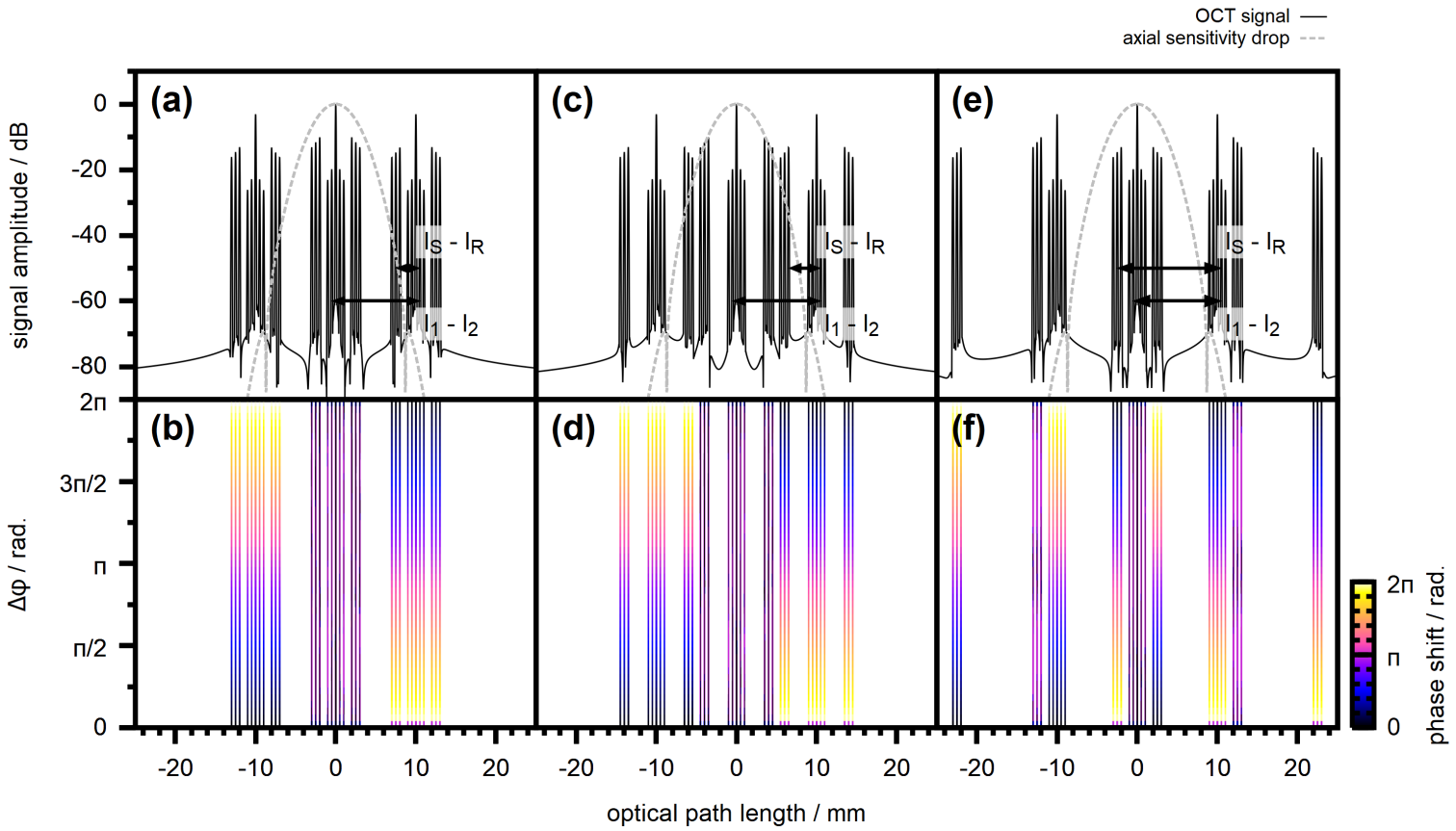

Figure 5.11: **Calculated double interferometer OCT signal.** (a) Signal amplitude for a sample consisting of three reflective layers. The difference $l_S - l_R$ between the lengths of the reference and sample beam is close to zero. (b) Phase at the respective signal peaks in case the phase difference $\Delta\varphi$ at the first interferometer is changed. (c) and (d) Same as (a) and (b), reference arm length reduced by 1.5 mm. (d) and (e) Same as (a) and (b), reference arm length reduced by 10 mm. Image adapted from [162].

5.4.2 Numerical calculation

The expected OCT signal is explicitly calculated. To this end a Matlab script is used to evaluate the spectrum of a broadband light source at a densely spaced frequency grid. The source spectrum is multiplied by the complex-valued transfer function of the double-interferometer OCT design which is analytically found for the one dimensional model analogue to the previous discussion [162]. The OCT signal is then calculated from the IFFT of the resulting power spectral density. The simulation code is available online [182]. The arm length difference is assumed to read $\Delta l = 10$ mm, which is close to the experimental value (9.7 mm). For illustratory purposes a rather low source bandwidth of 5 nm, which yields broad OCT signal peaks, and a layered sample with layer spacing of 0.5 mm is chosen.

The OCT signal which is expected for the double-interferometer design is illustrated in Fig. 5.11(a). The axial sensitivity loss of due to a finite spectral resolution is not taken into account for the calculation of the OCT signal. Close the $z = 0$ the signal which corresponds to the first term in Eq. 5.14 is evident. This signal corresponds to the signal observed with a conventional SD-OCT system. The signal, hence, features a strong DC peak at $z = 0$ and autocorrelation artefacts close to the DC peak. Mutual interference and mirror signals are observed at $z = l_S - l_R = \pm 2$ mm and feature a larger amplitude compared to autocorrelation artefacts. Due to the double interferometer design additional copies of this signal are observed which are shifted by $\pm\Delta l = \pm(l_1 - l_2)$ with respect to the axial scale of the scan (compare Eq. 5.14).

To better identify the impact of the individual signal components the effect of phase shifting at the first interferometer is considered. To this end the calculation of the OCT signal is repeated for $|r_1| = |r_2| = 1$ and for different values of $\Delta\varphi = arg(r_1) - arg(r_2)$, which is the phase difference between the two interferometer arms. The OCT signal which is reproduced close to $z = 0$ is expected to be insensitive to the phase difference $\Delta\varphi$ since the corresponding signal components results from the incoherent superposition if the two beams which are reflected at the first interferometer (first term in Eq. 5.14). In contrast, the signal which is shifted by the distance $-\Delta l$ with respect to the axial scale is expected to be proportional to $exp(i\Delta\varphi)$ (second term in Eq. 5.14) whereas the signal which is shifted by $+\Delta l$ is proportional to $exp(-i\Delta\varphi)$ (third term in Eq. 5.14). Figure 5.11(b) illustrates the phase of the calculated OCT signal at the positions of the respective signal peaks. Indeed this behaviour is found with the numerically calculated signal, as well.

5.4.3 Independent phase manipulation

The axial sensitivity loss which is resulting from the finite spectral resolution of the OCT system is drawn to Fig. 5.11(a). This data corresponds to the fit functions found for the experimentally observed sensitivity drop which is discussed in Sec. 5.3.3. As is evident from Fig. 5.11(a) the additional axially displaced signal components are effectively suppressed due to the finite spectral resolution of the SD-OCT system in case the arm length difference $\Delta l = l_1 - l_2$ at the first interferometer is chosen to be sufficiently large.

Mutual interference signal components Γ_{RS} and mirror artefacts Γ_{SR} depend on the lengths of the reference and sample beam, respectively. The position at which these signal components are detected in the scan, hence, can be shifted by changing the length of the reference arm l_R. To enable beam shaping and phase manipulation with the OCT system the reference arm length is chosen such that the arm length difference at the first interferometer is compensated, i.e. $l_S - l_R \approx l_1 - l_2$, and such that $l_S - l_R$ is sufficiently large compared to the axial field of view of the OCT system. In this case the mutual coherence and mirror signal components which correspond to the first term in Eq. 5.14 and which are detected at $z = \pm(l_S - l_R)$ are moved outside of the axial FOV. Mutual interference signals corresponding to the second term in Eq. 5.14 are detected at $z = (l_S - l_R) - (l_1 - l_2)$ and, hence, are moved close to $z = 0$. The same applies to mirror artefacts which correspond to the third term in Eq. 5.14 and which are detected at $z = -(l_S - l_R) + (l_1 - l_2)$. The effect is illustrated in Fig. 5.11.

In this case the OCT system detects mutual interference signals which are proportional to $exp(i\Delta\varphi)$, where $\Delta\varphi$ is the relative phase difference between the two arms of the first interferometer, and mirror artefacts which are proportional to $exp(-i\Delta\varphi)$. This is exactly the behaviour which is expected if phase shifting is directly enabled at the individual arms of a conventional SD-OCT system as discussed in Sec. 2.2.3.

5.4.4 Experimental phase manipulation

The previous numeric results are validated experimentally. To this end the OCT signal is taken at a sample consisting of a stack of cover glass slides (*CG15CH2*, Thorlabs, USA). The resulting signal amplitude is illustrated in Fig. 5.12(a). At path lengths below $|z| = 1$ mm a number of autocorrelation signals are detected. Beyond this range the observed signal peaks correspond to mutual interference and mirror signals which are detected from the reflections at the individual sample interfaces. Analogue to the numeric calculation presented in Fig. 5.11(f) the SLM is used to apply a uniform phase delay to the lower beam of the first interferometer (Fig. 5.1). According to the previous discussion this is considered to correspond to a positive phase delay $\Delta\varphi$. Figure 5.12 (b) illustrates the phase of the complex-valued OCT signal which is detected at the signal peaks whose amplitude is above a threshold. Similar to the numeric calculations (Fig. 5.11(f)) the phase at mutual interference signal components is found to be proportional to the phase which is applied by the SLM. Figure 5.12(c) illustrates the average phase shift at the four rightmost signal peaks in Fig. 5.12(a). The data aligns well to the previous phase calibration of the SLM (Figs. 5.5 and 5.7).

5.4.5 Independent beam shaping

The effect of (lateral) beam shaping is not described in terms of the one dimensional model. Investigating the expected signal in terms of the impulse responses yields some insight, nonetheless. In principle the OCT signal can be written in terms of Eqs. 2.17 and 5.7. Only signal components located close to $z = 0$ are detected due to the finite spectral resolution. Considering the previous discussion, in case the length of the reference arm

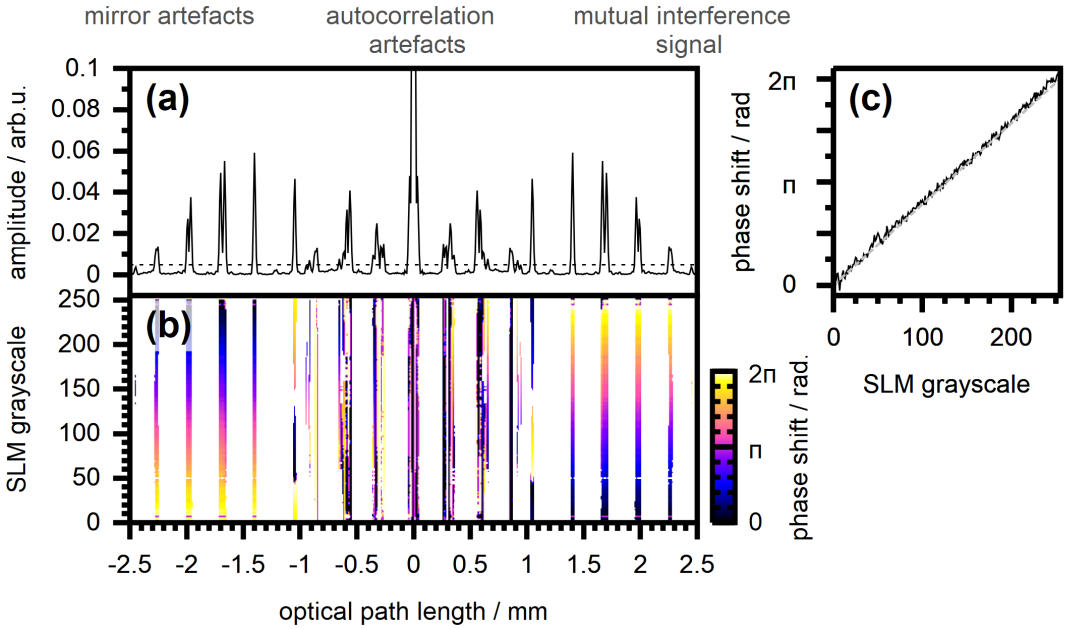

Figure 5.12: **SLM-based phase shifting with the OCT system.** (a) OCT signal amplitude observed with a sample consisting of four reflective layers. (b) Phase of signal components above amplitude threshold (dashed line in Panel (a)) if the SLM is used to manipulate the phase delay at the effective reference beam. (c) Average phase at the four rightmost signal peaks. Image adapted from [162].

is chosen according to $l_S - l_R \approx l_1 - l_2$ the signal reads:

$$\begin{aligned} I^{SD}_{double}(\tau) \approx [H_{11}(\tau) + H_{22}(\tau)] \circledast [\Gamma_{RR}(\tau) + \Gamma_{SS}(\tau)] \\ + H_{12}(\tau) \circledast \Gamma_{RS}(\tau) + H_{21}(\tau) \circledast \Gamma_{SR}(\tau) \end{aligned} \tag{5.15}$$

The first term yields autocorrelation artefacts, the second and third term describe mutual interference and mirror signals. Analogue to the discussion given in Sec. 5.4.1 the fields reflected from the reference and sample beam can be written in terms of the impulse responses h_R and h_S of the respective arms of the second interferometer:

$$\Gamma_{RS} = [h_R \circledast E_{src}] * [h_S \circledast E_{src}] \tag{5.16}$$

The operator $*$ denotes the cross-correlation according to Eq. 2.4. Taking use of the identity $[h_1 * h_2] \circledast [E_R * E_S] = [h_1 \circledast E_R] * [h_2 \circledast E_S]$ (compare Sec. 5.4.1), the second term in Eq. 5.15 reads:

$$H_{12} \circledast \Gamma_{RS} = [h_1 \circledast h_R \circledast E_{src}] * [h_2 \circledast h_S \circledast E_{src}] \tag{5.17}$$

Obviously, this signal corresponds to mutual interference of the beam which is reflected at one arm of the first interferometer and at the reference arm (described by the compound impulse response $(h_1 \circledast h_R)$) with the beam which is reflected at the other arm of the first interferometer and which is reflected at the sample (described by the impulse response $(h_2 \circledast h_S)$). Thus, the two beams can be considered to be the effective reference and sample beam for the double interferometer OCT design.

Similarly, the first term in Eq. 5.15 is found to yield the sum of the autocorrelations of the terms $[h_1 \circledast h_R \circledast E_{src}]$, $[h_2 \circledast h_R \circledast E_{src}]$, $[h_1 \circledast h_S \circledast E_{src}]$ and $[h_2 \circledast h_S \circledast E_{src}]$. The signal, hence, corresponds to the summed autocorrelation of all four beams (reflected at either arm at the first interferometer and at either arm of the second interferometer) which are created by the double interferometer design (compare [168, 169]). Thus, not only the autocorrelation of the effective sample and reference beam alone are observed, but additional autocorrelation artefacts, as well.

Considering the symmetry of the cross-correlation (Eq. 2.5) and the properties of the convolution with respect to time reversal and complex conjugation the third term in Eq. 5.15 is verified to yield the mirror image of the effective mutual interference signal:

$$[H_{21} \circledast \Gamma_{SR}](\tau) = [H_{12} \circledast \Gamma_{RS}]^*(-\tau) \tag{5.18}$$

The effect of beam shaping can be considered by taking the spatial dependence of the respective impulse responses into account in case optical propagation is assumed to be translation invariant or otherwise by describing the linear optical propagation in terms of Green's functions. A detailed analysis is beyond the scope of this work. The one-dimensional model demonstrates that the mutual interference OCT signal and the mirror image result from the cross-correlation of the effective reference and sample beam, which correspond to reflections at either arm of the first interferometer. A spatial light modulator is used as end mirror at both interferometer arms, and, thus, allows to manipulate the phase or the shape of these beams independently (Fig. 5.1). The capability for phase manipulation is demonstrated experimentally in Sec. 5.4.4 and is utilized in this work to implement phase shifting algorithms to suppress SD-OCT image artefacts. The beam shaping capabilities are demonstrated in the upcoming Chapters.

6 Iterative wavefront shaping

Iterative wavefront shaping manipulates the spatial profile of the beam which is incident to a turbid sample such that a focal spot is created from scattered light. Further details are discussed in Sec. 3.3. Due to the iterative optimization approach the technique requires no detailed knowledge about the imaging properties of the optical system. The technique, hence, is experimentally robust and is well-suited to investigate principal effects of beam shaping applied to OCT imaging with strongly scattering samples. On the other hand, the approach is rather slow and, thus, not suited for full image enhancement. A quantitative analysis of wavefront shaping with OCT systems, hence, is deferred to implementations with improved algorithms which are discussed in Chapter 7 and 8. Parts of the contents presented in this Chapter have already been published [162, 183].

6.1 Algorithm and implementation

Iterative wavefront shaping based on optical coherence tomography is implemented with a genetic algorithm which was presented by Conkey et al. in 2012 [131]. In principle, the algorithm applies a set of random phase patterns to the SLM, determines the OCT signal resulting from illumination with the respective wavefronts and then optimizes the phase patterns such that the signal is maximized. The genetic algorithm allows to test the effect of phase patterns which span the full diameter of the illuminating beam at once. Furthermore, the algorithm was shown to yield a faster signal enhancement at a low number of iterations compared to other iterative algorithms and to perform better in the presence of experimental noise [131]. Further details are discussed in Sec. 3.3.3.

The algorithm groups the pixels of the SLM to a set of N segments (or macropixels) with uniform phase each (compare Sec. 3.3.3). Only those segments which are located within the circular area at which the two beams are reflected at the SLM (compare Sec. 5.2.3) are manipulated. With the experimental design presented in Chap. 5 the optimization algorithm, thus, can be used for beam shaping either at the reference or at the sample beam. For each phase pattern which is applied to the SLM the resulting OCT A-scan is acquired. A scalar feedback value is calculated by evaluating the average amplitude of the signal detected at a previously set target depth. A finite target size is chosen to account for small sample displacements during the acquisition. The iterative wavefront shaping algorithm optimizes the pattern which is applied to the SLM such that the feedback value, i.e. the OCT signal at the target depth, is maximized.

The algorithm can be combined with phase shifting approaches (Sec. 2.2.3) to enhance the SNR and to suppress OCT image artefacts during the acquisition. This is implemented by either using the SLM to manipulate the phase at the other beam which is not shaped by the optimization algorithm or by superimposing the respective phase

shifts to the phase patterns applied to the shaped beam. The feedback value for the optimization algorithm is taken from the amplitude of the OCT signal retrieved from the phase shifting algorithm.

The optimization algorithm can be used with a scalar feedback which is obtained from any other sensor, as well. To verify the functionality, the algorithm was tested in a conventional wavefront shaping setup, where a camera is used to monitor the speckle pattern resulting from light transmitted through a scattering sample. The feedback value is calculated from the intensity detected at one spot at the camera. Wavefront optimization with this setup enhances the intensity observed at the target and creates a focal spot on top of a speckle background (compare Sec. 3.3) [23, 131].

6.2 Local signal enhancement

To verify the approach and to demonstrate the capability of the OCT design presented in Chap. 5 to manipulate the reference and the sample beam independently, the effect of wavefront shaping at both beams is demonstrated experimentally. To this end, optical aberrations are introduced to the reference beam on purpose by displacing the reference mirror M_2 from the focal plane of the reference arm objective lens MO_2 (Fig. 5.1). The OCT signal is taken at a sample consisting of multiple layers of scattering polymer film (*Parafilm M*, Pechiney Plastic Packaging, USA). The sample's extinction coefficient was estimated to be (6.9 ± 1.2) mm^{-1} from Beer's law.

6.2.1 Axial localization

Figure 6.1(a) illustrates the A-scan which is acquired in case a uniform phase pattern is applied to the SLM. The signal is taken with a four-step phase shifting algorithm (Eq. 2.21) to enhance the SNR. Signal peaks which correspond to reflections at the cover glass slide placed on top of the sample ($z = 0.15$ mm) and to reflections at the interfaces between the individual polymer layers are clearly visible. The optical thickness of the respective sample layers is found to be approximately 0.2 mm.

The iterative wavefront shaping algorithm is used to enhance the OCT signal which corresponds to the reflection at the interface between the fifth and sixth polymer layer. The feedback for the optimization algorithm is calculated from the amplitude of the OCT signal, integrated at the axial range illustrated in Fig. 6.1(a). Figure 6.1(b) displays the feedback value which corresponds to the respective best (top-ranked) phase pattern throughout the optimization process while optimizing the wavefront at the sample beam. The feedback signal is incremented step-wise each time the algorithm finds a new optimal wavefront. With increasing number of iterations the initial slope tapers off. Both observations are expected for the genetic algorithm [131].

Figure 6.1, Panels (d) and (e) illustrate the final phase patterns which are found in case the optimization algorithm is used to shape the wavefront applied to the reference and sample beam, respectively. The pattern applied to the reference beam resembles the wavefront which corresponds to spherical aberrations. In contrast, the phase pattern applied to the sample beam is highly heterogeneous and random-like. This is expected

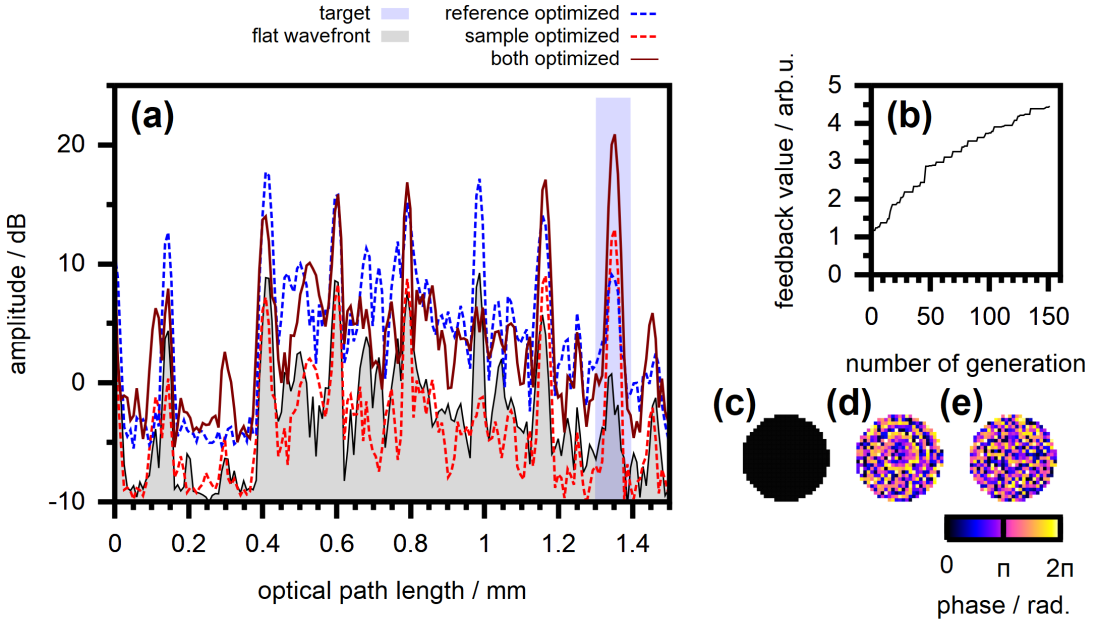

Figure 6.1: **Iterative wavefront shaping with a layered sample and misaligned reference beam.** (a) OCT signal acquired with flat wavefronts applied to both beams, with wavefront shaping at the reference and sample beam, respectively, and with both optimized phase patterns applied simultaneously. (b) Feedback value corresponding to the best-ranked phase pattern during wavefront shaping at the sample beam. (c) Phase pattern corresponding to a flat wavefront. (d) Optimized phase patterns at the reference and (e) at the sample beam.

for wavefront shaping with a strongly scattering sample. The optimized wavefront does not actually compensate optical aberrations but rather shifts the phase of the individual wavefront segments such that constructive interference is created from scattered light (Sec. 3.3).

Figure 6.1(a) presents the OCT signals which are acquired once the optimized phase patterns are applied to the respective beams. In case the shaped wavefront is applied to the reference beam the total amplitude of the detected OCT signal is observed to be increased. The signal enhancement reads 8.4 dB (7.0-fold linear enhancement) at the target. With the presented experimental data the misalignment of the reference arm causes the power which is detected from the reference beam to be actually lower than the power which is detected from the sample. The shaped reference beam couples more light to the point detector and, hence, increases the amplitude of the observed OCT signal.

In contrast, in case the beam incident to the sample is shaped a local signal enhancement only at the target depth results which reads 10.0 dB (10.0-fold linear enhancement) (Fig. 6.1(a)). This behaviour is expected for wavefront shaping with a scattering sam-

ple. In principle, the optimization algorithm creates constructive interference from signal contributions which are detected at a finite time-of-flight window, i. e. at the target, only. At other depths, no such effect results (compare Sec. 4.3).

Finally, Fig. 6.1(a) also displays the signal which is acquired in case both optimized phase patterns are applied to the respective beams at the same time. The effects of both wavefronts add up and a local signal enhancement at the target due to shaping of the sample beam as well as a general signal enhancement due to the increased coupling of the reference beam to the detector is observed. The resulting signal increase at the target reads 18.0 dB (63.0-fold linear enhancement).

6.2.2 Lateral localization

In this Section the effect of lateral sample displacement is investigated. To this end, a piezoelectric stage is used to mechanically move the sample in front of the OCT system after wavefront shaping. Similar to the A-scans presented in Fig. 6.1(a) a volume scan is captured after applying the optimized phase patterns to the SLM. The phase patterns remain static throughout the respective acquisition.

Figure 6.2(a1) illustrates a cross-sectional B-scan (image plane perpendicular to the sample surface) retrieved from the volume scan in case a flat phase pattern is applied to the SLM. Panel (a2) presents a close-up to the position which corresponds to the target for the wavefront shaping algorithm. Panel (a3) illustrates an En-Face scan (image plane parallel to the sample surface) in the plane of the target depth. Figure 6.2 Panels (b1) to (b3) illustrate the same data in case the wavefront is optimized at the reference beam. Obviously, the total image brightness, i.e. signal amplitude, is enhanced. The shape of the observed signal remains the same, on the other hand. This is evident by comparing Panels (a3) and (b3). The image correlation between the two panels reads 0.87, i.e. both scans present nearly the same speckle pattern. This finding is not surprising. Speckle observed by the OCT system result from constructive or destructive interference of light which is backscattered to the detector as the sample is scanned [46, 184]. The observed speckle pattern, hence, is not expected to change in case a different static wavefront is applied to the reference beam

Figure 6.2 Panels (c1) to (c3) illustrates the signal which is taken after application of the shaped wavefront to the sample beam. Obviously, only close to the target position for which the wavefront is optimized (centred in Panels (c2) and (c3)) a visible enhancement of the signal amplitude is evident. In case of large sample displacements only speckle are observed (Fig. 6.2(c3)), similar to the acquisition with a flat wavefront. The speckle patterns observed in both cases are found to be uncorrelated, on the other hand. The image correlation between Panels (a3) and (c3) reads -0.02. This behaviour is expected since illuminating the sample with differently shaped beams affects the shape of the backscattered field as well and, hence, produces different speckle patterns. Figure 6.2 Panels (d1) to (d3) presents the scans which are taken in case the respective optimized wavefronts are applied to both beams at the same time. Once again, the effects of wavefront optimization at the reference and at the sample beam cumulate. The image correlation between Panels (c3) and (d3) reads 0.96.

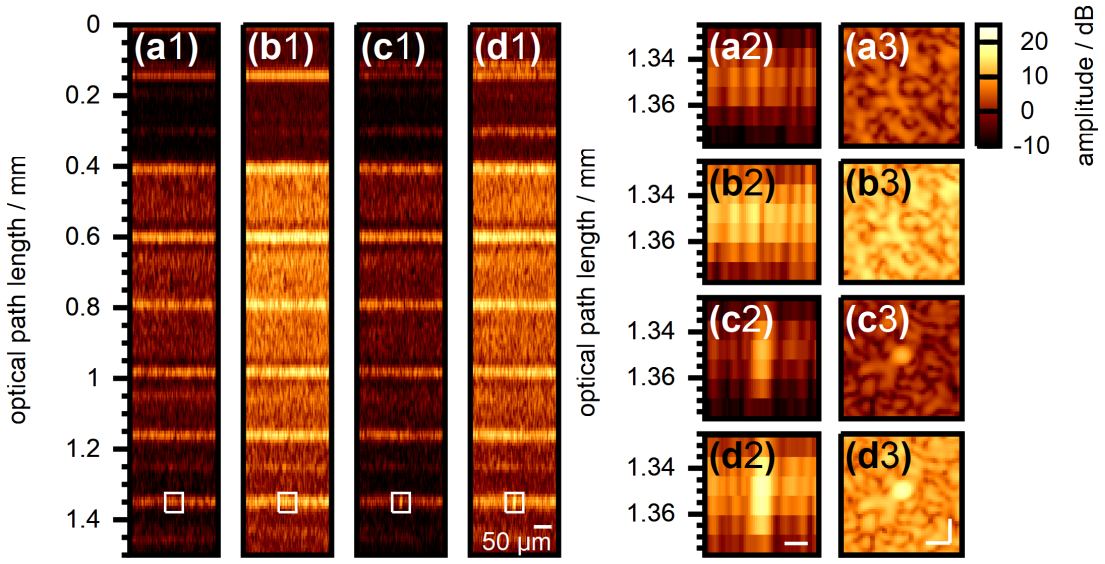

Figure 6.2: **Impact of sample displacement on signal enhancement through wavefront shaping.** (a1) B-scan taken with flat wavefront applied to both beams. (a2) Close-up to the target position for wavefront shaping. (a3) En-Face scan in the plane of the target depth. (b1 to b3) Same as (a1 to a3), wavefront optimized at reference beam. (c1 to c3) Wavefront optimized at sample beam. (d1 to d3) Wavefront optimized at both beams. Scalebar 10 µm. Image adapted from [162].

The effect of wavefront shaping on the OCT signal is observed to be limited to a narrow lateral range. Vellekoop et al. demonstrated iterative wavefront shaping with a monochromatic source and in transmission geometry to produce a focal spot whose intensity profile matches the autocorrelation of the observed speckle pattern [115]. The size of the focal spot, hence, is comparable to the observed speckle size. Choi et al. demonstrated selective enhancement of the OCT signal similar to iterative wavefront shaping, which is discussed in this Chapter [30]. The approach was shown to create a laterally confined focal spot from light which is backscattered from the sample, analogue to the experiments in transmission geometry [30]. Due to the confocal detection geometry of the SD-OCT system presented in this work, the point at which the sample is illuminated and the point from which the signal is detected are scanned simultaneously, though. As a consequence, a focal spot which is created from backscattered light due to wavefront shaping is not directly observed at the point detector.

The OCT system captures the field which is backscattered from the sample and which is integrated at the detector. As the sample is scanned, speckle are observed due to constructive or destructive interference of the detected field [46, 184]. The field which is backscattered to the detector does not decorrelate immediately in case the sample beam or the sample is moved, on the other hand. With anisotropically scattering media, for example, laterally scanning the incident beam over a limited range causes the scattered

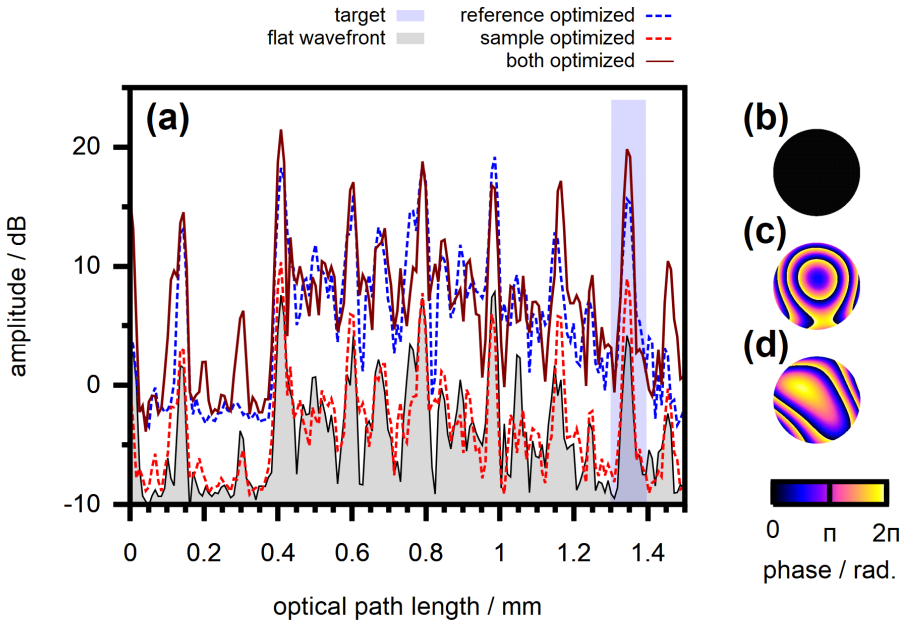

Figure 6.3: **Effect of sensorless adaptive optics correction on the OCT signal.** Same as Fig. 6.1 with optimized wavefronts calculated by the adaptive optics algorithm. Image adapted from [162].

beam to shift accordingly without fully decorrelating [104]. As a consequence, a finite speckle size is observed. Correlations of the scattered field apply in case a shaped beam is incident to the sample, as well [104] (compare Sec. 3.2.1). The lateral range at which the OCT signal is enhanced as an effect of wavefront shaping, hence, corresponds to speckle size which is observed during scanning (compare Fig. 6.2).

6.3 Comparison to adaptive optics

For comparison an algorithm for sensorless adaptive optical correction is implemented which is based on the work presented by Jian et al. [185]. The algorithm calculates a scalar feedback from the amplitude of the OCT signal similar to the approach used for iterative wavefront shaping. In contrast, the corrective phase pattern which is applied to the individual beams is assumed to be a linear superposition of Zernike modes. The algorithm tries to find the coefficients for the respective modes such that the received feedback value is maximized.

The individual coefficients are optimized one at a time. For each mode a discrete and uniformly sampled set of coefficients is chosen and the feedback value, i.e. the intensity of the OCT signal at the target, is measured. Subsequently, a set of more closely sampled coefficients centred at the previous optimal value is tested to determine the coefficient with improved accuracy. The process is repeated for all modes individually, but modes under test are superimposed with the pre-optimized phase pattern. The algorithm, thus,

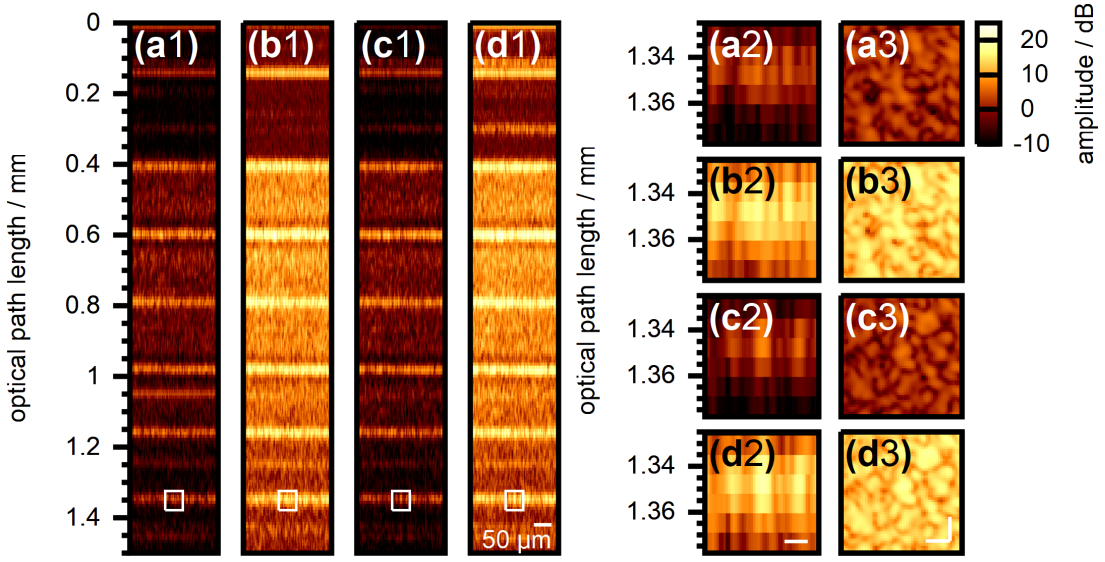

Figure 6.4: **Impact of sample displacement on the OCT signal with adaptive optics correction.** Same as Fig. 6.2 with optimized wavefronts calculated by the adaptive optics algorithm (compare Fig. 6.3). Image adapted from [162].

is sensitive to the chosen sequence of Zernike modes. For the data presented in this work the algorithms starts with the correction of defocus, astigmatism, tip and tilt before optimizing the residual modes up to the fourth radial order (14 modes in total).

The effect on the resulting OCT scan is illustrated in Fig. 6.3. The signal is taken with the same sample which was considered in the previous Section and, hence, can directly be compared to the effect of iterative wavefront shaping. The total amplitude of the OCT scan is observed to be enhanced in case of adaptive optics correction at the reference beam, similar to the data presented in Fig. 6.1(a). The signal enhancement at the target depth reads 11.7 dB (14.6-fold linear enhancement). The optimized wavefront (Fig. 6.3(c)) is dominated by defocus and resembles the phase pattern found by the iterative algorithm (Fig. 6.1(d)). In contrast, only a minor signal enhancement of 3.8 dB (2.4-fold linear enhancement) results in case the adaptive optimization algorithm is applied to the sample beam. The algorithm finds a rather smooth wavefront (Fig. 6.3(d)) which is, in contrast to the random-like phase pattern found by the iterative algorithm (Fig. 6.1(e)), not able to account for scattering at the sample.

Figure 6.4 presents the signal received in case the sample is scanned with the respective optimized phase patterns applied, analogue to the data shown for the iterative algorithm (Fig. 6.2). The effect of wavefront optimization at the reference beam is comparable for both approaches. In contrast, in case the sample beam is manipulated a local signal enhancement is observed only with the iterative optimization algorithm (Fig. 6.2) but not with the adaptive optics algorithm. The iterative wavefront shaping algorithm finds a phase pattern which creates constructive interference from scattered light and is, hence,

sensitive to minor sample displacements (Fig. 6.2). No such effect is observed with adaptive optics wavefront correction, which corrects for low-order aberrations only.

6.4 Imaging applications

Iterative wavefront shaping can be applied to directly enhance the amplitude of the detected OCT signal. Due to the axially and laterally localized effect the signal needs to be optimized for each point of the scan anew, on the other hand. The approach is demonstrated in Fig. 6.5. Panel (a) illustrates a set of color-coded A-scans. Each row corresponds to a single scan which has been optimized for point-wise signal enhancement at different target depths, respectively. The diagonal elements in the figure reflect the in-target amplitude of the optimized OCT signals. The wavefront shaping algorithm is observed to yield a visible signal enhancement at the respective target position. Next to the target depth, i.e. at positions where the signal is not optimized on purpose, no similar effect is visible. This observation aligns well with previous works [26]. A fully-optimized A-scan is constructed by stitching the diagonal elements [26]. The resulting signal is illustrated in Fig 6.5 Panels (b) and (c). Panel (d) presents the relative enhancement of the optimized scan compared to the signal acquired with a flat wavefront.

As is evident from Fig. 6.5 Panels (b) to (d), iterative wavefront shaping indeed can significantly enhance the amplitude of the OCT scan. The approach was demonstrated in previous works with similar algorithms, as well [26–29]. The iterative optimization algorithm presented in this work is much too slow for any practical imaging applications, on the other hand. For the data illustrated in Fig. 6.5 the acquisition of a single point-optimized scan took 40 min. The process is repeated for each pixel in the axial FOV of the A-scan anew to optimize the signal at each target depth individually. In total, the acquisition of the fully-optimized signal, which is taken from 137 point optimized scans for the data presented in Fig. 6.5, took approximately four days. In the next Chapters algorithms are presented which significantly speed up the process and which enable a comparable acquisition in just a few minutes. A quantitative discussion of the effect of wavefront shaping on OCT imaging, hence, is deferred to these approaches.

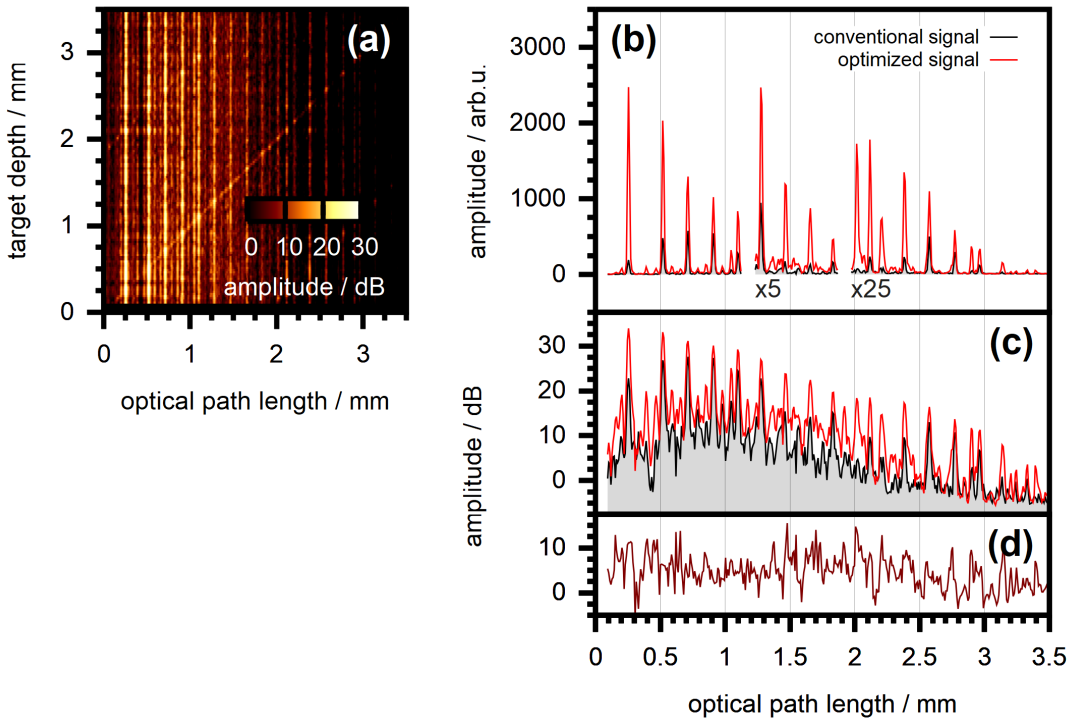

Figure 6.5: **Full A-scan optimization with iterative wavefront shaping.** (a) A-scans taken with point-wise signal enhancement at different target depths. (b) and (c) A-scan stitched from the in-target amplitude of the point-optimized scans, respectively. The data corresponds to the diagonal elements in Panel (a). (d) Relative signal enhancement compared to the scan acquired with a flat wavefront. Image adapted from [183].

7 Reflection matrix approach

In this Chapter an enhanced algorithm for wavefront shaping based on the time-resolved reflection matrix is presented. The matrix describes the linear dependence between the time-of-flight or depth-resolved backscattered field, which is the received SD-OCT signal, and the field which is incident to the sample (Sec. 4.4). Once the matrix is determined, a wavefront which yields a selective enhancement of the OCT signal can directly be calculated similar to the approaches discussed in Sec. 3.4.2. In contrast to the iterative algorithm presented in the previous Chapter, the reflection matrix tests the optical response of the sample, i.e. the backscattered field, in a controlled rather than in a random way. The algorithm also takes additional information into account, such as the linearity of the OCT signal, the signal phase and the phase shifting characteristics of the SLM. Furthermore, the full field of view of the OCT system is considered rather than just the signal received from a confined target position. As a consequence, the approach yields a significant increase in acquisition speed compared to the iterative algorithm.

The acquisition of the time-resolved reflection matrix was initially presented by Choi et al. in 2013 [30] (Sec. 4.4). The group demonstrated wavefront optimization based on the matrix to selective enhance of the SD-OCT signal received from a scattering sample and presented the approach to enhance the intensity of light which is delivered to a given target depth, similar to non-invasive focusing. The group did not discuss the impact of signal artefacts which are detected with SD-OCT systems, on the other hand, and imaging applications are not yet demonstrated. This Chapter extends on the previous work and tries to resolve these problems. Parts of the presented contents have already been published [186].

7.1 Matrix formalism applied to spectral domain OCT

7.1.1 Definition of the time-resolved reflection matrix

A detailed formalism on how the time-resolved reflection matrix relates to the signal which is acquired with a SD-OCT system is not yet reported in literature. In Sec. 2.2 it was demonstrated that the SD-OCT signal can be written in terms of the autocorrelations (Γ_{RR} and Γ_{SS}) and cross-correlations (Γ_{RS} and Γ_{SR}) of the reference field E_R and the field E_S which is backscattered from the sample to the detector. The reflection matrix describes the relation between the detected OCT signal and the field which is incident to the sample. Hence, single-pass wavefront shaping at sample beam is considered, i.e. the beam which is incident to the sample is manipulated once and does not pass the spatial light modulator again after reflection at the sample and acquisition at the detector.

The field in the plane of the spatial light modulator is assumed to read E_{in}. This field is constructed from a linear superposition of basis modes whose electric field reads $e_n^{in}(\mathbf{r}', t)$, respectively, where $\mathbf{r}'$ is a two-dimensional vector which describes the lateral coordinate in the plane of the SLM:

$$E_{in}(\mathbf{r}', t) = \sum_{n=1}^{N} A_n \, e_n^{in}(\mathbf{r}', t) \tag{7.1}$$

Optical propagation through the imaging system and scattering at the sample is considered to be a linear process [119]. The field which is backscattered to the detector, thus, can be written:

$$E_S(\mathbf{r}, t) = \sum_{n=1}^{N} A_n \, e_n^{S}(\mathbf{r}, t) \tag{7.2}$$

The term $e_n^S(\mathbf{r}, t)$ corresponds to the field which is scattered form the respective source modes $e_n^{in}(\mathbf{r}', t)$ to the detector. The explicit form is found in terms of the Green's function g which describes the linear propagation between the plane of the SLM and the plane of the detector [119, 187]:

$$e_n^S(\mathbf{r}, t) = \iint_{A_{src}} \int_{-\infty}^{\infty} e_n^{in}(\mathbf{r}', t') \, g(\mathbf{r}, \mathbf{r}', t - t') \, d\mathbf{r}' dt' \tag{7.3}$$

The integration is performed over the area A_{src} which is covered by the beam in the initial plane. The Green's function implicitly contains the temporal delay of the beam upon reflection at the sample and, hence, determines the shape of the detected OCT signal. Since the system is considered to be time invariant, the function depends on the relative temporal delay $(t - t')$ only. The function further describes the lateral propagation of the beam between the two planes. With a scattering sample, the lateral propagation is not assumed to be translation invariant and, hence, cannot be described by convolving the incident field with a constant PSF. Detailed knowledge of Green's function is not required for the following discussion, on the other hand.

The individual components of the detected SD-OCT signal are found from Eq. 7.2 and from the definition of the cross-correlation (Eq. 2.4). The reference field is considered to be static.

$$\Gamma_{RR}(\tau) = \iint_{A_{det}} \left\langle E_R(\mathbf{r}, t+\tau)\, \overline{E_R}(\mathbf{r}, t) \right\rangle \, d\mathbf{r} \tag{7.4}$$

$$\Gamma_{SS}(\tau) = \sum_{n=1}^{N} \sum_{n'=1}^{N} A_n \overline{A_{n'}}\, \Gamma_{nn'}(\tau) \tag{7.5}$$

$$\Gamma_{RS}(\tau) = \sum_{n=1}^{N} \overline{A_n}\, \Gamma_{Rn}(\tau) \tag{7.6}$$

$$\Gamma_{SR}(\tau) = \sum_{n=1}^{N} A_n\, \overline{\Gamma_{Rn}}(-\tau) \tag{7.7}$$

$$\Gamma_{nn'}(\tau) = \iint_{A_{det}} \left\langle e_n^S(\mathbf{r}, t+\tau)\, \overline{e_{n'}^S}(\mathbf{r}, t) \right\rangle \, d\mathbf{r} \tag{7.8}$$

$$\Gamma_{Rn}(\tau) = \iint_{A_{det}} \left\langle E_R(\mathbf{r}, t+\tau)\, \overline{e_n^S}(\mathbf{r}, t) \right\rangle \, d\mathbf{r} \tag{7.9}$$

The detected SD-OCT signal corresponds to the sum of Eqs. 7.4 to 7.7 (compare Eq. 2.17). The integration is performed over the active area A_{det} of the detector. The temporal average $\langle \bullet \rangle$ is taken with respect to the integration time of the detector. Due to the time-invariance of propagation this term does not depend on the absolute temporal scale t. For convenience, complex conjugation is denoted with overlined quantities $\overline{\bullet}$ in this Chapter.

Equation 7.4 yields the reference beam autocorrelation. Obviously, this signal component is not affected by wavefront manipulation at the sample beam. Equation 7.5 yields the autocorrelation of the sample beam. This signal is described by the autocorrelation Γ_{nn} and the cross-correlation $\Gamma_{nn',n\neq n'}$ off the individual source modes which are applied to the sample beam (Eq. 7.8) and depends non-linearly on the amplitudes A_n of the modes (Eq. 7.5). Equation 7.6 yields the mutual interference signal as defined in Chap. 2. This signal is described by a linear combination of the cross-correlations Γ_{Rn} of the reference field with the respective backscattered source modes (Eq. 7.9). The signal is proportional to the complex conjugate amplitude $\overline{A_n}$ of the individual modes. This behaviour is expected. According to the definition used in this work (Eq. 2.4) the cross-correlation Γ_{RS} is proportional to the complex conjugate field E_S at the sample beam. Equation 7.7 yields the mirror image of the mutual interference signal. This term is found from the symmetry of the cross-correlation (Eq. 2.5).

As discussed in Sec. 2.2.4 the signal which is acquired with any practical SD-OCT system is discretized with respect to the temporal scale $\tau_m = m\, d_\tau + \tau_0$, where m is the index and M the total number of pixels. The mirror signal, hence, can be written in matrix notation due to the linearity of Eq. 7.7 :

$$\Gamma_{SR}[m] = \sum_{n=1}^{N} R_{mn}^{mirror} A_n \tag{7.10}$$

$$R_{mn}^{mirror} = \overline{\Gamma_{Rn}}[M+1-m] \tag{7.11}$$

The inverse discrete Fourier transform, from which the OCT signal is calculated, is periodic with respect to the total number of pixels M [63]. The term $M+1-m$ yields the pixel index which corresponds to a time-of-flight of $-\tau_m$.

For imaging one is interested in the mutual interference signal Γ_{RS}, on the other hand. A linear description of this component is found by considering the complex conjugate of Eq. 7.6:

$$\overline{\Gamma_{RS}}[m] = \sum_{n=1} R_{mn} A_n \tag{7.12}$$

$$R_{mn} = \overline{\Gamma_{Rn}}[m] \tag{7.13}$$

Equation 7.13 yields the definition of the time-resolved reflection matrix which is used in this work. The matrix provides a linear description of the mutual interference signal in terms of the field incident to the sample, characterized by the amplitudes A_n.

7.1.2 Phase conjugation applied to optical coherence tomography

On optimized wavefront which selectively enhances the acquired OCT signal, similar to iterative wavefront shaping, is found directly from the reflection matrix using a phase conjugation approach analogue to the technique presented in Sec. 3.4.2. To this end, a $M \times 1$ vector V^{target} is created which reflects the target pixels. The optimal amplitudes of the respective basis modes which are applied to the sample beam (Eq. 7.1) are found from the complex-conjugate of the reflection matrix [24, 118, 119]:

$$A_n^{opt} = \sum_{m=1}^{M} \overline{R_{mn}} V_m^{target} \tag{7.14}$$

In matrix notation, this equation reads $A^{opt} = R^\dagger V^{target}$, where $R^\dagger$ is the conjugate transpose reflection matrix. The optimized wavefront is found by superimposing all basis modes with the respective complex-valued amplitude A_n^{opt} applied (Eq. 7.1).

In case only a single pixel of the OCT scan, denoted by the index m_t, is targeted, the target vector reads $V^{target} = \delta_{m,m_t}$ where δ is the Kronecker symbol. The optimal amplitudes of the incident modes, thus, correspond to the m_t-th row of the conjugate reflection matrix $A_n^{opt} = \overline{R_{m_t n}}$ (compare Eq. 3.6). In case of multiple or spatially extended targets, the optimized incident field calculated from Eq. 7.14, hence, can be understood to be found from a linear superposition of wavefronts which are calculated for signal enhancement at the individual target pixels, respectively.

The effect of phase conjugation on the acquired mutual interference OCT signal Γ_{RS} is found by inserting Eq. 7.14 into Eq. 7.12. Considering a single target pixel m_t, the signal reads:

$$\overline{\Gamma_{RS}}[m] = \sum_{n=1}^{N} R_{mn} \overline{R_{m_t n}} \tag{7.15}$$

At the target $m = m_t$ the individual summands read $|R_{m_t n}|^2$, i.e. the respective contributions from individual modes to the superimposed OCT signal are all aligned to the

real axis. As a consequence, the signal amplitude $|\Gamma_{RS}|$ is enhanced at the target. In contrast, at $m \neq m_t$ the phase of the individual summands is randomly distributed and, hence, no amplitude enhancement results. The effect is equivalent to phase conjugation with the transmission matrix, which is discussed in Sec. 3.4.2.

The target pixel m_t corresponds to a given time-of-flight, depending on the axial scale of the OCT system, and the phase conjugation algorithm enhances the signal amplitude at the selected target time-of-flight only. The approach can be understood to manipulate the phase of the individual modes which are incident to the sample such that the respective contributions to the OCT signal are aligned to the same phase at the target, resulting in a large amplitude of the superimposed signal. The temporal profile of the scattered modes differs, on the other hand. As a consequence, the incident beam needs to be optimized for each target time-of-flight individually.

An interesting feature results from the fact that the reference field E_R remains static throughout the process. The phase of the OCT signal which is detected at the target effectively probes the average phase difference between the reference field and the backscattered sample field in the plane of the detector (Eq. 7.9). Phase conjugation constructs an incident wavefront such that this phase difference is aligned to the same value for signal contributions from the respective modes and at the target time-of-flight only. Since the reference beam remains static, on the other hand, this implies that actually contributions to the backscattered sample beam field E_S (Eq. 7.2) are aligned in phase. As a consequence, phase conjugation with the OCT signal enhances the amplitude of light which is backscattered to the detector at the selected time-of-flight. The technique, thus, enables spatial and temporal focusing of backscattered light, similar to the approaches discussed in Sec. 4.3. This effect was directly observed by Choi et al. [30].

Neglecting the effects of multiple scattering at the sample, the axial time-of-flight scale of the OCT signal, or the corresponding optical path length scale, directly relates to the penetration depth in the sample. Light which is detected at a given target time-of-flight, thus, can be considered to be backscattered from the corresponding target depth. For convenience, the term target depth is used in this Chapter rather than the term target time-of-flight.

7.2 Experimental implementation

7.2.1 Reflection matrix acquisition

The time-resolved reflection matrix is acquired experimentally with the setup presented in Chap. 5. Similar to the approach presented in Chap. 6 multiple pixels of the pattern which is applied to the SLM are grouped to larger segments with uniform phase each. A set of L active segments with linear index l is manipulated only. The segments are chosen such that the area at which the sample beam is reflected at the SLM is covered (compare Secs. 5.2.3 and 6.1). A set of N basis modes is constructed from the $L \times N$ basis matrix B. The n-th column of the matrix yields the complex-valued amplitude pattern which is applied to the linearly indexed SLM segments and which corresponds to the n-th basis mode. For the data presented in this Chapter a Hadamard basis is chosen

(Sec. 3.4.1). The columns of the matrix are mutually orthogonal and feature values of ± 1 only, which aligns well to a phase-only modulation of 0 and π. The basis matrix B is a $N \times N$ square matrix in this case.

To acquire the time-resolved reflection matrix only a single basis mode is applied to the sample beam one at a time. The mutual interference signal which is acquired in this case reads $\Gamma_{RS}[m] = \overline{R_{mn}}$ (Eq. 7.12). The complex-conjugated OCT signal which is captured with the n-th mode, hence, yields the n-th column of the matrix. The full reflection matrix is acquired by sequentially applying all modes.

The complex-valued OCT signal is taken directly from the inverse discrete Fourier transform of the spectral raw data. Since this data is real-valued, the complex OCT signal is Hermitian symmetric and additional signal artefacts are observed. The effect is discussed in Sec. 7.4. At this point we may assume the OCT system to capture the mutual interference signal Γ_{RS} only. This can be achieved through phase shifting algorithms (Sec. 2.2.3), similar to the approach presented in the previous Chapter.

7.2.2 Phase conjugation

To selectively enhance the OCT signal once the reflection matrix is determined, the amplitudes A_n^{opt} of the incident modes for focusing at the respective target depth are calculated from Eq. 7.14. The phase ϕ_l^{opt} which is applied to the individual segments of the SLM, i.e. the optimized sample beam wavefront, is found from the linear combination of modes, whose phase pattern is described by the basis matrix B_{ln} [30]:

$$\phi_l^{opt} = arg\left(\sum_{n=1}^{N} B_{ln} A_n^{opt}\right) \tag{7.16}$$

Due to the modulation characteristics of the SLM, only the phase of the individual segments is set. The full complex-valued amplitude A_n^{opt} of the individual modes is considered for the calculation of the optimized phase pattern, nonetheless. The magnitude $|A_n^{opt}|$ can considered to be a weighting factor for phase-contributions from individual modes.

7.2.3 Speckle compounding

The OCT signal which is acquired with any static wavefront applied to the sample is subject to interference of the backscattered beam. As a consequence, a randomly distributed amplitude results for the OCT signal and speckle are observed in case the sample is scanned [46, 184, 188]. Compounding algorithms were demonstrated to significantly reduce the speckle contrast by averaging the OCT signal over multiple independent realizations of the speckle pattern [184, 188], for example by illuminating the sample under different angles [184], by slightly displacing the sample beam [184] or by randomly modulating the wavefront at the sample beam [188]. With the algorithm presented in the previous Section the acquired reflection matrix already probes the OCT signal which is resulting from sample illumination with a set of independent wavefronts. A signal

with reduced speckle contrast, thus, can be acquired in post-processing by averaging the amplitude of the respective signals, i.e. by averaging the columns of the matrix. The approach is similar to the technique presented by Liba et al. [188] and does not require any additional signal acquisition once the reflection matrix is captured. The compounding algorithm is used in this work for a quantitative comparison to the effects of phase conjugation.

7.3 Selective signal enhancement with artefact suppression

The acquisition of the time-resolved reflection matrix is demonstrated experimentally with a scattering sample consisting of a set of stacked layers of pergamin paper (*Whatman 2122*, GE Healthcare, United Kingdom) (Fig. 7.1(a)). The sample's extinction coefficient was estimated to be 30 ± 10 mm^{-1} from Beer's law. A five-step phase shifting algorithm [58], similar to the four-step algorithm presented in Sec. 2.2.3, is used to suppress all components of the SD-OCT signal except the mutual interference signal Γ_{RS}. To determine the dependence of Γ_{RS} on the field which is incident to the sample, the sample's time-resolved reflection matrix is experimentally acquired for a set of 1024 Hadamard basis modes.

Figure 7.1(b) illustrates the OCT signal which is acquired with a flat wavefront applied to the sample beam as well as the signal which is taken from the reflection matrix using the compounding algorithm presented in Sec. 7.2.3. Obviously, with the compounding algorithm the apparent fluctuations of the signal amplitude are reduced. Furthermore, similar to the compounding algorithm which reflects the mean value of the signal amplitudes which result from sample illumination with a random wavefront, the 95-th percentile of the amplitudes is illustrated, as well. This value gives a good estimate to the maximal signal which is expected in case the beam incident to the sample is not controlled. The signal resulting from sample illumination with a flat wavefront does not exceed this level.

Figure 7.1 further illustrates the OCT signal which is detected once the reflection matrix is used to find an optimized wavefront which selectively enhances the signal (Fig. 7.1 Panels (d) and (e)). Similar to the algorithm presented in Chap. 6 the optimized phase patterns are observed to be random-like (compare Fig. 6.1(e)). After application to the sample beam, a significant amplitude enhancement at the target depth results which reads 15.0 dB (31.6-fold linear enhancement) and 11.4 dB (13.9-fold linear enhancement) compared to the compounding algorithm, respectively. Similar to the discussion given in Sec. 6.2, the apparent signal enhancement is limited to the axial and lateral target position for which is wavefront is optimized.

In contrast to the iterative algorithm which is presented in Chap. 6, phase conjugation based on the time-resolved reflection matrix allows to directly calculate an optimized wavefront which selectively enhances the signal amplitude at any point within the field of view of the OCT system without further acquisition. Figure 7.2(a) illustrates a set of A-scans which are point-optimized for different target depths, similar to the data presented in Fig. 6.5. The sample's mutual interference signal is evident in the right hemisphere

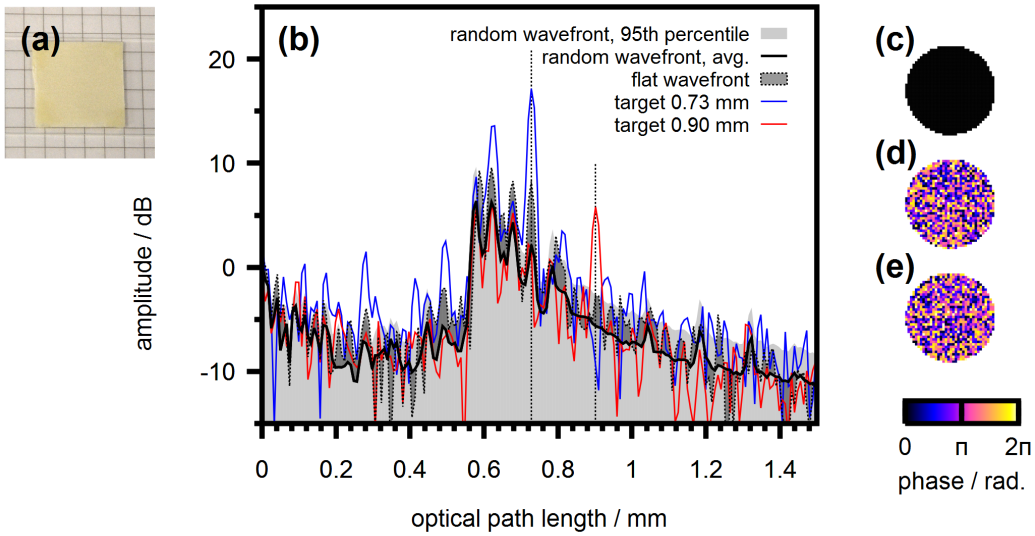

Figure 7.1: **Selective signal enhancement through phase conjugation.** (a) Sample photograph. (b) A-scan taken with a flat wavefront and with optimized phase patterns. The average signal amplitude resulting from random sample illumination is illustrated for comparison. (c) to (e) Phase patterns applied to the sample beam, respectively. Image adapted from [186].

(first and fourth quadrant in Fig. 7.2(a)). Due to the phase shifting algorithm, DC, autocorrelation and mirror artefacts are suppressed. The diagonal elements in Fig. 6.5(a) reflect the amplitude of the OCT signal at the respective target position. Similar to the iterative optimization algorithm (Fig. 6.5) a selective signal enhancement at the target results which is limited to those positions at which a mutual interference signal is observed.

Figure 7.2(b) illustrates the signal amplitude at the respective target depths only. This data corresponds to the diagonal elements in Panel (a) and yields a fully-optimized scan [26]. A significant amplitude enhancement is evident at the position of the mutual interference signal. At a depth of about 1 mm the slope of the OCT signal decreases, which hints on the detected signal to be dominated by strongly multiple scattered light (Sec. 2.3.2). Phase conjugation is observed to enhance the corresponding signal, as well.

7.4 Impact of image artefacts

In the previous Section the acquisition of the reflection matrix is demonstrated with a five-step phase shifting algorithm. Conventional approaches to determine the transmission or the reflection matrix require interferometric techniques such as phase shifting interferometry to determine the phase of the scattered field from the real-valued intensity data which is captured with a sensor such as a CMOS camera (Sec. 3.4.1). In

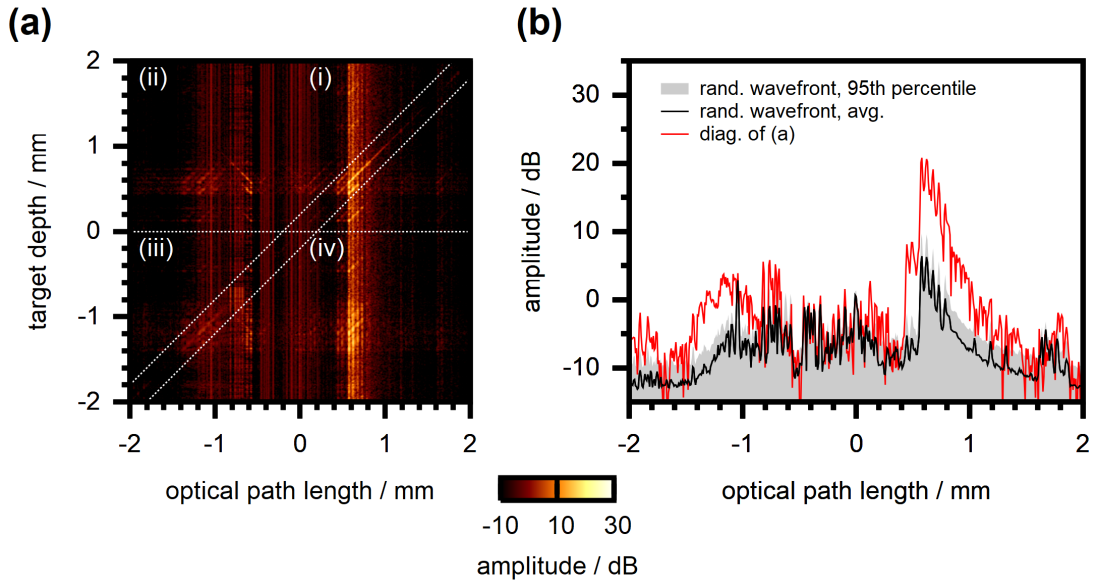

Figure 7.2: **Full A-scan optimization with phase conjugation.** (a) A-scans taken with a five-step phase shifting algorithm and optimized for signal enhancement at different target depths. Quadrants are labelled by Roman numbers. (b) Signal amplitude at in-target (diagonal) elements of Panel (a) only. This data corresponds to a fully optimized A-scan (compare Fig. 6.5). Image adapted from [186].

contrast, optical coherence tomography is already an interferometric technique itself and does not require additional approaches to determine the phase of the backscattered field. With SD-OCT systems, for example, the phase is encoded in the offset of interference fringes which are observed in the raw spectral data and can be acquired from the complex inverse Fourier transform. The time-resolved reflection matrix, hence, can be taken directly from the conventional SD-OCT signal. The approach requires a single signal acquisition for each basis mode applied to the sample and, thus, yields a five-fold increase in acquisition speed compared to the sequential five-step phase shifting algorithm which is demonstrated in the previous Section. The approach was first demonstrated by Choi et al. in 2013 [30].

With the conventional SD-OCT signal image artefacts are observed, on the other hand (Sec. 2.2.1), which contribute to the experimentally observed reflection matrix R^{obs}_{mn} taken from the complex-conjugated signal (Sec. 7.2). These artefacts ultimately arise from the fact that the spectral raw data is real-valued, resulting in the OCT signal to be Hermitian symmetric, and from the fact that the SD-OCT system does not actually capture the cross-correlation Γ_{RS} of the reference and the sample beam but the autocorrelation of the superimposed beams (Sec. 2.2.1). The reflection matrix R_{mn} is assumed to yield a linear description of the mutual interference signal Γ_{RS} only, on the other hand (Eq. 7.12).

Typically, the individual components of the SD-OCT signal are detected at different positions within the scan. DC and autocorrelation artefacts, for example, are detected close to $z = 0$ and are not affected by the length of the reference arm. In contrast, the position at which mutual interference and mirror signals are detected can be manipulated by changing the reference arm length. Typically, the reference mirror is aligned such that mutual interference and mirror signals do not overlap with each other or with autocorrelation signals.

The phase conjugation algorithm requires knowledge of the rows of the reflection matrix which correspond to the signal detected at the target time-of-flight only. Signal enhancement at the m_t-th pixel requires knowledge of the m_t-th row of the reflection matrix, for example. In this Section, hence, the signal at the target is assumed to be dominated by just one signal component to investigate the impact of image artefacts on phase conjugation with the reflection matrix. The case multiple signal components overlap is discussed in Sec. 7.4.5.

7.4.1 Target signal dominated by mutual interference components

First we may consider the case the OCT signal at the target pixel m_t is dominated by mutual interference signals. The m_t-th row of the observed reflection matrix $R^{obs}_{m_t n}$ which is taken from the experimental SD-OCT signal, hence, matches the same row of the matrix $R_{m_t n}$, which corresponds to the mutual interference signal only (Eq. 7.12). The optimized wavefront to enhance the signal at the target is calculated from Eq. 7.14 using the experimentally acquired matrix R^{obs}_{mn}. Since only mutual interference signals are detected at the target, the effect on the resulting OCT signal is the same as if the matrix R_{mn} was used. As a consequence, phase conjugation is expected to selectively enhance the signal at the target depth.

Due to the Hermitian symmetry of the conventional SD-OCT signal which is acquired once the optimized wavefront is applied to the sample beam, the signal amplitude at the mirror position of the target depth is enhanced, too. Furthermore, a selective enhancement of autocorrelation artefacts is expected. In Sec. 7.1.2 reasons are presented indicating that phase conjugation actually enhances the amplitude of light which is backscattered from the target depth to the detector, assuming multiple scattering to be negligible. Autocorrelation artefacts which result from mutual interference of light reflected at the target depth with light which is backscattered from another strongly reflecting layer of the sample, for example the sample front surface, are expected to be enhanced as a result of phase conjugation, as well.

7.4.2 Target signal dominated by mirror artefacts

Mirror artefacts depend linearly on the field incident to the sample and, hence, can be written in terms of the matrix R^{mirror}_{mn} similar to the time-resolved reflection matrix (Eq. 7.10). The experimentally observed reflection matrix R^{obs}_{mn} is acquired from the complex-conjugated OCT signal, on the other hand. Hence, the m_t-th row of that matrix reads $R^{obs}_{m_t n} = \overline{R^{mirror}_{m_t m}}$ if the signal at the m_t-th pixel is dominated by mirror

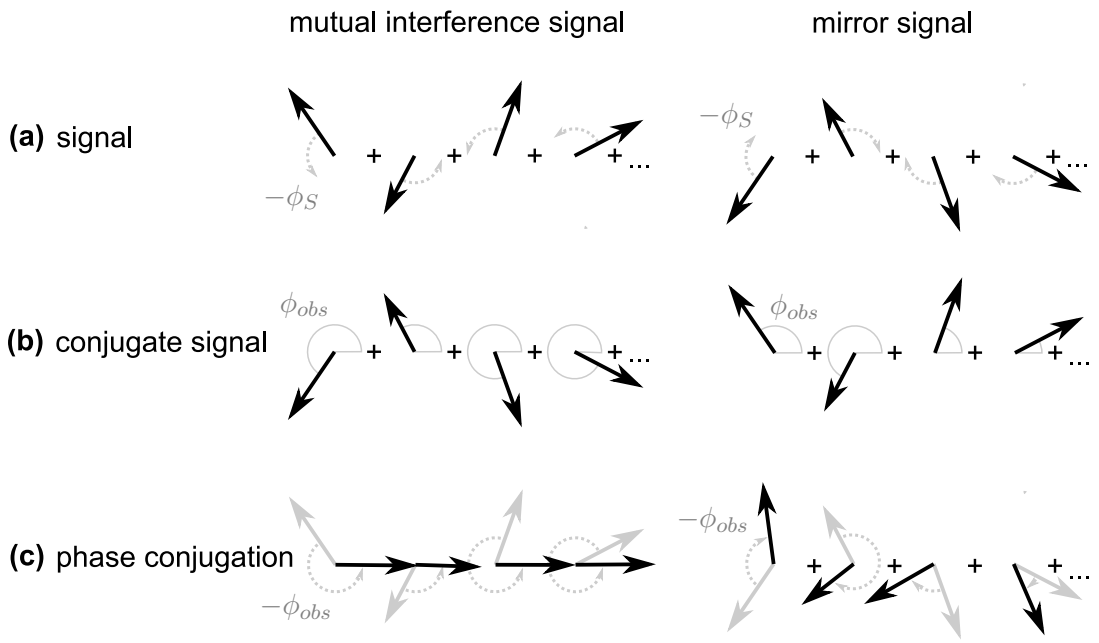

Figure 7.3: **Effect of phase conjugation on mutual interference and mirror signals.** (a) Phasor diagram for contributions from individual basis modes to the OCT signal detected at the target depth. The rotation direction in case a negative phase delay $-\phi_S$ is applied to the sample beam is illustrated. (b) The reflection matrix is found from the complex-conjugate signal. (c) The phase conjugation algorithm applies a negative phase delay $-\phi_{obs}$, where ϕ_{obs} is the phase of the individual reflection matrix elements, to the sample beam. Contributions to the mutual interference signal are aligned to the real axis.

artefacts. The phase conjugation algorithm calculates an optimized wavefront from the complex conjugate of the experimentally observed matrix (Eq. 7.14). Inserting into Eq. 7.10 yields the effect on the OCT signal in case mirror artefacts are dominant at the target depth:

$$\Gamma_{SR}[m] = \sum_{n=1}^{N} R_{mn}^{mirror} R_{m_t n}^{mirror} \tag{7.17}$$

In contrast to phase conjugation with the mutual interference signal (Eq. 7.15), this equation corresponds to a sum of complex values with randomly distributed phase at the target $m = m_t$. As a consequence, no significant signal enhancement results.

The phase conjugation algorithm, hence, selectively enhances the OCT signal if mutual interference components Γ_{RS} are targeted, but no similar effect is expected if mirror artefacts Γ_{SR} are targeted. This behaviour results from both signal components being complex conjugated with respect to each other. The effect is illustrated in Fig. 7.3. Panel (a) illustrates the phasors which correspond to the contributions from individual

source modes to the detected OCT signal, i.e. the summands in Eqs. 7.10 and 7.12. The application of a negative phase delay $-\phi_S$ to the sample beam rotates contributions to the mutual interference signal in mathematically positive direction and contributions to mirror components in negative direction. The reflection matrix is acquired from the complex conjugate signal (Fig. 7.3(b)). The phase conjugation algorithm probes the phase ϕ_{obs} of the individual reflection matrix elements and applies a negative phase delay $-\phi_{obs}$ to the individual source modes at the sample beam. As a consequence, the contributions from the individual modes to the mutual interference signal are all aligned to the real axis and a large amplitude results for the superimposed signal. In contrast, if the mirror signal is targeted the contributions from individual modes still feature a randomly distributed phase after the application of the phase conjugation algorithm. No significant amplitude enhancement results for the superimposed signal.

It is a matter of definition which signal component is termed mutual interference and which is termed mirror artefact. Both signal components yield the same information and, thus, are suited to image the sample morphology. The phase conjugation algorithm presented in this Chapter can easily be changed to enhance the amplitude of those signal components which are termed mirror artefacts in this work, but not mutual interference signals. This is readily achieved by calculating the experimentally observed reflection matrix R^{obs}_{mn} directly from the OCT signal and not from the complex conjugated signal. The matrix yields a linear description of mirror artefacts (Eq. 7.10) but not of mutual interference signals (Eq. 7.12) in this case.

7.4.3 Target signal dominated by autocorrelation artefacts

In case the signal at the target is dominated by autocorrelation artefacts, the corresponding row of the observed reflection matrix reads $R^{obs}_{m_t n} = \overline{\Gamma_{RR}}[m_t] + \overline{\Gamma_{nn}}[m_t]$ (Eqs. 7.4 and 7.5). The autocorrelation of the reference beam Γ_{RR} remains static throughout the acquisition and, hence, is constant. The autocorrelation of the sample beam Γ_{SS} depends on the wavefront which is applied to the sample and, in principle, is fully described by the term $\Gamma_{nn'}$ (Eq. 7.5), which is the cross-correlation of the n-th and the n'-th source mode after reflection at the sample. During the acquisition of the reflection matrix only isolated modes are applied and, thus, the cross terms $\Gamma_{nn',n\neq n'}$ are not accessed, on the other hand. As a consequence, the experimentally acquired reflection matrix does not sufficiently probe the autocorrelation terms. Furthermore, the autocorrelation signal does not depend linearly on the field at the sample beam, which is a requirement for the phase conjugation algorithm. As a consequence, no signal enhancement is expected from phase conjugation if autocorrelation artefacts are targeted.

7.4.4 Impact of the double interferometer OCT design

The analytic discussion of the time-resolved reflection matrix and subsequent phase conjugation (Sec. 7.1) is based on the assumption that only the field which is applied to the sample beam is modulated, whereas the reference field remains static. This is not fully true for the double-interferometer OCT design which is used in this work.

In Sec. 5.4.5 it was demonstrated that the mutual interference and the mirror signal which are detected by the OCT system correspond to the cross-correlation between the effective reference and sample beam. The SLM enables independent single-pass beam shaping at either beam, respectively. During the experimental acquisition of the time-resolved reflection matrix, the wavefront at the effective sample beam is manipulated only, the effective reference beam remains static. The mutual interference and mirror signals which are detected with the double-interferometer design, thus, can indeed be described in terms of the formalism which is discussed in Sec. 7.1.

The detected autocorrelation signal results from the autocorrelation of the effective reference and sample beam, respectively. These signal components are included in the analytic discussion given in Sec. 7.1. As a consequence of the double-interferometer design additional signal artefacts are observed, though. These signal components correspond to the autocorrelation of the beam which is reflected at the part of the SLM at which the (sample beam) wavefront is modulated and which is reflected at the reference mirror, as well as the autocorrelation of the beam reflected at the static half of the SLM and reflected at the sample (Sec. 5.4.5). These additional signal components are not included to the model which is presented in Sec. 7.1. The autocorrelation signals resulting from the effective reference and sample beam are not enhanced with the phase conjugation algorithm (Sec. 7.4.3). A similar behaviour is expected for the additional autocorrelation artefacts, as well.

7.4.5 Overlapping signal components

In practical applications, multiple signal components can be detected at the same time-of-flight. In case the length of the reference arm is chosen to be too short, for example, mutual interference signals might overlap with mirror signals or with autocorrelation artefacts. The previous Sections demonstrated the phase conjugation algorithm to enhance the mutual interference signal only. Further signal components which are detected at the same time-of-flight result from reflections at different depths at the sample and, hence, can be considered to be uncorrelated. As a consequence, the effect of image artefacts can be treated similar to experimental noise.

Experimental noise which is detected during signal acquisition introduces phase errors to the reflection matrix. As a consequence, the phase conjugation algorithm does not align the contributions from individual source modes exactly in phase. On the other hand, the amplitude of the superimposed OCT signal is enhanced in case the individual modes are only roughly aligned to one direction in the complex plane, as well. Compared to ideal phase conjugation a lower signal enhancement results, though. The effect can be exploited for binary amplitude-only wavefront optimization and is discussed in Chap. 8.

A detailed discussion requires a sophisticated SNR analysis of the phase conjugation approach which needs to take the statistical properties of the reflection matrix into account and which is beyond the scope of this work. In general, a limited enhancement of mutual interference signals is expected with the phase conjugation algorithm even in case image artefacts are detected at the same time-of-flight. The signal enhancement is expected to drop with increasing artefact amplitude.

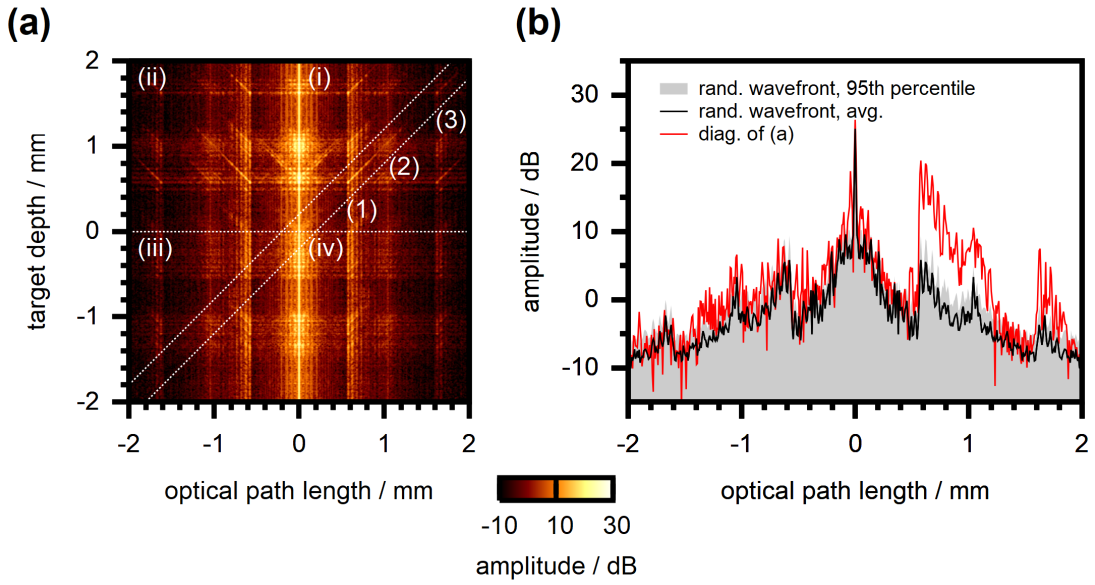

Figure 7.4: **Impact of image artefacts on phase conjugation.** (a) Conventional A-scans taken after phase conjugation for signal enhancement at different target depths. Image artefacts were not suppressed during the acquisition of the reflection matrix. (b) Signal amplitude at the in-target (diagonal) elements of Panel (a). Image adapted from [186].

7.4.6 Experimental validation

The previous considerations are verified experimentally. The acquisition which is presented in Sec. 7.3 is repeated with the same experimental parameters. The time-resolved reflection matrix is taken directly from the conventional complex-valued SD-OCT signal without phase shifting algorithm this time. Figure 7.4(a) illustrates a set of A-scans for which the phase conjugation algorithm was used to enhance the signal at different target depths. The signal is symmetric with respect to the vertical axis since mirror artefacts are not suppressed in contrast to the data presented in Fig. 7.2(a). Additional strong autocorrelation artefacts are evident close to $z = 0$.

The phase conjugation algorithm yields different effects depending on what kind of signal dominates at the target depth, i.e. at the diagonal elements in Fig. 7.4(a). At label (1) autocorrelation artefacts dominate at the target. As a consequence, no significant effect on the amplitude of the OCT signal is evident. In contrast, at label (2) the mutual interference signal which is detected from the sample is targeted (compare Fig. 7.2(a)). As a consequence, the amplitude at the target position as well as the amplitude of the corresponding mirror image is enhanced. Furthermore, faint ghost images of the sample are observed which are axially displaced by approximately 1 mm. One of the ghost images is, for example, evident at a depth of 1.6 mm. The amplitude of the ghost images is observed to be enhanced, as well, in case the mutual interference signal

is targeted. Finally, a selective enhancement of autocorrelation artefacts is observed in case mutual interference signals are targeted (compare Sec. 7.4.1). At label (3) a ghost image is targeted by the phase conjugation algorithm. A selective enhancement at the target and at the mutual interference signal which corresponds to the ghost image is observed. The lower hemisphere of Fig. 7.4(a) (third and fourth quadrant) corresponds to the case only autocorrelation and mirror artefacts are targeted by the algorithm. No significant effect on the amplitude of the received signal is evident.

As discussed in Sec. 7.3, the diagonal elements of Fig. 7.4(a) yield an OCT signal which is optimized at the full axial scan range [26] (Fig. 7.4(b)). Similar to the same approach based on phase-shifting interferometry (Fig. 7.2(b)), the amplitude of mutual interference signals is observed to be enhanced. No comparable effect results for autocorrelation and mirror artefacts, even though these signal components are not suppressed during the measurement of the time-resolved reflection matrix or during the subsequent signal acquisition.

7.5 Quantitative signal enhancement

Figure 7.5(b) illustrates the amplitude of the enhanced OCT signal in case the number of modes for which the reflection matrix is acquired is changed. The resulting optimized phase patterns which are found by the phase conjugation algorithm are illustrated in Fig. 7.5(e). Similar to the observations made by Choi et al. [30], the slope of the signal enhancement reads approximately 5 dB per decade, i.e. if the number of modes is increased by a factor 100 (two decades), the OCT signal is enhanced by an additional factor of ten (10 dB). With a large number of modes, starting at $N = 1024$ for the presented data, the amplitude enhancement resulting from phase conjugation is observed to taper off (compare [30]).

Figure 7.5(c) illustrates the average signal amplitude which is resulting from sample illumination with a random phase pattern. This data is taken directly from the acquired reflection matrix (Sec. 7.2.3). Hence, the parameters of the random wavefront, such as the segment size and the physical beam diameter, are equal to the optimized wavefront. With increasing number of modes, i.e. with a higher spatial wavefront resolution, the amplitude of the OCT signal is observed to drop. Imperfections of the experimentally applied wavefront arise whenever there is a step in the phase pattern at the SLM due to cross-talk between the individual pixels. The number of these phase steps rises with increasing number of modes (Fig. 7.5(e)) and, hence, the SLM is expected to perform worse when operated at a high spatial resolution. Furthermore, diffraction occurs at phase steps between neighbouring wavefront segments and a part of the diffracted light does not reach the sample. The amount of diffraction losses is expected to be increased with rising number of modes, as well. Both effects can be reduced by increasing the beam diameter in the plane of the SLM.

A number of reports discussed on the quantitative signal enhancement which is expected from iterative wavefront shaping or from optical phase conjugation (Sec. 3.3), whereas both approaches are considered to be mathematically equivalent [119]. The en-

hancement factor η is defined according to $\eta = I_{opt}/I_{ref}$, where I_{opt} is the peak intensity at the target after phase conjugation [115]. I_{ref} corresponds to the ensemble average of the intensity which is detected for different realizations of the random medium [23, 115] or to the average intensity which is detected outside of the target with the optimized wavefront applied to the sample [119]. In an equivalent approach, in this work I_{ref} is estimated from the mean signal which is resulting at the target but with a random wavefront whose parameters match those of the optimized wavefront applied to the sample (Fig. 7.5(c)). Figure 7.5(d) illustrates the relative amplitude enhancement which is achieved with the phase conjugation algorithm. With the number of modes chosen to be as low as 32 the amplitude of the OCT signal is already observed to be enhanced approximately four-fold (6 dB) and the reflection matrix can be acquired very quickly. With 128 modes a signal enhancement close to ten-fold (10 dB) is achieved.

In addition, Fig. 7.5(d) illustrates the theoretically expected amplitude enhancement. In case the complex-valued amplitude of the incident wave is manipulated, the intensity enhancement is expected to read $\eta = N$ [115, 119], where N is the number of degrees of freedom of the shaped wavefront, i.e. the number of modes. In case of phase-only wavefront manipulation the enhancement reads approximately $0.78\,N$ [23, 118, 119]. The signal enhancement is further expected to drop proportional to $1/M$, where M is the number of degrees of freedom of the scattered field at the target [118]. If the algorithm is used to enhance the signal at two independent point targets at the same time, for example, the shaped field is assumed to be equally focused to both targets and the resulting peak-intensity is reduced by 50 %, respectively [118]. In case a broadband light source is used, one has to take into account that the scattered field is correlated at a finite spectral range $\delta\omega$ only [150, 153, 155, 156, 189–191]. Phase conjugation with the broadband light source, hence, is considered to create constructive interference from a set of M independent spectral channels simultaneously, resulting in a reduced intensity enhancement which is proportional to $1/M$ [156, 157, 189, 192]. The number M can be estimated from the spectral correlation length $\delta\omega$ and from the source bandwidth $\Delta\omega$ to be $M = \Delta\omega/\delta\omega$ [157].

In Sec. 7.1.2 it was shown that phase conjugation with the SD-OCT signal enhances the amplitude of light which is backscattered to the detector at the selected target time-of-flight. The resulting OCT signal does not probe the intensity $|E_S|^2$ of the backscattered field, but the cross-correlation with the static reference beam. The cross-correlation is proportional to the field amplitude $|E_S|$ (compare Eqs. 2.4 and 2.17). The phase conjugation algorithm, hence, is expected to yield an enhancement of the OCT signal amplitude which is proportional to the square root of the intensity enhancement, i.e. $\eta = \sqrt{0.78\,N/M}$ [30, 151]. As is evident from Fig. 7.5(d), the experimental data is well-described by this function and the experimental system performs close to the predictions for $M = 1$, i.e. close to the optimal value. A brief discussion on this effect is provided.

The spectral correlation length $\delta\omega$, and, hence, the number M, is not accessible with the experimental system which is used in this work. $\delta\omega$ can easily be tested by implementing monochromatic phase conjugation with a wavelength tunable source [155] or with a SS-OCT system which enables wavefront manipulation similar to this work. The

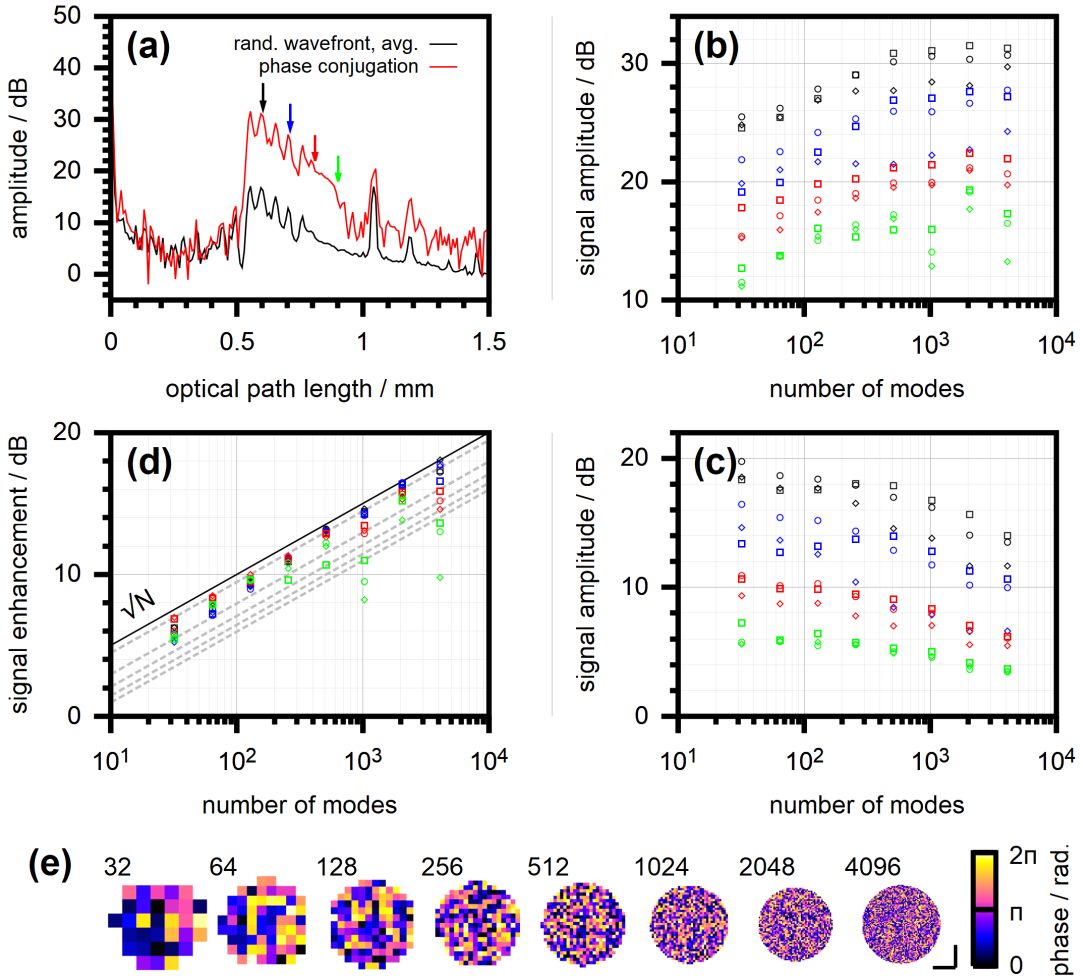

Figure 7.5: **Quantitative signal enhancement.** (a) Fully optimized A-scan acquired with a set of $N = 1024$ modes (compare Fig. 7.4(b)). The target depths at which the signal enhancement is evaluated are marked by arrows. (b) Amplitude of the optimized signal at the respective target depths (○) and at next signal pixel to the left (□) and to the right (◇). (c) Mean signal amplitude at the targets resulting from random wavefront illumination. (d) Relative enhancement of the optimized signal (Panel (b)) compared to random wavefront illumination (Panel (c)). The dashed lines represent the expected amplitude enhancement which reads $\sqrt{0.78N/M}$ with $M = 1$ to $M = 5$ from the topmost to the bottom line. (e) Phase patterns found for signal enhancement at the second target depth (blue arrow) for different numbers of modes. Scalebar 1 mm.

spectral correlation length is related to the time-of-flight distribution of the detected light [150, 153, 155, 156, 189–191, 193]. In case circular Gaussian scattering statistics are assumed (similar to the assumptions made for the theoretical discussion on the effect of phase conjugation [119]) the frequency cross-correlation between scattered fields can be written [190, 191]:

$$\langle E(\omega + \Delta\omega) E^*(\omega) \rangle \propto P(\Delta\omega) \tag{7.18}$$

$$P(\Delta\omega) = \int_{-\infty}^{\infty} p(t) e^{-i\Delta\omega\, t}\, dt \tag{7.19}$$

$P(\Delta\omega)$ yields the Fourier transform of $p(t)$, which is the probability density function of the time-of-flight distribution of scattered light [190, 191]. A broad time-of-flight distribution, hence, results in a small spectral correlation length and in a large number of independent spectral channels which, in turn, reduce the efficiency of phase conjugation.

Point-wise phase conjugation with the OCT signal, as presented in this Chapter, enhances the signal which is detected at a finite time-of-flight window only. The width of this time-of-flight window corresponds to the axial resolution of the OCT system, which is the inverse Fourier transform of the source power spectral density (Sec. 2.1.2). As a consequence, the effective spectral correlation length $\delta\omega$ is comparable to the source bandwidth $\Delta\omega$ and the number of effective independent spectral channels M can be considered to be approximately unity. The experimental system (Fig. 7.5), hence, is observed to perform close the theoretical prediction for $M = 1$.

7.6 Axially extended signal enhancement

So far, the phase conjugation algorithm was only demonstrated for signal enhancement at single point-like targets. The approach is also capable to enhance the OCT signal which is received from an extended or from multiple target depths simultaneously. As discussed in the previous Section, this comes at the price of a reduced peak amplitude enhancement which is proportional to $\sqrt{1/M}$ where M is the number of independent signal pixels at the target.

The approach is demonstrated in Fig. 7.6 with the same sample which is used in the previous acquisitions. Figure 7.6(a) presents a B-scan which is captured at the sample. The signal corresponding to the reflection at the sample front surface is evident at a depth of about 0.8 mm. Figure 7.6(b) illustrates the B-scan which is captured at the sample in case the phase-conjugation algorithm is used for point-like signal enhancement. The point-optimized wavefront is applied to the sample beam and remains static throughout the acquisition of the B-scan, similar to the data presented in Sec. 6.2. The lateral position to which the scanner was fixed during the acquisition of the reflection matrix is centred in the B-scan. Similar to the observations made for iterative wavefront shaping (Sec. 6.2), a significant enhancement of the OCT signal is only evident at the axial target depth and at the lateral position at which the reflection matrix was acquired and for which, hence, the phase conjugation algorithm finds a valid optimized wavefront. Figure 7.6, Panels (c) to (f) present the same data, but the phase conjugation algorithm

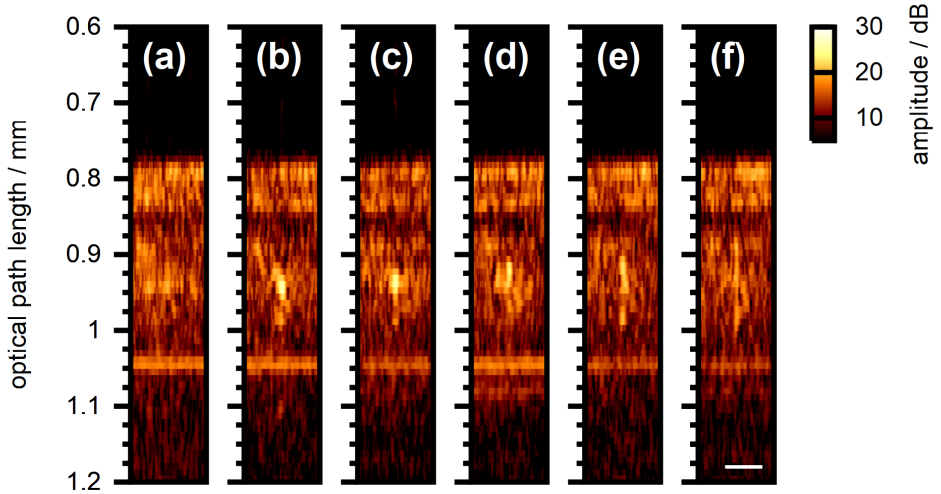

Figure 7.6: **Phase conjugation with extended targets.** (a) B-scan taken with a uniform wavefront applied to the sample beam. (b) B-scan taken with the wavefront for point-wise phase conjugation at a depth of 0.95 mm applied (compare Fig. 6.2). (c) to (f) same as Panel (b) with phase patterns calculated for axially extended signal enhancement. The enhanced depth-ranges are chosen to be 25 µm (3 A-scan pixel, Panel (c)), 50 µm (6 pixel, Panel (d)), 75 µm (9 pixel, Panel (e)) and 100 µm (12 pixel, Panel (f)), respectively. Scalebar 50 µm.

is now used to find a single optimized wavefront which enhances the OCT signal at up to 12 pixels simultaneously according to Eq. 7.14. As a result, the signal indeed appears to be enhanced at an extended depth range, but only at the lateral position at which the reflection matrix was acquired. Hence, a needle-like signal is evident in Fig. 7.6 Panels (e) and (f). The amplitude at the extended target is not observed to be homogeneous after phase conjugation. This is most likely an effect of the sample‘s reflectivity profile not being homogeneous at the target range, resulting in an inhomogeneous OCT signal, as well.

8 Reflection matrix approach applied to binary amplitude-only wavefront shaping

In this Chapter the reflection matrix approach is translated to binary amplitude-only wavefront manipulation. In contrast to phase conjugation with the reflection matrix, the technique can directly be implemented with wavefront control enabled by micro-electromechanical systems such as digital micromirror devices which feature frame rates in the kHz range and which, hence, enable high-speed imaging applications. The presented technique is inspired by similar approaches which were demonstrated for iterative wavefront shaping [120] and for optical phase conjugation [102] in transmission geometry with monochromatic sources. This Chapter presents to my knowledge the first report on the acquisition of the time-resolved reflection matrix based on binary amplitude-only wavefront manipulation and the subsequent application for OCT signal enhancement.

8.1 Principles

8.1.1 Matrix acquisition

The time-resolved reflection matrix which is discussed in the previous Chapter probes the linear dependence of the field backscattered from the sample on the incident field. The experimental acquisition is discussed in Secs. 7.1 and 7.2. A spatial light modulator is used to apply a set of basis modes to the sample beam and the resulting SD-OCT signal, which reflects the amplitude and the phase of the time-resolved backscattered field, is captured, respectively. Phase control of the incident beam is not necessary to determine the phase of the scattered field, but allows to suppress SD-OCT image artefacts by using phase shifting algorithms. The reflection matrix, thus, can be acquired with a set of amplitude-only patterns, which are applied to the sample beam to create the respective basis modes, just as well as with basis modes which are created by phase-only wavefront control.

8.1.2 OCT signal enhancement

The phase conjugation algorithm (Sec. 7.1.2), which is in the previous Chapter shown to selectively enhance the OCT signal, is not feasible for amplitude-only wavefront manipulation; the phases of the individual modes cannot directly be manipulated to create constructive interference from the scattered field. Instead, an optimized wavefront is constructed by switching individual modes which are incident to the sample on (unity amplitude) or off (zero amplitude) [102, 120]. The approach is illustrated in Fig. 8.1.

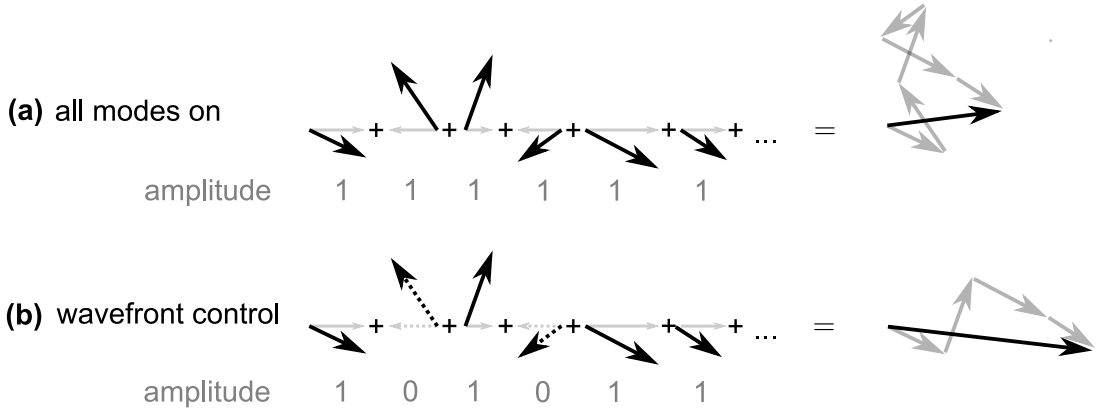

Figure 8.1: **Principle of binary amplitude-only wavefront manipulation.** (a) Phasor diagram of contributions from individual modes to the OCT signal which is received at the target (compare Fig. 7.3) and the corresponding projections to the real axis. Applying all modes with unity amplitude to the sample beam results in a low amplitude of the superimposed OCT signal. (b) Applying only those modes whose phasors point in the same hemisphere of the complex plane (real part > 0) yields an OCT signal with enhanced amplitude. Compare [120]

Each mode which is applied to the sample beam yields an OCT signal at the target depth whose amplitude and phase is randomly distributed. In case all modes are superimposed, the corresponding signal contributions are superimposed as well due to the linearity of the OCT signal. A low overall signal amplitude results from the sum of random phasors (Fig. 8.1(a)).

Without loss of generality the supposed optimized OCT signal is assumed to be aligned to the real axis. An optimized wavefront is found by superimposing only those modes, for which the projection of the respective OCT signal to the real axis is larger than zero (Fig. 8.1(b)) [102, 120]. Modes which reduce the signal amplitude, i.e. whose projection to the real axis is negative, are switched off. Hence, only modes whose contributions to the OCT signal add up constructively are applied to the sample beam and a local amplitude enhancement at the target results.

The phase of the OCT signal which is resulting from illumination with the respective source modes is encoded in the reflection matrix. The matrix further describes the signal at the full axial field of view of the OCT system. Hence, similar to the phase conjugation algorithm, an optimized wavefront which enhances the signal at any point within the FOV can directly be calculated once the matrix is determined.

8.2 Experimental implementation

8.2.1 Reflection matrix acquisition

The acquisition of the reflection matrix with binary amplitude only wavefront manipulation is enabled analogue to the approach discussed in Sec. 7.2. Multiple pixel of the pattern which is applied to the SLM are grouped to larger segments. Binary amplitude-only wavefront manipulation is implemented with the phase-only SLM, which is used in this work, by assigning an amplitude of either zero ore one to each segment, respectively. For those segments which are switched on (unity amplitude), a uniform phase of zero is applied to all pixels which are grouped to the corresponding segment. For those segments which are switched off (zero amplitude) a random phase pattern is applied to the underlying pixels. Light which is reflected at segments which are switched off produces a diffusive speckle pattern which yields a negligible amplitude in the plane of the sample.

Similar to the previous approach (Sec. 7.2), a set of L active segments is manipulated only. The active segments are chosen such that the area at which the sample beam is reflected from the SLM is covered. A set of N basis modes is constructed from a $L \times N$ basis matrix B. In contrast to the previous Chapter, B is considered to be a binary matrix with values of zero or one. For the experiments presented in this Chapter, B is created by thresholding a Hadamard matrix, which was used in the previous Chapter to define the basis modes, as well (Sec. 7.2). The n-th column of the basis matrix B corresponds to the amplitude pattern which is applied to the set of (linearly indexed) active SLM segments to create the n-th mode.

The reflection matrix is acquired by sequentially applying each mode to the SLM and by saving the complex-valued SD-OCT signal which is resulting from illumination with the respective wavefront to the n-th column of the matrix. In contrast to the approach presented in the previous Chapter, complex conjugation of the OCT signal is not required.

8.2.2 Mode superposition approach

Signal enhancement at a single target time-of-flight, corresponding to the m_t-th pixel of the OCT signal, is considered. Once again, the calculation of an optimized wavefront which enhances the signal at the target requires knowledge of the m_t-th row of the reflection matrix only. The complex-valued matrix element $R_{m_t n}$ reflects the phase of the OCT signal which is resulting at the target time-of-flight from illumination with the n-th mode. To each mode, an optimal binary amplitude A_n^{opt} is assigned which is, according to the discussion given in Sec. 8.1.2, chosen such that only those modes whose projection to the real axis is positive at the target are switched on (compare Fig. 8.1):

$$A_n^{opt} = \begin{cases} 1 & \text{if} \quad \Re\{R_{m_t n}\, e^{-i\phi_{m_t}^{mean}}\} > 0 \\ 0 & \text{else} \end{cases} \tag{8.1}$$

The term $\phi_{m_t}^{mean} = arg(\sum_{n=1}^{N} R_{m_t n})$ yields the mean phase of the m_t-th row of the reflection matrix, which is the mean phase of the OCT signal detected at the target.

The final binary amplitude-only wavefront which is applied to the sample beam is found by superimposing the individual basis modes with their respective amplitudes A_n^{opt} applied. The amplitude A_l^{opt} of the l-th active SLM segment, thus, reads in principle $A_l^{opt} = \sum_{n=1}^{N} B_{ln} A_n^{opt}$, where B_{ln} is the basis matrix. On the other hand, due to the binary modulation scheme an exact superposition of the individual amplitude patterns is not possible since amplitudes A_l^{opt} other than zero or one are not allowed. Instead, an approximate wavefront is found with the method presented by Jang et al. [26] by thresholding the amplitude pattern such that half of the SLM segments are switched on and the other half of the segments are switched off [26, 194]. This method is termed *mode superposition* in the context of this Chapter:

$$A_l^{opt} = \begin{cases} 1 & \text{if} \quad \sum_{n=1}^{N} B_{ln} A_n^{opt} > A_{med} \\ 0 & \text{else} \end{cases} \tag{8.2}$$

The term A_{med} corresponds to the median of the ideal amplitude pattern $\sum_{n=1}^{N} B_{ln} A_n^{opt}$.

8.2.3 Segment superposition approach

Due to amplitude thresholding, only an approximate to the optimal wavefront is found with the mode superposition approach. Thresholding can be avoided by directly testing the OCT signal with a segment-by-segment basis, i.e. by switching only single segments of the sample beam wavefront on and saving the resulting OCT signal to the reflection matrix. The approach allows to decide for each mode individually whether it needs to be switched on or off [102, 120]. The technique was demonstrated by Akbulut et al. for iterative wavefront shaping in transmission geometry with a monochromatic source [120]. The signal which is received with only a small fraction of the incident beam switched on is very weak, on the other hand, and a low SNR results if the segment size is chosen to be small or if a large number of segments, i.e. a high spatial resolution of the shaped wavefront, is used. Hence, a hybrid approach is presented which tests the field which is backscattered from the sample with a set of modes which span the full diameter of the sample beam but which calculates the optimized wavefront in terms of a segment-by-segment basis and which, hence, requires no amplitude thresholding. The approach is termed *segment superposition* in the context of this Chapter.

The optimized wavefront is calculated from the same reflection matrix R_{mn} which is used for the previous mode superposition approach. The matrix has size $M \times N$ and probes the OCT signal (pixel count M) which is resulting from illumination with the set of N Hadamard basis modes. The pseudoinverse B^{-1} of the basis matrix B, which yields the amplitude patterns corresponding to the individual source modes in terms of the respective SLM segments, is calculated using the Matlab function *mldivide* according to $B^{-1} = mldivide(B, I^L)$. The algorithm calculates B^{-1} such that $BB^{-1} = I^L$, where I^L is the $L \times L$ identity matrix. The reflection matrix R_{mn}, which is experimentally acquired with the set of Hadamard modes, is then transformed to a segment-by-segment basis using the right-hand side multiplication with the pseudoinverse basis matrix: $\widetilde{R}_{ml} = \sum_{n=1}^{N} R_{mn} B_{nl}^{-1}$.

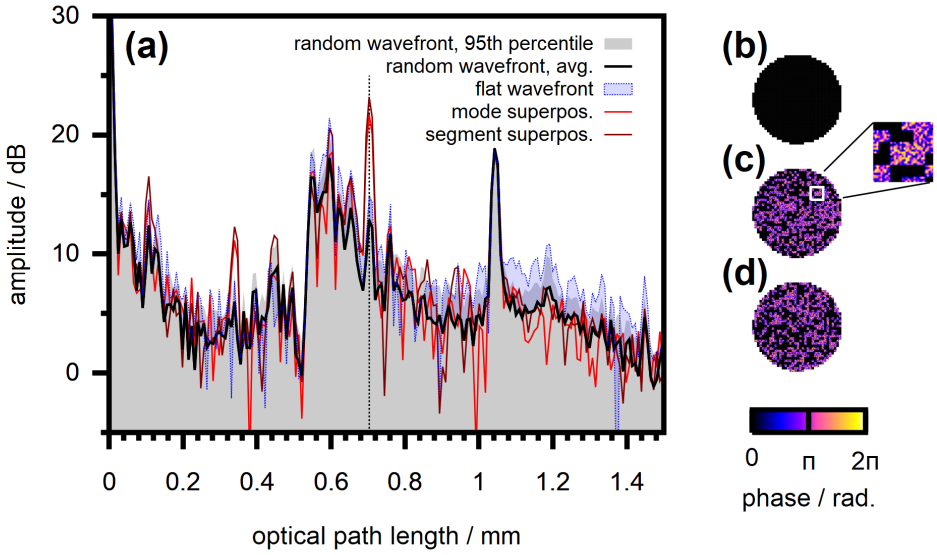

Figure 8.2: **Signal enhancement through binary amplitude-only wavefront manipulation.** (a) A-scan taken with a flat wavefront and with optimized wavefronts applied to the sample beam, respectively. (b) Flat wavefront. All segments switched on. (c) Wavefront calculated with the mode superposition algorithm and (d) with segment superposition. Compare Fig. 7.1.

$\widetilde{R}_{ml}$ is a $M \times L$ matrix which yields the phase of the OCT signal which is resulting from sample illumination with the respective wavefront segments (indexed l) at different time-of-flights (indexed m). The optimized wavefront is found analogue to the previous approach (Eq. 8.1) by directly switching only those segments on whose projection to the real axis is positive:

$$A_l^{opt} = \begin{cases} 1 & \text{if} \quad \Re\{\widetilde{R}_{m_t l}\, e^{-i\widetilde{\phi}_{m_t}^{mean}}\} > 0 \\ 0 & \text{else} \end{cases} \tag{8.3}$$

In contrast to the previous technique, the algorithm directly yields an amplitude of zero or one for each segment of the optimized wavefront.

8.3 Selective signal enhancement

The approach is demonstrated experimentally with a sample consisting of multiple layers of stacked pergamin paper. The same sample which is presented in Sec. 7.3 is used. Figure 8.2(a) illustrates the OCT signal taken with a flat wavefront applied to the sample beam, i.e. with all active SLM segments switched on (Fig. 8.2(b)). The reflection matrix is acquired with the algorithm discussed in Sec. 8.2.1 for a set of $N = 1024$ basis modes. Similar to the compounding algorithm which is presented in Sec. 7.2.3, the average of the matrix yields the mean signal and the 95-th percentile yields the maximal signal

which is expected from sample illumination with a random wavefront. The amplitude of the signal which is captured with a flat wavefront applied to the sample beam is found to exceed both of these signals (Fig. 8.2(a)). With the flat wavefront, the full diameter of the sample beam is switched on. In contrast, during the acquisition of the reflection matrix only a fraction of the active SLM segments are switched on to create the respective basis modes and, hence, a weaker signal amplitude results.

Figure 8.2(a) further presents the OCT signal which is acquired once the mode superposition and the segment superposition algorithm presented in Sec. 8.2 are used to selectively enhance the signal which is received from a depth of 0.703 mm. The corresponding patterns which are applied to the SLM are illustrated in Fig. 8.2 Panels (c) and (d). The SLM which is utilized in this work enables phase-only wavefront control only. As is visible from the inset in Fig. 8.2(c), the optimized wavefront is constructed from non-overlapping square segments with uniform phase (unity amplitude) and from segments to which a random phase pattern is applied (zero amplitude).

As is evident from Fig. 8.2, both algorithms significantly enhance the signal amplitude at the target by switching off half of the sample beam in a controlled way. With the mode superposition approach, the signal at the target depth is observed to be enhanced by 9.7 dB (9.3-fold linear enhancement) compared to the average signal which is resulting from random illumination. With the segment superposition approach this value reads 11.2 dB (13.2-fold linear enhancement).

8.4 Impact of image artefacts

The algorithms are used to enhance the signal which is received from different target depths, similar to the experimental data presented in Sec. 7.4.6. The resulting data is illustrated in Fig. 8.3 for the mode superposition approach and in Fig. 8.4 for the segment superposition algorithm.

Similar to phase conjugation with the time-resolved reflection matrix (Fig. 7.4), both algorithms selectively enhance the mutual interference signal which is received from the sample and which is observed at a depth of approximately 0.6 mm. The signal enhancement is limited to the respective target depth, i.e. to the diagonal elements of Fig. 8.3(a) and 8.4(a). The individual point-optimized A-scans are Hermitian symmetric since the conventional SD-OCT signal is detected after applying the optimized wavefronts to the sample beam, respectively. The signals which are illustrated in Figs. 8.3(a) and 8.4(a), hence, are symmetric with respect to the vertical axis.

In contrast to phase conjugation (Fig. 7.4), binary wavefront optimization is observed to enhance mirror artefacts in addition to the mutual interference signal. As a consequence, the fully-optimized A-scan, which is stitched from the in-target amplitude of the respective point-optimized scans analogue to the approach given in the previous Chapter, appears to be symmetric with respect to $z = 0$ (Fig. 8.3 and 8.4 Panel (b)). The mode superposition approach is found to not increase autocorrelation artefacts which are detected close to $z = 0$. In contrast, the segment superposition approach is found to enhance these signal components, as well.

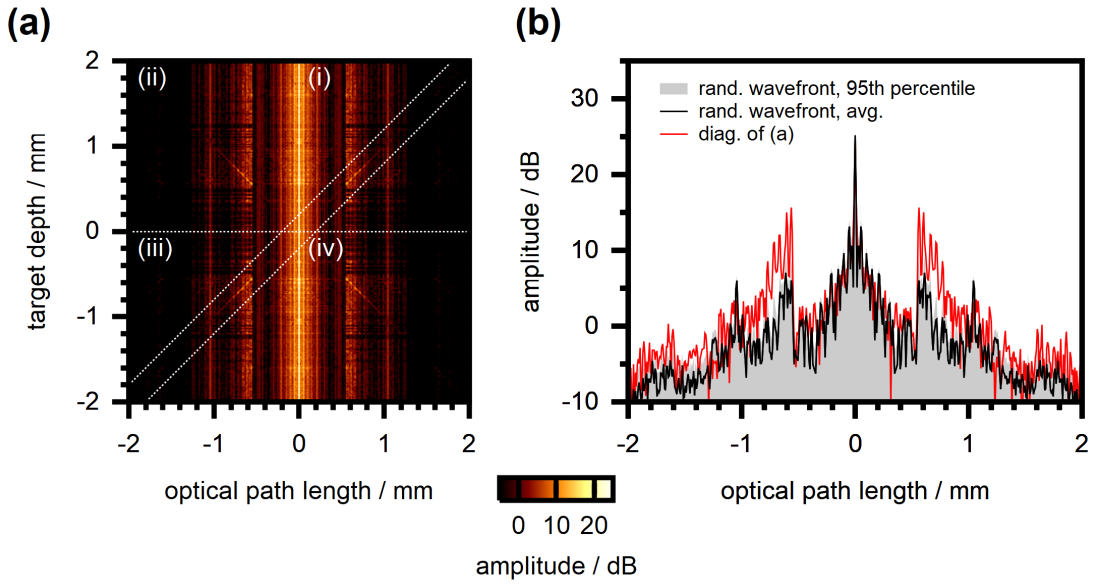

Figure 8.3: **Impact of image artefacts on the mode superposition algorithm.** (a) A-scans taken at a scattering sample after using the algorithm for signal enhancement at different target depths. (b) Signal amplitude at in-target (diagonal) elements of Panel (a) only.

The binary wavefront optimization algorithms which are presented in this Chapter are expected to enhance mirror artefacts in the same way as the mutual interference OCT signal. The algorithms switch those modes or segments on for which the real part of the corresponding OCT signal is larger than zero (Sec. 8.2). Obviously, the approach is insensitive to complex conjugation of the signal. Due to the Hermitian symmetry of the complex-valued SD-OCT signal ($I^{SD}(z) = [I^{SD}(-z)]^*$) the algorithms, hence, are expected to find exactly the same optimized wavefront in case the depth z or if the corresponding mirror image located at $-z$ is targeted.

Autocorrelation artefacts result from mutual interference of the sample beam reflected from different depths. Binary wavefront optimization switches those modes on whose contributions to the OCT signal have roughly the same phase, resulting in constructive interference with the optimized wavefront and an enhanced signal amplitude. In principle, there is no reason why the algorithm should not enhance autocorrelation artefacts in the same way it enhances mutual interference and mirror components. On the other hand, the binary Hadamard-like basis which is used for the mode superposition approach is not orthogonal, in contrast to the phase-only Hadamard basis which is used in the previous Chapter. Furthermore, due to the binarisation of the optimized amplitude pattern (Sec. 8.2.2) an additional mixing of modes occurs. Differences between the ideal and the approximated and experimentally applied wavefront affect autocorrelation artefacts which are sensitive to the sample beam wavefront and whose amplitude, as a conse-

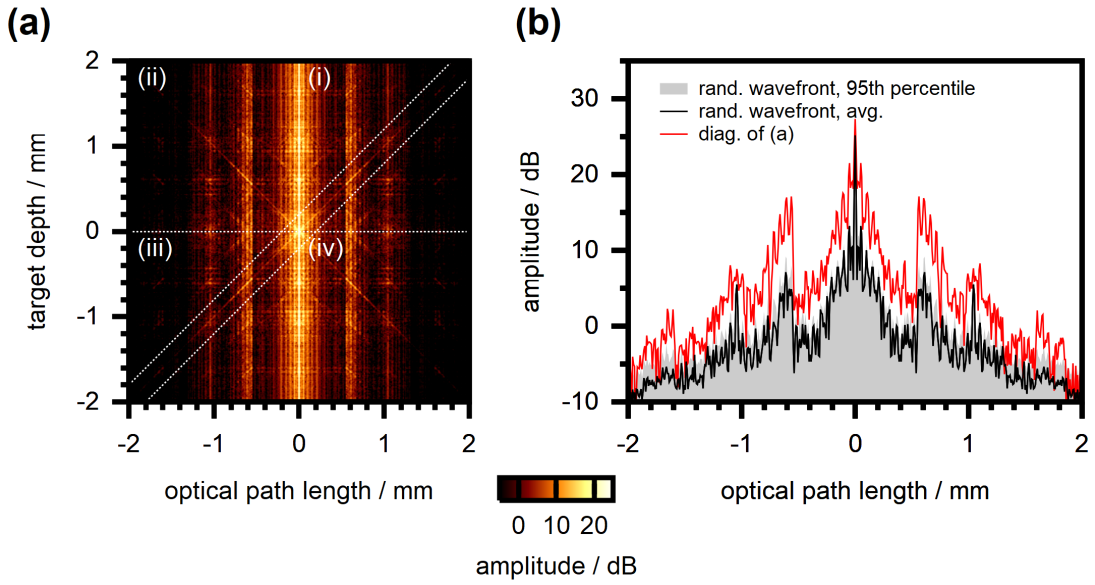

Figure 8.4: **Impact of image artefacts on the segment superposition algorithm.** (a) A-scans taken at a scattering sample after using the algorithm for signal enhancement at different target depths. (b) Signal amplitude at in-target (diagonal) elements of Panel (a) only.

quence, is not enhanced. In contrast, the segment superposition algorithm calculates the optimized wavefront in terms of the field which is reflected from individual spatially non-overlapping segments of the SLM (Sec. 8.2.3). This is an orthogonal basis of the electric field [136] and no mixing of modes occurs with the algorithm. As a consequence, the optimized wavefront is observed to enhance autocorrelation artefacts, as well.

8.5 Quantitative signal enhancement

Similar to the discussion given in Sec. 7.5 the algorithms presented in this Chapter are evaluated for different numbers of basis modes for which the reflection matrix is acquired. Binary amplitude-only wavefront optimization is evaluated with the same sample which is used in Sec. 7.5 and with the same experimental parameters. The data presented in this Section, hence, can directly be compared to the data presented in the previous Chapter for phase-only wavefront optimization.

Figure 8.5 illustrates the relative enhancement of the OCT signal amplitude which is achieved with the segment superposition algorithm. Similar to the data presented in Fig. 7.5(d), the signal enhancement is calculated from the ratio of the amplitude of the optimized OCT signal compared to the average amplitude which is resulting from sample illumination with a random wavefront. The signal resulting from random wavefront illumination is taken from the average amplitude of the reflection matrix (Sec. 7.2.3).

Similar to phase-only wavefront optimization, the slope of the signal enhancement is observed to read approximately 5 dB per decade, i.e. the signal enhancement is approximately proportional to $\sqrt{N}$.

The theoretical intensity enhancement which is expected for binary wavefront manipulation reads $\eta = I_{opt}/I_{ref} = 1 + (N' + 1)/\pi$ according to Akbulut et al. [102, 120], where N' is the number of wavefront segments which are switched on with the optimized wavefront [120]. In case the number of segments is chosen to be sufficiently large, approximately half of the segments are switched on and the intensity enhancement reads $\eta \approx N/(2\pi)$. The OCT signal probes the amplitude of the backscattered field. The amplitude enhancement, thus, is expected to read $\sqrt{N/(2\pi)}$ (compare Sec. 7.5). As is evident from Fig. 8.5(b) the experimental data is well described by this function.

The reference intensity I_{ref}, which is used to determine the relative signal enhancement, is defined to equal the intensity of the scattered field which is observed outside of the target position in case the optimized wavefront is applied to the sample [102, 120]. In this work, in an equivalent approach the reference signal is evaluated from the signal which is detected at the target but with a set of random binary wavefronts whose parameters match those of the optimized wavefront applied to the sample (compare Sec. 7.5). On average, only half of the wavefront segments are switched on in case of random wavefront illumination, on the other hand. Compared to sample illumination with the full beam, as implemented with the phase conjugation algorithm which is discussed in the previous Chapter, the reference intensity is reduced by approximately 50 % [120] and the relative amplitude enhancement expected from binary wavefront shaping, thus, reads only $\sqrt{N/(4\pi)}$.

For a quantitative comparison to phase-only wavefront optimization, the relative signal enhancement is calculated by using the average signal received with a set of random phase-only wavefronts as reference, instead as random binary wavefronts (Fig. 8.5(b)). This reference amplitude is illustrated in Fig. 7.5(c) and was used to calculate the signal enhancement achieved with the phase conjugation algorithm, as well. The resulting data is presented in Fig. 8.5(c) for the segment superposition algorithm and in Fig. 8.5(d) for the mode superposition approach. In addition, the theoretically expected value which reads $\sqrt{N/(4\pi)}$ is illustrated. The segment superposition algorithm is found to perform slightly better compared to the expectation. The mode superposition algorithm, on the other hand, performs significantly worse. This behaviour is expected since the mode superposition approach utilizes a thresholding operation to approximate the optimal wavefront with a binary amplitude pattern (Sec. 8.2.2). In contrast, no such approximation is used with the segment superposition algorithm (Sec. 8.2.3).

Both approaches are found to perform worse compared to phase-only modulation (Fig. 7.5(d)). The phase conjugation algorithm, for example, yields a signal enhancement of approximately 10 dB with a set of 128 modes (Fig. 7.5(d)). With binary amplitude modulation, a comparable enhancement requires to use a set of 1024 modes (Fig. 8.5(c)). The expected signal enhancement reads $\sqrt{N/(4\pi)}$ for binary wavefront control and $\sqrt{0.78\,N}$ for phase-only wavefront control (Sec. 7.5). As a consequence, binary wavefront manipulation yields a signal enhancement which is 4.95 dB lower than the value which is expected for phase-only modulation with the same number of modes.

Considering the slope of the signal enhancement to be 5 dB per decade, which results from the enhancement being proportional to $\sqrt{N}$, binary amplitude control requires to use approximately ten times as many modes to yield an amplitude enhancement which is comparable to phase-only wavefront optimization.

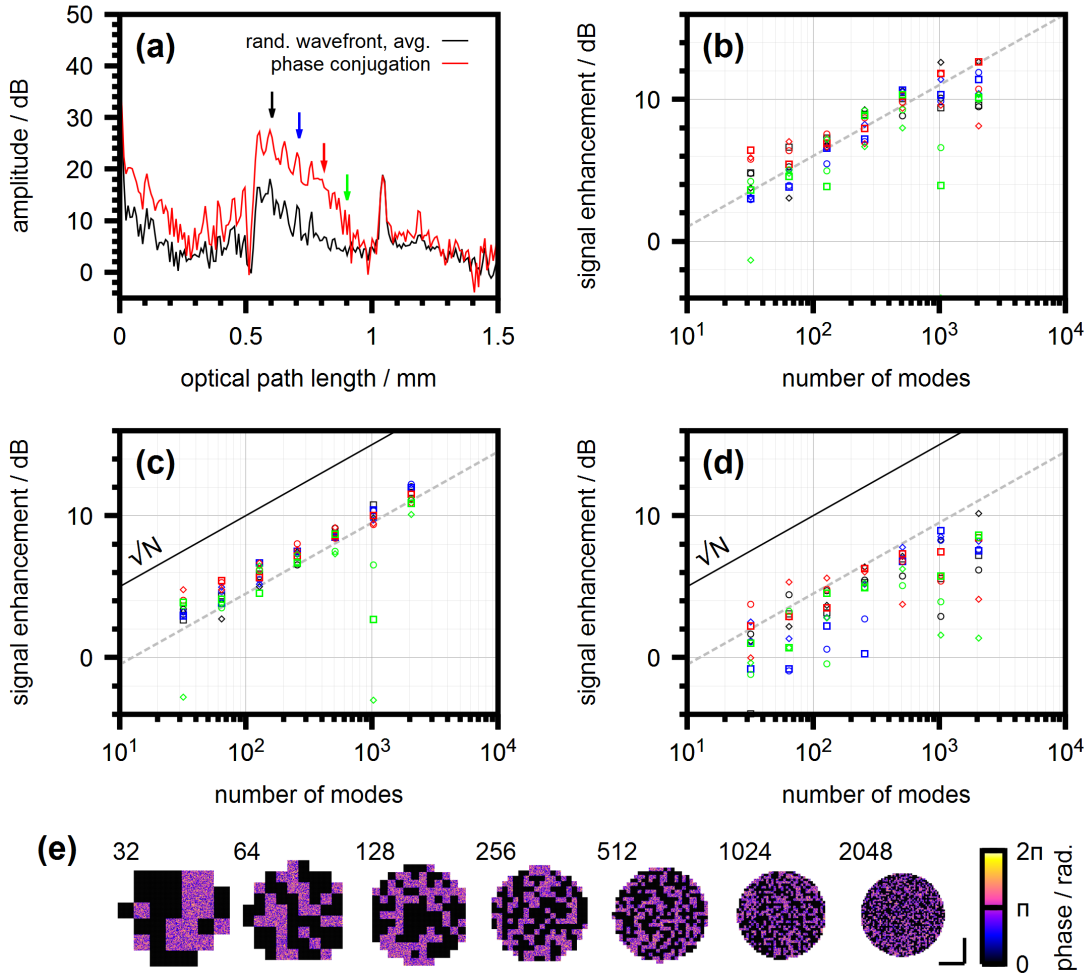

Figure 8.5: **Quantitative signal enhancement with binary amplitude-only wavefront modulation.** (a) Optimized A-scan acquired with the segment superposition algorithm for a set of $N = 1024$ modes. The target depths at which the signal enhancement is evaluated are marked by arrows. (b) Relative enhancement of the OCT signal amplitude compared to sample illumination with a random binary wavefront. The enhancement is evaluated at the targets marked in Panel (a) (○) and at the next signal pixels to the left (□) and to the right (◇), respectively. Dashed line: $\sqrt{N/(2\pi)}$. (c) Relative amplitude enhancement compared to sample illumination with a random phase-only wavefront (Fig. 7.5(c)). Dashed line: $\sqrt{N/(4\pi)}$. (d) Same as Panel (c) with wavefront optimized by the mode superposition algorithm. (e) Optimized phase patterns calculated by the segment superposition algorithm for signal enhancement at the second target (blue arrow). Scalebar 1 mm.

9 Imaging Applications

9.1 Principles

The methods which are presented in Chapter 7 and 8 enable the acquisition of A-scans which are optimized at the full axial field of view of the OCT system. The approach is illustrated with the pseudocode presented in Fig. 9.1. For each A-scan, the reflection matrix is captured once. Subsequent phase conjugation (Chap. 7) or binary wavefront optimization (Chap. 8) allows to enhance the amplitude of the OCT signal which is received at a selected target time-of-flight. Similar to the technique presented by Jang et al. [26, 27] a fully optimized A-scan is acquired by point-optimizing the signal at different depths and stitching the scan from the in-target amplitude of the respective point-optimized signals. On the other hand, the field which is scattered at the sample quickly decorrelates in case the sample beam is moved (Sec. 6.2). Wavefront shaping, hence, allows to enhance the OCT signal only close to the lateral position at which the reflection matrix was acquired. As a consequence, for cross-sectional or volume imaging the process needs to be repeated at each lateral scan position anew, including the acquisition of the reflection matrix once per A-scan (compare [27]).

Full image enhancement based on the algorithm is demonstrated with a scattering phantom consisting of iterating layers of pergamin paper (*Whatman 2122*, GE Healthcare, United Kingdom) and cover glass slides (*CG15CH2*, Thorlabs, United States). Figure 9.2(a) presents a conventional B-scan. The sample is tilted with respect to the optical axis and aligned such that mutual interference and mirror signals overlap. As a consequence, the morphology of the sample is not easily determined from the scan. Figure 9.2(b) presents a scan which is acquired with the compounding algorithm presented in Sec. 7.2.3. The data corresponds to the average signal amplitude received from sample illumination with a random phase-only wavefront. Speckle noise is reduced and deeper layers of the sample are visible. Figure 9.2(c) illustrates the signal which is acquired with wavefront optimization. Phase-only wavefront control and the phase conjugation algorithm presented in Chap. 7 are used. The approach features an improved performance compared to binary amplitude-only wavefront modulation (Chap. 8). The mutual interference signal, which yields an unambiguous image of the sample morphology, is observed to be enhanced with the phase conjugation algorithm. Image artefacts, on the other hand, are present in the image but are not enhanced (compare Sec. 7.4).

The effect can be exploited to additionally suppress image artefacts in post-processing. The amplitude of signal components which are not affected by phase conjugation is estimated from the 95-th percentile of the amplitude of the individual columns of the reflection matrix (compare Figs. 7.1(b), 7.2(b) and 7.4(b)). Similar to the compounding algorithm (Sec. 7.2.3) this data corresponds to the maximal signal amplitude which is

```
for l = 1 to numberLateralScanPositions
    // for each A-scan
    move sample beam to lateral scan position

    // acquire reflection matrix
    for n = 1 to numberModes
        apply phase pattern corresponding to n-th mode to SLM
        acquire raw spectrum
        interpolate spectrum to linear wavenumber grid
        calculate SD-OCT signal from complex IFFT
        save conjugate signal to n-th column of reflection matrix
    end

    // acquire optimized A-scan
    initialise optimized A-scan with NaN values
    for m = 1 to numberOptimizedPixel
        // capture point-optimized OCT signal
        apply phase pattern for focusing at m-th pixel to the SLM
        acquire raw spectrum
        interpolate spectrum to linear wavenumber grid
        calculate SD-OCT signal from complex IFFT of spectrum
        // stitch fully-optimized scan
        save m-th pixel of SD-OCT signal to m-th pixel of the
        optimized A-scan
    end
end
```

Figure 9.1: **Pseudocode for SD-OCT imaging based on phase conjugation with the time-resolved reflection matrix.** Comments are marked red.

expected in case of sample illumination with a random wavefront. This background data is then subtracted from the image which is retrieved with the wavefront optimization algorithm. The result is illustrated in Fig. 9.2(d). Residual artefacts are suppressed and a clear sample image is gained. Some dark spots result at those positions where the amplitude of image artefacts is overestimated by the algorithm, though.

9.2 Impact of phase conjugation on imaging

As is evident from Fig. 9.2, phase conjugation yields a significant amplitude enhancement with the signal received from the sample. The signal which is received from depths between the individual strongly reflecting layers is enhanced as well, on the other hand. These positions correspond to the bulk-volume of the cover glass slides from which no reflection is expected. The observed signal, hence, is considered to result from light

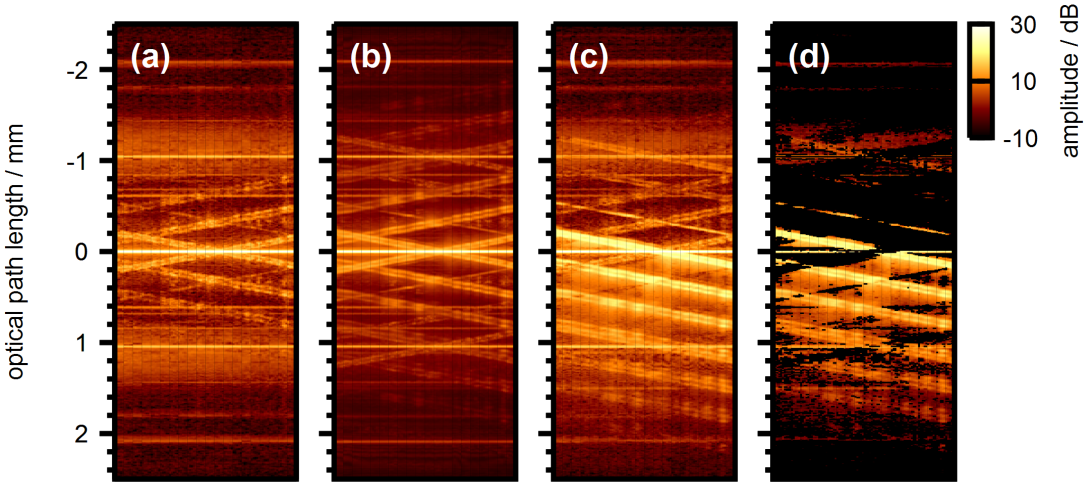

Figure 9.2: **Application of phase conjugation to imaging.** (a) Conventional OCT scan taken at a layered sample. (b) Image captured with the compounding algorithm. (c) Scan acquired with phase conjugation. Number of modes $N = 256$. (d) Phase conjugation with additional artefact suppression. Image adapted from [186].

which is multiple scattered at the previous sample layers and whose optical path length does not match the actual penetration depth in the sample.

OCT imaging is based on the suppression of multiple scattered light, which yields a diffusive time-of-flight distribution, compared to single- or weakly scattered light whose time-of-flight is correlated to the position of reflecting sample structures. No benefit for depth enhanced imaging results if both signal contributions are equally enhanced. The signal-to-noise ratio of the data presented in Fig. 9.2 is estimated by taking the average of the six rightmost A-scans (Fig. 9.2 Panels (b) and (c)) and fitting a third-order polynomial to the signal baseline. The resulting data is illustrated in Fig. 9.3. The SNR correspond to the peak-to-valley distance of the respective scans and is observed to be increased by about 4 dB with phase conjugation compared to speckle compounding. As a consequence, the OCT signal which is received from the sixth interface of the scattering phantom is clearly visibly with the signal captured with the phase conjugation algorithm (Fig. 9.2(c)), but not with the compounding algorithm (Fig. 9.2(b)).

Finally, the approach is demonstrated with biological tissue. Figure 9.4 presents imaging with a sample cut from a food-quality chicken thigh. The conventional OCT signal (Fig. 9.4(a)) is subject to strong speckle which appear to be rather coarse due to the large lateral step width which is chosen to be 20 µm for the presented data. As a consequence, the lower boundary of the epidermis is not clearly visible, even though avian skin is rather thin compared to that of mammals [195], and the tissue morphology is not evident from the OCT signal. With the compounding algorithm (Fig. 9.4(b)), speckle are reduced and the boundary between the epidermis and the dermis becomes visible at a depth of about 1.1 mm as well as some structures which are located deeper in the

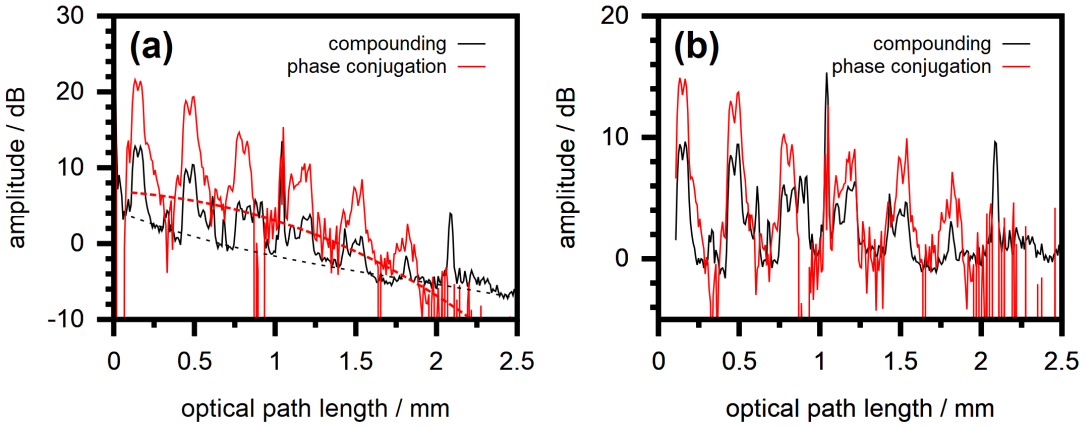

Figure 9.3: **SNR estimation of the enhanced OCT signal.** (a) Average of the six right-most A-scans in Fig. 9.2 Panels (b) and (d). Fitted baselines are illustrated by dashed lines. (b) Baseline-subtracted signals. Image adapted from [186].

dermis. The epidermis produces a stronger OCT signal and, hence, the position of the dermal-epidermal junction is also evident from the single A-scan illustrated in Panel (e). Figure 9.4(c) illustrates the image which is captured with the phase conjugation algorithm. To better estimate the SNR, the amplitude color-scale is chosen to cover the same dynamic range of 30 dB which is used for Panels (a) and (b), as well. With the phase conjugation algorithm the signal amplitude received from backscattering sample structures such as the epidermis is enhanced. This effect is also evident from the single A-scan illustrated in Panel (e). An increased image contrast compared to the compounding algorithm (Fig. 9.4(b)) and, hence, a better SNR is observed. Furthermore, considering Panel (c), the phase conjugation algorithm is found to reduce the speckle contrast similar to the compounding algorithm. This effect is not surprising, though. Speckle result from interference of uncontrolled waves which are randomly backscattered to the detector. The phase conjugation algorithm stitches the OCT image from a set of scans which are optimized for signal enhancement, i.e. for constructive interference of the backscattered field, at each voxel of the OCT scan individually. The image which is received with the phase conjugation algorithm, hence, can be considered to be constructed from bright speckles only.

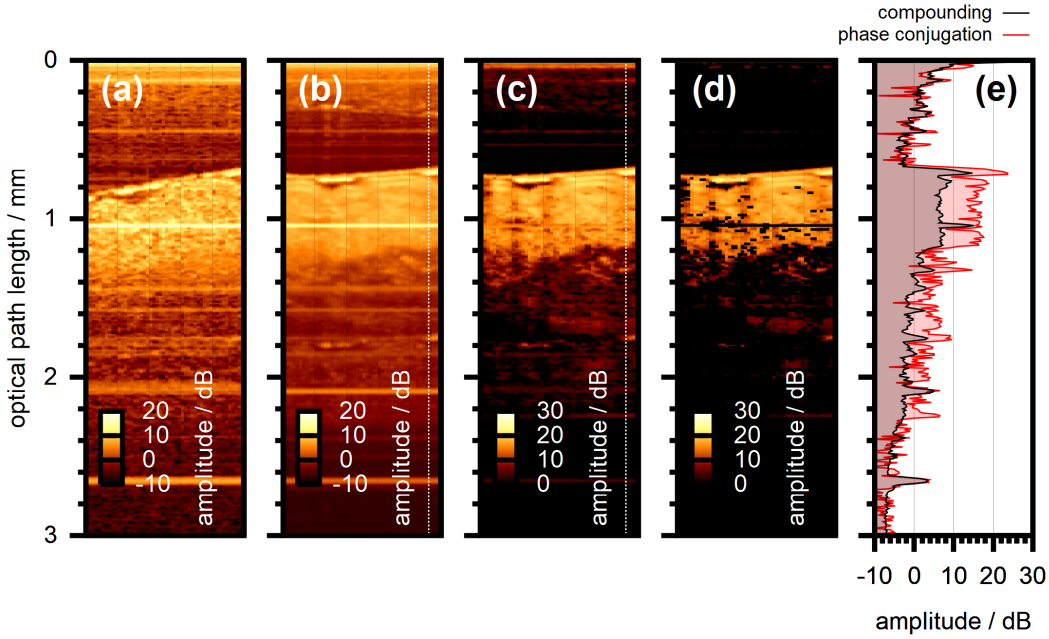

Figure 9.4: **Phase conjugation with biological tissue.** (a) Conventional OCT scan. (b) Image captured with the compounding algorithm. (c) Scan acquired with phase conjugation. Number of modes $N = 256$. (d) Phase conjugation with additional artefact suppression. (e) Amplitude of the two A-scans marked by the dashed line in Panel (b) and (c), respectively. The amplitude color-scale corresponds to the same dynamic range of 30 dB for all scans. Panels (a) to (d) adapted from [186].

10 Discussion

10.1 Double interferometer OCT design

The experimental part of this work is based on a double interferometer OCT design which is presented in Chap. 5. The design was analytically, numerically and experimentally demonstrated to be capable of independent phase manipulation at the reference and sample beam of the OCT system, respectively. This capability was used to implement phase-shifting algorithms to suppress SD-OCT image artefacts (Sec. 2.2.3) for the data presented in Chap. 6 and in Sec. 7.3. The one dimensional analytic model which is presented in Sec. 5.4 to analyse the OCT design does not cover the effects of spatial wavefront shaping since lateral beam propagation is neglected. The experimental data shown in this work, especially the data presented in Chap. 6, supports the claim that the reference and sample beam, indeed, can be shaped independently, on the other hand.

OCT imaging can benefit from a number of different approaches for wavefront shaping at the sample beam. Some of them are presented in this work, others include adaptive optics [84, 90, 91, 185], Bessel beam illumination to enhance the penetration depth [196, 197], or multi beam illumination to enhance the frame rate of the OCT system. In general, the reference beam needs to be efficiently coupled to the detector as well and, hence, the reference beam should be adapted to the illumination scheme. With the design presented in this work, multiple illumination schemes can be applied to the reference and the sample beam, respectively, and can be digitally switched.

In contrast to conventional SD-OCT designs, the amplitude of autocorrelation artefacts is enhanced two-fold with the double interferometer design presented in this work (Sec. 5.4). On the other hand, the simplified experimental design yields a major benefit compared to a Mach-Zehnder setup, which too enables independent beam shaping (Sec. 4.1). Compared to a conventional OCT interferometer only the source arm needs to be modified. Beam shaping, thus, can be implemented with existing SD-OCT systems by making only minor modifications to existing free space scanners, similar to the concept illustrated in Fig. 10.1. In this case, the imaging system does not need to be fully re-designed and already implemented (high-speed) data acquisition and data processing algorithms of the existing OCT system can be utilized.

10.2 Acquisition speed and improvements

The acquisition of a single A-scan optimized with the phase conjugation algorithm took approximately four minutes for the data presented in Fig. 9.4. The reflection matrix was acquired for a set of $N = 256$ modes and each A-scan was stitched from a set of 377

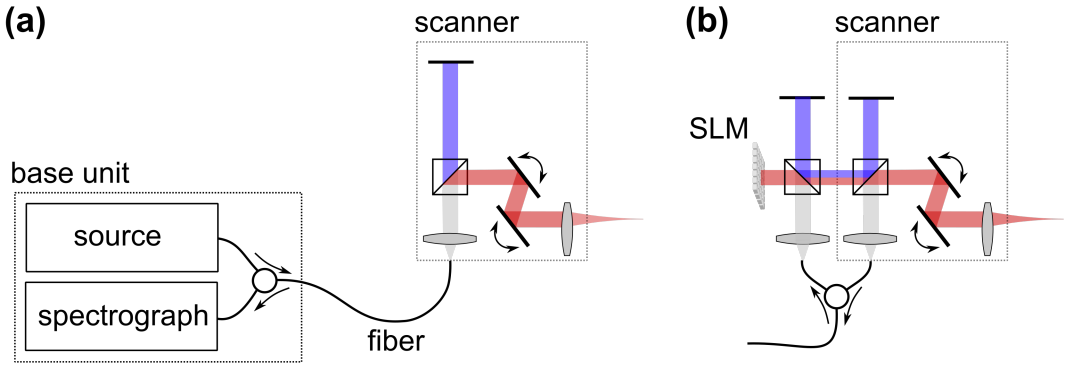

Figure 10.1: **Double interferometer design implemented with a commercial SD-OCT system.** (a) Conventional SD-OCT system consisting of a base unit (e.g. *TEL320*, Thorlabs, United States) and a scanner which contains the reference and sample beam optics (e.g. *OCTP-1300/M*, Thorlabs, United States). (b) Scanner modified for independent wavefront shaping at the sample beam, similar to the setup used in this work (Fig. 5.1).

point-optimized scans (compare, for example, Fig. 7.4). As a consequence, each A-scan required a set of 633 acquisitions in total, whereas different phase patterns need to be applied to the SLM, respectively.

Even though the approaches presented in Chapter 7 and 8 are significantly faster compared to iterative wavefront shaping (Sec. 6.4), an acquisition time of several minutes for a single A-scan does not allow to apply the technique to image large samples within a reasonable time. Furthermore, as discussed in Sec. 3.3.4, the field which is scattered at living biological tissue is observed to decorrelate within milliseconds due to macroscopic tissue movement, blood flow and cellular movement [101–103, 112]. As a consequence, the acquisition of the reflection matrix and subsequent phase conjugation need to be completed within a comparable time span.

On the other hand, the acquisition speed is mostly limited by technical constraints of the experimental design, such as the low frame rate of the SLM (compare Sec. 5.2.4). The imaging algorithms which are presented in Chaps. 7 and 8 are divided in two steps: The measurement of the time-resolved reflection matrix and the subsequent acquisition of the enhanced OCT signal based on the matrix (compare Fig. 9.1). Approaches to increase the speed of both steps are discussed.

10.2.1 Reflection matrix acquisition

The reflection matrix probes the optical response of a scattering sample in case of illumination with a set of different wavefronts. As a consequence, the time required to capture the reflection matrix is proportional to N, where N is the number of degrees of freedom of the incident field or the number of independent modes. In general, phase conjugation is expected to become more effective with increasing number N (compare

Secs. 7.5 and 8.5). On the other hand, even with a rather low number of modes in the order of 100 the amplitude of the OCT signal can already be increased approximately ten-fold with the phase conjugation algorithm (Sec. 7.5).

In general, one wants to capture the reflection matrix for as many modes as possible within a short amount of time. The acquisition time per mode depends on the number of measurements required to determine the complex-valued signal which is resulting from sample illumination with a single mode. In case the matrix is directly captured from the conventional SD-OCT signal, as presented in Chapter 7 and 8, only a single acquisition of the corresponding spectral raw data is required [30]. In principle, the reflection matrix cannot be determined faster than that. The approach reduces the number of measurements 25-fold compared to the algorithm presented by Jang et al. [26–29] who used an approach similar to phase conjugation and who presented the only application to direct OCT image enhancement, comparable to the techniques presented in this work, which is reported to date.

The acquisition time of the reflection matrix is also proportional to the time which is required to update the wavefront which is incident to the sample and to capture the resulting OCT signal. The OCT system and the data processing which is used in this work is optimized for a high versatility rather than for a high acquisition speed. Contemporary commercial SD-OCT systems can achieve A-scan rates well above 100 kHz, though. The speed of wavefront control is determined by the frame rate of the spatial light modulator. The approaches presented in this work are based on phase-only wavefront modulation. High-speed phase modulation can be implemented with micro-electro-mechanical systems such as deformable or segmented mirrors [105, 133, 137, 159, 198, 199]. Furthermore, holographic approaches can be used to implement phase-only wavefront modulation with fast amplitude-only SLMs such as digital micromirror devices, similar to the approach presented by Conkey et al. [194]. The algorithms which are presented in Chap. 8 require binary amplitude-only wavefront control and can directly be implemented with DMDs.

Finally, I would like to point out that the time-resolved reflection matrix probes the dependence of the OCT signal on the incident wavefront accurately at the complete field of view of the OCT system as long as the sample beam is not displaced or scanned. With the system presented in this work, the FOV corresponds to a single line scan perpendicular to the sample surface. The FOV can easily be extended by implementing a multi-beam acquisition, for example by using the SLM to split the sample and the reference beam, respectively, and by using a linear fibre bundle to couple the respective back-scattered beams to the spectrograph. The acquisition of the reflection matrix and phase conjugation can be conducted at each beam in parallel and, hence, the total time required to capture an optimized B-scan is reduced. Alternatively, the reflection matrix can be acquired with a FF-OCT system, as discussed in Sec. 4.2. In this case the FOV for which the reflection matrix remains valid corresponds to a plane parallel to the sample surface. Similarly, a line-field SD-OCT or SS-OCT system can be utilized which probes a plane perpendicular to the sample surface [30, 200]. Ultimately, a full-field SS-OCT system may be used to probe the whole sample volume at once [201]. The observations which are made for a conventional SD-OCT system in this work are expected to hold for

line-field and full-field SS-OCT systems, as well. The approach can significantly speed up the imaging process since the sample does not need to be scanned for imaging and, thus, the reflection matrix does not need to be reacquired at each lateral image position. On the other hand, large datasets have to be dealt with and the implementation of efficient real-time data processing may prove to be challenging.

10.2.2 Image acquisition

The image acquisition algorithm presented in this work uses wavefront optimization to acquire a set of point-optimized scans. A fully-optimized scan is stitched from these signals, similar to the approach presented by Jang et al. [26–29] (compare Fig. 9.1). As a consequence, for each voxel of the optimized image a single OCT signal needs to be acquired with individually optimized wavefront applied to the sample beam, respectively. The time required to capture the image, thus, depends on the frame rates of the OCT system and the SLM, which is discussed in the previous Section, and is proportional to the number of image voxels. The latter can be reduced by either cropping the field of view or by reducing the spatial resolution of the scan. Neither approach is beneficial for imaging, though.

Alternatively, the phase conjugation algorithm may be used to enhance the signal at multiple voxels simultaneously. The approach is presented in Sec. 7.6. Enhancing the signal at two voxels at the same time, for example, already yields a two-fold reduction of the number of acquisitions which are required to capture an optimized image. The amplitude enhancement which is expected in case of phase conjugation with an extended target is expected to drop, though [118] (Secs. 7.5 and 7.6). On the other hand, the sample‘s reflectivity profile and the resulting OCT signal are not uniform. The phase conjugation algorithm, thus, is expected to predominantly enhance the signal which is received from strongly reflecting layers placed in the extended target, resulting in an increased image contrast. Further experimental verification is required, though.

Alternatively, a singular value decomposition of the reflection matrix may be used to identify phase patterns which enable focusing at dominant backscattering sample features [137, 140, 143, 144, 148] (Sec. 3.4.4). An OCT image can directly be acquired from the corresponding eigenvalues [143], in which case no additional signal acquisition is necessary once the reflection matrix is captured, or from the OCT signal which is measured once the incident beam is focused to the dominant sample features. The number of additional signal acquisitions corresponds to the number of dominant eigenvalues in the latter case. The approach was successfully demonstrated with FF-OCT systems (Sec. 4.2). The application to SD-OCT is not yet reported and requires further careful analysis, though.

10.3 Comparison of phase-only and binary amplitude-only wavefront control

The acquisition of the time-resolved reflection matrix and subsequent phase conjugation is shown to selectively enhance the OCT signal in Chap. 7. The approach was originally demonstrated by Choi et al. [30]. In addition to the previous work, an analytic framework on how the time-resolved reflection matrix relates to the complex-valued SD-OCT signal is presented (Sec. 7.1). From this, the technique is originally shown to locally enhance the OCT signal but not image artefacts, even though artefacts are not actively suppressed (Sec. 7.4). Furthermore, applications for direct OCT image enhancement are presented in Chap. 9 for the first time.

In Chap. 8 the acquisition of the time-resolved reflection matrix and subsequent wavefront optimization is originally demonstrated based on binary amplitude-only beam shaping. The mode superposition approach presented in Sec. 8.2 can directly be compared to the iterative wavefront shaping algorithm which was demonstrated by Jang et al. [26–29]. The group demonstrated the only application of wavefront shaping for direct OCT image enhancement and for depth enhanced imaging, comparable to this work, which is reported to date. In contrast to the algorithm presented by Jang et al., binary wavefront optimization based on the time-resolved reflection matrix reduces the number of signal acquisitions required to find an optimal wavefront which selectively enhances the OCT signal 25-fold.

OCT signal enhancement based on phase-only wavefront shaping (Chap. 7) is shown to outperform binary amplitude-only wavefront shaping (Chap. 8) in a number of aspects in this work. In contrast to binary wavefront shaping, phase conjugation enhances the mutual interference OCT signal only, but not mirror and autocorrelation artefacts (Sec. 7.4). The effect can be used to enhance the OCT signal and to suppress image artefacts in post-processing without additional signal acquisitions and without phase shifting approaches (Chap. 9). Furthermore, the amplitude enhancement which is expected with phase-only modulation is approximately 5 dB higher compared to binary wavefront shaping with the same number of modes (Sec. 8.5).

As a major benefit, binary amplitude-only wavefront shaping can directly be implemented with digital micromirror devices which enable high-speed and high-resolution beam shaping. On the other hand, binary wavefront shaping requires approximately ten-times as many signal acquisitions to yield the amplitude enhancement which is achieved with phase-only wavefront control (Sec. 8.5) and, thus, the speed advantage is partially eaten up. Furthermore, phase only wavefront control can be implemented with DMDs as well, for example by using the DMD to apply a binary amplitude hologram which creates the desired phase pattern from diffracted light [194]. The approach requires a more sophisticated experimental design, though, and a stronger light source since only a part of the diffracted light (e.g. the first diffraction order [194]) can be used.

10.4 Depth enhanced imaging

This work demonstrates wavefront shaping techniques to be able to significantly enhance the signal amplitude which is detected with a SD-OCT system from a scattering sample. This result aligns well with previous observations [26–30]. To date, imaging applications are demonstrated with binary amplitude modulation only [27–29]. The approach is comparable to the mode superposition algorithm presented in Chap. 8. The techniques which are demonstrated in this work feature a number of improvements compared to the previous approach which are relevant for imaging.

The mode superposition algorithm which is presented in Sec. 8.2.2 requires a significantly reduced number of measurements compared to previous works [26–29] (Sec. 10.2.1). The segment superposition approach presented in Sec. 8.2.3 is further shown to yield a higher signal enhancement compared to mode superposition (Sec. 8.5) and phase-only wavefront optimization (Chap. 7) is demonstrated to outperform both binary amplitude-only wavefront shaping approaches in this aspect. The effect of wavefront shaping on SD-OCT image artefacts is not yet discussed in literature. In this work, binary amplitude-only wavefront shaping is demonstrated to enhance the mutual interference OCT signal and image artefacts, as well (Sec. 8.4). In contrast, phase-only wavefront shaping is shown to affect the mutual interference OCT signal, which reflects the sample structure, only (Sec. 7.4). Furthermore, phase conjugation is demonstrated to reduce the speckle contrast of the OCT signal similar to a compounding algorithm (Chap. 9). This effect is not yet demonstrated in literature. Altogether, the approaches presented in this work are expected to perform better compared to previous wavefront shaping techniques which were demonstrated for direct OCT signal enhancement [26–29]. First applications which are given in Chap. 9 yield substantially improved OCT images compared to these works.

Yu et al. demonstrated wavefront shaping to extend the penetration depth of OCT systems with scattering media [27]. The group estimated the penetration depth by fitting an exponential function to the OCT signal received from a scattering sample and by determining the depth at which the exponential fit drops below the noise threshold [27]. Considering this criterion, the phase conjugation algorithm presented in this work is expected to yield a greater increase in penetration depth due to the improved signal enhancement compared to binary amplitude-only wavefront shaping. On the other hand, the OCT image contrast is determined by the suppression of multiple scattered light compared to weakly scattered light. As demonstrated in Chap. 9, wavefront optimization is observed to enhance the amplitude of multiple scattered light as well and, hence, no benefit for depth enhanced imaging results if both signal contributions are enhanced by the same amount. The effect is not yet discussed in literature and the criterion which is used by Yu et al. to determine the penetration depth of the OCT system does not address this problem [27].

Depth enhanced OCT imaging is enabled in case the signal, which is resulting from weakly scattered light detected from strongly reflecting sample features, is enhanced more strongly than diffusively multiple scattered light. This effect can in principle be enabled since wavefront optimization couples light to dominant eigenchannels of the

scattering sample which correspond to reflections at dominant reflecting layers [144, 160, 161]. The effect is discussed in Sec. 4.4.2 in detail. This behaviour is not yet verified for SD-OCT imaging and requires further careful analysis, though. Furthermore, as discussed in Sec. 7.5, phase conjugation is expected to enhance light which is detected from a narrow time-of-flight window more strongly than light detected from a wide time-of-flight range. In principle, the different time-of-flight statistics of weakly and strongly multiple scattered light can be exploited to enhance the SD-OCT image contrast. The approach should be evaluated in future studies.

First imaging applications which are presented in Chap. 9 demonstrate phase conjugation to indeed yield an enhanced image contrast, or signal-to-noise ratio, with scattering media. This work focuses on algorithms and principle effects of wavefront shaping applied to optical coherence tomography, though. The experimental system which is used has a high versatility to enable the presented proof-of-concept experiments, but is too slow to enable a quantitative study with a large number of samples. Further quantitative analysis, hence, should be conducted with an enhanced experimental design which is based on the approaches demonstrated in this work and on the concepts discussed in Secs. 10.1 and 10.2.

10.5 Applications and outlook

The techniques which are presented in this work can directly be used to enhance the signal amplitude when imaging scattering media with SD-OCT systems. For practical applications the acquisition speed needs to be enhanced, though. In the next step the double interferometer OCT design which is presented in this work should be realized within a commercial SD-OCT system which already incorporates data acquisition and data processing algorithms which are sufficiently fast for real-time *in-vivo* OCT imaging (compare Fig. 10.1). The crucial aspect of the approach is the implementation of high-speed wavefront manipulation which needs to synchronized to the acquisition of the OCT signal. Phase-only wavefront manipulation should be implemented with holographic techniques and with a high-resolution DMD [194]. In principle, full-complex wavefront control can be realized with this approach, as well [194], and yields a further increased signal enhancement compared to phase-only control [119]. The algorithms which are presented in this work can directly be applied to such a system. First proof-of-concept imaging approaches presented in Chap. 9 yield promising results for depth enhanced imaging with scattering biological tissue and should be further validated with the high-speed system.

The OCT signal which is detected from a certain depth is to some extend related to the amplitude of light which is backscattered from the corresponding position in the sample, depending on whether the OCT signal is dominated by weakly scattered or by strongly multiple scattered light. Using phase conjugation to selectively enhance the OCT signal which is received from a small target, thus, can selectively and non-invasively focus light to that position. The approach was demonstrated experimentally by Fiolka et al. [25] and is discussed in detail in Sec. 4.4.2. Applications of non-invasive focusing in scattering

media such as biological tissue include, for example, optogenetics or phototherapy and can be combined with OCT imaging to locate the target structures for focusing.

Multimodal imaging approaches which require focusing at the sample can benefit from OCT-based phase conjugation, as well. Adding, for example, a monochromatic light-source to the SD-OCT system allows to use the setup for confocal Raman imaging and to investigate the sample‘s chemical structure. OCT imaging can be used to investigate the sample morphology and to identify points of interest, for example pathological tissue structures. OCT-based phase conjugation finds an optimized wavefront which couples light backscattered from the target structure more efficiently to the detector. Subsequent switching to the monochromatic source can allow to selectively couple Raman-shifted light which is backscattered from the target to the detector, as well. The approach, thus, enables the selective investigation of the sample‘s chemical structure at the target and can be used for applications such as non-invasive deep-tissue diagnostics.

11 Conclusion

In this work the combination of wavefront shaping and spectral domain optical coherence tomography is demonstrated. Wavefront shaping techniques try to manipulate the beam which is incident to a scattering sample such that constructive interference at the detector is created from scattered light. Applied to OCT imaging, the technique allows to focus light which is backscattered at a given time-of-flight to the detector, resulting in the amplitude of the OCT signal to be increased.

Wavefront manipulation is demonstrated with a double-interferometer SD-OCT design which includes a spatial light modulator for beam shaping to the first interferometer. The experimental system is shown to enable independent phase shifting and beam shaping at the reference and at the sample beam, respectively. In contrast to comparable approaches, such as a Mach-Zehnder OCT design, the setup is rather compact and requires to modify the optical elements at the source path only compared to a conventional (single interferometer) free space SD-OCT system or OCT scanner.

In a first application, iterative wavefront shaping is demonstrated. The approach is based on an iterative algorithm which optimizes the phase pattern applied to the sample beam such that the amplitude of the OCT signal detected at an arbitrarily chosen target time-of-flight is enhanced. The approach is experimentally robust but requires a rather long optimization time. The resulting signal enhancement is observed to be limited only to the target time-of-flight and to the lateral position of the sample beam for which the wavefront is optimized. Signal enhancement at another axial or lateral target position requires to repeat the optimization process.

In a more sophisticated approach, the acquisition of the time-resolved reflection matrix is demonstrated. The reflection matrix describes the linear dependence of the complex-valued time-of-flight-resolved backscattered field, which is the detected OCT signal, on the field which is applied to the sample beam. Phase conjugation based on the reflection matrix allows to find an optimized wavefront which locally enhances the OCT signal at an arbitrarily chosen position within the observed field of view. The approach, hence, is comparable to iterative wavefront optimization but allows to substantially increase the acquisition speed. The technique was initially demonstrated by Choi et al. [30], but a detailed discussion on how the matrix relates to the SD-OCT signal and on the impact of image artefacts which are detected with SD-OCT systems had not yet been reported. In this work, such an analytic model is developed. Based on the model, the phase conjugation algorithm is shown to enhance the OCT signal, but not image artefacts. The result is verified experimentally.

Acquisition time is critical in case the technique is applied to *in-vivo* imaging. Hence, the acquisition of the time-resolved reflection matrix and subsequent wavefront optimization is demonstrated for the first time based on binary amplitude-only wavefront

manipulation. The presented algorithm is comparable to previous iterative wavefront shaping approaches [26] but requires a significantly reduced number of signal acquisitions to find an optimized wavefront. Wavefront manipulation is based on an on/off modulation of individual segments of the sample beam. The technique, thus, can be implemented with fast micro-electro-mechanical systems such as digital micromirror devices. On the other hand and in contrast to the presented phase-conjugation algorithm, binary amplitude-only wavefront optimization is found to enhance the amplitude of OCT image artefacts, as well. Furthermore, the approach requires to control approximately ten times as many modes at the sample beam to yield an overall signal enhancement which is comparable to the effect of phase-only wavefront shaping.

Finally, first imaging applications are presented. Similar to previous works based on iterative wavefront optimization [27], the phase conjugation algorithm is utilized to directly enhance the amplitude of the SD-OCT signal which is captured from a scattering sample. Since image artefacts are not enhanced, these artefacts can be suppressed in post-processing without further signal acquisition. Phase conjugation is demonstrated to enhance the signal-to-noise ratio and the penetration depth when imaging turbid media such as biological tissue. In addition, the approach is shown to reduce the observed speckle contrast, similar to compounding algorithms.

Previous works demonstrated iterative wavefront shaping techniques to enhance the penetration depth of OCT systems when imaging scattering media and biological tissue [26–29]. The algorithms which are presented in this work perform substantially better in terms of the required number of measurements, i.e. the acquisition speed, and in terms of the achieved signal enhancement compared to the iterative approach.

Depth enhanced OCT imaging can increase the utility of non-invasive OCT imaging for medical diagnostics. When investigating samples such as the human skin, for example, structures of interest such as lesions and pathological tissue changes can easily extend beyond the penetration depth of a conventional OCT system, effectively rendering the system useless for diagnostic purposes. Wavefront shaping approaches can help to increase the penetration depth and the SNR when investigating such samples and first imaging applications yield promising results in this context. The major challenge which needs to be addressed to apply the technique to *in-vivo* imaging is the required acquisition time, though. The experimental approach which is demonstrated in this work can be implemented with modifications of commercial (high-speed) SD-OCT systems and with high-speed wavefront manipulation enabled by micro-electro-mechanical systems. The presented algorithms, in principle, require a minimal number of measurements to find an optimal wavefront at the sample beam and can directly be used with such a system. It can, thus, be expected that the presented approaches provide valuable tools for future deep-tissue OCT imaging and for non-invasive medical diagnostics.

References

[1] D. Huang, E. A. Swanson, C. P. Lin, J. S. Schuman, W. G. Stinson, W. Chang, M. R. Hee, T. Flotte, K. Gregory, C. A. Puliafito, and J. G. Fujimoto, "Optical coherence tomography", Science **254**, 1178–1181 (1991).

[2] A. M. Zysk, F. T. Nguyen, A. L. Oldenburg, D. L. Marks, and S. A. Boppart, "Optical coherence tomography: a review of clinical development from bench to bedside", Journal of Biomedical Optics **12**, 051403 (2007).

[3] L. M. Sakata, J. Deleon-Ortega, V. Sakata, and C. A. Girkin, "Optical coherence tomography of the retina and optic nerve - a review", Clinical & Experimental Ophthalmology **37**, 90–99 (2009).

[4] W. Geitzenauer, C. K. Hitzenberger, and U. M. Schmidt-Erfurth, "Retinal optical coherence tomography: past, present and future perspectives", The British Journal of Ophthalmology **95**, 171–177 (2011).

[5] S. Brand, J. M. Poneros, B. E. Bouma, G. J. Tearney, C. C. Compton, and N. S. Nishioka, "Optical coherence tomography in the gastrointestinal tract", Endoscopy **32**, 796–803 (2000).

[6] M. V. Sivak, K. Kobayashi, J. A. Izatt, A. M. Rollins, R. Ung-runyawee, A. Chak, R. C. K. Wong, G. A. Isenberg, and J. Willis, "High-resolution endoscopic imaging of the GI tract using optical coherence tomography", Gastrointestinal Endoscopy **51**, 474–479 (2000).

[7] F. Prati, E. Regar, G. S. Mintz, E. Arbustini, C. Di Mario, I.-K. Jang, T. Akasaka, M. Costa, G. Guagliumi, E. Grube, Y. Ozaki, F. Pinto, and P. W. J. Serruys, "Expert review document on methodology, terminology, and clinical applications of optical coherence tomography: physical principles, methodology of image acquisition, and clinical application for assessment of coronary arteries and atherosclerosis", European Heart Journal **31**, 401–415 (2010).

[8] H. G. Bezerra, M. A. Costa, G. Guagliumi, A. M. Rollins, and D. I. Simon, "Intracoronary optical coherence tomography: a comprehensive review", JACC: Cardiovascular Interventions **2**, 1035–1046 (2009).

[9] J. Welzel, "Optical coherence tomography in dermatology: a review", Skin Research and Technologty **7**, 1–9 (2001).

[10] M. C. Pierce, J. Strasswimmer, B. H. Park, B. Cense, and J. F. de Boer, "Advances in optical coherence tomography imaging for dermatology", Journal of Investigative Dermatology **123**, 458–463 (2004).

[11] E. Sattler, R. Kästle, and J. Welzel, "Optical coherence tomography in dermatology", Journal of Biomedical Optics **18**, 061224 (2013).

[12] J. Olsen, J. Holmes, and G. B. Jemec, "Advances in optical coherence tomography in dermatology - a review", Journal of Biomedical Optics **23**, 040901 (2018).

[13] B. W. Colston Jr., U. S. Sathyam, L. B. DaSilva, M. J. Everett, P. Stroeve, and L. L. Otis, "Dental OCT", Optics Express **3**, 230–238 (1998).

[14] Y.-S. Hsieh, Y.-C. Ho, S.-Y. Lee, C.-C. Chuang, J.-C. Tsai, K.-F. Lin, and C.-W. Sun, "Dental optical coherence tomography", Sensors **13**, 8928–8949 (2013).

[15] J. F. de Boer and T. E. Milner, "Review of polarization sensitive optical coherence tomography and Stokes vector determination", Journal of Biomedical Optics **7**, 359–371 (2002).

[16] J. F. de Boer, C. K. Hitzenberger, and Y. Yasuno, "Polarization sensitive optical coherence tomography - a review", Biomedical Optics Express **8**, 1838–1873 (2017).

[17] U. Morgner, W. Drexler, F. X. Kärtner, X. D. Li, C. Pitris, E. P. Ippen, and J. G. Fujimoto, "Spectroscopic optical coherence tomography", Optics Letters **25**, 111–113 (2000).

[18] D. J. Faber, E. G. Mik, M. C. G. Aalders, and T. G. van Leeuwen, "Light absorption of (oxy-)hemoglobin assessed by spectroscopic optical coherence tomography", Optics Letters **28**, 1436–1438 (2003).

[19] F. E. Robles, C. Wilson, G. Grant, and A. Wax, "Molecular imaging true-colour spectroscopic optical coherence tomography", Nature Photonics **5**, 744–747 (2011).

[20] M. S. Mahmud, D. W. Cadotte, B. Vuong, C. Sun, T. W. H. Luk, A. Mariampillai, and V. X. D. Yang, "Review of speckle and phase variance optical coherence tomography to visualize microvascular networks", Journal of Biomedical Optics **18**, 050901 (2013).

[21] R. A. Leitgeb, R. M. Werkmeister, C. Blatter, and L. Schmetterer, "Doppler optical coherence tomography", Progress in Retinal and Eye Research **41**, 26–43 (2014).

[22] A. Zhang, Q. Zhang, C.-L. Chen, and R. K. Wang, "Methods and algorithms for optical coherence tomography-based angiography: a review and comparison", Journal of Biomedical Optics **20**, 100901 (2015).

[23] I. M. Vellekoop and A. P. Mosk, "Focusing coherent light through opaque strongly scattering media", Optics Letters **32**, 2309–2311 (2007).

[24] S. M. Popoff, G. Lerosey, R. Carminati, M. Fink, A. C. Boccara, and S. Gigan, "Measuring the transmission matrix in optics: an approach to the study and control of light propagation in disordered media", Physical Review Letters **104**, 100601 (2010).

[25] R. Fiolka, K. Si, and M. Cui, "Complex wavefront corrections for deep tissue focusing using low coherence backscattered light", Optics Express **20**, 16532–16543 (2012).

[26] J. Jang, J. Lim, H. Yu, H. Choi, J. Ha, J.-H. Park, W.-Y. Oh, W. Jang, S. Lee, and Y. Park, "Complex wavefront shaping for optimal depth-selective focusing in optical coherence tomography", Optics Express **21**, 2890–2902 (2013).

[27] H. Yu, J. Jang, J. Lim, J.-H. Park, W. Jang, J.-Y. Kim, and Y. Park, "Depth-enhanced 2-D optical coherence tomography using complex wavefront shaping", Optics Express **22**, 7514–7523 (2014).

[28] H. Yu, P. Lee, K. Lee, J. Jang, J. Lim, W. Jang, Y. Jeong, and Y. Park, "In vivo deep tissue imaging using wavefront shaping optical coherence tomography", Journal of Biomedical Optics **21**, 101406 (2016).

[29] H. Yu, P. Lee, Y. Jo, K. Lee, V. V. Tuchin, Y. Jeong, and Y. Park, "Collaborative effects of wavefront shaping and optical clearing agent in optical coherence tomography", Journal of Biomedical Optics **21**, 121510 (2016).

[30] Y. Choi, T. R. Hillman, W. Choi, N. Lue, R. R. Dasari, P. T. C. So, W. Choi, and Z. Yaqoob, "Measurement of the time-resolved reflection matrix for enhancing light energy delivery into a scattering medium", Physical Review Letters **111**, 243901 (2013).

[31] R. C. Youngquist, S. Carr, and D. E. N. Davies, "Optical coherence-domain reflectometry: A new optical evaluation technique", Optics Letters **12**, 158–160 (1987).

[32] K. Takada, I. Yokohama, K. Chida, and J. Noda, "New measurement system for fault location in optical waveguide devices based on an interferometric technique", Applied Optics **26**, 1603–1606 (1987).

[33] A. F. Fercher, K. Mengedoht, and W. Werner, "Eye-length measurement by interferometry with partially coherent light", Optics Letters **13**, 186–188 (1988).

[34] D. Huang, J. Wang, C. P. Lin, C. A. Puliafito, and J. G. Fujimoto, "Micron-resolution ranging of cornea anterior chamber by optical reflectometry", Lasers in Surgery and Medicine **11**, 419–425 (1991).

[35] A. F. Fercher, C. K. Hitzenberger, W. Drexler, G. Kamp, and H. Sattmann, "In vivo optical coherence tomography", American Journal of Ophthalomology **116**, 113–115 (1993).

[36] E. A. Swanson, J. A. Izatt, M. R. Hee, D. Huang, C. P. Lin, J. S. Schuman, C. A. Puliafito, and J. G. Fujimoto, "In vivo retinal imaging by optical coherence tomography", Optics Letters **18**, 1864–1866 (1993).

[37] J. M. Schmitt, A. R. Knüttel, M. J. Yadlowsky, and M. A. Eckhaus, "Optical-coherence tomography of a dense tissue: statistics of attenuation and backscattering", Physics in Medicine & Biology **39**, 1705–1720 (1994).

[38] J. G. Fujimoto, M. E. Brezinski, G. J. Tearney, S. A. Boppart, B. E. Bouma, M. R. Hee, J. F. Southern, and E. A. Swanson, "Optical biopsy and imaging using optical coherence tomography", Nature Medicine **1**, 970–972 (1995).

[39] M. E. Brezinski, G. J. Tearney, B. E. Bouma, J. A. Izatt, M. R. Hee, E. A. Swanson, J. F. Southern, and J. G. Fujimoto, "Optical coherence tomography for optical biopsy", Circulation **93**, 1206–1213 (1996).

[40] W. Lauterborn and T. Kurz, *Coherent optics, Fundamentals and applications*, 2nd ed. (Springer-Verlag Berlin Heidelberg, 2003).

[41] W. Demtröder, *Laser spectroscopy, Basic concepts and instrumentation* (Springer-Verlag Berlin Heidelberg, 2003).

[42] J. M. Schmitt, "Optical coherence tomography (OCT): a review", IEEE Journal of Selected Topics in Quantum Electronics **5**, 1205–1215 (1999).

[43] A. F. Fercher, W. Drexler, C. K. Hitzenberger, and T. Lasser, "Optical coherence tomography - principles and applications", Reports on Progress in Physics **66**, 239–303 (2003).

[44] J. W. Goodman, *Statistical optics*, 1st ed. (Wiley-Interscience, 2000).

[45] B. Girod, R. Rabenstein, and A. Stenger, *Einführung in die Systemtheorie, Signale und Systeme in der Elektrotechnik und Informationstechnik*, 2nd ed. (Vieweg+Teubner Verlag / Springer Fachmedien Wiesbaden GmbH, Wiesbaden, 2003).

[46] W. Drexler and J. G. Fujimoto, eds., *Optical coherence tomography, Technology and applications* (Springer-Verlag Berlin Heidelberg, 2008).

[47] D. W. Ricker, *Echo signal processing* (Springer Science+Business Media, New York, 2003).

[48] I. N. Bronstein, K. A. Semendjajew, G. Musiol, and H. Mühlig, *Taschenbuch der Mathematik*, 7th ed. (Harri Deutsch, Frankfurt am Main, 2008).

[49] C. Akcay, P. Parrein, and J. P. Rolland, "Estimation of longitudinal resolution in optical coherence imaging", Applied Optics **41**, 5256–5262 (2002).

[50] A. F. Fercher, C. K. Hitzenberger, G. Kamp, and S. Y. El-Zaiat, "Measurement of intraocular distances by backscattering spectral interferometry", Optics Communications **117**, 43–48 (1995).

[51] S. R. Chinn, E. A. Swanson, and J. G. Fujimoto, "Optical coherence tomography using a frequency-tunable optical source", Optics Letters **22**, 340–342 (1997).

[52] M. Wojtkowski, R. A. Leitgeb, A. Kowalczyk, T. Bajraszewski, and A. F. Fercher, "In vivo human retinal imaging by Fourier domain optical coherence tomography", Journal of Biomedical Optics **7**, 457–463 (2002).

[53] R. A. Leitgeb, C. K. Hitzenberger, and A. F. Fercher, "Performance of fourier domain vs. time domain optical coherence tomography", Optics Express **11**, 889–894 (2003).

[54] M. A. Choma, M. V. Sarunic, C. Yang, and J. A. Izatt, "Sensitivity advantage of swept source and Fourier domain optical coherence tomography", Optics Express **11**, 2183–2189 (2003).

[55] J. F. de Boer, B. H. Park, M. C. Pierce, G. J. Tearney, and B. E. Bouma, "Improved signal-to-noise ratio in spectral-domain compared with time-domain optical coherence tomography", Optics Letters **28**, 2067–2069 (2003).

[56] A. F. Fercher, R. A. Leitgeb, C. K. Hitzenberger, H. Sattmann, and M. Wojtkowski, "Complex spectral interferometry OCT", in Medical Applications of Lasers in Dermatology, Cardiology, Ophthalmology, and Dentistry II, Proceedings of SPIE 3564 (International Society for Optics and Photonics, 1999), pp. 173–178.

[57] P. Targowski, M. Wojtkowski, A. Kowalczyk, T. Bajraszewski, M. Szkulmowski, and I. Gorczyńska, "Complex spectral OCT in human eye imaging in vivo", Optics Communications **229**, 79–84 (2004).

[58] M. Wojtkowski, A. Kowalczyk, R. A. Leitgeb, and A. F. Fercher, "Full range complex spectral optical coherence tomography technique in eye imaging", Optics Letters **27**, 1415–1417 (2002).

[59] R. A. Leitgeb, C. K. Hitzenberger, A. F. Fercher, and T. Bajraszewski, "Phase-shifting algorithm to achieve high-speed long-depth range probing by frequency domain optical coherence tomography", Optics Letters **28**, 2201–2203 (2003).

[60] M. V. Sarunic, M. A. Choma, C. Yang, and J. A. Izatt, "Instantaneous complex conjugate resolved spectral domain and swept-source OCT using 3x3 fiber couplers", Optics Express **13**, 957–967 (2005).

[61] M. V. Sarunic, B. E. Applegate, and J. A. Izatt, "Real-time quadrature projection complex conjugate resolved Fourier domain optical coherence tomography", Optics Letters **31**, 2426–2428 (2006).

[62] B. J. Vakoc, S.-H. Yun, G. J. Tearney, and B. E. Bouma, "Elimination of depth degeneracy in optical frequency-domain imaging through polarization based optical demodulation", Optics Letters **31**, 362–364 (2006).

[63] K.-D. Kammeyer and K. Kroschel, *Digitale Signalverarbeitung, Filterung und Spektralanalyse mit MATLAB-Übungen*, 5th ed. (Vieweg+Teubner Verlag / Springer Fachmedien Wiesbaden GmbH, Wiesbaden, 2002).

[64] M. Meyer, *Signalverarbeitung, Analoge und digitale Signale, Systeme und Filter*, 8th ed. (Vieweg+Teubner Verlag / Springer Fachmedien Wiesbaden GmbH, Wiesbaden, 2017).

[65] T. Schmoll, E. Götzinger, M. Pircher, C. K. Hitzenberger, and R. A. Leitgeb, "Single camera polarization sensitive spectral domain OCT by spatial frequency encoding", Optics Letters **35**, 241–243 (2010).

[66] R. F. Lutomirski and H. T. Yura, "Propagation of a finite optical beam in an inhomogenious medium", Applied Optics **10**, 1652–1658 (1971).

[67] R. F. Lutomirski, "Atmospheric degradation of electrooptical system performance", Applied Optics **17**, 3915–3921 (1978).

[68] L. Thrane, H. T. Yura, and P. E. Andersen, "Analysis of optical coherence tomography systems based on the extended Huygens-Fresnel principle", Journal of the Optical Society of America A **17**, 484–490 (2000).

[69] J. M. Schmitt and G. Kumar, "Optical scattering properties of soft tissue: a discrete particle model", Applied Optics **37**, 2788–2797 (1998).

[70] L. G. Henyey and J. L. Greenstein, "Diffuse radiation in the galaxy", Astrophysical Journal **93**, 70–83 (1942).

[71] M. J. C. van Gemert, S. L. Jacques, H. J. C. M. Sterenborg, and W. M. Star, "Skin optics", IEEE Transactions on Biomedical Engineering **36**, 1146–1154 (1989).

[72] W.-F. Cheong, S. A. Prahl, and A. J. Welch, "A review of the optical properties of biological tissues", IEEE Journal of Quantum Electronics **26**, 2166–2185 (1990).

[73] S. L. Jacques, "Optical properties of biological tissues: a review", Physics in Medicine and Biology **58**, R37–R61 (2013).

[74] A. N. Bashkatov, E. A. Genina, and V. V. Tuchin, "Optical properties of skin, subcutaneous, and muscle tissues: a review", Journal of Innovative Optical Health Sciences **4**, 9–38 (2011).

[75] J. A. Parrish, "New concepts in therapeutic photomedicine: photochemistry, optical targeting and the therapeutic window", Journal of Investigative Dermatology **77**, 45–50 (1981).

[76] J. M. Schmitt, A. R. Knüttel, A. H. Gandjbakhche, and R. F. Bonner, "Optical characterization of dense tissues using low-coherence interferometry", in Holography, Interferometry, and Optical Pattern Recognition in Biomedicine III, Proceedings of SPIE 1889 (International Society for Optics and Photonics, 1993), pp. 197–211.

[77] J. M. Schmitt, A. R. Knüttel, and R. F. Bonner, "Measurement of optical properties of biological tissues by low-coherence reflectometry", Applied Optics **32**, 6032–6042 (1993).

[78] M. J. Yadlowsky, J. M. Schmitt, and R. F. Bonner, "Multiple scattering in optical coherence microscopy", Applied Optics **34**, 5699–5707 (1995).

[79] D. J. Smithies, T. Lindmo, Z. Chen, J. S. Nelson, and T. E. Milner, "Signal attenuation and localization in optical coherence tomography studied by Monte Carlo simulation", Physics in Medicine & Biology **43**, 3025–3044 (1998).

[80] I. V. Turchin, E. A. Sergeeva, L. S. Dolin, V. A. Kamensky, N. M. Shakhova, and R. Richards-Kortum, "Novel algorithm of processing OCT images for differentiation of biological tissue pathologies", Journal of Biomedical Optics **10**, 064024 (2005).

[81] Y. Pan, R. Birngruber, and R. Engelhardt, "Contrast limits of coherence-gated imaging in scattering media", Applied Optics **36**, 2979–2983 (1997).

[82] G. Yao and L. V. Wang, "Monte Carlo simulation of an optical coherence tomography signal in homogeneous turbid media", Physics in Medicine and Biology **44**, 2307–2320 (1999).

[83] R. K. Wang, "Signal degradation by multiple scattering in optical coherence tomography of dense tissue: a Monte Carlo study towards optical clearing of biotissues", Physics in Medicine and Biology **47**, 2281–2299 (2002).

[84] M. Pircher and R. J. Zawadzki, "Combining adaptive optics with optical coherence tomography: unveiling the cellular structure of the human retina in vivo", Expert Review of Ophthalmology **2**, 1019–1035 (2014).

[85] F. Roddier, ed., *Adaptive optics in astronomy* (Cambridge University Press, Cambridge, 1999).

[86] R. K. Tyson, *Principles of adaptive optics*, 4th ed. (Chapman and Hall/CRC, Boca Raton, 2015).

[87] M. J. Booth, "Adaptive optics in microscopy", Philosophical Transactions of the Royal Society A - Mathematical, physical, and engineering sciences **365**, 2829–2843 (2007).

[88] D. T. Miller, O. P. Kocaoglu, Q. Wang, and S. Lee, "Adaptive optics and the eye (super resolution OCT)", Eye **25**, 321–330 (2011).

[89] M. J. Booth, "Adaptive optical microscopy: the ongoing quest for a perfect image", Light: Science & Applications **3**, e165 (2014).

[90] R. S. Jonnal, O. P. Kocaoglu, R. J. Zawadzki, Z. Liu, D. T. Miller, and J. S. Werner, "A review of adaptive optics optical coherence tomography: technical advances, scientific applications, and the future", Investigative Ophthalmology & Visual Science **57**, OCT51–68 (2016).

[91] M. Pircher and R. J. Zawadzki, "Review of adaptive optics OCT (AO-OCT): principles and applications for retinal imaging", Biomedical Optics Express **8**, 2536–2562 (2017).

[92] A. Derode, P. Roux, and M. Fink, "Robust acoustic time reversal with high-order multiple scattering", Physical Review Letters **75**, 4206–4210 (1995).

[93] A. Derode, A. Tourin, and M. Fink, "Random multiple scattering of ultrasound. II. is time reversal a self-averaging process?", Physical Review E **64**, 036606 (2001).

[94] F. Lemoult, G. Lerosey, J. de Rosny, and M. Fink, "Manipulating spatiotemporal degrees of freedom of waves in random media", Physical Review Letters **103**, 173902 (2009).

[95] E. N. Leith and J. Upatnieks, "Holographic imagery through diffusing media", Journal of the Optical Society of America **56**, 523 (1966).

[96] Z. Yaqoob, D. Psaltis, M. S. Feld, and C. Yang, "Optical phase conjugation for turbidity suppression in biological samples", Nature Photonics **2**, 110–115 (2008).

[97] M. Cui and C. Yang, "Implementation of a digital optical phase conjugation system and its application to study the robustness of turbidity suppression by phase conjugation", Optics Express **18**, 3444–3455 (2010).

[98] C.-L. Hsieh, Y. Pu, R. Grange, and D. Psaltis, "Digital phase conjugation of second harmonic radiation emitted by nanoparticles in turbid media", Optics Express **18**, 12283–12290 (2010).

[99] C.-L. Hsieh, Y. Pu, R. Grange, G. Laporte, and D. Psaltis, "Imaging through turbid layers by scanning the phase conjugated second harmonic radiation from a nanoparticle", Optics Express **18**, 20723–20731 (2010).

[100] T. R. Hillman, T. Yamauchi, W. Choi, R. R. Dasari, M. S. Feld, Y. Park, and Z. Yaqoob, "Digital optical phase conjugation for delivering two-dimensional images through turbid media", Scientific Reports **3**, 1909 (2013).

[101] M. Cui, E. J. McDowell, and C. Yang, "An in vivo study of turbidity suppression by optical phase conjugation (TSOPC) on rabbit ear", Optics Express **18**, 25–30 (2010).

[102] D. Wang, E. H. Zhou, J. Brake, H. Ruan, M. Jang, and C. Yang, "Focusing through dynamic tissue with millisecond digital optical phase conjugation", Optica **2**, 728–735 (2015).

[103] M. Jang, H. Ruan, I. M. Vellekoop, B. Judkewitz, E. Chung, and C. Yang, "Relation between speckle decorrelation and optical phase conjugation (OPC)-based turbidity suppression through dynamic scattering media: a study on in vivo mouse skin", Biomedical Optics Express **6**, 72–85 (2015).

[104] B. Judkewitz, R. Horstmeyer, I. M. Vellekoop, I. N. Papadopoulos, and C. Yang, "Translation correlations in anisotropically scattering media", Nature Physics **11**, 684–689 (2015).

[105] L. Kong and M. Cui, "In vivo fluorescence microscopy via iterative multi-photon adaptive compensation technique", Optics Express **22**, 23786–23794 (2014).

[106] L. Kong, J. Tang, and M. Cui, "In vivo volumetric imaging of biological dynamics in deep tissue via wavefront engineering", Optics Express **24**, 1214–1221 (2016).

[107] S. Feng, C. Kane, P. A. Lee, and A. D. Stone, "Correlations and fluctuations of coherent wave transmission through disordered media", Physical Review Letters **61**, 834–837 (1988).

[108] I. Freund, "Looking through walls and around corners", Physica A **168**, 49–65 (1990).

[109] X. Xu and L. V. Wang, "Time-reversed ultrasonically encoded optical focusing into scattering media", Nature Photonics **5**, 154–157 (2011).

[110] B. Judkewitz, Y. M. Wang, R. Horstmeyer, A. Mathy, and C. Yang, "Speckle-scale focusing in the diffusive regime with time-reversal of variance-encoded light (TROVE)", Nature Photonics **7**, 300–305 (2013).

[111] E. H. Zhou, H. Ruan, C. Yang, and B. Judkewitz, "Focusing on moving targets through scattering samples", Optica **1**, 227–232 (2014).

[112] Y. Liu, P. Lai, C. Ma, X. Xu, A. A. Grabar, and L. V. Wang, "Optical focusing deep inside dynamic scattering media with near-infrared time-reversed ultrasonically encoded (TRUE) light", Nature Communications **6**, 5904 (2015).

[113] Y. M. Wang, B. Judkewitz, C. A. DiMarzio, and C. Yang, "Deep-tissue focal fluorescence imaging with digitally time-reversed ultrasound-encoded light", Nature Communications **3**, 928 (2012).

[114] K. Si, R. Fiolka, and M. Cui, "Fluorescence imaging beyond the ballistic regime by ultrasound-pulse-guided digital phase conjugation", Nature Photonics **6**, 657–661 (2012).

[115] I. M. Vellekoop, A. Lagendijk, and A. P. Mosk, "Exploiting disorder for perfect focusing", Nature Photonics **4**, 320–322 (2010).

[116] B. R. Anderson, R. Gunawidjaja, and H. Eilers, "Effect of experimental parameters on optimal transmission of light through opaque media", Physical Review A **90**, 053826 (2014).

[117] B. R. Anderson, R. Gunawidjaja, and H. Eilers, "Effect of experimental parameters on optimal reflection of light from opaque media", Physical Review A **93**, 013813 (2016).

[118] I. M. Vellekoop, E. G. van Putten, A. Lagendijk, and A. P. Mosk, "Demixing light paths inside disordered metamaterials", Optics Express **16**, 67–80 (2008).

[119] S. M. Popoff, G. Lerosey, M. Fink, A. C. Boccara, and S. Gigan, "Controlling light through optical disordered media: transmission matrix approach", New Journal of Physics **13**, 123021 (2011).

[120] D. Akbulut, T. J. Huisman, E. G. van Putten, W. L. Vos, and A. P. Mosk, "Focusing light through random photonic media by binary amplitude modulation", Optics Express **19**, 4017–4029 (2011).

[121] O. Katz, E. Small, Y. Bromberg, and Y. Silberberg, "Focusing and compression of ultrashort pulses through scattering media", Nature Photonics **5**, 372–377 (2011).

[122] J. Tang, R. N. Germain, and M. Cui, "Superpenetration optical microscopy by iterative multiphoton adaptive compensation technique", Proceedings of the National Academy of Sciences of the United States of America **109**, 8434–8439 (2012).

[123] O. Katz, E. Small, Y. Guan, and Y. Silberberg, "Noninvasive nonlinear focusing and imaging through strongly scattering turbid layers", Optica **1**, 170–174 (2014).

[124] J. W. Tay, P. Lai, Y. Suzuki, and L. V. Wang, "Ultrasonically encoded wavefront shaping for focusing into random media", Scientific Reports **4**, 3918 (2014).

[125] F. Kong, R. H. Silverman, L. Liu, P. V. Chitnis, K. K. Lee, and Y.-C. Chen, "Photoacoustic-guided convergence of Light through optically diffusive media", Optics Letters **36**, 2053–2055 (2011).

[126] A. M. Caravaca-Aguirre, D. B. Conkey, J. D. Dove, H. Ju, T. W. Murray, and R. Piestun, "High contrast three-dimensional photoacoustic imaging through scattering media by localized optical fluence enhancement", Optics Express **21**, 26671–26676 (2013).

[127] D. B. Conkey, A. M. Caravaca-Aguirre, J. D. Dove, H. Ju, T. W. Murray, and R. Piestun, "Super-resolution photoacoustic imaging through a scattering wall", Nature Communications **6**, 7902 (2015).

[128] P. Lai, L. Wang, J. W. Tay, and L. V. Wang, "Photoacoustically guided wavefront shaping for enhanced optical focusing in scattering media", Nature Photonics **9**, 126–132 (2015).

[129] O. Tzang, E. Niv, A. M. Caravaca-Aguirre, and R. Piestun, "Thermal expansion feedback for wave-front shaping", Optics Express **25**, 6122–6131 (2017).

[130] I. M. Vellekoop and A. P. Mosk, "Phase control algorithms for focusing light through turbid media", Optics Communications **281**, 3071–3080 (2008).

[131] D. B. Conkey, A. N. Brown, A. M. Caravaca-Aguirre, and R. Piestun, "Genetic algorithm optimization for focusing through turbid media in noisy environments", Optics Express **20**, 4840–4849 (2012).

[132] M. Cui, "Parallel wavefront optimization method for focusing light through random scattering media", Optics Letters **36**, 870–872 (2011).

[133] B. Blochet, L. Bourdieu, and S. Gigan, "Focusing light through dynamical samples using fast continuous wavefront optimization", Optics Letters **42**, 4994–4997 (2017).

[134] A. S. Hemphill, J. W. Tay, and L. V. Wang, "Hybridized wavefront shaping for high-speed, high-efficiency focusing through dynamic diffusive media", Journal of Biomedical Optics **21**, 121502 (2016).

[135] D. Feldkhun, O. Tzang, K. H. Wagner, and R. Piestun, "Focusing and scanning through scattering media in microseconds", Optica **6**, 72–75 (2019).

[136] T. Cizmar, M. Mazilu, and K. Dholakia, "In situ wavefront correction and its application to micromanipulation", Nature Photonics **4**, 388–394 (2010).

[137] T. Chaigne, O. Katz, A. C. Boccara, M. Fink, E. Bossy, and S. Gigan, "Controlling light in scattering media non-invasively using the photoacoustic transmission matrix", Nature Photonics **8**, 58–64 (2014).

[138] S. M. Popoff, G. Lerosey, M. Fink, A. C. Boccara, and S. Gigan, "Image transmission through an opaque material", Nature Communications **1**, 81 (2010).

[139] Y. Choi, T. D. Yang, C. Fang-Yen, P. Kang, K. J. Lee, R. R. Dasari, M. S. Feld, and W. Choi, "Overcoming the diffraction limit using multiple light scattering in a highly disordered medium", Physical Review Letters **107**, 023902 (2011).

[140] S. M. Popoff, A. Aubry, G. Lerosey, M. Fink, A. C. Boccara, and S. Gigan, "Exploiting the time-reversal operator for adaptive optics, selective focusing, and scattering pattern analysis", Physical Review Letters **107**, 263901 (2011).

[141] H. Yu, J.-H. Park, and Y. Park, "Measuring large optical reflection matrices of turbid media", Optics Communications **352**, 33–38 (2015).

[142] C. Prada, S. Manneville, D. Spoliansky, and M. Fink, "Decomposition of the time reversal operator: detection and selective focusing on two scatterers", Journal of the Acoustical Society of America **99**, 2067–2076 (1996).

[143] A. Badon, D. Li, G. Lerosey, A. C. Boccara, M. Fink, and A. Aubry, "Smart optical coherence tomography for ultra-deep imaging through highly scattering media", Science Advances **2**, e1600370 (2016).

[144] S. Jeong, Y.-R. Lee, W. Choi, S. Kang, J. H. Hong, J.-S. Park, Y.-S. Lim, H.-G. Park, and W. Choi, "Focusing of light energy inside a scattering medium by controlling the time-gated multiple light scattering", Nature Photonics **12**, 277–283 (2018).

[145] S. Kang, S. Jeong, W. Choi, H. Ko, T. D. Yang, J. H. Joo, J.-S. Lee, Y.-S. Lim, Q.-H. Park, and W. Choi, "Imaging deep within a scattering medium using collective accumulation of single-scattered waves", Nature Photonics **9**, 253–258 (2015).

[146] S. Kang, P. Kang, S. Jeong, Y. Kwon, T. D. Yang, J. H. Hong, M. Kim, K.-D. Song, J. H. Park, J. H. Lee, M. J. Kim, K. H. Kim, and W. Choi, "High-resolution adaptive optical imaging within thick scattering media using closed-loop accumulation of single scattering", Nature Communications **8**, 2157 (2017).

[147] Q. Yang, Y. Miao, T. Huo, Y. Li, E. Heidari, J. Zhu, and Z. Chen, "Deep imaging in highly scattering media by combining reflection matrix measurement with Bessel-like beam based optical coherence tomography", Applied Physics Letters **113**, 011106 (2018).

[148] A. Badon, V. Barolle, K. Irsch, A. C. Boccara, M. Fink, and A. Aubry, *Distortion matrix concept for deep imaging in optical coherence microscopy*, arXiv:1910.07252v1, 2019.

[149] D. J. McCabe, A. Tajalli, D. R. Austin, P. Bondareff, I. A. Walmsley, S. Gigan, and B. Chatel, "Spatio-temporal focusing of an ultrafast pulse through a multiply scattering medium", Nature Communications **2**, 447 (2011).

[150] E. Small, O. Katz, Y. Guan, and Y. Silberberg, "Spectral control of broadband light through random media by wavefront shaping", Optics Letters **37**, 3429–3431 (2012).

[151] J. Aulbach, B. Gjonaj, P. M. Johnson, A. P. Mosk, and A. Lagendijk, "Control of light transmission through opaque scattering media in space and time", Physical Review Letters **106**, 103901 (2011).

[152] M. Mounaix, H. Defienne, and S. Gigan, "Deterministic light focusing in space and time through multiple scattering media with a time-resolved transmission matrix approach", Physical Review A **94**, 041802 (2016).

[153] M. Mounaix, D. M. Ta, and S. Gigan, "Transmission matrix approaches for nonlinear fluorescence excitation through multiple scattering media", Optics Letters **43**, 2831–2834 (2018).

[154] J.-H. Park, C. Park, H. Yu, Y.-H. Cho, and Y. Park, "Active spectral filtering through turbid media", Optics Letters **37**, 3261–3263 (2012).

[155] F. van Beijnum, E. G. van Putten, A. Lagendijk, and A. P. Mosk, "Frequency bandwidth of light focused through turbid media", Optics Letters **36**, 373–375 (2011).

[156] D. Andreoli, G. Volpe, S. M. Popoff, O. Katz, S. Grésillon, and S. Gigan, "Deterministic control of broadband light through a multiply scattering medium via the multispectral transmission matrix", Scientific Reports **5**, 10347 (2015).

[157] M. Mounaix, D. Andreoli, H. Defienne, G. Volpe, O. Katz, S. Grésillon, and S. Gigan, "Spatiotemporal coherent control of light through a multiple scattering medium with the multispectral transmission matrix", Physical Review Letters **116**, 253901 (2016).

[158] H. P. Paudel, C. Stockbridge, J. Mertz, and T. Bifano, "Focusing polychromatic light through strongly scattering media", Optics Express **21**, 17299–17308 (2013).

[159] R. Fiolka and M. Cui, "High speed phase distortion measurement and compensation for focusing in space and time", in Three-Dimensional and Multidimensional Microscopy: Image Acquisition and Processing XX, Proceedings of SPIE 8589 (International Society for Optics and Photonics, 2013), p. 85890V.

[160] W. Choi, M. Kim, D. Kim, C. Yoon, C. Fang-Yen, Q.-H. Park, and W. Choi, "Preferential coupling of an incident wave to reflection eigenchannels of disordered media", Scientific Reports **5**, 11393 (2015).

[161] S. Jeong, D.-Y. Kim, Y.-R. Lee, W. Choi, and W. Choi, "Iterative optimization of time-gated reflectance for the efficient light energy delivery within scattering media", Optics Express **27**, 10936 (2019).

[162] J. Kanngiesser, M. Rahlves, and B. Roth, "Double interferometer design for independent wavefront manipulation in spectral domain optical coherence tomography", Scientific Reports **9**, 14651 (2019).

[163] M. Davidson, K. Kaufman, I. Mazor, and F. Cohen, "An application of interference microscopy to integrated circuit inspection and metrology", in Integrated Circuit Metrology, Inspection, & Process Control, Vol. 0775, Proceedings of SPIE 0775 (International Society for Optics and Photonics, 1987), pp. 233–247.

[164] A. Dubois, L. Vabre, A. C. Boccara, and E. Beaurepaire, "High-resolution full-field optical coherence tomography with a Linnik microscope", Applied Optics **41**, 805–812 (2002).

[165] J. Bush, P. G. Davis, and M. A. Marcus, "All-fiber optic coherence domain interferometric techniques", in Fiber Optic Sensor Technology II, Proceedings of SPIE 4204 (International Society for Optics and Photonics, 2000), pp. 71–80.

[166] F. Feldchtein, J. Bush, G. Gelikonov, V. Gelikonov, and S. Piyevsky, "Cost-effective all-fiber autocorrelator-based 1300-nm OCT system", in Coherence Domain Optical Methods and Optical Coherence Tomography in Biomedicine IX, Proceedings of SPIE 5690 (International Society for Optics and Photonics, 2005), pp. 349–355.

[167] U. Sharma, N. M. Fried, and J. U. Kang, "All-fiber common-path optical coherence tomography: sensitivity optimization and system analysis", IEEE Journal of Selected Topics in Quantum Electronics **11**, 799–805 (2005).

[168] A. H. Bachmann, R. Michaely, T. Lasser, and R. A. Leitgeb, "Dual beam heterodyne Fourier domain optical coherence tomography", Optics Express **15**, 9254–9266 (2007).

[169] S. Vergnole, G. Lamouche, M. Dufour, and B. Gauthier, "Common path swept-source OCT interferometer with artifact removal", in Coherence Domain Optical Methods and Optical Coherence Tomography in Biomedicine XII, Proceedings of SPIE 6847 (International Society for Optics and Photonics, 2008), 68472W.

[170] J. S. Park, Z. Chen, M. Y. Jeong, and C.-S. Kim, "Double common-path interferometer for flexible optical probe of optical coherence tomography", Optics Express **20**, 1102–1112 (2012).

[171] C. Wang, Q. Zhang, Y. Wang, X. Zhang, and L. Zhang, "Long-range common-path spectral domain optical coherence tomography", Optics Express **27**, 12483–12490 (2019).

[172] Holoeye Photonics AG, ed., *PLUTO phase only spatial light modulators, Device operating instructions*, version 2.13, 2017.

[173] N. Collings, T. Davey, J. Christmas, D. Chu, and B. Crossland, "The applications and technology of phase-only liquid crystal on silicon devices", Journal of Display Technology **7**, 112–119 (2011).

[174] L. M. Blinov and V. G. Chigrinov, *Electrooptic effects in liquid crystal materials* (Springer New York, New York, 1994).

[175] Z. Zhang, Z. You, and D. Chu, "Fundamentals of phase-only liquid crystal on silicon (LCOS) devices", Light: Science & Applications **3**, e213 (2014).

[176] F. Li, N. Mukohzaka, N. Yoshida, Y. Igasaki, H. Toyoda, T. Inoue, Y. Kobayashi, and T. Hara, "Phase modulation characteristics analysis of optically-addressed parallel-aligned nematic liquid crystal phase-only spatial light modulator combined with a liquid crystal display", Optical Review **5**, 174–178 (1998).

[177] J. L. M. Fuentes, E. J. Fernández, P. M. Prieto, and P. Artal, "Interferometric method for phase calibration in liquid crystal spatial light modulators using a self-generated diffraction-grating", Optics Express **24**, 14159–14171 (2016).

[178] A. Farre, M. Shayegan, C. Lopez-Quesada, G. A. Blab, M. Montes-Usategui, N. R. Forde, and E. Martin-Badosa, "Positional stability of holographic optical traps", Optics Express **19**, 21370–21384 (2011).

[179] A. Kramida, Y. Ralchenko, J. Reader, and NIST ASD Team, *NIST Atomic Spectra Database (ver. 5.6.1)*, National Institute of Standards and Technology, 2018, `https://physics.nist.gov/asd` (visited on 07/17/2019).

[180] O. Katz, P. Heidemann, M. Fink, and S. Gigan, "Non-invasive single-shot imaging through scattering layers and around corners via speckle correlations", Nature Photonics **8**, 784–790 (2014).

[181] J. Bertolotti, E. G. van Putten, C. Blum, A. Lagendijk, W. L. Vos, and A. P. Mosk, "Non-invasive imaging through opaque scattering layers", Nature **491**, 232–234 (2012).

[182] J. Kanngiesser, *Numerical calculation of the SD-OCT signal expected with a double interferometer design*, `https://doi.org/10.6084/m9.figshare.9708083.v2`.

[183] J. Kanngiesser, M. Rahlves, and B. Roth, "Iterative wavefront correction for complex spectral domain optical coherence tomography", Optics Letters **44**, 1347–1350 (2019).

[184] J. M. Schmitt, S. Xiang, and K. M. Yung, "Speckle in optical coherence tomography", Journal of Biomedical Optics **4**, 95–105 (1999).

[185] Y. Jian, J. Xu, M. A. Gradowski, S. Bonora, R. J. Zawadzki, and M. V. Sarunic, "Wavefront sensorless adaptive optics optical coherence tomography for in vivo retinal imaging in mice", Biomedical Optics Express **5**, 547–559 (2014).

[186] J. Kanngiesser and B. Roth, "Effect of image artefacts on phase conjugation with spectral domain optical coherence tomography", Optics Express **28**, 18224–18240 (2020).

[187] R. K. Tyson, *Principles and applications of Fourier optics* (IOP Publishing, Bristol, 2014).

[188] O. Liba, M. D. Lew, E. D. SoRelle, R. Dutta, D. Sen, D. M. Moshfeghi, S. Chu, and A. de la Zerda, "Speckle-modulating optical coherence tomography in living mice and humans", Nature Communications **8**, 15845 (2017).

[189] A. P. Mosk, A. Lagendijk, G. Lerosey, and M. Fink, "Controlling waves in space and time for imaging and focusing in complex media", Nature Photonics **6**, 283–292 (2012).

[190] A. Z. Genack and J. M. Drake, "Relationship between optical intensity, fluctuations and pulse propagation in random media", Europhysics Letters **11**, 331–336 (1990).

[191] M. A. Webster, K. J. Webb, A. M. Weiner, J. Xu, and H. Cao, "Temporal response of a random medium from speckle intensity frequency correlations", Journal of the Optical Society of America A **20**, 2057–2070 (2003).

[192] M. Mounaix, H. B. de Aguiar, and S. Gigan, "Temporal recompression through a scattering medium via a broadband transmission matrix", Optica **4**, 1289 (2017).

[193] E. Small, O. Katz, and Y. Silberberg, "Spatiotemporal focusing through a thin scattering layer", Optics Express **20**, 5189–5195 (2012).

[194] D. B. Conkey, A. M. Caravaca-Aguirre, and R. Piestun, "High-speed scattering medium characterization with application to focusing light through turbid media", Optics Express **20**, 1733–1740 (2011).

[195] M. Couteaudier and C. Denesvre, "Marek's disease virus and skin interactions", Veterinary Research **45**, 36 (2014).

[196] Z. Ding, H. Ren, Y. Zhao, J. S. Nelson, and Z. Chen, "High-resolution optical coherence tomography over a large depth range with an axicon lens", Optics Letters **27**, 243–245 (2002).

[197] R. A. Leitgeb, M. Villiger, A. H. Bachmann, L. Steinmann, and T. Lasser, "Extended focus depth for Fourier domain optical coherence microscopy", Optics Letters **31**, 2450–2452 (2006).

[198] C. Stockbridge, Y. Lu, J. Moore, S. Hoffman, R. G. Paxman, K. C. Toussaint, and T. Bifano, "Focusing through dynamic scattering media", Optics Express **20**, 15086–15092 (2012).

[199] O. Tzang, E. Niv, S. Singh, S. Labousse, G. Myatt, and R. Piestun, *Wavefront shaping in complex media at 350 kHz with a 1D to 2D transform*, arXiv:1808.09025, 2018.

[200] D. J. Fechtig, B. Grajciar, T. Schmoll, C. Blatter, R. M. Werkmeister, W. Drexler, and R. A. Leitgeb, "Line-field parallel swept source MHz OCT for structural and functional retinal imaging", Biomedical Optics Express **6**, 716–735 (2015).

[201] M. V. Sarunic, S. Weinberg, and J. A. Izatt, "Full-field swept source phase microscopy", Optics Letters **31**, 1462–1464 (2006).

Resume – Jonas Peter Kanngießer

born 23.01.1991 in Rotenburg an der Fulda (Germany)
Married

Education

04/2014 – 09/2016 **Master of Science (Physics)**
Leibniz Universität Hannover
Master thesis: *Pyro- und piezoelektrische Antwort dünner PVDF-Folien auf kurze Laserpulse*

04/2011 – 03/2014 **Bachelor of Science (Physics)**
Philipps-Universität Marburg
Bachelor thesis: *Entwicklung und Test eines Shuttersystems für die Zweiphotonen Photoemission*

09/2001 – 07/2010 **Abitur**
Jakob-Grimm-Schule, Rotenburg an der Fulda

Professional Experience

05/2020 **Software Developer**
MeKo Laser Material Processing, Sarstedt

10/2019 – 04/2020 **Research Assistant**
Cluster of Excellence PhoenixD, Leibniz Universität Hannover

10/2016 – 10/2019 **Research Assistant (scholarship)**
PhD Program Tailored Light, Leibniz Universität Hannover

Scholarships

10/2016 – 10/2019 **Georg-Christoph-Lichtenberg-Stipendium**
Lower Saxony Ministry for Culture and Science (MWK)

2014 **Niedersachsenstipendium**

List of Publications

Peer reviewed articles

J. Kanngiesser, and B. Roth, "Effect of image artefacts on phase conjugation with spectral domain optical coherence tomography", Optics Express **28**(12), 18224–18240 (2020)

J. Kanngiesser, M. Rahlves, and B. Roth, "Double interferometer design for independent wavefront manipulation in spectral domain optical coherence tomography", Scientific Reports **9**, 14651 (2019)

J. Kanngiesser, M. Rahlves, and B. Roth, "Iterative wavefront correction for complex spectral domain optical coherence tomography", Optics Letters **44**(6), 1347–1350 (2019)

E. Blumenröther, O. Melchert, J. Kanngiesser, M. Wollweber, and B. Roth, "Single transparent piezoelectric detector for optoacoustic sensing - design and signal processing", Sensors **19**(9), 2195 (2019)

Proceedings

J. Kanngiesser, M. Rahlves, and B. Roth, "Fast wavefront manipulation for OCT signal enhancement", in DGaO-Proceedings 2019 (Deutsche Gesellschaft für angewandte Optik, 2019), paper no. A2

J. Kanngiesser, M. Rahlves, and B. Roth, "Wavefront shaping in complex spectral domain optical coherence tomography (CSD-OCT)", in Proceedings of EOS topical meeting on Waves in Complex Photonics Media: Fundamentals and Device Applications (European Optical Society, 2018)

J. Kanngiesser, M. Rahlves, and B. Roth, "OCT-based wavefront shaping: towards OCT image enhancement and depth-selective focusing", in Imaging and Applied Optics 2018 (3D, AO, AIO, COSI, DH, IS, LACSEA, LS&C, MATH, pcAOP) (Optical Society of America, 2018), paper no. AW2A.3

J. Kanngiesser, M. Rahlves, and B. Roth, "OCT-guided wavefront shaping for non-invasive depth-selective focusing", in DGaO-Proceedings 2018 (Deutsche Gesellschaft für angewandte Optik, 2018), paper no. A15

J. Kanngiesser, M. Rahlves, and B. Roth, "Focusing light through turbid media: methods and imaging applications", in DGaO-Proceedings 2017 (Deutsche Gesellschaft für angewandte Optik, 2017), paper no. A28

Presentations

J. Kanngiesser, and B. Roth, "Exploiting the optical reflection matrix for OCT signal enhancement", Conference on Lasers & Electro-Optics / Europe and European Quantum Electronics Electronics Conference (CLEO / Europe – EQEC), Munich, Germany, paper no. CH-10.5 (2019)

J. Kanngiesser, M. Rahlves, and B. Roth, "Fast wavefront manipulation for OCT signal enhancement", 120th annual meeting of the German Optical Society (Deutsche Gesellschaft für angewandte Optik DGAO), Darmstadt, Germany, paper no. A2 (2019)

J. Kanngiesser, M. Rahlves, and B. Roth, "Wavefront shaping in complex spectral domain optical coherence tomography (CSD-OCT)", EOS topical meeting on Waves in Complex Photonics Media: Fundamentals and Device Applications, Anacapri, Italy (2018)

J. Kanngiesser, M. Rahlves, and B. Roth, "OCT-based wavefront shaping: towards OCT image enhancement and depth-selective focusing", OSA Imaging and Applied Optics 2018 (3D, AO, AIO, COSI, DH, IS, LACSEA, LS&C, MATH, pcAOP), Orlando, United States, paper no. AW2A.3 (2018)

J. Kanngiesser, M. Rahlves, and B. Roth, "OCT-guided wavefront shaping for non-invasive depth-selective focusing", 119th annual meeting of the German Optical Society (Deutsche Gesellschaft für angewandte Optik DGAO), Aalen, Germany, paper no. A15 (2018)

J. Kanngiesser, M. Rahlves, and B. Roth, "Focusing light through turbid media: methods and imaging applications", 118th annual meeting of the German Optical Society (Deutsche Gesellschaft für angewandte Optik DGAO), Dresden, Germany, paper no. A28 (2017)

Poster presentations

J. Kanngiesser, and B. Roth, "Utilizing the depth-gated reflection matrix for spectral domain optical coherence tomography imaging", Adaptive Optics and Wavefront Control for Biological Systems VI, BiOS 2020, San Francisco, United States, paper no. 11248-336 (2020)

Other

J. Kanngiesser, "Numerical calculation of the SD-OCT signal expected with a double interferometer design", Figshare, `https://doi.org/10.6084/m9.figshare.9708083.v2`

Danksagung - Acknowledgements

Dieses Arbeit wäre ohne eine Reihe von besonders engagierten Menschen nicht, oder zumindest nicht in dieser Form, möglich gewesen. Die Arbeit wurde durch das Forschungsprojekt *Tailored Light*, finanziert vom Niedersächsischen Ministerium für Wissenschaft und Kultur (MWK, Projekt Nr. 78904-63-6/16), und teilweise durch das Exzellenzcluster *PhoenixD*, finanziert durch die Deutsche Forschungsgemeinschaft (DFG, Projekt Nr. 390833453), unterstützt. Besonders bedanken möchte ich mich bei Prof. Berhard Roth, Prof. Roland Lachmeyer und bei Dr. Maik Rahlves, die das Projekt *Tailored Light* erfolgreich eingeworben und geleitet haben, sowie bei Dr. Alexander Wolf, der das Projekt im Unialltag führte und für uns als Doktoranden immer als kompetenter und engagierter Ansprechpartner zur Verfügung stand.

Ich möchte mich darüber hinaus bei Herrn Prof. Roth und bei Dr. Merve Wollweber für die Unterstützung beim Verfassen der Arbeit bedanken, sowie für die Zeit und Mühe die Herr Roth, ebenso wie Herr Prof. Heisterkamp und Herr Prof. Kowalsky, in die Ausarbeitung der Gutachten und in die Vorbereitung der Promotionsprüfung gesteckt haben.

Des Weiteren wäre die Arbeit nicht ohne die langjährige Unterstützung meiner Kolleginnen und Kollegen am Hannoverschen Zentrum für Optische Technologien möglich gewesen. In guter Erinnerung sind mir insbesondere Elias, der mich schon als Student betreut und von manchen Irrwegen abgehalten hat, Arthur, Martin und Sebastian geblieben, sowie Dierk, der im selben Forschungsprojekt promovierte und der als "last man standing" bis zuletzt mit mir Stellung im Büro bezog. Gabi und Vera, die das langjährige Herz des Institutes darstellen, ermöglichten es uns durch ihre Unterstützung erst den Forschungsalltag zu meistern und verdienen eine besondere Anerkennung.

Nicht zuletzt möchte ich mich bei meiner Familie bedanken. Das Studium und das anschließende Promotionsverfahren wäre nicht ohne die finanzielle und moralische Unterstützung durch meine Eltern möglich gewesen. Mein besonderer Dank gilt meiner Frau Kathleen, die während der langen Zeit und auch dann, wenn ich mal wieder einen Abend oder ein ganzes Wochenende damit verbrachte an dieser Forschungsarbeit zu schreiben, trotz allem immer zu mir hielt und mich unterstützte. Und ja, auch unser vierbeiniger Begleiter stand uns beiden während dieser Zeit immer treu zur Seite und verdient ein kleines Dankeschön.